NUREG/CR-7226

U.S.NRC
United States Nuclear Regulatory Commission
*Protecting People and the Environment*

# Primary Water Stress Corrosion Cracking of High-Chromium, Nickel-Base Welds Near Dissimilar Metal Weld Interfaces

Office of Nuclear Regulatory Research

# AVAILABILITY OF REFERENCE MATERIALS IN NRC PUBLICATIONS

## NRC Reference Material

As of November 1999, you may electronically access NUREG-series publications and other NRC records at the NRC's Public Electronic Reading Room at http://www.nrc.gov/reading-rm.html. Publicly released records include, to name a few, NUREG-series publications; *Federal Register* notices; applicant, licensee, and vendor documents and correspondence; NRC correspondence and internal memoranda; bulletins and information notices; inspection and investigative reports; licensee event reports; and Commission papers and their attachments.

NRC publications in the NUREG series, NRC regulations, and Title 10, "Energy," in the *Code of Federal Regulations* may also be purchased from one of these two sources.

1. **The Superintendent of Documents**
   U.S. Government Publishing Office
   Mail Stop SSOP
   Washington, DC 20402-0001
   Internet: http://bookstore.gpo.gov
   Telephone: 1-866-512-1800
   Fax: (202) 512-2104

2. **The National Technical Information Service**
   5301 Shawnee Road
   Alexandria, VA 22161-0002
   http://www.ntis.gov
   1-800-553-6847 or, locally, (703) 605-6000

A single copy of each NRC draft report for comment is available free, to the extent of supply, upon written request as follows:

**U.S. Nuclear Regulatory Commission**
Office of Administration
Publications Branch
Washington, DC 20555-0001
E-mail: distribution.resource@nrc.gov
Facsimile: (301) 415-2289

Some publications in the NUREG series that are posted at the NRC's Web site address http://www.nrc.gov/reading-rm/doc-collections/nuregs are updated periodically and may differ from the last printed version. Although references to material found on a Web site bear the date the material was accessed, the material available on the date cited may subsequently be removed from the site.

## Non-NRC Reference Material

Documents available from public and special technical libraries include all open literature items, such as books, journal articles, transactions, *Federal Register* notices, Federal and State legislation, and congressional reports. Such documents as theses, dissertations, foreign reports and translations, and non-NRC conference proceedings may be purchased from their sponsoring organization.

Copies of industry codes and standards used in a substantive manner in the NRC regulatory process are maintained at—

**The NRC Technical Library**
Two White Flint North
11545 Rockville Pike
Rockville, MD 20852-2738

These standards are available in the library for reference use by the public. Codes and standards are usually copyrighted and may be purchased from the originating organization or, if they are American National Standards, from—

**American National Standards Institute**
11 West 42nd Street
New York, NY 10036-8002
http://www.ansi.org
(212) 642-4900

Legally binding regulatory requirements are stated only in laws; NRC regulations; licenses, including technical specifications; or orders, not in NUREG-series publications. The views expressed in contractor-prepared publications in this series are not necessarily those of the NRC.

The NUREG series comprises (1) technical and administrative reports and books prepared by the staff (NUREG-XXXX) or agency contractors (NUREG/CR-XXXX), (2) proceedings of conferences (NUREG/CP-XXXX), (3) reports resulting from international agreements (NUREG/IA-XXXX), (4) brochures (NUREG/BR-XXXX), and (5) compilations of legal decisions and orders of the Commission and Atomic and Safety Licensing Boards and of Directors' decisions under Section 2.206 of NRC's regulations (NUREG-0750).

NUREG/CR-7226

U.S.NRC
United States Nuclear Regulatory Commission
*Protecting People and the Environment*

# Primary Water Stress Corrosion Cracking of High-Chromium, Nickel-Base Welds Near Dissimilar Metal Weld Interfaces

Manuscript Completed: February 2016
Date Published: January 2018

Prepared by:
B. Alexandreanu, Y. Chen, K. Natesan, and W. J. Shack

Argonne National Laboratory
Argonne, IL 60439

M. Audrain, NRC Project Manager

Office of Nuclear Regulatory Research

# ABSTRACT

The report summarizes the results of a testing program to evaluate the stress corrosion cracking (SCC) susceptibility at or near the interface between Alloy 52 and 152 weld metals and other weld or base metals. Alloys 52 and 152 are high-chromium weld metals used in reactor pressure vessel head penetration nozzles and as overlays, inlays, or onlays for dissimilar metal piping welds. Alloys 52 and 152 typically show very low SCC growth rates in laboratory testing and are not known to have cracked in service. Nevertheless questions remain as to whether the localized dilution of chromium content or the presence of microstructural features near the interface with the low-chromium weld metals Alloy 82 and 182, as in the case of a weld overlay (WOL), or with steel, as in the case of a head penetration nozzle, could affect the SCC response. For this study, SCC growth rates were measured on a WOL mockup with Alloy 52M (a compositional variant of Alloy 52) on Alloy 182 and on a butt weld mockup with Alloy 152 joined to low-alloy steel (LAS). For the WOL mockup, tests were performed in which the crack growth direction was either from Alloy 182 directly into Alloy 52M or along their interface. In the butt weld mockup, measurements were made in the first layer of weld butter beads, within about 1 mm of the interface with LAS. The tests on both mockups resulted in crack growth rates in Alloy 52M and 152 that are higher than have been previously reported for the weld metals, even though the dendrites were not favorably oriented for cracking. In the WOL mockup, crack branching along the interface was observed when the cracking direction was perpendicular to the interface. In the butt weld mockup, material compositional analyses taken along the crack path indicated that locations with the highest measured crack growth rates did not necessarily correlate with the lowest chromium content. This suggests that microstructural factors, in addition to the chromium content, could affect the SCC susceptibility near the interface.

# FOREWORD

This report describes a study sponsored by the NRC Office of Nuclear Regulatory Research (RES) to investigate the stress corrosion cracking (SCC) susceptibility at or near the interface between Alloy 52 and 152 weld metals and other weld or base metals. SCC of nickel-based weld metals, such as those used for reactor vessel head penetration nozzles and reactor coolant system nozzles, is a degradation mechanism that can affect the operational safety of pressurized water reactors (PWRs). For instance, through-wall cracking was detected in an Alloy 82 and 182 hot leg nozzle weld at the V.C. Summer plant in 2000. Alloys 52 and 152 are thought to be more resistant to SCC than Alloys 82 and 182 because of higher chromium content, and there is no operational experience of their cracking in service. In light of the positive service history and low crack growth rates measured in laboratory testing sponsored by the industry, utilities have submitted requests to the Office of Nuclear Reactor Regulation (NRR) for relief from the inspection requirements found in Title 10 of the Code of Federal Regulations, Section 50.55a, including a 10 year interval for volumetric examination of pressure vessel head nozzles.

In the course of reviewing the relief requests and test results from industry-sponsored research, RES and NRR staff raised questions with respect to the potential for SCC susceptibility to be enhanced by localized dilution of chromium in the Alloy 52 and 152 weld metals near interfaces with other weld or base metals. These include interfaces with Alloys 82 and 182 in the case of weld overlays (WOLs), inlays, and onlays, or with stainless and low-alloy steel (LAS) in vessel head penetration nozzles and piping welds. For this study, SCC growth rates were measured on a WOL mockup with Alloy 52M (a compositional variant of Alloy 52) deposited on Alloy 182 and on a butt weld mockup with Alloy 152 joined to LAS. For the WOL mockup, tests were performed in which the crack growth direction was both normal to and along the weld metal interfaces. In the butt weld mockup, measurements were made in the first layer of weld butter beads, within 1 mm of the interface with LAS.

The tests on both mockups resulted in crack growth rates in Alloy 52M or 152 that were higher than have been reported in previous tests for the weld metals, and similar to those typically found in Alloys 82 and 182. In the WOL mockup, crack branching along the interface was observed even when the test was intended to propagate the crack perpendicular to the interface, suggesting high SCC susceptibility at the interface between the two welds. In the butt weld mockup, material compositional analyses taken along the crack path indicated that locations with the highest measured crack growth rate did not necessarily correlate with the lowest chromium content. This suggests that microstructural factors, in addition to the chromium content, could affect the SCC susceptibility near the interface.

These data highlighted to both NRC and the industry the need for additional testing at weld interfaces to better understand the mechanistic basis for the reported behavior. The application of the test results to plant components is particularly challenging given the large number of potential variations in weld designs and configurations that are found in service. Nevertheless, such tests are ongoing and will continue to inform the evaluations by NRR to determine whether inspections for components with Alloy 52 and 152 welds provide a reasonable assurance of safety.

# TABLE OF CONTENTS

**ABSTRACT** ..... **iii**

**FOREWORD** ..... **v**

**TABLE OF CONTENTS** ..... **vii**

**LIST OF FIGURES** ..... **ix**

**LIST OF TABLES** ..... **xix**

**EXECUTIVE SUMMARY** ..... **xxi**

**ACKNOWLEDGMENTS** ..... **xxiii**

**ABBREVIATIONS AND ACRONYMS** ..... **xxv**

**1 INTRODUCTION** ..... **1**

**2 EXPERIMENTAL SETUP AND METHODOLOGY** ..... **3**
2.1 Alloy 52M WOL ..... 3
2.2 Alloy 690 to Alloy 533 Grade B Joint ..... 3
2.2.1 Alloy 152 Weld Buttering ..... 4
2.2.2 Alloy 152 Butt Weld ..... 5
2.3 CT Specimens ..... 5
2.4 PWSCC Test Facilities ..... 6
2.5 CGR Test Methodology ..... 9
2.6 Analysis of CGR Data ..... 11

**3 RESULTS** ..... **17**
3.1 SCC CGR Testing of Alloy 52M WOL ..... 17
3.1.1 Specimen A52M-182-TS-3 ..... 17
3.1.2 Specimen A52M-182-TS-1 ..... 36
3.1.3 SCC Along the Alloy 52M-182 Interface, Specimen WOL-ST-1 ..... 49
3.1.4 SCC in Alloy 52M Near the Interface with Alloy 182, Specimen WOL-ST-2 ..... 65
3.2 SCC CGR Testing of Alloy 152-LAS 1st Dilution Layer ..... 86
3.2.1 SCC CGR Test on 1st layer Alloy 152 Weld Butter Specimen N152-LAS-1 ..... 86
3.2.2 SCC CGR Test on 1st Layer Alloy 152 Weld Butter Specimen N152-LAS-11 ..... 105

**4 DISCUSSION** ..... **127**
4.1 SCC CGR Response of Alloy 52M WOL ..... 127
4.2 1st Layer Alloy 152-LAS Cyclic and SCC CGR Response ..... 129
4.3 Comparison of Cyclic and SCC CGR Responses in 1st Layer Alloy 152-LAS and 1st Layer Alloy 52M-182 WOL ..... 130

4.4 The Effect of Local Cr Concentration and that of the Substrate on the Cyclic and SCC CGR Response of a Cr-Depleted 1st Layer High Cr Ni-Base Weldment ..... 131

**5 CONCLUSIONS ..... 133**

**6 REFERENCES ..... 135**

# LIST OF FIGURES


Figure 2-1 (a) Conceptual schematic (units in inch), and (b) photograph of the resulting Alloy 52M-182 weld overlay. The continuous welded restraints used during the Alloy 52M WOL deposition are visible in the photograph. ..... 3

Figure 2-2 Joint design, Alloy 690 to SA-533 Gr B. Units are in inch..... 4

Figure 2-3 Configuration of the (a) 1-T and (b) ½-T CT specimens used for this study. Dimensions are in mm. ..... 6

Figure 2-4 Layout of the 2-liter SCC test system. ..... 7

Figure 2-5 Photograph of the specimen load train for the 2-liter autoclave ..... 7

Figure 2-6 Schematic diagram of the recirculating 2-liter autoclave system. ..... 8

Figure 2-7 Principle of crack length measurement by the DC potential method. ..... 9

Figure 2-8 CGRs in air and environment for Alloys 600, 690 and Ni-base welds as a function of predicted rates in air for Alloy 600 (data taken from Refs. 12, 13, 20). ..... 13

Figure 2-9 Cyclic CGRs for typical Ni-base weld tested in a PWR environment. Expected corrosion fatigue (Eq. 7, green) and SCC (Eq. 9, blue) curves are included. ..... 14

Figure 2-10 (a) Cyclic CGR data for the Alloy 152 weld tested in primary water environment, and (b) Alloy 152 weld produced in a double-J geometry. ..... 15

Figure 3-1 Photograph of the Alloy 52M-182 WOL. The SCC CGR test directions, TS and ST, are indicated in the figure. ..... 17

Figure 3-2 Photograph of Alloy 52M-182 WOL specimen A52M-182-TS-3 prior to the SCC test. ..... 18

Figure 3-3 Crack–length–vs.–time for specimen A52M-182-TS-3 in simulated PWR environment during test periods: (a) precracking-4, (b) 5-8, (c) 9-14, (d) 15-19, (c) 18-23, (f) 24-25. (g) 24-79, (h) 80-89, (i) 90-98, and (j) 99-106..... 21

Figure 3-4 The two side surfaces of Specimen A52M-182-TS-3. Crack advance is from left to right (a), and right to left (b). The green arrows show the interface between the two welds and the red arrows indicate the end of the test. ..... 25

Figure 3-5 Interaction with the Alloy 52M interface (a) location A in Fig. 3-4a, crack propagation is from left to right, and (b) location B in Fig. 3-4b, crack propagation is from right to left. ..... 26

Figure 3-6 SCC interaction with the Alloy 52M WOL interface (location A in Fig. 3-4a): (a) overlap of SEM image and elemental map, and (b) Cr concentration (wt. %) at each location. Crack propagation is from left to right. Green arrows indicate the Alloy 52M-182 interface. ..... 27

Figure 3-7 SCC interaction with the Alloy 52M WOL interface (location B in Fig. 3-4b): (a) overlap of SEM image and Cr map, and (b) Cr concentration (wt. %) at each location. Crack propagation is from right to left. Green arrows indicate the Alloy 52M-182 interface. ..... 28

Figure 3-8 Fracture surfaces of Specimen A52M-182-TS-3. ..... 29

Figure 3-9 Crack interaction with the Alloy 52M interface. Crack propagation is from left to right. The major crack directions are indicated. ..... 29

Figure 3-10 The two halves of fractured specimen A52M-182-TS-3. ..... 30

Figure 3-11 Fractured specimen A52M-182-TS-3 ..... 30

Figure 3-12 Fracture surface of Specimen A52M-182-TS-3 (a) photograph, and (b) SEM micrograph. Regions marked “A” and “B” represent the two most prominent regions of IG SCC propagation into the Alloy 52M WOL. Crack propagation is from bottom to top. ..... 31

Figure 3-13 Crack transition across the Alloy 52M-182 interface at locations (a) A, and (b) in Fig. 3-12b. Crack advance is from bottom to top. ..... 32

Figure 3-14 Fracture surface of specimen A52M-182-TS-3. The arrow indicates the beginning of transitioning to IG in Alloy 52M. Crack advance is from bottom to top. ..... 33

Figure 3-15 Cyclic CGR data in PWR environment for (a) specimen A52M-182-TS-3 and specimen A182-TS-1 of the same alloy tested previously (without WOL), (b) specimen A52M-182-TS-3 and Alloy 152 specimen A152-TS-4 under similar loading, and Alloy 52 data from the literature [24, 25], (c) Comparison between Alloy 52M data obtained in the current test and Alloy 52 data from the literature [24, 25], (d) Transitioning in Alloy 52M, periods 78-93. ..... 34

Figure 3-16 SCC CGR in Specimen A52M-182-TS-3 as a function of distance to the 182/52M interface ..... 36

Figure 3-17 Photographs of the two sides of the 52M/182 weld overlay specimen A52M-182-TS-1. ..... 36

Figure 3-18 Crack–length–vs.–time for WOL specimen A52M-182-TS-1 in simulated PWR environment during test periods (a) precracking-2, (b) 3-5, (c) 6-11, (d) 12-19, (e) 20-21, (f) 22-25, (g) 26-27, (h) 28, (i) 30, (j) 31-32, (k) 33, and (l) 33-42. ..... 39

Figure 3-19 (a, b) The two halves of fractured specimen A52M-182-TS-1. Crack advance is from bottom to top. (c,d) Same fracture surfaces photographed at an angle to show the cracking pattern at the interface. ..... 42

Figure 3-20 Fracture surface of specimen A52M-182-TS-1. The interface is indicated by black arrows. Crack advance is from bottom to top. The units of the bottom and side rulers are mm. ..... 43

Figure 3-21 Specimen A52M-182-TS-1: (a) first half of fracture surface, (b) detail at location 1, and (c) detail at location 2. Crack advance is from bottom to top. ..... 44

Figure 3-22 Specimen A52M-182-TS-1: (a) detail at location 3, and (b) detail at location 4 in Fig. 3-21a. Crack advance is from bottom to top. ..... 45

Figure 3-23 Specimen A52M-182-TS-1: (a) second half of fracture surface, (b) detail at location 1, and (c) detail at location 2. Crack advance is from bottom to top. ..... 46

Figure 3-24 Cyclic CGR data for Alloy 52M WOL specimen A52M-182-TS-1 in simulated PWR environment during (a) precracking and transitioning in Alloy 182, and (b) at the end of the test in Alloy 52M. The dotted blue line shows the “air line” for Alloy 52M obtained in the prior test. ..... 47

Figure 3-25 SCC CGR vs. distance for the two Alloy 52M-182 WOL specimens tested in the TS orientation. ..... 48

Figure 3-26 Specimens for SCC CGR testing of Alloy 52M-182 WOL in the ST orientation. ..... 49

Figure 3-27 Notch area in specimen WOL-ST-1. P3 and P8 represent the approximate locations where SCC CGR measurements were made in Alloy 600 HAZ, and P19 represents the approximate location where the crack was to intersect the interface with the Alloy 52M WOL. ..... 50

Figure 3-28 (a) Cyclic CGR data for the Alloy 600 (HAZ) region of specimen WOL-ST-1 in simulated PWR environment; (b) SCC CGR data for the Alloy 600 (HAZ) region of specimen WOL-ST-1 and MRP-55 disposition curve for Alloy 600 [11]. The data obtained prior to the first test period at constant load (3) is shown with dark blue symbols, and the data obtained prior to the second test period at constant load (8) is shown with light blue symbols). ..... 51

Figure 3-29 Cyclic CGR data for the Alloy 182 region of specimen WOL-ST-1 in simulated PWR environment. ..... 52

Figure 3-30 Crack–length–vs.–time for specimen WOL-ST-1 in simulated PWR environment during (a) precracking-2, (b) 3, (c) 4-7, (d) 8, (e) 9, (f) 10-18, and (g) 19. ..... 53

Figure 3-31 Post-test specimen WOL-ST-1 seen from both sides: (a) side 1, and (b) side 2. The red arrows indicate the Alloy 52M WOL interface. Crack advance is from left to right. ..... 55

Figure 3-32 Cross sections of specimen WOL-ST-1: (a) side 1, and (b) side 2. Blue arrows indicate the Alloy 600/182 interface and the red arrows indicate the Alloy 182-52M interface. Crack advance is from left to right. ..... 57

Figure 3-33 Micrographs on the cross section of specimen WOL-ST-1 on: side 1 taken at location (a) 1A, and (b) 1B in Fig. 3-32a, and side 2 taken at location (c) 2A and (d) 2B in Fig. 3-32b. Inserts show the local Cr concentrations (wt. %). Crack advance is from left to right. ..... 58

Figure 3-34 Fracture surface of specimen WOL-ST-1. Blue arrows indicate the Alloy 600-Alloy 182 interface, green arrows indicate the Alloy 182-Alloy 52M interface, and the red arrows and line mark the end of the test. The locations of the two test periods in Alloy 600 (P3 and P8) and along the Alloy 52M-182 interface (P19) are indicated in the figure. Crack advance is from bottom to top ..... 59

Figure 3-35 Fracture surface of specimen WOL-ST-1. Blue arrows indicate the Alloy 600-Alloy 182 interface, green arrows indicate the Alloy 182-Alloy 52M interface, and the red arrows and line mark the end of the test. Crack advance is from bottom to top. ..... 60

Figure 3-36 Fracture surface of specimen WOL-ST-1 at location 1 in Fig. 3-35. The blue arrows designate the intersection with the Alloy 182 weld, and the white arrows show areas of TG obtained most likely during fast cycling in at the beginning of test period 9, Table 3-4. Crack advance is from bottom to top. ..... 61

Figure 3-37 Fracture surface of specimen WOL-ST-1 at location 2 in Fig. 3-35. The blue arrows indicate the onset of cracking in Alloy 182, and white arrows indicate the occasional TG fracture that occurred prior to transitioning into Alloy 52M. An early occurrence of IG is indicated with a green arrow. Crack advance is from bottom to top. ..... 62

Figure 3-38 Fracture surface of specimen WOL-ST-1 at location 3 in Fig. 3-35. The green arrows indicate the onset of IG along the interface. Crack advance is from bottom to top. ..... 63

Figure 3-39 Fracture surface of specimen WOL-ST-1 at (a) location 4, and (b) location 5 in Fig. 3-35. Crack advance is from bottom to top. . ..... 64

Figure 3-40 Fracture surface of specimen WOL-ST-1 at (a) locations 6 in Fig. 3-35, and (b) detail at the white arrow in (a). Crack advance is from bottom to top. ..... 64

Figure 3-41 Fracture surface of specimen WOL-ST-1 at (a) location 7, and (b) location 8 in Fig. 3-35. The red arrows indicate IG fracture mode at the end of the test. Crack advance is from bottom to top. ..... 65

Figure 3-42 Notch area in specimen WOL-ST-2. P16 and P33 represent the approximate locations where SCC CGR measurements were made in this specimen. ..... 65

Figure 3-43 Cyclic CGRs for Alloy 52M specimen WOL-ST-2 in simulated PWR environment. Also included are Alloy 52 data from the literature [24, 25] obtained in air at room temperature and in PWR environment..... 68

Figure 3-44 Environmental enhancement of two control test conditions vs. calculated distance to the interface. Crack propagation is from right to left (see also Fig. 3-25 for guidance). ..... 68

Figure 3-45 Crack–length–vs.–time for Alloy 52M specimen WOL-ST-2 in simulated PWR environment during test periods (a) precracking, (b) 1-3, (c) 4-7, (d) 8-9, (e) 10-12, (f) 13-15, (g) 16, (h) 17-19, (i) 20-27, (j) 28-32, (k) 31, (l) 33, (m) detail in the first part of test period 33, (n) detail in the second part of test period 33, and (o) 34. ..... 69

Figure 3-46 Notch area post-test in specimen WOL-ST-2 seen from both sides: (a) side 1, and (b) side 2. The red arrows indicate the WOL interface. Crack advance is from right to left. ..... 75

Figure 3-47 Cross section of specimen WOL-ST-2: (a) side 1, and (b) side 2. Crack advance is from right to left. The red arrows indicate the WOL interface. ..... 76

Figure 3-48 Crack tip region on the first side surface of specimen WOL-ST-2 (side 1, location 1A in Fig. 3-47a). Crack advance is from right to left. Cr concentration at select locations is indicated in the figure. The red arrows indicate the WOL interface. ..... 77

Figure 3-49 Crack tip regions on the second side surface of specimen WOL-ST-2 (side 2, location 2A in Fig. 3-47b). Crack advance is from right to left. Cr concentration at select locations is indicated in the figure. The red arrow indicates the WOL interface. ..... 78

Figure 3-50 Cross section of specimen WOL-ST-2: taken in the middle of the specimen (side M). Crack advance is from right to left. The red arrows indicate the WOL interface. ..... 79

Figure 3-51 Crack tip regions on the second side surface of specimen WOL-ST-2 (side M, location A in Fig. 3-50). Crack advance is from right to left. Cr concentration at select locations is indicated in the figure. The red arrow indicates the WOL interface. ..... 80

Figure 3-52 Fracture surface of specimen WOL-ST-2. The yellow arrows indicate the beginning of SCC growth, the red arrows show the end of the test, and the green arrows indicate the region where the crack would have intersected the interface. Crack advance is from bottom to top. ..... 82

Figure 3-53 (a) First half (right hand side of Fig. 3-52a) of the fracture surface of specimen WOL-ST-2 obtained under constant load in simulated primary water. (b) location 1, (c) location 2, and (d) location 3. Crack advance is from bottom to top. ..... 83

Figure 3-54 Fracture surface of specimen WOL-ST-2 at (a) location 4, and (b) location 5 in Fig. 3-53a. The white arrow indicates an unbroken ligament. Crack advance is from bottom to top. ..... 84

Figure 3-55 Second half (left hand side of Fig. 3-52a) of the fracture surface of specimen WOL-ST-2 obtained under constant load in simulated primary water. (b) location 1, and (c) location 2. Crack advance is from bottom to top. ..... 85

Figure 3-56 Fracture surface of specimen WOL-ST-2 at location 3 in Fig. 3-55a. Crack advance is from bottom to top. ..... 85

Figure 3-57 Photograph of the Alloy 152 weld joining Alloy 690 and Alloy 533 LAS. SCC CGR test specimens were aligned in the 1st layer of Alloy 152 butter. ..... 86

Figure 3-58 Specimen N152-LAS-1, overlapped images before and after the specimen notch was machined: (a) side 1, and (b) side 2. Units of the rulers are mm. ..... 87

Figure 3-59 Environmental enhancement of two control test conditions and SCC CGRs vs. distance from the specimen notch for Specimen N152-LAS-1. Test periods are indicated in the figure. ..... 89

Figure 3-60 Crack–length–vs.–time for dilution specimen N152-LAS-1 in simulated PWR environment during test periods (a) precracking-2, (b) 3-4, (c) 5, (d) 6, (e) 7-10, (f) 11-17, (g) 18, (h) 19-20, (i) 21, (j) 22-23, and (k) 24. ..... 90

Figure 3-61 The two sides of the dilution specimen N152-LAS-1 after testing in primary water: (a) side 1, and (b) side 2. The red arrows indicate the approximate location of the end of the test as determined on the fracture surface. Units of the side rulers are mm. ..... 94

Figure 3-62 (a) Cross section 1 of Specimen N152-LAS-1, (b) detail at location 1 in (a), and (c) detail at location 2 in (a). The local Cr concentration is shown in red. Crack advance is from left to right. ..... 96

Figure 3-63 (a) Cross section 2 of Specimen N152-LAS-1, (b) detail at location 1 in (a), and (c) detail at location 2 in (a). Crack advance is from left to right. ..... 97

Figure 3-64 Fracture surface (A, Fig. 3-63) of specimen N152-LAS-1 tilted to show the final IG region. Two regions of interest, R1 and R2 are marked in the figure. Crack advance is from bottom to top. ..... 98

Figure 3-65 Region R1 on the fracture surface A of specimen N152-LAS-1 (Fig. 3-64). Blue arrows indicate the transition from LAS to Alloy 152, and two additional locations of interest: IG-1 (location 1) and the second intersection of the crack with the LAS interface (location 2), labelled LAS-i. Crack advance is from bottom to top. ..... 99

Figure 3-66 Fracture surface of specimen N152-LAS-1, locations: (a) 1, and (b) 2 in region R1, Fig. 3-65. Crack advance is from bottom to top. ..... 100

Figure 3-67 Region R2 on the fracture surface A of specimen N152-LAS-1 (Fig. 3-64). Blue arrows indicate the transition from LAS to Alloy 152, and two additional locations of interest: IG-1 (location 1) and the second intersection of the crack with the LAS interface (location 2), labelled LAS-i. Crack advance is from bottom to top. ..... 101

Figure 3-68 Fracture surface of specimen N152-LAS-1, locations: (a) 1, and (b) 2 in region R2, Fig. 3-67. Crack advance is from bottom to top. ..... 102

Figure 3-69 Fracture surface of N152-LAS-1, region IG-2 (Fig. 3-64): (a) first half of the fracture surface, (b) detail at location 1, and (c) detail at location 2.Crack advance is from bottom to top. ..... 103

Figure 3-70. Fracture surface of N152-LAS-1, region IG-2 (Fig. 3-64): (a) second half of the fracture surface, (b) detail at location 3, and (c) detail at location 4. Crack advance is from bottom to top. ..... 104

Figure 3-71 Approximate locations of the CT specimen blanks for first layer and second layer weld butter SCC CGR testing. The specimen blank that will later become CT test specimen N152-LAS-11 is indicated in the figure. ..... 105

Figure 3-72 The two sides of specimen N152-LAS-11 prior to the SSC test: (a) side 1, and (b) side 2. Alloy 152 is in the top half, and the LAS is in the bottom half of both pictures. ..... 106

Figure 3-73. Environmental enhancement of two control test conditions and SCC CGRs vs. distance from the specimen notch for Specimen N152-LAS-11. Test periods are indicated in the figure. ..... 108

Figure 3-74 Crack–length–vs.–time for dilution specimen N152-LAS-11 in simulated PWR environment during test periods (a) precracking-2, (b) 3-5, (c) 6, (d) 7-9, (e) 10, (f) 11-13, (g) 14-15, (h) 16-27, and (i) 28. ..... 108

Figure 3-75 SEM images of the two sides of the dilution specimen N152-LAS-11 after the test: (a) side 1, and (b) side 2. Alloy 152 and the LAS are as marked in each picture. The red arrows mark the end of the test. ..... 112

Figure 3-76 (a) Side surface 2 of Specimen N152-LAS-11; Regions with low (b) and high (c) SCC CGRs as observed on the side surface “2” at locations 1 and 3. Local Cr concentration (wt. %) measurements are indicated with red in each figure. Crack propagation is from left to right. ..... 113

Figure 3-77 “Swirls” appearing to slow down/arrest crack propagation observed on the side surface 2 in specimen N152-LAS-11 (locations 2 and 3 in Fig. 2-9b). Measured Cr concentration (wt. %) for each “swirl” is indicated with red in the figure. Crack propagation is from left to right. ..... 114

Figure 3-78 Fracture surface of specimen N152-LAS-11. The red lateral arrows indicate the end of cyclic loading and the beginning of the final constant load test period. Measured Fe concentration (wt. %) for at several locations is indicated on a blue background in the figure. Crack advance is from bottom to top. ..... 115

Figure 3-79 Fracture surface of specimen N152-LAS-11. Crack advance is from bottom to top. ..... 116

Figure 3-80 Fracture surface of specimen N152-LAS-11 at locations (a) 1, and (b) 2 in Fig. 2-3. Crack advance is from bottom to top. ..... 117

Figure 3-81 Fracture surface of specimen N152-LAS-11 at location: (a) 3, and (b) 4b in Fig. 3-79. Crack advance is from bottom to top. ..... 118

Figure 3-82 Fracture surface of specimen N152-LAS-11 at location 4a in Fig. 3-79. Crack advance is from bottom to top. ..... 119

Figure 3-83 Fracture surface of specimen N152-LAS-11 at location: (a) 5, and (b) 6 in Fig. 3-79. Crack advance is from bottom to top. ..... 120

Figure 3-84 Fracture surface of specimen N152-LAS-11 at location: (a) 7, and (b) 8 in Fig. 3-79. Arrows indicate unbroken ligaments. Crack advance is from bottom to top. ..... 121

Figure 3-85 (a) Fracture surface of specimen N152-LAS-11. Additional cross sections were obtained along directions “11” (a), and “22” (b). Red arrows are placed at the specimen notch and indicate the direction of propagation. Green arrows indicate the end of the test. ..... 123

Figure 3-86 SEM (a) and EBSD (b) map obtained on cross section “22” (Fig. 3-85) of Specimen N152-LAS-11. The yellow arrow points to a set of aligned boundaries that could plausibly explain the crack path in this test [28]. Crack propagation is from right to left. ..... 124

Figure 3-87 SEM (a) and EBSD (b) map obtained on side surface 2 (Figs. 3-75b and 3-76) of Specimen N152-LAS-11. The blue arrows point to sets of aligned boundaries in the next weld bead [29]. Red arrows are placed at the specimen notch and indicate the direction of propagation. Green arrows indicate the end of the test. Crack propagation is from left to right. ..... 125

Figure 4-1 SCC CGRs in an Alloy 52M-182 overlay: (a) Schematic showing the test specimen orientations with respect to the Alloy 52M-182 WOL, and (b) SCC CGRs vs. distance to the Alloy 52M-182 interface. ..... 127

Figure 4-2 SCC CGRs in the Alloy 52M-182 overlay: (a) along the Alloy 52-182 interface in specimen WOL-ST-1, and (b) as a function of average Cr content in specimen WOL-ST-2. Also included are Alloy 152 data generated at ANL [22,23] and the MRP-115 disposition curve for Alloys 82/182 [1]. ..... 128

Figure 4-3 Environmental enhancement of two control test conditions and SCC CGRs vs. distance from the specimen notch for (a) N152-LAS-1, and (b) N152-LAS-11. Crack propagation is from left to right. ..... 129

Figure 4-4 SCC CGRs in and 1st layer Alloy 152-LAS specimens. Also included are Alloy 152 data generated at ANL [22, 23] and the 75th percentile MRP-115 disposition curve for Alloys 82/182 [1]. ..... 130

Figure 4-5 Environmental enhancement of two control test conditions and SCC CGRs vs. distance from the specimen notch for 1st layer (a) Alloy 52-182 specimen WOL-ST-2, and (b) Alloy 152-LAS specimen N152-LAS-11. ..... 131

Figure 4-6 SCC fracture modes the regions near the interface in (a) Alloy 152 – LAS, and (b) Alloy 52M WOL specimens tested in simulated primary water environment. SCC propagation is from bottom to top. ..... 131

# LIST OF TABLES


Table 2-1 Chemical composition (wt.%) of Alloy 182 double-J weld and Alloy 52M WOL ..... 3

Table 2-2 Welding process and conditions for various weld passes used for fabricating the A152 butter ..... 4

Table 2-3 Chemical composition (wt.%) of Alloy 152 heat 720129 used to produce the 1st layer of buttering. ..... 5

Table 2-4 Welding process and conditions for various weld passes used for fabricating the A152 butt weld. ..... 5

Table 3-1 Crack growth data for specimen A52M-182-TS-3 of Alloy 152 weld in PWR water[a,b] ..... 19

Table 3-2 Summary of SCC CGR and cyclic (control cycle) data for specimen A52M-182-TS-3 ..... 35

Table 3-3 Crack growth data for WOL specimen A52M-182-TS-1 in PWR water[a,b]. ..... 38

Table 3-4 Crack growth data for specimen WOL-ST-1 in PWR water[a,b] ..... 51

Table 3-5 Crack growth data for 52M specimen WOL-ST-2 in PWR water[a,b] ..... 67

Table 3-6 Crack growth data for dilution specimen N152-LAS-1 in PWR water[a,b,c] ..... 88

Table 3-7 Crack growth data for Alloy 152 dilution specimen N152-LAS-11 in PWR water[a,b,c] ..... 107

# EXECUTIVE SUMMARY

Nickel-base Alloy 690 and the associated weld Alloys 52 and 152 are typically used for nozzle penetrations in replacement heads for pressurized water reactor (PWR) vessels, because of their increased resistance to stress corrosion cracking (SCC) relative to Alloys 600, 82, and 182. This is attributed to a higher chromium content. In addition, many PWRs use Alloys 52 or 152 as weld overlays (WOLs), inlays, or onlays to mitigate SCC on Alloy 82 or 182 dissimilar metal piping welds. However, questions remain about whether localized chromium dilution could increase the SCC susceptibility in Alloys 52 and 152 at or near interfaces with Alloys 82 and 182, as in the case of a WOL, or with steel, as in the case of a head penetration nozzle. While Alloys 52 and 152 have generally shown very low SCC growth rates in laboratory testing, there has been limited prior testing on what is often referred to as the weld dilution zone. To address this knowledge gap, Argonne National Laboratory (ANL) fabricated two mockups, the testing of which is the subject of this report. The first was a WOL mockup with Alloy 52M (a compositional variant of Alloy 52) on Alloy 182. The second was a butt weld mockup with Alloy 152 joined to low-alloy steel (LAS).

SCC testing on the Alloy 52M-182 WOL was conducted in two orientations, TS (weld interface is perpendicular to the crack growth direction) and ST (crack growth direction is parallel to the weld interface). In the orientation referred to as TS, the interface was perpendicular to the crack growth plane and the crack was grown from the Alloy 182 weld directly into the Alloy 52M overlay. The nominal chromium content in Alloy 182 is in the range of 13 to 17%, and in Alloy 52M is in the range of 28 to 31.5%. Compositional analyses showed that the chromium content in Alloy 52M could be diluted to as low as 22 to 23 percent within 0.5 mm of the interface with Alloy 182. In the orientation referred to as ST, the crack growth plane was along the interface between Alloys 182 and 52M. For two specimens tested in the TS orientation, it was found that as cracks in Alloy 182 approached within 1 mm of the interface, the crack growth rates (CGRs) decreased by approximately one order of magnitude compared to those measured farther away. In both specimens, it was also observed that when cracks intersected the interface, they would branch such that one front would continue to grow straight into the Alloy 52M overlay, while other fronts would propagate along the interface between Alloys 52M and 182, even though this was not the intended growth direction. For the specimens with the ST orientation, relatively high CGRs were measured both along the interface between Alloys 182 and 52M and in the first layer of Alloy 52M weld beads next to the interface. The SCC CGRs along the interface between the two weld metals were found to be as high as the 75$^{th}$ percentile curve for Alloys 82 and 182 reported in the Electric Power Research Institute Report, MRP-115, “Crack Growth Rates for Evaluating Primary Water Stress Corrosion Cracking (PWSCC) of Alloy 82, 182, and 132 Welds” [1]. The SCC CGR in the first layer of Alloy 52M weld was a factor of two lower than the 75$^{th}$ percentile curve reported in MRP-115 [1], despite the fact that the crack propagation direction was perpendicular to the dendritic grains. This direction is expected to be less susceptible to crack growth.

For the butt weld mockup, Alloy 152 butter and weld filler metal were joined to a piece of Alloy 533-Grade B LAS that was recovered from the reactor pressure vessel lower head for the cancelled Midland nuclear power plant. Two specimens were aligned to place the crack growth plane in the first layer of weld beads, parallel to, and at a distance of approximately 1 mm from the interface with LAS. The nominal chromium content in Alloy 152 is in the range of 28 to 31.5%, while LAS has essentially no chromium. Compositional analyses showed that the chromium content in Alloy 152 could be diluted to as low as 19 to 20 percent within 0.5 mm of the interface with LAS. The environmental enhancement of fatigue crack growth was found to

be a good predictor for the SCC response. Both fatigue and SCC CGR responses were similar to those observed in the first layer of weld beads in the Alloy 52M overlaid on Alloy 182. In both cases, in the most favorable orientations, the SCC CGRs were within a factor of two of the MRP-115 75$^{th}$ percentile curve [1]. Material compositional analyses taken along the crack path indicated that locations with the highest measured crack growth did not necessarily correlate with the lowest chromium content. This suggests that microstructural factors, in addition to the chromium content, could affect the SCC susceptibility near the interface.

# ACKNOWLEDGMENTS

The authors thank E. Listwan and Z. Zheng and their contributions to the experimental effort, as well as the ANL Electron Microscopy Center. This work is sponsored by the Office of Nuclear Regulatory Research, U.S. Nuclear Regulatory Commission, under Contract NRC-HQ-60-16-T-0001; Program Manager: G. Oberson.

# ABBREVIATIONS AND ACRONYMS

| | |
|---|---|
| ANL | Argonne National Laboratory |
| ASTM | American Society for Testing and Materials |
| B&W | Babcock and Wilcox |
| BPR | Back Pressure Regulator |
| BWR | Boiling Water Reactor |
| CGR | Crack Growth Rate |
| CL | Constant Load |
| CMTR | Certified Material Test Report |
| CRDM | Control Rod Drive Mechanism |
| CT | Compact Tension |
| DO | Dissolved Oxygen |
| ECP | Electrochemical Potential |
| EDX | Energy Dispersive X-ray Spectroscopy |
| EPRI MRP | Electric Power Research Institute Materials Reliability Program |
| GTAW | Gas Tungsten Arc Welding |
| HAZ | Heat Affected Zone |
| HX | Heat Exchanger |
| IG | Intergranular |
| LAS | Low Alloy Steel |
| LWR | Light Water Reactor |
| NRC | Nuclear Regulatory Commission |
| PNNL | Pacific Northwest National Laboratory |
| PPU | Partial Periodic Unloading |
| PWR | Pressurized Water Reactor |
| PWHT | Post Weld Heat Treatment |
| PWSCC | Primary Water Stress Corrosion Cracking |
| SCC | Stress Corrosion Cracking |
| SEM | Scanning Electron Microscopy |
| SMAW | Shielded Metal Arc Welding |
| SS | Stainless Steel |
| S | Side |
| T | Transverse |
| TC | Thermocouple |
| TG | Transgranular |
| WOL | Weld Overlay |
| WPS | Weld Procedure Specification |

# 1 INTRODUCTION

Alloy 600, a nickel-based alloy, was used at the time of construction in light water reactors (LWRs), and has over the years proven to be susceptible to stress corrosion cracking (SCC). Such cracking was first observed in steam generator tubes, but it has also occurred in components such as instrument nozzles and heater thermal sleeves in the pressurizer and control-rod drive mechanism (CRDM) housings in reactor pressure vessel upper closure heads, as in the notable case of the Davis-Besse plant in 2002. In operating plants, the nickel-based weld Alloys 82 and 182 are used with Alloy 600, and are themselves also susceptible to SCC. Through-wall cracking was detected in an Alloy 82 and 182 hot leg nozzle weld at the V.C. Summer plant in 2000. Alloy 690, which has higher chromium (Cr) content than Alloy 600, has been widely used since the 1980s to replace Alloy 600 components in pressurized water reactors (PWRs), beginning with thin-walled steam generator tubes, and eventually including thick-section nozzle penetrations in reactor pressure vessel heads. This choice was made following numerous laboratory studies worldwide which established an excellent resistance to SCC in reactor coolant primary water for this alloy [2-4]. Alloys 52 and 152 are the higher Cr content nickel-based weld metals that are used for joining Alloy 690 components, and which are also used for overlays (WOLs), inlays, or onlays to mitigate the SCC susceptibility of Alloy 82 and 182 welds. To date, there are no known cases of in-service SCC of Alloys 690, 52, and 152.

Despite the increased resistance to SCC of Alloy 52 and 152 welds in laboratory tests and the positive service history, questions remain about whether localized Cr dilution could increase the SCC susceptibility in Alloys 52 and 152 at or near interfaces with Alloys 82 and 182, as in the case of a WOL, or with steel, as in the case of a dissimilar metal weld (DMW) or head penetration nozzle. There has been limited testing of what is referred to as the weld dilution zone. This zone may extend up to several hundred microns from the weld interface, To address this knowledge gap, Argonne National Laboratory (ANL) fabricated two mockups, the testing of which is the subject of this report. The first was a WOL mockup with Alloy 52M (a compositional variant of Alloy 52) on Alloy 182. The second was a butt weld mockup with Alloy 152 joined to low-alloy steel (LAS).

Chapter 2 of this report describes the mockups used for testing, including the materials of fabrication, the schematic design of the welds, and the weld fabrication processes. It was intended that the materials and welding parameters should be representative of those used for actual welds used in service. Chapter 2 also discusses the SCC testing equipment and experimental approach. ANL generally followed well-established testing practices that have been employed for a number of years and were reported in previous ANL reports. Chapter 3 provides the testing results for the WOL and butt weld mockups. The plots are provided to show the crack extension as a function of time, and photographs and micrographs are given to document the appearances of the fracture surfaces. The WOL was tested in two different orientation, the first of which involved crack growth from Alloy 182 into Alloy 52M, directly through the interface, which was aligned perpendicular to the crack growth plane. In the second orientation, crack growth was measured along the interface between Alloys 182 and 52M. For the butt weld mockup, the crack growth was measured in the first layer of Alloy 152 weld beads, parallel to, and less than 1 mm from the interface with LAS. Chapter 4 includes a discussion of the testing results, including compositional and microstructural factors that could affect the SCC response. Comparisons are made between Alloy 182 and LAS with respect to their effects on the adjoining Alloy 52 or 152 weld metal. Finally, Chapter 5 gives a summary of the main findings and conclusions.

# 2 EXPERIMENTAL SETUP AND METHODOLOGY

This section describes the fabrication of the Alloy 52M and Alloy 152 weldments, the configuration of test specimens, and the CGR test apparatus and experimental approach.

## 2.1 Alloy 52M WOL

The Alloy 52M (Heat NX75W1TK) WOL (Figure 2-1) was deposited on top of an existing Alloy 182 weld [5]. The chemical compositions of the two welds provided in Table 2-1 shows that the Cr concentrations for the two alloys were 29.98% and 14.35%, respectively. The Alloy 182 weld had been tested previously (without the overlay), and a set of both cyclic and SCC CGR data existed for this weld [6].

The Alloy 52M WOL was produced at ANL Central Shops using welding parameters prototypical of those used in the nuclear industry. The Alloy 52M deposit was made with 1/8"-dia. wire, current 158-160A, voltage 16V, travel speed 3.5-4 in./min, 99.99% Ar shield gas 22-26 $ft^3$/hr (CFH), oscillation approximately ¼", and weave approximately ¼".

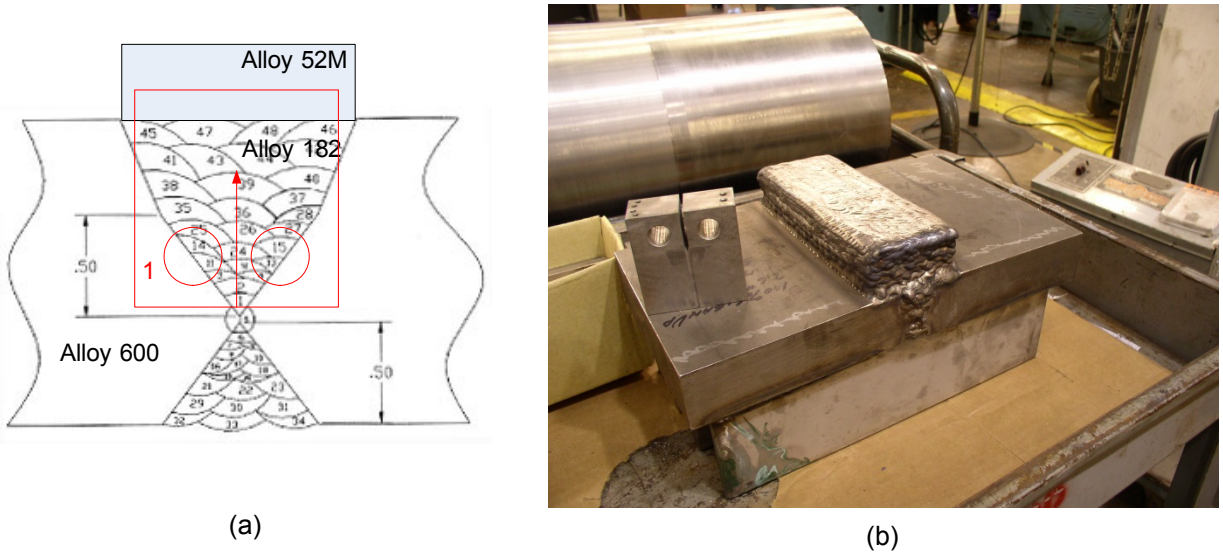


**Figure 2-1 (a) Conceptual schematic (units in inch), and (b) photograph of the resulting Alloy 52M-182 weld overlay. The continuous welded restraints used during the Alloy 52M WOL deposition are visible in the photograph.**

**Table 2-1 Chemical composition (wt.%) of Alloy 182 double-J weld and Alloy 52M WOL**

| Alloy ID | Analysis | C | Mn | Fe | S | P | Si | Cu | Ni | Cr | Ti | Nb | Co |
|---|---|---|---|---|---|---|---|---|---|---|---|---|---|
| Alloy 182 double-J | ANL | 0.0415 | 7.095 | 6.005 | 0.008 | 0.06 | 0.53 | 0.03 | 65 | 14.35 | 0.43 | 1.585 | 0.03 |
| Alloy 52M | CMTR | 0.019 | 0.81 | 8.80 | <0.0005 | 0.003 | 0.11 | 0.03 | 59.6 | 29.98 | 0.20 | 0.88 | 0.01 |

## 2.2 Alloy 690 to Alloy 533 Grade B Joint

This subsection documents the steps taken to produce a 3-inch thick butt weld for Alloy 690 (Heat NX3297HK12) welded to SA-533 Gr B class 1 steel (Heat A5466-2 from the Midland reactor lower head [7]) buttered with Alloy 152 filler metal. The geometry of the joint is shown in Figure 2-2. The joint was designed with a straight edge on the Alloy 690 side to facilitate SCC

CGR testing of the Alloy 690 heat affected zone (HAZ) which was also of interest in the research program. The SMAW welding procedure was qualified to ASME Section IX by ANL Central Shops [5].

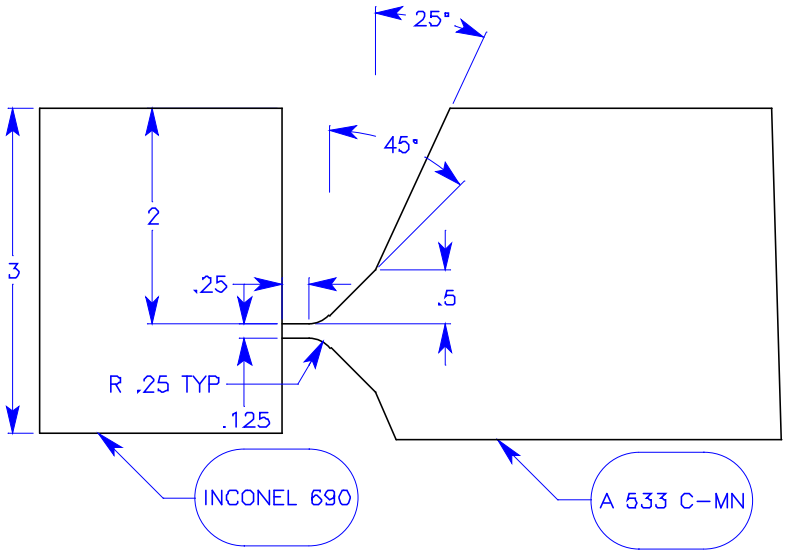


**Figure 2-2 Joint design, Alloy 690 to SA-533 Gr B. Units are in inch.**

### 2.2.1 Alloy 152 Weld Buttering

The LAS plate was machined with a bevel on one end. The beveled end was buttered with Alloy 152 F43 filler metal. A record was kept of the number and location of weld passes together with the heat code of the filler metal used, and the welding parameters that were used [5]. This record is shown in Table 2-2. After each layer, a liquid penetrant (LP) check was performed. After buttering, the LAS piece was stress relieved at 1150 ± 25ºF for 3h. The chemical composition of the Alloy 152 filler heat 720129 that was used to produce the first layer of buttering is given in Table 2-3.

**Table 2-2 Welding process and conditions for various weld passes used for fabricating the A152 butter**

| Weld Pass | Process | Filler Metal | Filler Size, in. | Heat Code | Type Polarity | Current, A | Voltage, V | Travel Speed, in./min | Notes |
|---|---|---|---|---|---|---|---|---|---|
| 1 – 23 | SMAW | Alloy 152, EniCrFe-7 | 1/8 | 720129 | DCRP | 97-102 | 21 – 23 | 5 | Layer 1 LP |
| 24-44 | SMAW | Alloy 152, EniCrFe-7 | 5/32 | 146444 | DCRP | 113-117 | 25 – 26 | 5 | Layer 2 LP |
| 45-65 | SMAW | Alloy 152, EniCrFe-7 | 5/32 | 146444 | DCRP | 113-117 | 25 – 26 | 5 | Layer 3 LP |

DCRP = direct current reverse polarity

**Table 2-3 Chemical composition (wt.%) of Alloy 152 heat 720129 used to produce the 1st layer of buttering.**

| Alloy ID | Analysis | C | Mn | Fe | S | P | Si | Cu | Ni | Cr | Ti | Nb+Ta | Co |
|---|---|---|---|---|---|---|---|---|---|---|---|---|---|
| Alloy 152 | CMTR | 0.037 | 3.70 | 9.28 | <0.001 | <0.003 | 0.51 | 0.01 | 55.26 | 28.92 | 0.12 | 1.92 | <0.01 |

### 2.2.2 Alloy 152 Butt Weld

The buttered LAS piece described in the previous sub-section was beveled on the buttered edge leaving ¼" of Alloy 152 F43 weld material on the face, and a section of Alloy 690 plate was used to make the opposing part of the butt weld. A double bevel J-grove weld was produced according to the design shown in Figure 2-2, and the number and location of weld passes together with the heat code of the filler metal used, as well as the welding parameters are given in Table 2-2 [5]. The root pass of the weld and back grind was LP tested, and the final weld surface was also LP tested. The final weld was radiographed per ASME Section IX.

**Table 2-4 Welding process and conditions for various weld passes used for fabricating the A152 butt weld.**

| Weld Pass | Process | Filler Metal | Filler Size, in. | Heat Code | Type Polarity | Current, A | Voltage, V | Travel Speed, in./min | Notes |
|---|---|---|---|---|---|---|---|---|---|
| 1 – 8 | SMAW | Alloy 152, EniCrFe-7 | 1/8 | 720129 | DCRP | 97-102 | 21 – 23 | 5 | |
| 9-14 | SMAW | Alloy 152, EniCrFe-7 | 1/8 | 146444 | DCRP | 97-102 | 25 – 26 | 5 | Root LP BG LP |
| 15-26 | SMAW | Alloy 152, EniCrFe-7 | 5/32 | 146444 | DCRP | 113-117 | 25 – 26 | 5 | Final LP |
| 27-76 | SMAW | Alloy 152, EniCrFe-7 | 1/8 | WCO4F6 | DCRP | 97-102 | 25 – 26 | 5 | Final LP |

DCRP = direct current reverse polarity

## 2.3 CT Specimens

All CGR tests were conducted in simulated PWR environments at 320°C. The testing protocol was in accordance with ASTM E-647, "Standard Test Method for Measurement of Fatigue Crack Growth Rates,"[8] and ASTM E-1681, "Standard Test Method for Determining a Threshold Stress Intensity Factor for Environment-Assisted Cracking of Metallic Materials under Constant Load" [9]. Depending on the dimensions of the available materials, the tests were performed on either 1-T or ½-T compact tension (CT) specimens; the geometries of the CT specimens are shown in Figure 2-3.

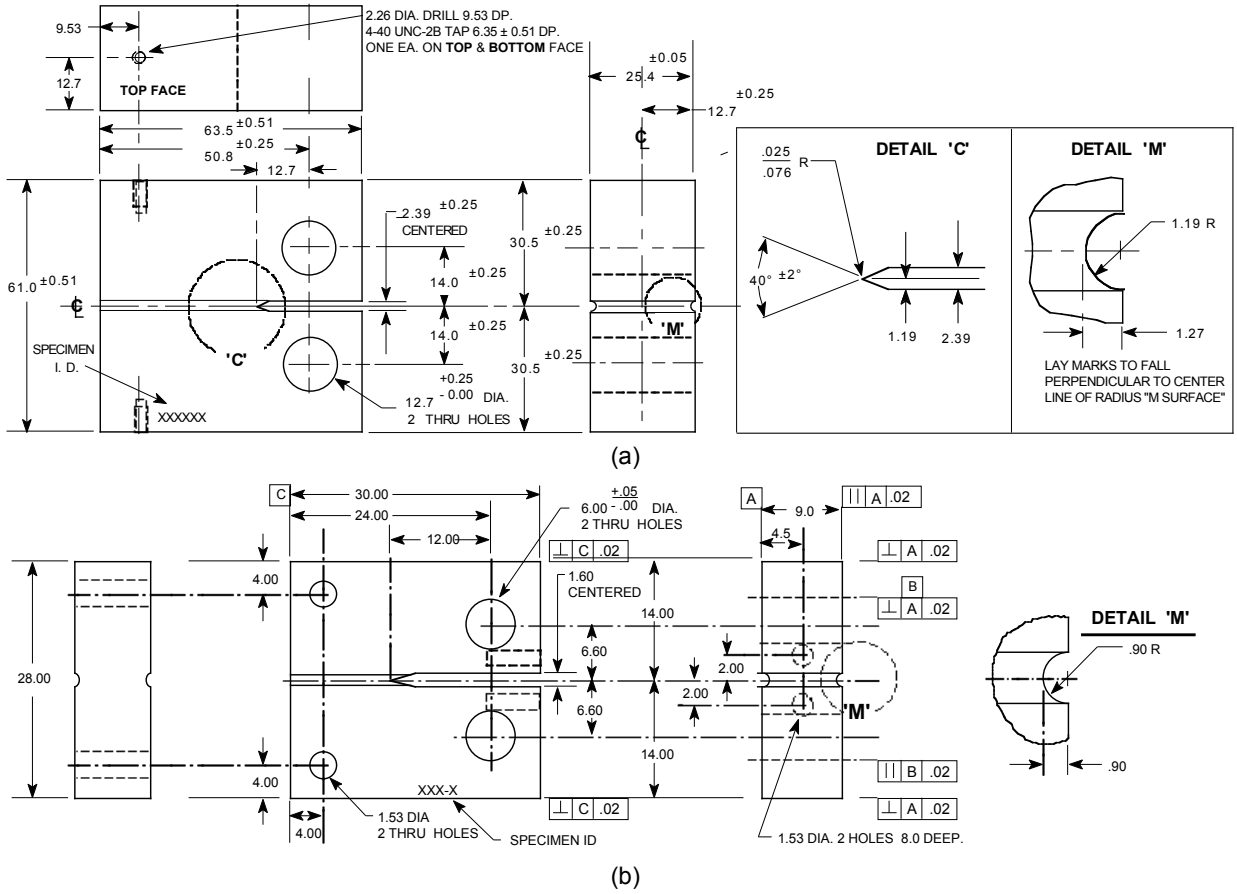


**Figure 2-3 Configuration of the (a) 1-T and (b) ½-T CT specimens used for this study. Dimensions are in mm.**

## 2.4 PWSCC Test Facilities

The CGR tests were conducted in test facilities equipped with either 2 or 6-liter stainless steel (SS) autoclaves. Each system has a suite of calibrated instrumentation, including digitally controlled hydraulic loading and load cells, and an independent water loop to maintain a simulated PWR environment with water chemistry monitoring. The test systems are nearly identical except for the maximum load rating of the test frame and the volume of the autoclave vessel. A detailed description of the test system with the 2-liter autoclave is provided in this section.

The 2-liter autoclave test facility allows test temperatures of up to 350°C [662°F]. Figure 2-4 is a photograph showing the entire test system. The servo-hydraulic test frame consists of a load train, an autoclave support frame, and autoclave. The hydraulic actuator is mounted on bottom of the test frame, with the load train components located above it. The load cell is located at the bottom of the pull rod. An Instron Model 8800 system is used to control the load on the specimen. The test temperature is maintained by heater bands mounted on the autoclave body.

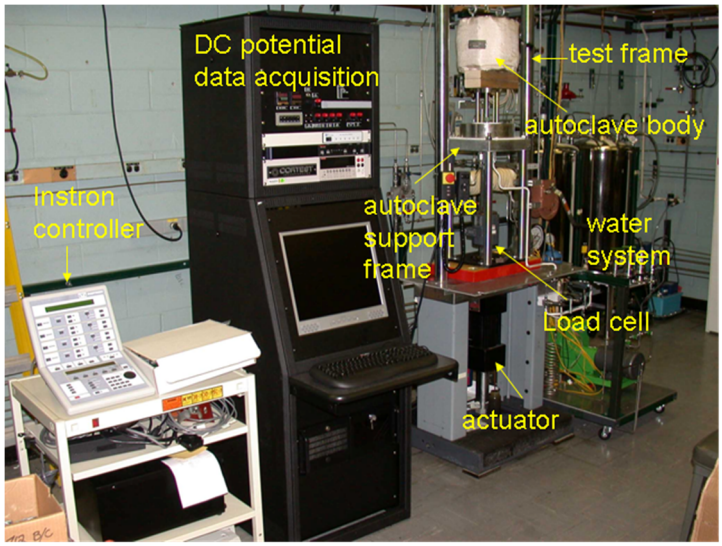


**Figure 2-4 Layout of the 2-liter SCC test system.**

The autoclave support frame consists of a thick plate supported by four compression rods (Figure 2-5). The internal load frame that contains the test specimen consists of a top plate supported by three rods. The upper two-piece clevis assembly is fastened to the top plate of the internal load frame, and the lower piece clevis assembly is connected to the pull rod. The specimen to be tested is mounted between the clevises. The specimen and clevises are kept electrically insulated from the load train by using oxidized Zircaloy pins and mica washers to connect the clevises to the rest of the load train. Water is circulated through a port in the autoclave head, which serves both as inlet and outlet. A schematic diagram of the recirculating water system is shown in Figure 2-6.

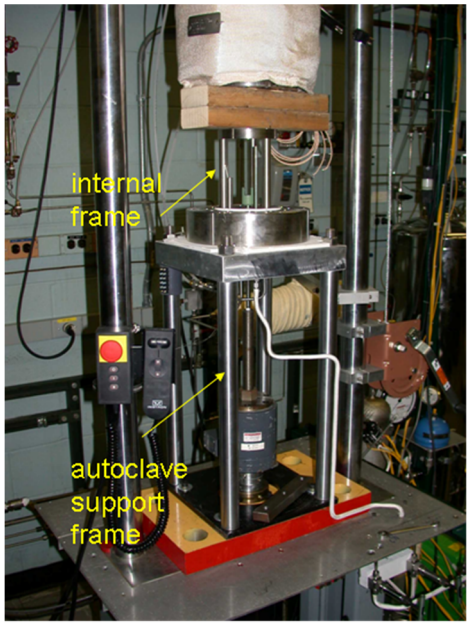


**Figure 2-5 Photograph of the specimen load train for the 2-liter autoclave.**

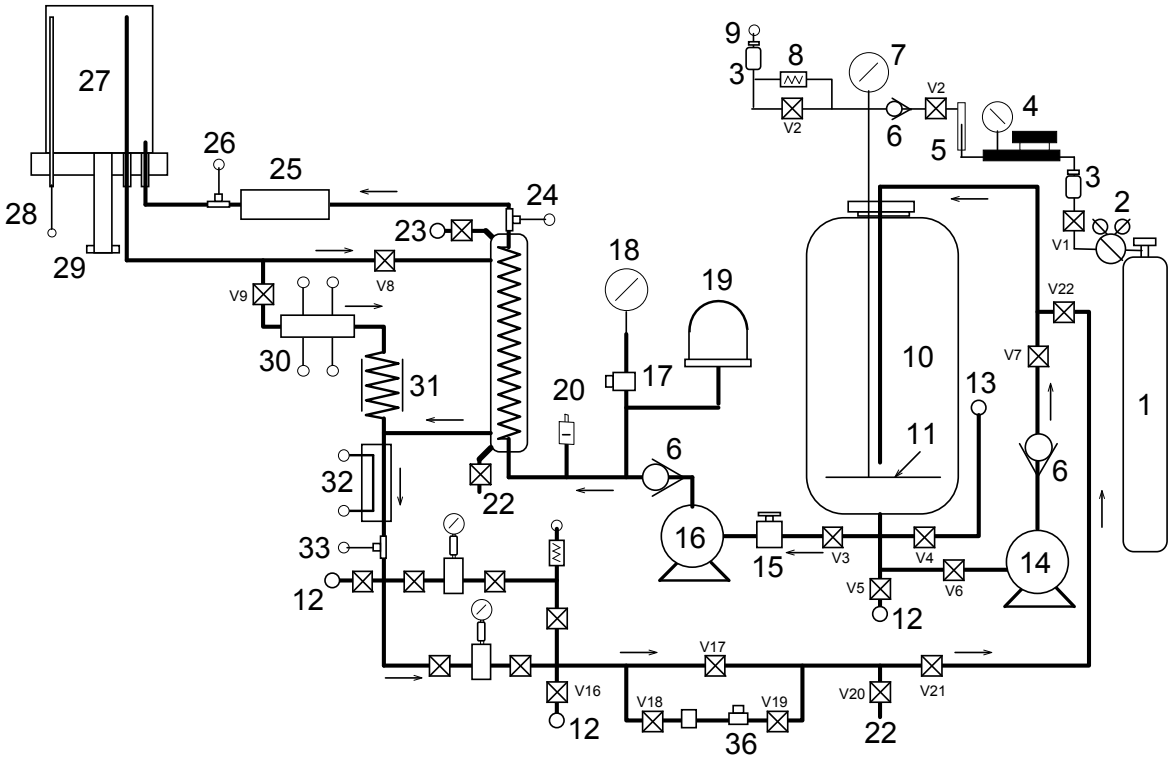


1. COVER GASS SUPPLY TANK
2. TWO-STAGE HIGH-PRESSURE REGULATOR
3. FLASH ARRESTOR
4. LOW-PRESSURE REGULATOR
5. FLOW METER
6. CHECK VALVE
7. COMPOUND VACUUM & PRESSURE GAUGE
8. PRESSURE RELIEF VALVE
9. VENT TO AIR & FLASH ARRESTOR
10. FEEDWATER STORAGE TANK
11. SPARGE TUBE
12. WATER SAMPLE PORT
13. FEEDWATER FILL PORT
14. FEEDWATER TANK RECIRCULATION PUMP
15. SOLENOID VALVE
16. HIGH-PRESSURE PUMP
17. PRESSURE TRANSDUCER
18. HIGH-PRESSURE GAUGE
19. ACCUMULATOR
20. RUPTURE DISC
21. HEAT EXCHANGER (HX)
22. DRAIN
23. SYSTEM BLEED PORT
24. HEAT EXCHANGER OUTLET TC
25. AUTOCLAVE PREHEATER
26. PREHEATER OUTLET TC
27. COMMERCIAL AUTOCLAVE
28. THERMOWELL
29. “BAL SEAL” RETAINER
30. ECP CELL
31. AIR-COOLED COIL
32. WATER COOLED HEAT EXCHANGER
33. BACK-PRESSURE REGULATOR (BPR) INLET TC
34. BPR
35. PH METER
36. CONDUCTIVITY METER

**Figure 2-6 Schematic diagram of the recirculating 2-liter autoclave system.**

The simulated PWR feedwater contains 2 ppm Li as LiOH, 1000 ppm B as $HBO_3$, ≈2 ppm dissolved hydrogen (≈23 $cm^3$/kg), and less than 10 ppb dissolved oxygen (DO) [10]. Water is circulated at relatively low flow rates (15-25 mL/min). The test temperatures were 320°C [608°F].

Crack extensions are monitored by the reversing-direct current (DC) potential difference method, Figure 2-7. In this method, a constant DC current is passed through the test specimen

and the crack length is measured through the changes in the electrical voltage at the crack mouth. The electrical voltage measured across the crack mouth is related to the unbroken crack ligament resistance through the Ohm's law. Thus, as the crack advances, the length of the unbroken ligament decreases and its resistance increases. In short, as the crack advances the voltage measured across the crack mouth increases. Figure 2-7 shows a typical configuration of a CT specimen instrumented for crack growth measurements by the DC potential method: the current leads are welded on the top and bottom surfaces of the specimen, and potential leads are welded on the front face of the specimen across the machined notch but on diagonal ends. Also, to compensate for the effects of changes in resistivity of the material with time, an internal reference bar of the same material being tested is installed in series, near the test specimen. The voltage readings across the reference bar are used to normalize potential drop measurements for the CT test specimen. The changes in potential drop measurements for the CT test specimen are transformed into crack advance data using correlations developed for the specimen geometry that is tested. In practice, voltage readings are taken successively as the current is reversed, and, typically, 800 voltage readings are needed to generate 1 crack advance data point, approximately every 4 min. with a resolution of approximately 1-2 μm [0.039-0.079 mils].

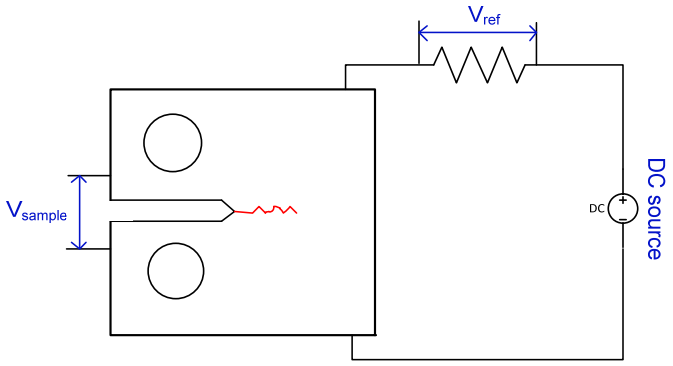


**Figure 2-7 Principle of crack length measurement by the DC potential method.**

## 2.5 CGR Test Methodology

A typical CGR test at ANL consists of three stages: in-situ precracking, transitioning to SCC, and the SCC growth stage. At the end of the test the specimen is broken open, and the fracture surface is examined. The objective of each stage will be highlighted next.

The objective of precracking is to produce a sharp crack tip. This is typically achieved by fatigue cracking, using a triangular waveform at load ratio R = 0.3[1], frequency of ≈1 Hz, and maximum stress intensity factor ($K_{max}$) of 20-25 MPa·$m^{1/2}$ [18.2-22.8 ksi·$in^{1/2}$]. Under rapid cyclic loading, the crack growth is dominated by mechanical fatigue; hence, the known fatigue behavior of the alloy being tested is expected to be reproduced. In turn, this step ensures that a straight crack front has been produced.

After approximately 0.5-mm (20 mils) extension in fatigue, the transitioning stage is initiated. The purpose of this stage is to transition from the fatigue/transgranular (TG) fracture mode to an SCC/intergranular (IG) fracture mode. As such, cycling is continued under loading conditions expected to foster environmental effects. In general, environmental enhancement of cyclic rates

[1] Load ratio R = $K_{min}/K_{max}$

is typically observed under loading conditions that would lead to CGRs between $10^{-11}$ and $10^{-9}$ m/s in air. To generate these rates, the load ratio R is increased incrementally to 0.5-0.7, and the loading waveform is changed to a slow/fast sawtooth with rise times of 30-1000 s and an unload time of 12 s. Transitioning to an IG SCC fracture mode is assessed by analyzing the cyclic response. The analysis, described in detail in the subsequent section, relies in principle on superposition. Under cyclic loading, the measured CGR is the superposition of mechanical fatigue, corrosion fatigue, and SCC components. Thus, a crack is considered "transitioned" when the SCC component is non-zero, that is, the measured CGR is larger than the sum of the fatigue and corrosion fatigue components. Once the crack is transitioned to IG SCC, the specimen is set at constant load. By eliminating the mechanical fatigue and corrosion fatigue components, constant load allows for the SCC CGR to be measured directly. However, as the crack grows in an IG fracture mode, it typically follows the least resistant grain boundary path. As such, crack branching develops, and that in turn results in unbroken/uncracked ligaments.

As described in the previous section, the DC potential method measures the potential drop across the unbroken ligament in the sample; hence, the ligaments formed during the preferential SCC path often confound the DC potential measurement by making the crack appear shorter than it is in reality. As a result, the crack advance measured on the fracture surface of the specimen at the end of the test is almost always longer than that measured in-situ. Therefore, a correction of the DC potential data is almost always needed after the test is completed, and the DC potential data is compared to the actual crack advance measured on the fracture surface. The downside of this approach is that in the case of SCC tests conducted under multiple conditions resulting in the same fracture mode, e.g., multiple stress intensity factors or multiple test temperatures, the fracture surface cannot be used to distinguish between the various test periods. Hence, in complex tests, there is almost always an uncertainty in correlating the test conditions to the resulting fracture surface. Nevertheless, the uncertainty regarding the amount of crack growth during a test period at constant load can be minimized by introducing cycling loading at the end of that test period. This cyclic loading is typically a well-known condition for which the CGR is known precisely. If ligaments form during constant load, the resulting CGR during this subsequent test period is typically higher than the known rate. This is the case for as long as ligaments are broken, then the CGR eventually settles to the known rate once that process is complete. The point at which the rate settles to the known rate can be conservatively interpreted to signal the actual extent of crack advance during the previous test period at constant load. This approach results in a conservative CGR as it does not take into account the growth due to cyclic loading.

As an alternative to the purely constant loading described previously, some form of cycling or partial periodic unloading (PPU) is introduced during the constant load test period with the purpose of breaking the ligaments as they form, and allow for a more realistic SCC CGR to be measured in real time. As a guideline, the cycle/periodic unloading is chosen to be subtle enough not to advance the crack by itself, but aggressive enough to be effective at breaking the ligaments. These experimental challenges have been recognized in industry publications [1,11], and periodic unloading is, in fact, recommended [1]. Such conditions have been used to generate a portion of the database used for generating the industry disposition curves [1,11]. The data generated at ANL conform to these guidelines. In addition, for each test conducted at ANL, the fatigue behavior is confirmed at the beginning of the test during precracking; this way the contributions from fatigue during constant load with periodic unloading or cycling plus hold conditions are calculated with precision during each test. Nevertheless, to increase confidence in the results, the objective of each ANL test is to measure the SCC CGR under not just one, but under several loading conditions.

There are two types of PPU used at ANL to supplement and/or confirm the SCC CGR determinations under constant load: “constant load with periodic unloading” and “cycle + hold”. They are in principle similar, in that the constant load is interrupted periodically (“hold” time) by a unload/reload cycle. However, the nature of the loading cycle is different in each case, hence a different approach is undertaken in the interpretation of the response. For constant load with periodic unloading, the cycle is essentially an aggressive fatigue cycle, e.g. R = 0.5, 12 s rise / 12 s unload times. This type of cycling results by itself in a transgranular (TG) fracture mode. Hence, if the resulting fracture mode is verified at the end on the test to be intergranular (IG), then it is assumed that most of the growth occurred at constant load during the hold time. The actual hold time under constant load can be set to result in a fatigue CGR less than the SCC CGR to be measured; for Alloy 52/152 weldments hold times of minimum 2h have typically been used to result in a $CGR_{air}$ of approx. $5\times10^{-12}$ m/s. By contrast, “cycle + hold” involves a gentle cycle, e.g. R = 0.5, 600 s rise / 12 s unload times. This type of cycle is used during transitioning from TG to IG, and by itself usually results in an IG fracture mode. Hence, under “cycle + hold” IG SCC growth occurs under both cyclic loading and constant load (hold). In this case, in order to calculate the SCC CGR component (SCC growth under constant load), the cyclic contribution to the total growth is subtracted. As before, hold times of minimum 2h have typically been used.

A post-test examination of the specimen is always conducted. Typically, all specimens are examined microscopically at the fracture surface and sometimes in the cross section. For the cross section examination, the two side surfaces are ground to remove the side grooves. The cross sections are then polished and etched. They are examined by scanning electron microscopy (SEM) to verify the planarity of the crack front and to determine the extent of crack branching. Next, the specimens are fractured to expose the fracture surface obtained during the test. The fracture surface is examined by SEM to measure the crack extension and to determine the fracture mode(s). The crack length measurements obtained on the fracture surface are used to correct the data obtained in-situ by the DC potential method. As described in the previous paragraph, the DC potential method typically underestimates the full extent of the crack, particularly during IG cracking. Hence, during the correction stage, the DC potential data is adjusted to match the measurements obtained on the fracture surface. The known relationships between the loading conditions and the expected fracture mode are used to the extent possible to substantiate the correction approach.

## 2.6 Analysis of CGR Data

Under cyclic loading, the CGR (m/s) in the environment, $\dot{a}_{env}$, can be expressed as the superposition of the rate in air (i.e., mechanical fatigue) and the rates due to corrosion fatigue and SCC ($\dot{a}_{CF}$ and $\dot{a}_{SCC}$, respectively), given in previous reports [12-14] as:

APPENDIX B $$\dot{a}_{env} = \dot{a}_{air} + \dot{a}_{CF} + \dot{a}_{SCC}\,. \qquad (1)$$

The cyclic CGRs for Ni alloys and welds in air were determined from correlations developed earlier at Argonne [12-14]:

APPENDIX A $$\dot{a}_{air} = \left(\frac{da}{dN}\right)/t_r = \left[C\cdot(1-0.82\cdot R)^{-2.2}\cdot(\Delta K)^{4.1}\right]/t_r\,, \quad (2)$$

where da/dN is the growth rate per cycle, $t_r$ is the rise time for the loading cycle, R is the load ratio (i.e., ratio of the minimum and maximum stress intensity factors $K_{min}/K_{max}$), $\Delta K$ is $K_{max} - K_{min}$

in Mpa $m^{1/2}$, and the constant C depends on the material and temperature. For Alloy 600, the constant ($C_{A600}$) is a third-order polynomial with respect to temperature T (°C) [12-14],

APPENDIX B $$C_{A600} = 4.835\times10^{-14} + (1.622\times10^{-17})T - (1.490\times10^{-18})T^2 + (4.355\times10^{-21})T^3 \quad .(3)$$

In LWR coolant environments, the CGRs of Alloy 600 show frequency-dependent enhancement under cyclic loading conditions. In high-DO water [i.e., normal water chemistry in boiling water reactor (BWR)], the environmental enhancement of the growth rates does not appear to depend on the material composition (e.g., C content) or material heat treatment. In contrast, environmental enhancement of CGRs of Alloy 600 in low-DO water does seem to be strongly dependent on material conditions. In the literature [15-19], such variability has been attributed to thermomechanically controlled parameters, such as yield strength and grain boundary coverage of carbides, although the evidence for this dependence is more substantial for steam generator tubing than for structural components.

For Alloy 690, the constant $C_{A690}$ is given by a third-order polynomial of temperature T (°C), expressed as [12]:

APPENDIX C $$C_{A690} = 5.423\times10^{-14} + (1.83\times10^{-16})T - (1.725\times10^{-18})T^2 + (5.490\times10^{-21})T^3. \quad (4)$$

For Ni-alloy welds, including Alloys 82/182 and 52/152, the constant $C_{Ni\text{-}weld}$ is given by a fourth-order polynomial with respect to temperature T (°C), expressed as [20]:

APPENDIX D $$C_{Ni\text{-}weld} = 8.659\times10^{-14} - (5.272\times10^{-17})T + (2.129\times10^{-18})T^2 - (1.965\times10^{-20})T^3 + (6.038\times10^{-23})T^4 \quad (5)$$

In earlier ANL work, correlations were developed to estimate the enhancement of cyclic CGRs in LWR environments relative to the CGRs in air under the same loading conditions. In the absence of any significant contribution of SCC to growth rate, the cyclic CGRs for Alloy 600, either in the solution annealed (SA) condition or the SA plus thermally treated (TT) condition, in ≈300 ppb DO water at 289°C are given by the expression [12]:

APPENDIX E $$\dot{a}_{env,A600} = \dot{a}_{air,A600} + 4.4\times10^{-7}\cdot\left(\dot{a}_{air,A600}\right)^{0.33}. \quad (6)$$

In low-DO environments (e.g., hydrogen water chemistry for the BWR or PWR environment) at 320°C (608°F), some alloys show little enhancement, while others show enhancement comparable to that predicted by Eq. 6. The environmental enhancement of Alloy 690 [12, 13] was found to be almost always less that that predicted by Eq. 6.

Similarly, correlations describing the cyclic CGRs of Ni-alloy welds (e.g., Alloys 182 and 82) have been developed [20, 21]. Under similar loading conditions, the CGRs of Ni-alloy welds are a factor of 2-3 higher than those of Alloy 600. The analysis indicated that the cyclic CGRs of Ni-alloy welds in PWR water are represented by the expression:

APPENDIX F $$\dot{a}_{env,Ni-weld} = \dot{a}_{air,Ni-weld} + 0.018\cdot\left(\dot{a}_{air,Ni-weld}\right)^{0.78}. \quad (7)$$

Figure 2-8 summarizes the expected behaviors for cyclic rates in air and environment for Alloys 600, 690 and Ni-base welds as described by Eqs. 2-7. All data is plotted as a function of the predicted behavior for Alloy 600 in air.

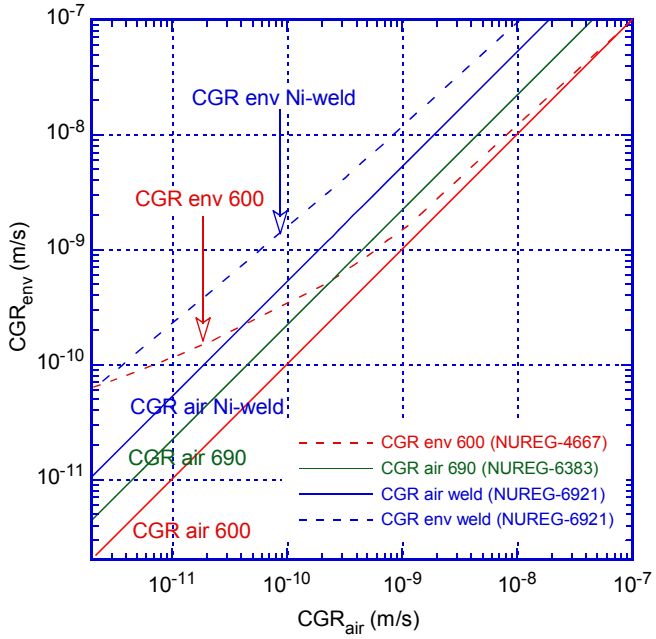


**Figure 2-8 CGRs in air and environment for Alloys 600, 690 and Ni-base welds as a function of predicted rates in air for Alloy 600 (data taken from Refs. 12, 13, 20).**

The SCC growth rate data for Alloy 600 and its weld metals have been reviewed in MRP-55 [11] and MRP-115 [1] to determine the effects of critical parameters such as stress intensity factor, temperature, material heat treatment, cold work, and water chemistry on growth rates. For Alloy 600, the CGR (m/s) under SCC conditions is represented by the expression [11],

APPENDIX G $$\dot{a}_{A600} = \alpha \exp\left[-\frac{Q}{R}\left(\frac{1}{T}-\frac{1}{T_{ref}}\right)\right](K-K_{th})^{\beta}, \quad (8)$$

where:
- $Q$ = activation energy for crack growth (130 kJ/mol for Alloy 600)
- $R$ = universal gas constant ($8.314\times10^{-3}$ kJ/mol K)
- $T$ = absolute operating temperature in units of K
- $T_{ref}$ = absolute reference temperature to normalize the CGR data (598 K)
- $\alpha$ = crack growth amplitude ($2.67\times10^{-12}$ at 325°C),
- $K$ = crack tip stress intensity factor in units of MPa·m$^{1/2}$,
- $K_{th}$ = crack tip stress intensity factor threshold (9 MPa·m$^{1/2}$), and
- $\beta$ = exponent 1.16.

The effect of K on the SCC growth rate for Ni-alloy welds in PWR environments has been represented by a modified [1] version of the above relationship. Unlike the CGR relationship for Alloy 600, the relationship for Ni-alloy welds has no threshold value for the stress intensity factor K,

APPENDIX H $$\dot{a}_{Ni-weld} = \alpha \exp\left[-\frac{Q}{R}\left(\frac{1}{T}-\frac{1}{T_{ref}}\right)\right]K^{\beta}, \quad (9)$$

where Q, R, T, and $T_{ref}$ are the same as in Eq. 8, the crack growth amplitude α is $1.5\times10^{-12}$ at 325°C, and exponent β is 1.6. Also, unlike Alloy 600, for which a reliable value for the activation energy for crack growth was determined, no such number is available for the Ni-weld alloys. Thus, for Ni-weld alloys, the activation energy is assumed to be the same as that for Alloy 600.

Figure 2-9 illustrates how the superposition concept introduced earlier is used to analyze the cyclic CGR data generated in a SCC test on Alloy 182 weld. A typical test at ANL consists of three stages: in-situ precracking, transitioning to SCC, and the SCC growth stage. The precracking stage is dominated by mechanical fatigue, hence, in this stage of the test where CGR rates are typically larger than $10^{-9}$ m/s, the expectation is that the measured CGRs are close to those expected under the same loading conditions in air, $\dot{a}_{air}$ (often called the "air line"), and is calculated using Eqs. 2 and 3. During the transitioning to IG SCC stage, cyclic loading is continued under loading conditions expected to induce environmental enhancement. The environmental enhancement is typically observed under loading conditions that lead to CGRs between $10^{-11}$ and $10^{-9}$ m/s in air, and the effect of the additional corrosion fatigue component is labeled $\dot{a}_{air}+\dot{a}_{CF}$ in the figure. For a typical Ni-base weld, the corrosion fatigue behavior is expressed by Eq. 6. Finally, if an SCC component is also present, the specimen response is expected to follow the curve labeled $\dot{a}_{air}+\dot{a}_{CF}+\dot{a}_{SCC}$ in the figure. For the purpose of the illustration shown in Figure 2-9, the $\dot{a}_{SCC}$ component was calculated using Eq. 9, and represents the SCC CGR of an alloy with a cracking susceptibility ranking at the 75th percentile.

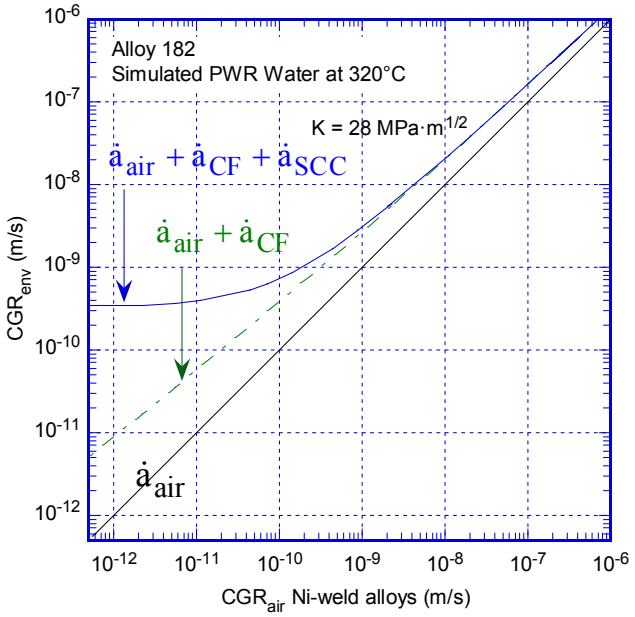


**Figure 2-9 Cyclic CGRs for typical Ni-base weld tested in a PWR environment. Expected corrosion fatigue (Eq. 7, green) and SCC (Eq. 9, blue) curves are included.**

In the specific case of tests in the first weld layer described in this report, the dendritic grains are normal to the crack growth plane, hence, in most cases, IG SCC is likely to be off-plane, in an orientation that prevents the CGR from being measured by DC potential correctly. Therefore, in order to be able to measure SCC growth in the current tests, locations prone to IG SCC propagating in the test crack growth plane had to be identified prior to the SCC CGR determinations. This was accomplished by monitoring the cyclic response and comparing that with prior experience. Specifically, in these tests, the crack was advanced until an environmental enhancement of similar to that obtained in prior tests on Alloy 152 in which the

direction of propagation was parallel to the dendritic grains. Of reference are tests conducted at ANL on an Alloy 152 weld that was produced in a symmetric, double-J geometry, as shown in Figure 2-10 [22, 23]. In those tests it was found that environmental enhancement peaks during cyclic with load ratios of R = 0.5, and rise time of 600s, and the resulting fracture mode is IG. Based on that experience, a similar level of environmental enhancement in the current tests will be interpreted as IG SCC propagation in a forward direction that can readily be measured by DC potential, and the specimen will be set at constant load.

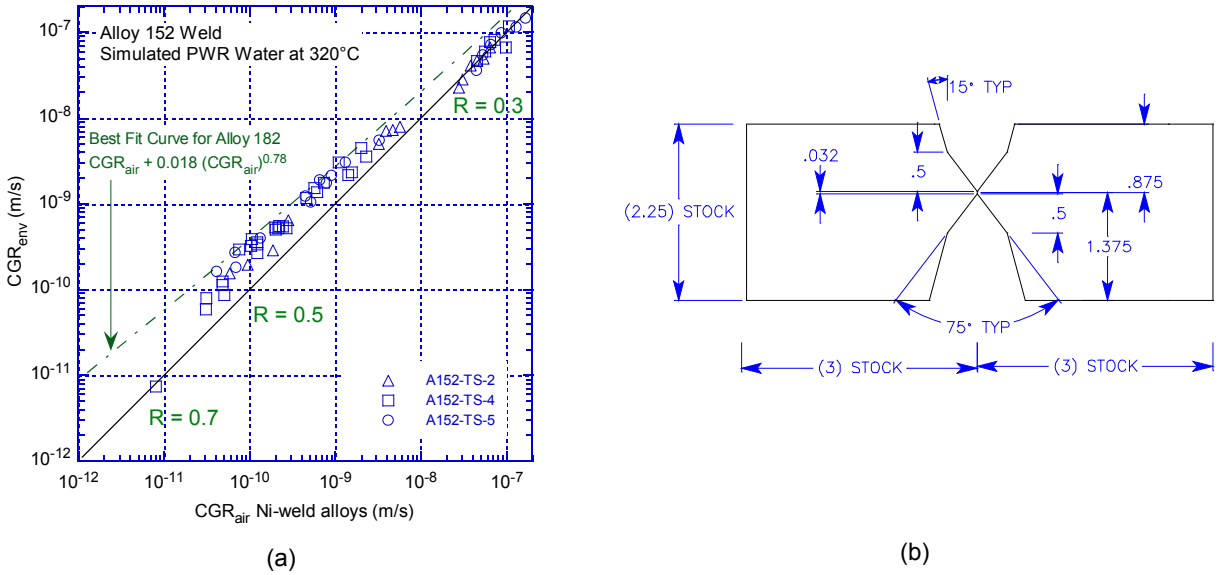


(a) (b)

**Figure 2-10 (a) Cyclic CGR data for the Alloy 152 weld tested in primary water environment, and (b) Alloy 152 weld produced in a double-J geometry.**

# 3 RESULTS

This section presents the SCC CGR test data obtained on Alloys 52M WOL and 152 weld in the first layer configuration. The tests are presented in chronological order, as "lessons learned" from the early tests were used to inform the management of the subsequent tests. The specimens and areas to be tested were selected randomly in the regions of interest. As described previously, the microstructural evaluation, including Cr levels were determined along the actual SCC paths during the post-test examination of the specimens.

## 3.1 SCC CGR Testing of Alloy 52M WOL

SCC CGR testing on the Alloy 52M-182 WOL was conducted in two orientations, TS and ST (Fig. 3-1). Initially, the SCC CGR testing was conducted in the TS orientation on two specimens with the purpose of observing the behavior of the SCC crack propagating from Alloy 182 into the Alloy 52M WOL. The subsequent testing in the ST orientation was conducted to confirm the observations resulting from the initial (TS-oriented) tests.

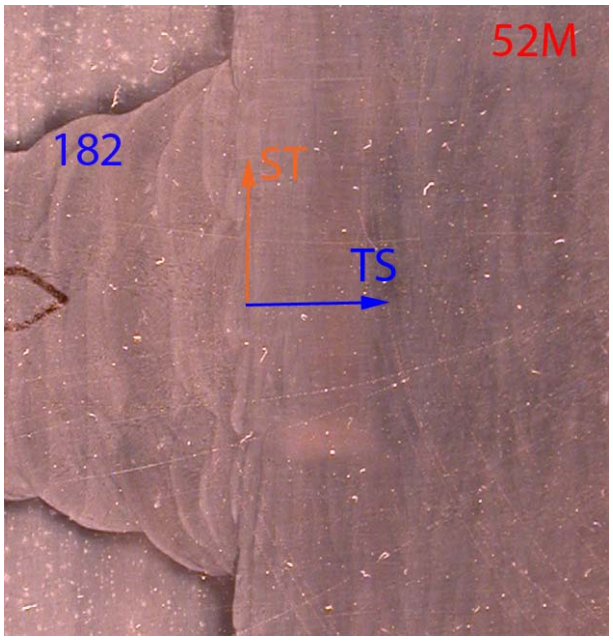


**Figure 3-1 Photograph of the Alloy 52M-182 WOL. The SCC CGR test directions, TS and ST, are indicated in the figure.**

### 3.1.1 Specimen A52M-182-TS-3

The first SCC CGR test involved specimen A52M-182-TS-3, shown in Fig. 3-2. The initial notch was measured on the lateral surfaces to be approximately 3.5 mm from the weld interface. The specimen was fatigue precracked and transitioned to SCC in Alloy 182. Then the crack was advanced toward the interface using gentle loading conditions to maintain the IG SCC fracture mode. Past the interface, the fast cycling resumed and the crack was advanced in Alloy 52M where it was transitioned again. Finally, the test ended with fast cycling to mark the fracture surface.

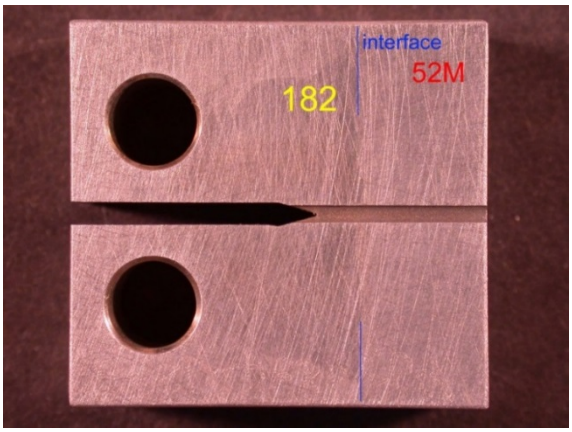


**Figure 3-2 Photograph of Alloy 52M-182 WOL specimen A52M-182-TS-3 prior to the SCC test.**

The testing conditions and resulting CGR data corrected as described in the previous section are given in Table 3-3; the portion on the test that took place in Alloy 182 is shaded with grey. The crack length and $K_{max}$ vs. time plots are shown in Fig. 3-2.

The test was initiated with precracking in the environment, followed by IG transitioning steps (periods precracking-4, Table 3-1). As expected, transitioning in Alloy 182 occurred readily, with cyclic rates in excellent agreement with previous data on the same weld alloy. Next, the specimen was set at constant load approximately 1 mm from the interface with Alloy 52M. The initial SCC CGR response (period 5) was in agreement with the rates measured previously on this weld (1.4 and $1.7 \times 10^{-10}$ m/s [6], shown on the plot in Figure 3-3b). Following an uncharacteristic slowing of the CGR (Figure 3-b), especially when compared to the known behavior (specimen A182-TS-1 was tested previously without the WOL), the immediate need was to straighten the crack front. Hence, a loading condition with well-known response was employed, sawtooth loading at R = 0.5, 1000s rise /12s down times, to advance the crack. Upon starting cycling (period 6), a "jump" in crack advance was observed immediately, suggesting that ligaments were being broken. Given the fact that in this type of test a precise measurement of the crack advance is essential, it was decided to continue the test with a succession of periods consisting of cycle ("control"), cycle + hold (C+H) and constant load with periodic unloading (CL + PU). These periods are marked in the plots shown in Fig. 3-3. By using superposition, SCC CGR components were calculated for all C+H conditions. The resulting rates were re-verified subsequently at CL + PU. The fracture surface will demonstrate that that all these loading conditions (periods 5-23, Table 3-1) maintained the IG fracture mode in both Alloys 182 and 52M.

After reaching the interface (test periods 17-18, Fig. 3-3d) the gentle cyclic conditions were maintained for approximately 3000h. The post-test examination of the specimen – which will be presented later in this section – showed that at this stage, the crack front branched along the interface, in a direction perpendicular to the original direction of propagation, and into Alloy 52M along the original direction of propagation.

Next, the crack was advanced in Alloy 52M (periods 24-72, Table 3-1). The response to fast cyclic conditions was inconsistent; the breaking of ligaments during the straightening of the crack front was also likely to play a role. A baseline fatigue response ("air line") for Alloy 52M cyclic rates could not be established. In addition, the now fully-grown interface cracks relieved

the stress driving the main crack. Very likely, the CGRs measured at this stage were affected by the diminished stress intensity factor at the crack tip.

Finally, the response to fast cycling stabilizes (periods 77-79), suggesting that the fracture surface has somewhat straightened. An “air line” for Alloy 52M could be established. The CGR response was overall much less than expected, perhaps due to the lower than calculated stress intensity factors. Nevertheless, the response was consistent and the known R-dependence (Fig. 2-10a) was reproduced. Test periods 80-96, Table 3-1, correspond to IG transitioning in Alloy 52M. Several SCC CGR determinations were made in Alloy 52M in test periods 94-98, however, given the abnormally low cyclic response preceding and subsequent to these measurements, the stress intensity factors are deemed highly unreliable.

**Table 3-1 Crack growth data for specimen A52M-182-TS-3 of Alloy 152 weld in PWR water[a,b]**

| Test Period | Test Time, h | Temp. °C | Load Ratio R | Rise Time, s | Down Time, s | Hold Time, s | $K_{max}$, Mpa·m$^{1/2}$ | $\Delta K$, Mpa·m$^{1/2}$ | $CGR_{env}$, m/s | Estimated $CGR_{air}$, m/s | Crack Length, mm |
|---|---|---|---|---|---|---|---|---|---|---|---|
| Pre a | 53 | 320.6 | 0.29 | 2 | 2 | | 21.4 | 15.2 | 3.02E-09 | 1.76E-08 | 12.079 |
| Pre b | 69 | 320.4 | 0.29 | 50 | 50 | | 21.5 | 15.3 | 2.69E-09 | 7.19E-10 | 12.158 |
| Pre c | 75 | 321.1 | 0.29 | 2 | 2 | | 23.1 | 16.4 | 5.42E-08 | 2.42E-08 | 12.683 |
| Pre d | 76 | 321.0 | 0.29 | 5 | 5 | | 23.2 | 16.5 | 3.75E-08 | 9.96E-09 | 12.780 |
| Pre e | 78 | 321.1 | 0.29 | 2 | 2 | | 23.8 | 16.9 | 8.53E-08 | 2.74E-08 | 12.941 |
| Pre f | 93 | 320.8 | 0.29 | 50 | 50 | | 24.5 | 17.4 | 5.88E-09 | 1.23E-09 | 13.144 |
| Pre g | 94 | 320.7 | 0.29 | 2 | 2 | | 25.2 | 17.9 | 9.79E-08 | 3.48E-08 | 13.351 |
| 1 | 100 | 321.1 | 0.49 | 50 | 12 | | 25.4 | 12.9 | 3.20E-09 | 6.29E-10 | 13.439 |
| 2 | 120 | 320.5 | 0.50 | 300 | 12 | | 25.8 | 12.9 | 9.62E-10 | 1.05E-10 | 13.501 |
| 3 | 145 | 320.7 | 0.50 | 600 | 12 | | 26.0 | 13.0 | 5.52E-10 | 5.45E-11 | 13.546 |
| 4 | 189 | 320.5 | 0.50 | 1000 | 12 | | 26.2 | 13.1 | 4.47E-10 | 3.38E-11 | 13.618 |
| 5 | 723 | 320.9 | 1.00 | 0 | 0 | | 26.7 | 0.0 | 1.30E-10 | - | 13.768 |
| 6 | 746 | 320.6 | 0.50 | 1000 | 12 | | 27.4 | 13.7 | 5.73E-10 | 4.04E-11 | 13.914 |
| 7 | 1,055 | 320.5 | 0.50 | 12 | 12 | 7,200 | 27.4 | 13.7 | 7.51E-11 | - | 13.918 |
| 8 | 1,078 | 320.5 | 0.50 | 1000 | 12 | | 27.8 | 13.9 | 3.49E-10 | 4.34E-11 | 14.019 |
| 9 | 1,107 | 320.7 | 0.50 | 1000 | 12 | 7,200 | 28.1 | 14.0 | 5.47E-11 | 5.49E-12 | 14.022 |
| 10 | 1,439 | 320.0 | 0.50 | 12 | 12 | 7,200 | 28.4 | 14.2 | 5.30E-11 | 6.52E-12 | 14.082 |
| 11 | 2,351 | 319.6 | 0.50 | 12 | 12 | 7,200 | 31.5 | 14.5 | 4.86E-11 | - | 14.250 |
| 12 | 2,613 | 319.7 | 0.54 | 1000 | 12 | | 32.4 | 14.9 | 1.98E-10 | - | 14.448 |
| 13 | 2,908 | 319.8 | 0.54 | 1000 | 12 | 3,600 | 32.8 | 15.1 | 8.00E-11 | 1.48E-11 | 14.513 |
| 14 | 3,959 | 320.4 | 0.54 | 12 | 12 | 7,200 | 33.5 | 15.4 | 3.24E-11 | - | 14.633 |
| 15 | 4,131 | 320.7 | 0.54 | 1000 | 12 | | 34.1 | 15.7 | 1.80E-10 | 8.10E-11 | 14.755 |
| 16 | 4,374 | 320.4 | 0.54 | 1000 | 12 | 3,600 | 34.4 | 15.8 | 6.73E-11 | 1.82E-11 | 14.795 |
| 17 | 5,062 | 321.7 | 0.54 | 12 | 12 | 7,200 | 34.7 | 15.9 | 2.69E-11 | - | 14.862 |
| 18 | 5,306 | 321.3 | 0.54 | 1000 | 12 | | 35.9 | 16.5 | 1.79E-10 | 1.00E-10 | 15.042 |
| 19 | 5,494 | 321.9 | 0.54 | 1000 | 12 | 3,600 | 36.1 | 16.6 | 6.22E-11 | 2.24E-11 | 15.065 |
| 20 | 5,974 | 322.2 | 0.54 | 12 | 12 | 7,200 | 36.3 | 16.7 | 2.44E-11 | - | 15.103 |
| 21 | 6,223 | 322.5 | 0.54 | 1000 | 12 | | 37.8 | 17.4 | 1.67E-10 | 1.25E-10 | 15.308 |
| 22 | 6,553 | 322.7 | 0.54 | 1000 | 12 | 3600 | 38.0 | 17.5 | 4.77E-11 | 3.58E-11 | 15.340 |
| 23 | 7,106 | 322.7 | 0.54 | 12 | 12 | 7200 | 38.2 | 17.6 | 1.83E-11 | - | 15.379 |
| 24 | 7,415 | 323.0 | 0.54 | 1000 | 12 | | 27.6 | 12.7 | 1.27E-11 | 3.51E-11 | 15.408 |
| 25 | 8,117 | 323.2 | 0.54 | 1000 | 12 | 3600 | 27.8 | 12.8 | 6.62E-12 | 7.77E-12 | 15.416 |
| 26 | 8,136 | 321.3 | 0.54 | 100 | 12 | | 27.8 | 12.8 | 2.78E-10 | 3.52E-10 | 15.480 |
| 27 | 8,160 | 321.4 | 0.54 | 100 | 12 | | 27.9 | 12.8 | 1.47E-10 | 3.57E-10 | 15.496 |
| 28 | 8,168 | 321.2 | 0.54 | 12 | 12 | | 28.0 | 12.9 | 7.23E-10 | 3.01E-09 | 15.507 |
| 29 | 8,184 | 321.3 | 0.54 | 100 | 12 | | 28.0 | 12.9 | 1.24E-10 | 3.63E-10 | 15.512 |
| 30 | 8,190 | 321.1 | 0.54 | 12 | 12 | | 28.1 | 12.9 | 6.30E-08 | 3.04E-09 | 15.525 |

**Table 3-1 (Cont.)**

| Test Period | Test Time, h | Temp. °C | Load Ratio R | Rise Time, s | Down Time, s | Hold Time, s | $K_{max}$, Mpa·$m^{1/2}$ | $\Delta K$, Mpa·$m^{1/2}$ | $CGR_{env}$, m/s | Estimated $CGR_{air}$, m/s | Crack Length, mm |
|---|---|---|---|---|---|---|---|---|---|---|---|
| 31 | 8,257 | 321.2 | 0.54 | 300 | 12 | | 28.1 | 12.9 | 4.70E-11 | 1.22E-10 | 15.533 |
| 32 | 8,263 | 321.3 | 0.54 | 12 | 12 | | 28.2 | 13.0 | 4.63E-10 | 3.09E-09 | 15.540 |
| 33 | 8,280 | 321.2 | 0.54 | 100 | 12 | | 28.2 | 13.0 | 1.09E-10 | 3.71E-10 | 15.545 |
| 34 | 8,288 | 321.5 | 0.54 | 12 | 12 | | 27.3 | 12.5 | 4.90E-10 | 2.70E-09 | 15.353 |
| 35 | 8,304 | 321.2 | 0.54 | 100 | 12 | | 28.3 | 13.0 | 9.36E-11 | 3.75E-10 | 15.557 |
| 36 | 8,315 | 321.3 | 0.54 | 12 | 12 | | 28.3 | 13.0 | 5.43E-10 | 3.16E-09 | 15.569 |
| 37 | 8,352 | 321.4 | 0.54 | 100 | 12 | | 28.4 | 13.0 | 9.15E-11 | 3.82E-10 | 15.578 |
| 38 | 8,360 | 321.4 | 0.54 | 12 | 12 | | 28.4 | 13.1 | 5.79E-10 | 3.22E-09 | 15.585 |
| 39 | 8,448 | 321.2 | 0.54 | 300 | 12 | | 28.5 | 13.1 | 4.58E-11 | 1.29E-10 | 15.598 |
| 40 | 8,450 | 321.4 | 0.54 | 12 | 12 | | 28.6 | 13.1 | 5.85E-10 | 3.27E-09 | 15.607 |
| 41 | 8,471 | 321.2 | 0.54 | 100 | 12 | | 28.6 | 13.1 | 9.24E-11 | 3.93E-10 | 15.611 |
| 42 | 8,480 | 321.3 | 0.54 | 12 | 12 | | 28.6 | 13.1 | 6.25E-10 | 3.27E-09 | 15.622 |
| 43 | 8,496 | 321.4 | 0.54 | 100 | 12 | | 28.6 | 13.2 | 1.09E-10 | 3.96E-10 | 15.627 |
| 44 | 8,505 | 321.3 | 0.54 | 12 | 12 | | 28.7 | 13.2 | 6.08E-10 | 3.33E-09 | 15.638 |
| 45 | 8,520 | 321.2 | 0.54 | 100 | 12 | | 28.9 | 13.3 | 9.48E-11 | 4.09E-10 | 15.671 |
| 46 | 8,528 | 321.3 | 0.54 | 12 | 12 | | 28.8 | 13.2 | 6.78E-10 | 3.36E-09 | 15.652 |
| 47 | 8,592 | 321.4 | 0.54 | 300 | 12 | | 28.8 | 13.2 | 4.71E-11 | 1.35E-10 | 15.662 |
| 48 | 8,600 | 321.5 | 0.54 | 12 | 12 | | 28.9 | 13.3 | 7.27E-10 | 3.43E-09 | 15.673 |
| 49 | 8,616 | 321.4 | 0.54 | 100 | 12 | | 28.9 | 13.3 | 9.66E-11 | 4.12E-10 | 15.678 |
| 50 | 8,619 | 321.1 | 0.30 | 5 | 5 | | 28.8 | 20.2 | 4.91E-09 | 2.33E-08 | 15.722 |
| 51 | 8,682 | 321.0 | 0.30 | 100 | 100 | | 29.0 | 20.3 | 2.72E-10 | 1.20E-09 | 15.748 |
| 52 | 8,686 | 321.0 | 0.30 | 10 | 10 | | 29.2 | 20.4 | 2.50E-09 | 1.23E-08 | 15.775 |
| 53 | 8,689 | 321.0 | 0.30 | 50 | 50 | | 29.3 | 20.5 | 5.21E-09 | 2.50E-08 | 15.800 |
| 54 | 8,708 | 321.1 | 0.30 | 50 | 50 | | 29.3 | 20.5 | 3.47E-10 | 2.52E-09 | 15.805 |
| 55 | 8,714 | 321.0 | 0.30 | 10 | 10 | | 29.4 | 20.6 | 1.36E-09 | 1.27E-08 | 15.821 |
| 56 | 8,734 | 321.1 | 0.30 | 50 | 50 | | 29.5 | 20.6 | 2.85E-10 | 2.56E-09 | 15.828 |
| 57 | 8,739 | 321.1 | 0.30 | 10 | 10 | | 29.6 | 20.7 | 1.15E-09 | 1.30E-08 | 15.845 |
| 58 | 8,756 | 321.1 | 0.30 | 50 | 50 | | 29.6 | 20.7 | 2.92E-10 | 2.60E-09 | 15.845 |
| 59 | 8,763 | 321.0 | 0.30 | 12 | 12 | | 29.7 | 20.8 | 9.12E-10 | 1.10E-08 | 15.866 |
| 60 | 8,778 | 321.0 | 0.30 | 50 | 50 | | 29.7 | 20.8 | 3.45E-10 | 2.65E-09 | 15.873 |
| 61 | 8,786 | 321.0 | 0.30 | 12 | 12 | | 29.8 | 20.9 | 1.17E-09 | 1.12E-08 | 15.893 |
| 62 | 8,874 | 321.0 | 0.30 | 100 | 100 | | 30.0 | 21.0 | 3.04E-10 | 1.38E-09 | 15.925 |
| 63 | 8,880 | 321.1 | 0.30 | 12 | 12 | | 30.2 | 21.1 | 1.36E-09 | 1.17E-08 | 15.947 |
| 64 | 8,949 | 321.1 | 0.30 | 50 | 50 | | 30.5 | 21.4 | 4.58E-10 | 2.95E-09 | 16.006 |
| 65 | 9,043 | 321.1 | 0.30 | 100 | 100 | | 30.8 | 21.6 | 3.27E-10 | 1.53E-09 | 16.052 |
| 66 | 9,050 | 321.2 | 0.30 | 50 | 50 | | 30.9 | 21.7 | 5.48E-10 | 3.13E-09 | 16.068 |
| 67 | 9,183 | 321.6 | 0.30 | 100 | 100 | | 31.4 | 22.0 | 3.70E-10 | 1.68E-09 | 16.157 |
| 68 | 9,192 | 321.4 | 0.30 | 2 | 2 | | 32.4 | 22.7 | 1.01E-08 | 9.45E-08 | 16.303 |
| 69 | 9,209 | 321.6 | 0.30 | 50 | 50 | | 32.5 | 22.8 | 7.65E-10 | 3.85E-09 | 16.321 |
| 70 | 9,216 | 321.9 | 0.30 | 2 | 2 | | 33.3 | 23.3 | 9.70E-09 | 1.06E-07 | 16.450 |
| 71 | 9,236 | 321.8 | 0.30 | 50 | 50 | | 33.5 | 23.4 | 8.21E-10 | 4.36E-09 | 16.472 |
| 72 | 9,242 | 321.7 | 0.30 | 2 | 2 | | 33.8 | 23.7 | 1.03E-08 | 1.14E-07 | 16.521 |
| 73 | 9,283 | 321.6 | 0.30 | 50 | 50 | | 34.8 | 24.4 | 9.13E-10 | 5.10E-09 | 16.649 |
| 74 | 9,287 | 321.5 | 0.30 | 2 | 2 | | 32.8 | 23.0 | 3.53E-09 | 9.95E-08 | 16.709 |
| 75 | 9,303 | 321.5 | 0.30 | 50 | 50 | | 33.3 | 23.3 | 2.52E-10 | 4.25E-09 | 16.713 |
| 76 | 9,312 | 321.6 | 0.30 | 2 | 2 | | 33.4 | 23.4 | 4.65E-09 | 1.08E-07 | 16.787 |
| 77 | 9,326 | 321.5 | 0.30 | 50 | 50 | | 34.1 | 23.9 | 4.21E-10 | 4.69E-09 | 16.792 |
| 78 | 9,336 | 321.6 | 0.30 | 2 | 2 | | 34.3 | 24.0 | 5.86E-09 | 1.19E-07 | 16.881 |
| 79 | 9,359 | 321.7 | 0.30 | 50 | 50 | | 34.5 | 24.1 | 5.45E-10 | 4.91E-09 | 16.898 |
| 80 | 9,383 | 321.7 | 0.50 | 100 | 12 | | 34.6 | 17.3 | 1.91E-10 | 1.08E-09 | 16.930 |
| 81 | 9,448 | 321.5 | 0.50 | 300 | 12 | | 34.8 | 17.4 | 3.73E-11 | 3.64E-10 | 16.948 |
| 82 | 9,545 | 321.7 | 0.50 | 600 | 12 | | 34.8 | 17.4 | 5.16E-11 | 1.84E-10 | 16.965 |
| 83 | 9,616 | 321.8 | 0.50 | 1000 | 12 | | 34.9 | 17.4 | 3.31E-11 | 1.11E-10 | 16.974 |
| 84 | 9,661 | 321.6 | 0.60 | 1000 | 12 | | 35.2 | 14.1 | 1.44E-11 | 6.41E-11 | 16.977 |
| 85 | 9,728 | 321.3 | 0.60 | 1000 | 12 | | 35.2 | 14.1 | 1.18E-11 | 6.39E-11 | 17.020 |
| 86 | 9,826 | 320.8 | 0.70 | 1000 | 12 | | 35.2 | 10.6 | 2.72E-12 | 2.88E-11 | 17.022 |
| 87 | 10,044 | 321.0 | 0.50 | 1000 | 12 | | 35.4 | 17.7 | 2.68E-11 | 1.17E-10 | 17.048 |
| 88 | 10,477 | 320.4 | 0.50 | 1000 | 12 | 7200 | 35.5 | 17.8 | 5.47E-12 | 1.43E-11 | 17.058 |
| 89 | 10,549 | 320.4 | 0.50 | 300 | 12 | | 36.1 | 18.0 | 1.08E-10 | 4.18E-10 | 17.119 |

**Table 3-1 (Cont.)**

| Test Period | Test Time, h | Temp. °C | Load Ratio R | Rise Time, s | Down Time, s | Hold Time, s | $K_{max}$, Mpa·m$^{1/2}$ | ΔK, Mpa·m$^{1/2}$ | $CGR_{env}$, m/s | Estimated $CGR_{air}$, m/s | Crack Length, mm |
|---|---|---|---|---|---|---|---|---|---|---|---|
| 90 | 10,740 | 320.0 | 0.50 | 600 | 12 | | 36.3 | 18.1 | 3.71E-11 | 2.13E-10 | 17.145 |
| 91 | 10,913 | 319.8 | 0.50 | 1000 | 12 | | 36.3 | 18.2 | 2.10E-11 | 1.28E-10 | 17.155 |
| 92 | 11,011 | 319.9 | 0.30 | 2300 | 12 | | 39.4 | 27.6 | 1.03E-10 | 1.81E-10 | 17.192 |
| 93 | 11,247 | 319.9 | 0.30 | 4600 | 12 | | 39.8 | 27.9 | 5.12E-11 | 9.42E-11 | 17.235 |
| 94 | 11,701 | 319.1 | 0.30 | 4600 | 12 | 7,200 | 40.1 | 28.1 | 2.44E-11 | 3.76E-11 | 17.269 |
| 95 | 11,966 | 319.3 | 0.30 | 4600 | 12 | 14,400 | 40.2 | 28.2 | 1.53E-11 | 2.36E-11 | 17.285 |
| 96 | 12,109 | 319.1 | 0.30 | 4600 | 12 | 28,800 | 40.3 | 28.2 | 8.72E-12 | 1.35E-11 | 17.289 |
| 97 | 12,124 | 319.0 | 0.50 | 12 | 12 | 28,800 | 40.3 | 20.2 | 4.04E-12 | 6.77E-12 | 17.289 |
| 98 | 12,241 | 319.4 | 1.00 | 0 | 0 | | 40.2 | 0.0 | 5.37E-12 | - | 17.297 |
| 99 | 12,246 | 319.2 | 0.50 | 12 | 12 | | 40.7 | 20.4 | 2.14E-09 | 1.70E-08 | 17.346 |
| 100 | 12,268 | 319.2 | 0.50 | 12 | 12 | | 40.9 | 20.4 | 1.55E-09 | 1.72E-08 | 17.359 |
| 101 | 10,350 | 319.2 | 0.50 | 20 | 20 | | 40.9 | 20.5 | 9.17E-10 | 1.04E-08 | 17.364 |
| 102 | 12,288 | 319.2 | 0.50 | 100 | 12 | | 41.0 | 20.5 | 2.17E-10 | 2.10E-09 | 17.375 |
| 103 | 12,292 | 319.2 | 0.50 | 12 | 12 | | 41.2 | 20.6 | 9.62E-10 | 1.77E-08 | 17.388 |
| 104 | 12,312 | 319.2 | 0.50 | 100 | 12 | | 41.2 | 20.6 | 1.72E-10 | 2.14E-09 | 17.397 |
| 105 | 12,316 | 319.2 | 0.50 | 12 | 12 | | 41.3 | 20.7 | 9.03E-10 | 1.80E-08 | 17.405 |
| 106 | 12,383 | 319.2 | 0.50 | 300 | 12 | | 41.4 | 20.7 | 8.83E-11 | 7.27E-10 | 17.414 |

[a] Simulated PWR water with 2 ppm Li, 1000 ppm B, and 2 ppm. DO<10 ppb. Conductivity was 21±3 µS/cm, and pH 6.4.
[b] Data was corrected using fractography.

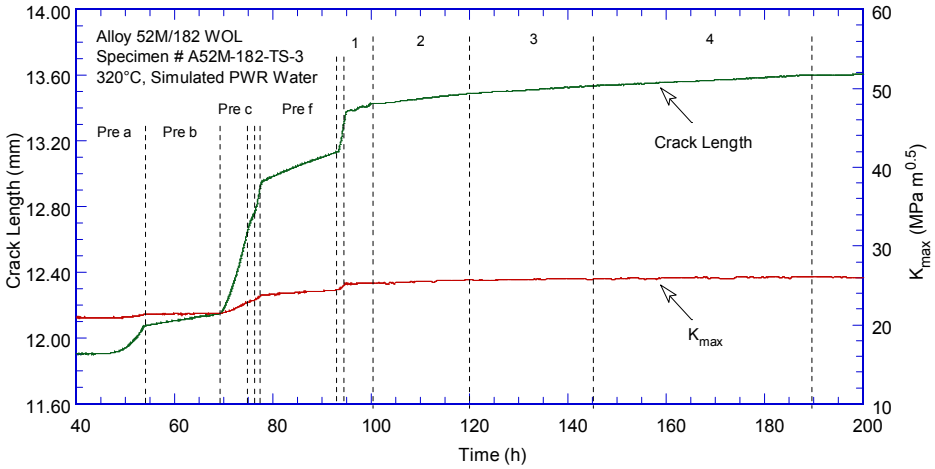


**Figure 3-3 Crack–length–vs.–time for specimen A52M-182-TS-3 in simulated PWR environment during test periods: (a) precracking-4, (b) 5-8, (c) 9-14, (d) 15-19, (c) 18-23, (f) 24-25. (g) 24-79, (h) 80-89, (i) 90-98, and (j) 99-106.**

**Figure 3-3 (Cont.)**

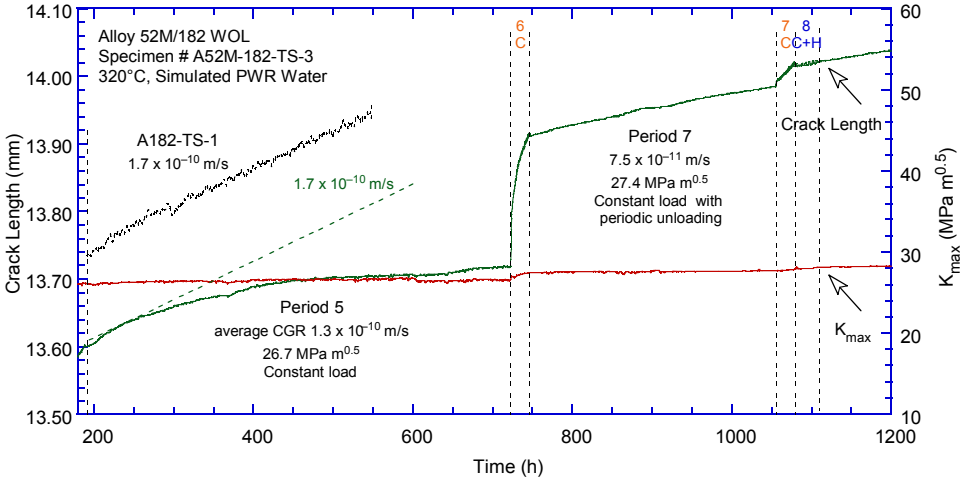


(b)

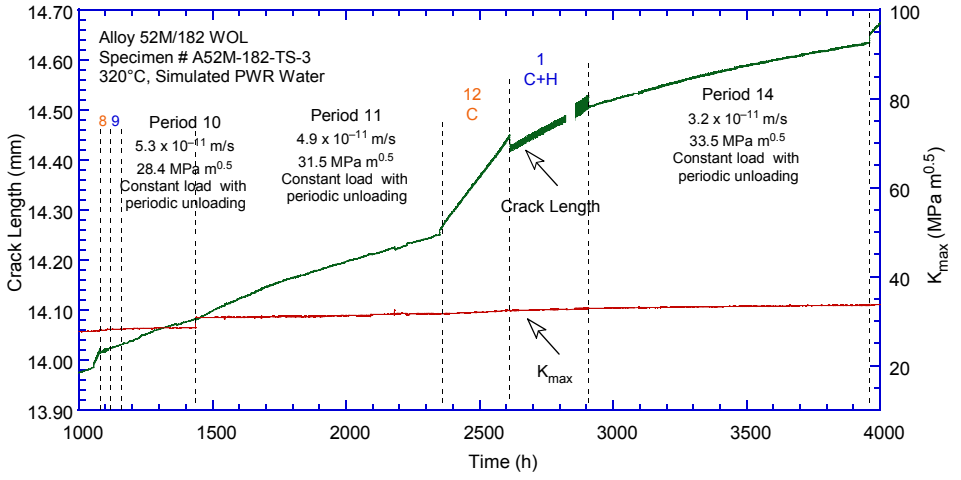


(c)

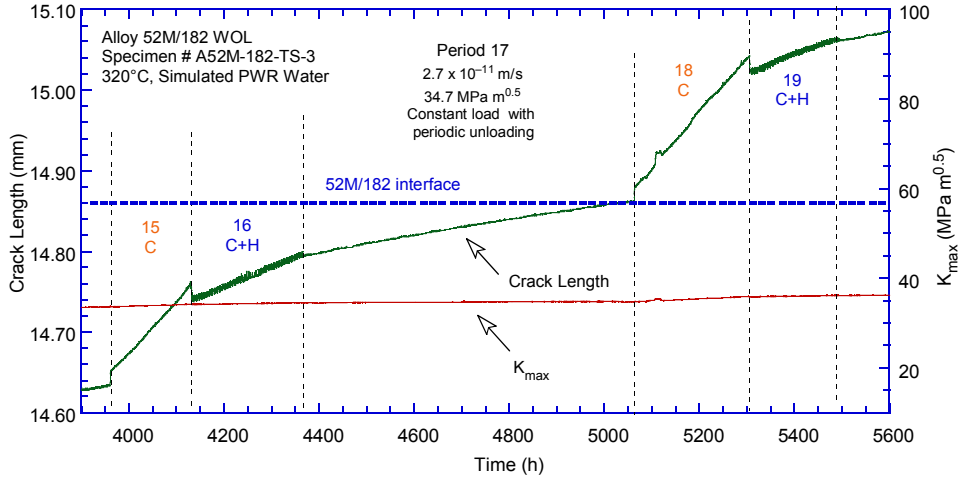


(d)

**Figure 3-3 (Cont.)**

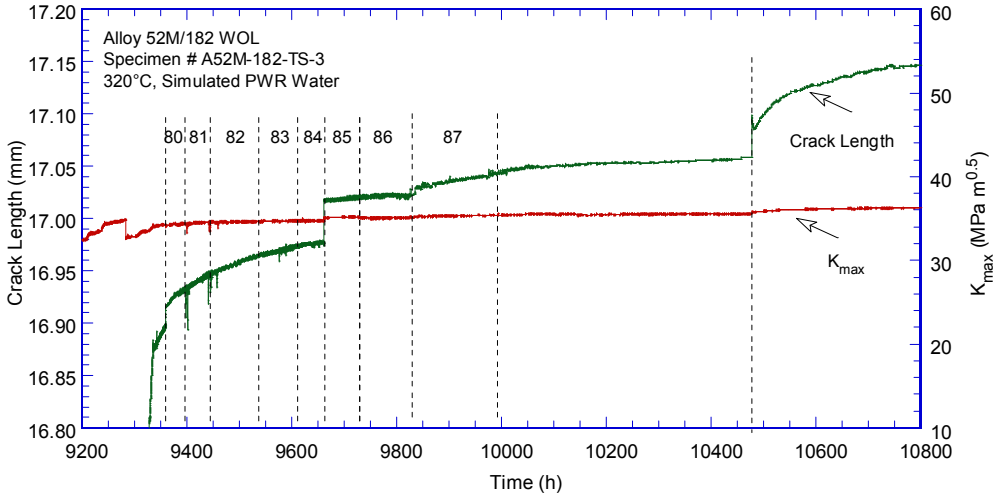


(h)

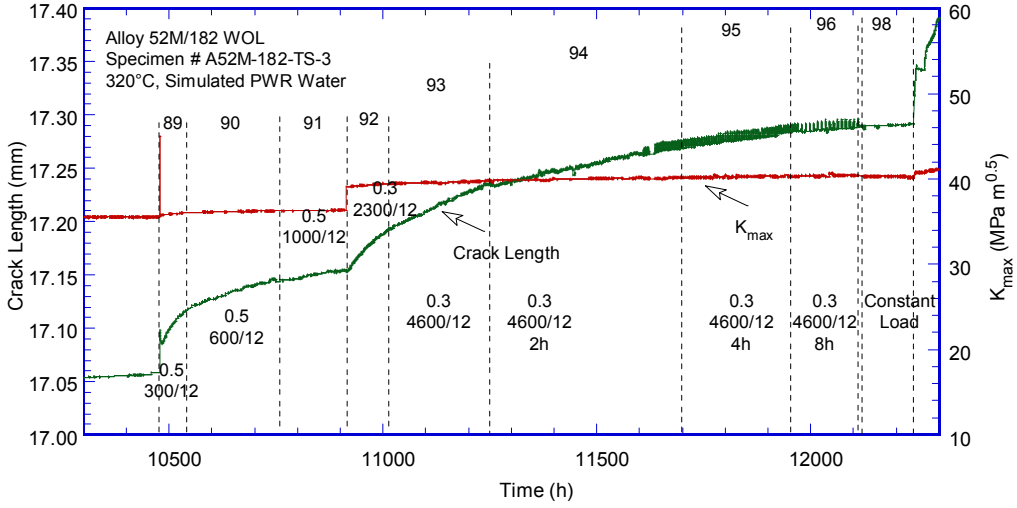


(i)

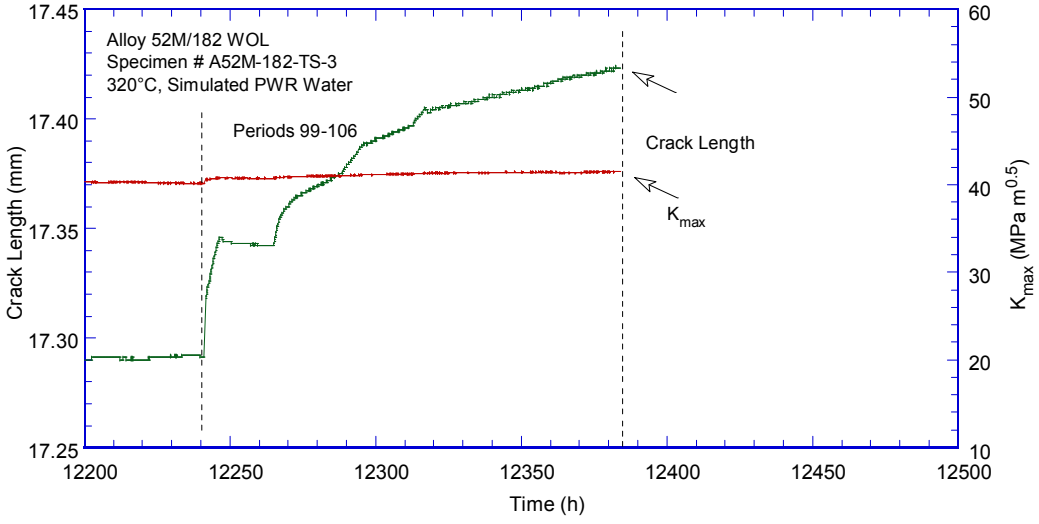


(j)

The first step in the post-test examination of this specimen involved the two side surfaces. For this purpose, the sides of the specimen were ground to remove the side grooves, then polished, and etched. The SEM images of the two cross sections are shown in Fig. 3-4. As expected, the crack initiated in the Alloy 182 weld and propagated into the Alloy 52M interface. In each figure, several locations of interest are marked, however, the region of highest interest was the interaction of the crack with the Alloy 52M WOL interface.

On the first cross section examined (Fig 3-4a), the crack started – as expected – as a fatigue crack and transitioned to SCC in Alloy 182. The first unusual behavior was observed at the interface with Alloy 52M (location A), where the crack changes direction and propagates along the interface. This behavior is shown with additional detail in Fig. 3-5a. The propagation along the interface is substantial, approximately 0.3 mm, then, the crack branches into Alloy 52M. The crack appearance suggests an IG fracture mode.

On the second cross section examined (Fig 3-4b), the crack started in similar fashion, as a fatigue crack and was transitioned to SCC in Alloy 182. Crack branching was observed at location A in Alloy 182, however, crack branching is typical for a weld alloy. Nevertheless, the introduction of periodic unloading apparently minimized the effect of the ligaments ahead of the interface. Moreover, given that crack branching occurred despite the periodic unloading, it appears that perhaps a more aggressive periodic unloading would have been more appropriate for this type of test.

The crack interaction with the Alloy 52M interface is similar to that observed on the first cross section (location B in Fig 3-4b). This behavior is shown with additional detail in Fig. 3-5b. Of interest is the crack that branches off the main crack front, and propagates in Alloy 52M near the interface, Fig. 3-5b. As with the crack observed on the first cross section, the growth is substantial, approximately 0.7 mm. The morphology seems IG, and it is possible for this particular crack to have propagated at a rate of the order $10^{-10}$ m/s since that amount of growth occurred over 2000-3000 h.

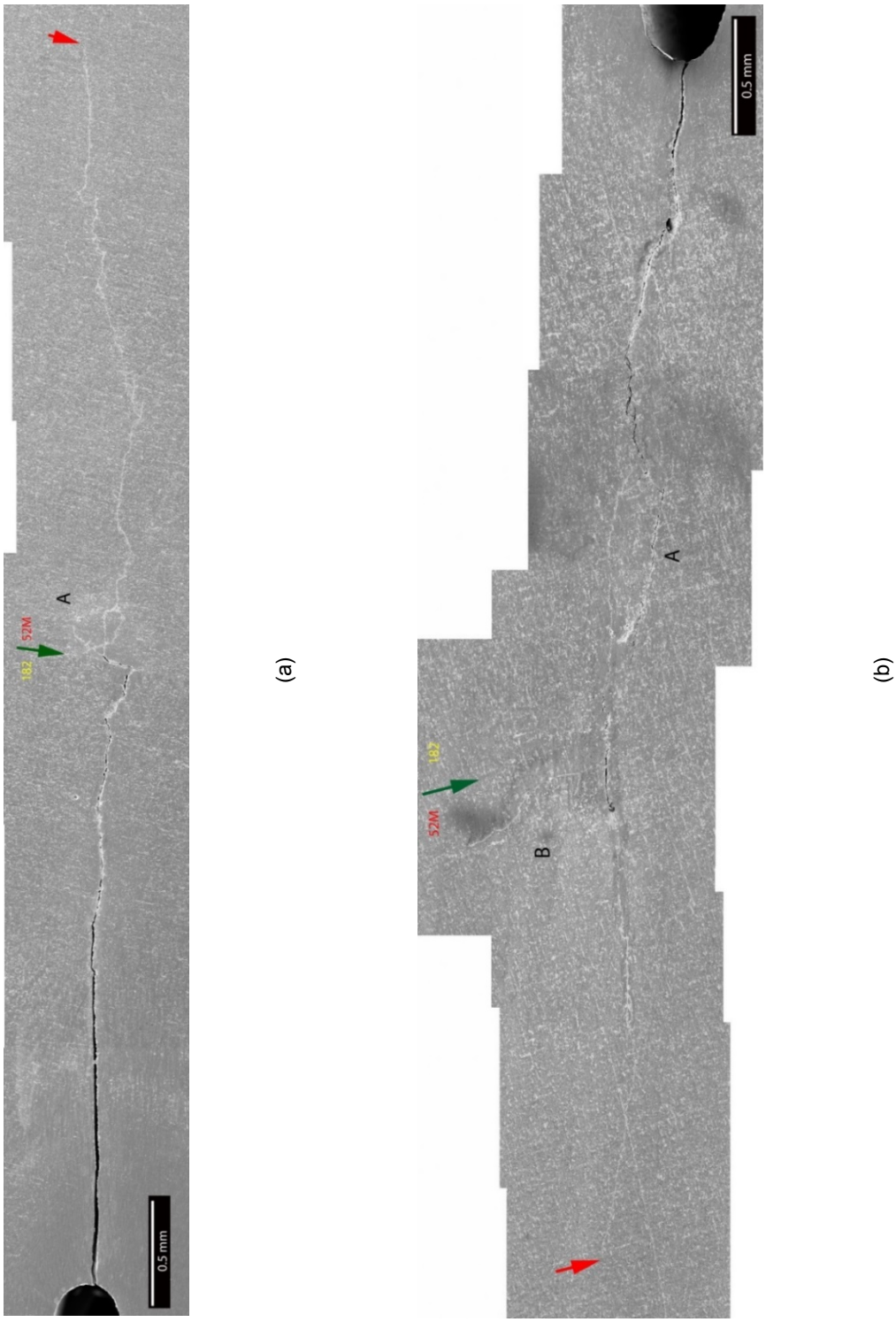


**Figure 3-4** **The two side surfaces of Specimen A52M-182-TS-3. Crack advance is from left to right (a), and right to left (b). The green arrows show the interface between the two welds and the red arrows indicate the end of the test.**

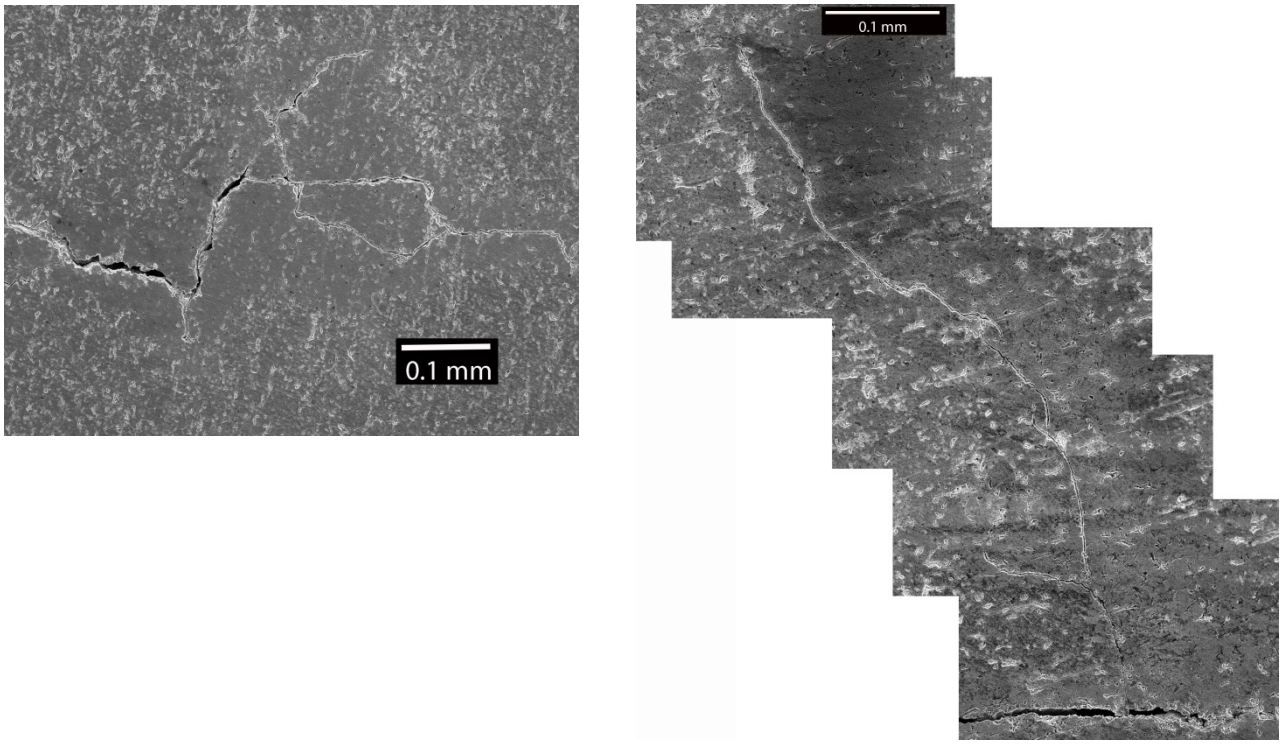


(a) (b)

**Figure 3-5 Interaction with the Alloy 52M interface (a) location A in Fig. 3-4a, crack propagation is from left to right, and (b) location B in Fig. 3-4b, crack propagation is from right to left.**

In order to further examine the crack behavior at the interface and the paths of the branching cracks, additional images were obtained at the crack intersection with the interface. Then, SEM Energy Dispersive X-ray Spectroscopy (EDX) Cr concentration maps were obtained from the same regions. In these maps, the higher color intensity reflects a higher Cr concentration. Finally, the backscatter SEM images were overlapped onto the Cr maps. The results for the two regions where the crack interacts with the Alloy 52M WOL are shown in Figs. 3-6 and 3-7. It appears that in both cases, the crack impinging on the interface branches at the interface or after crossing the interface, and propagates in Cr-diluted Alloy 52M, in a direction parallel to the interface, in what appears to be an IG mode. The observations are substantiated by the individual Cr concentrations measured by SEM EDX at select locations along those cracks. Overall, the examination of the two cross sections revealed that the test progressed largely as expected, and the crack advanced from Alloy 182 into Alloy 52M; extensive cracking propagating in Alloy 52M in a direction along the interface between the two welds was also observed.

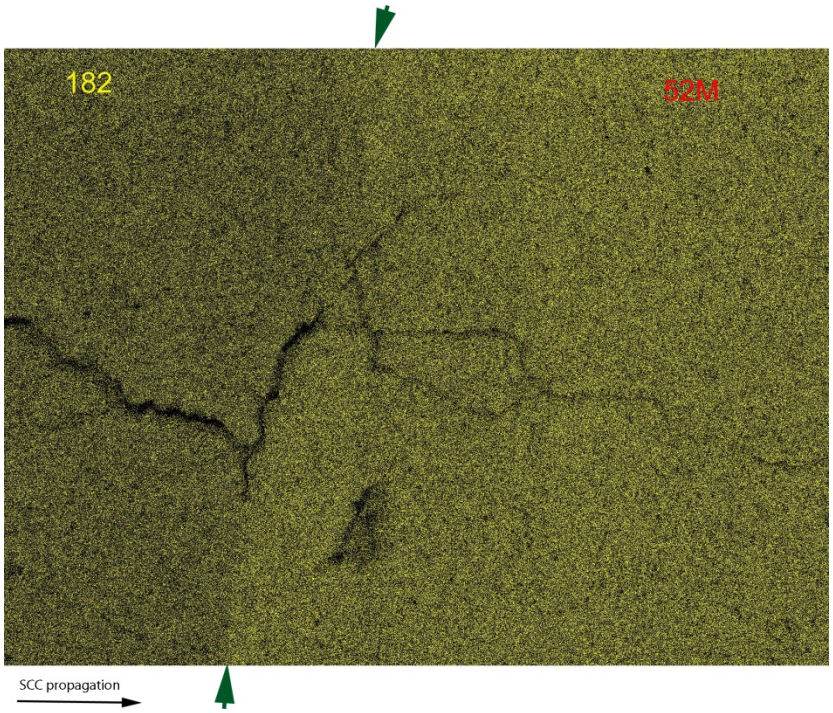


(a)

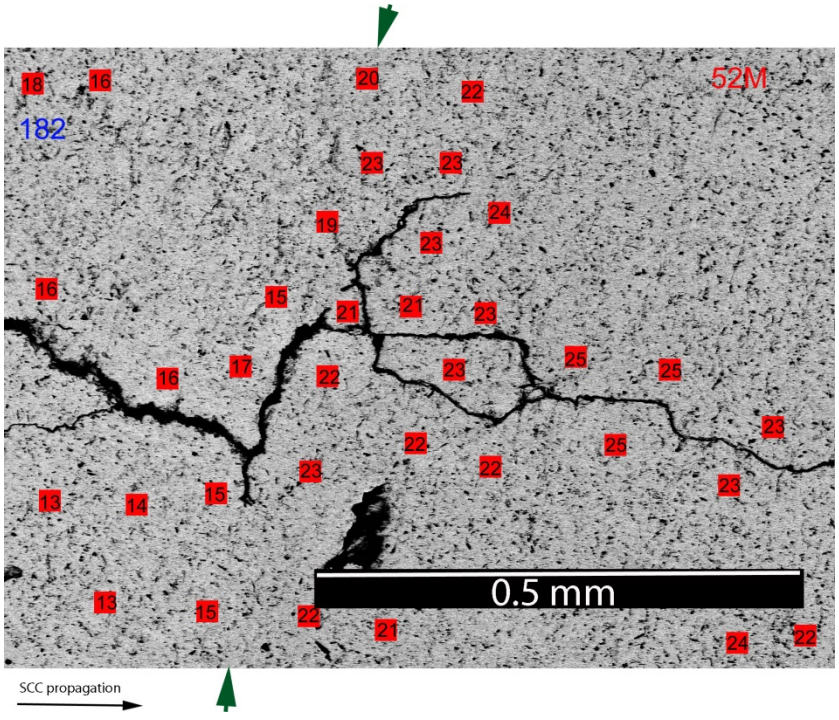


(b)

**Figure 3-6** **SCC interaction with the Alloy 52M WOL interface (location A in Fig. 3-4a): (a) overlap of SEM image and elemental map, and (b) Cr concentration (wt. %) at each location. Crack propagation is from left to right. Green arrows indicate the Alloy 52M-182 interface.**

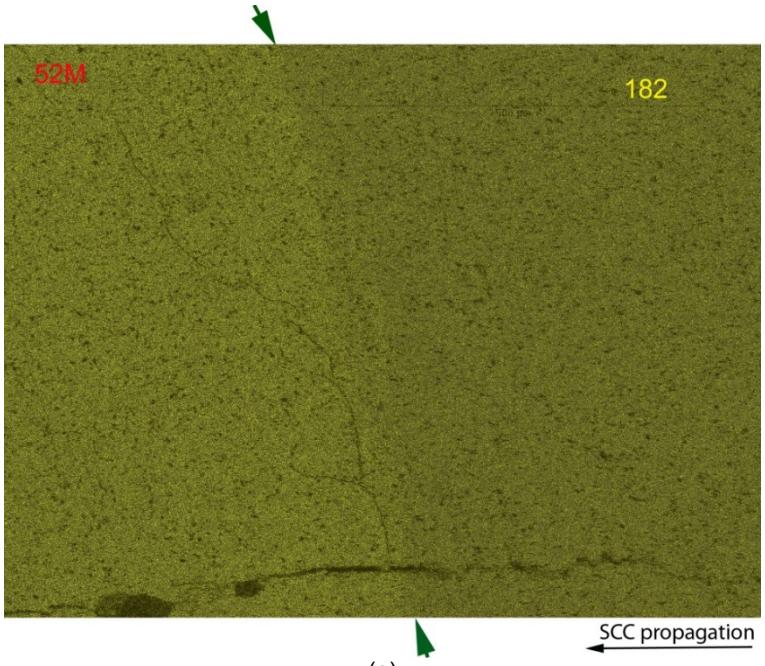


(a)

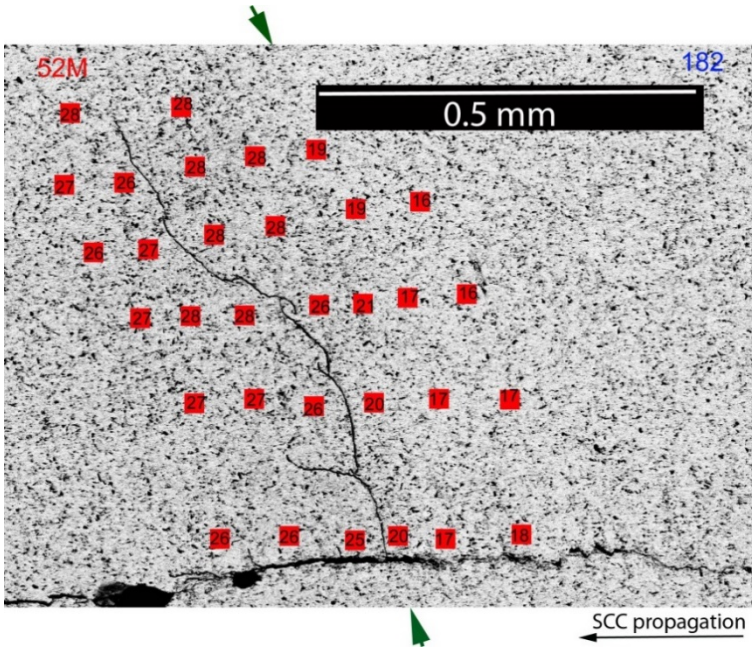


(b)

**Figure 3-7** **SCC interaction with the Alloy 52M WOL interface (location B in Fig. 3-4b): (a) overlap of SEM image and Cr map, and (b) Cr concentration (wt. %) at each location. Crack propagation is from right to left. Green arrows indicate the Alloy 52M-182 interface.**

Next, the specimen was broken into two halves to examine the fracture surface. The two resulting fracture surfaces are shown in Fig. 3-8. The outcome demonstrates that cracking along the Alloy 52M-182 interface was more severe than was originally inferred from the examination of the two lateral cross sections. In fact, for the most part, it was the major crack in this specimen. The schematic shown in Fig. 3-9 will be used to describe the observed behavior.

**Figure 3-8 Fracture surfaces of Specimen A52M-182-TS-3.**

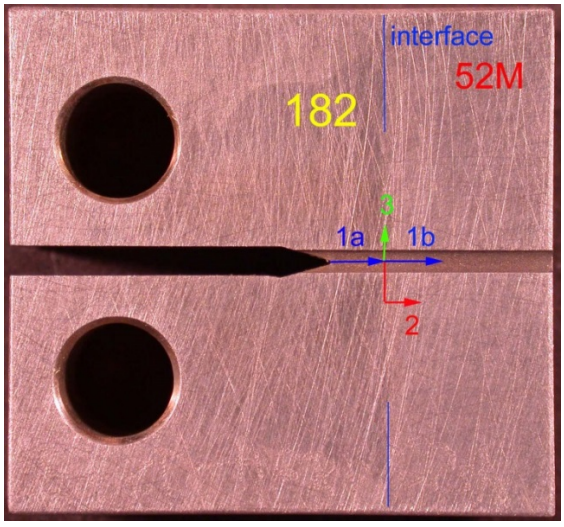


**Figure 3-9 Crack interaction with the Alloy 52M interface. Crack propagation is from left to right. The major crack directions are indicated.**

Figure 3-9 shows the cross section of the test specimen with several crack propagation directions marked. Initially, the crack propagated along direction 1a towards the interface. Upon reaching the interface, the crack branched into three directions. While the crack partially continued along the forward direction 1b, cracking also developed parallel along the interface and into Alloy 52M along directions 2 and 3. Direction 2 turned out to be the most prominent. Post test, the specimen fractured primarily along this direction.

Figure 3-10 shows additional images of the two resulting specimen halves; the photos were oriented to match the crack directions illustrated in Fig. 3-9. The crack propagated as expected in Alloy 182 along the initial direction 1a, then branched at the interface. There is evidence for propagation along the original (forward) direction 1b, and along the interface in both directions 2 and 3. As noted previously, propagation along direction 2 appeared to be the most severe.

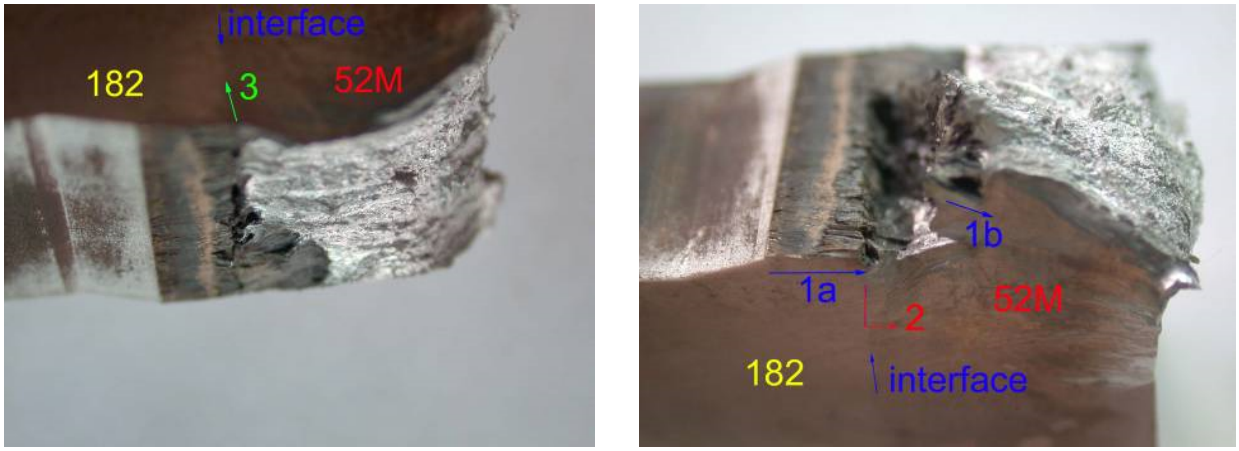


**Figure 3-10 The two halves of fractured specimen A52M-182-TS-3.**

Figure 3-11 shows additional pictures taken at various angles to better illustrate the severity of the cracking.

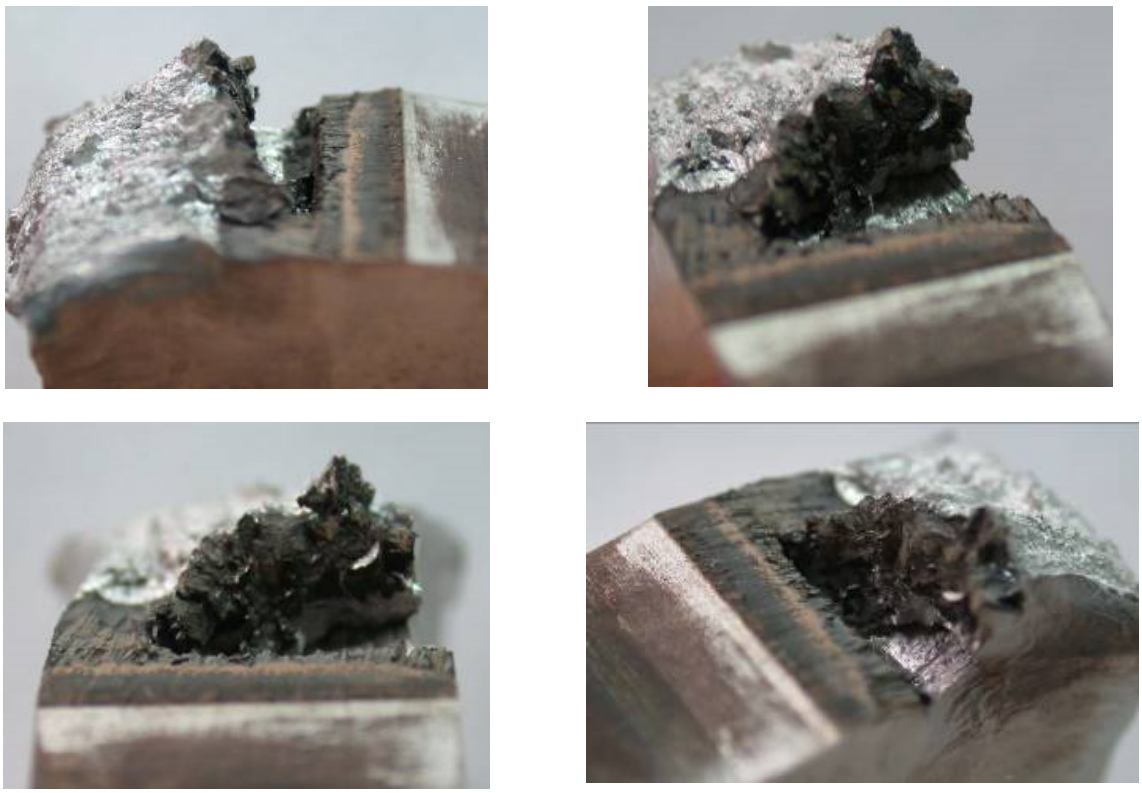

**Figure 3-11 Fractured specimen A52M-182-TS-3.**

For the CGR data analysis, the fracture surface shown on the left side of Fig. 3-8 was chosen because it was judged to possess the necessary details pertaining to propagation along the initial direction (direction 1 in Fig. 3-9). Such details are necessary for the correction and interpretation of the DC potential data. This fracture surface is shown in Fig. 3-12 both as a photograph and as an SEM micrograph. The relationship with respect to the two sides of the specimen discusses previously (Fig. 3-14) is indicated in each figure. Also, the interface between Alloys 182 and 52M is indicated by arrows. The fracture surfaces show that, as expected, the crack propagated from the initial notch, transitioned to an IG mode in Alloy 182 after approximately 1.9 mm, and reached the interface located at 2.9 mm from the initial notch. This SCC front in Alloy 182 appears straight, suggesting that the crack reached the interface as a front rather than as individual "fingers".

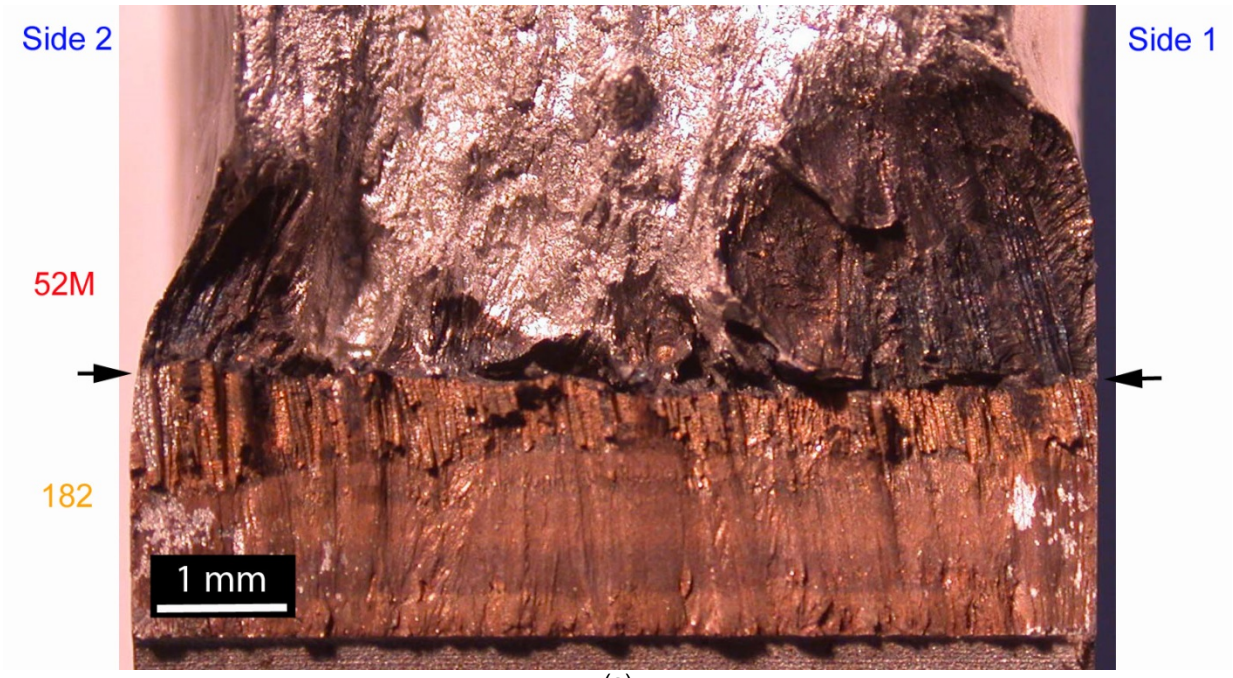


(a)

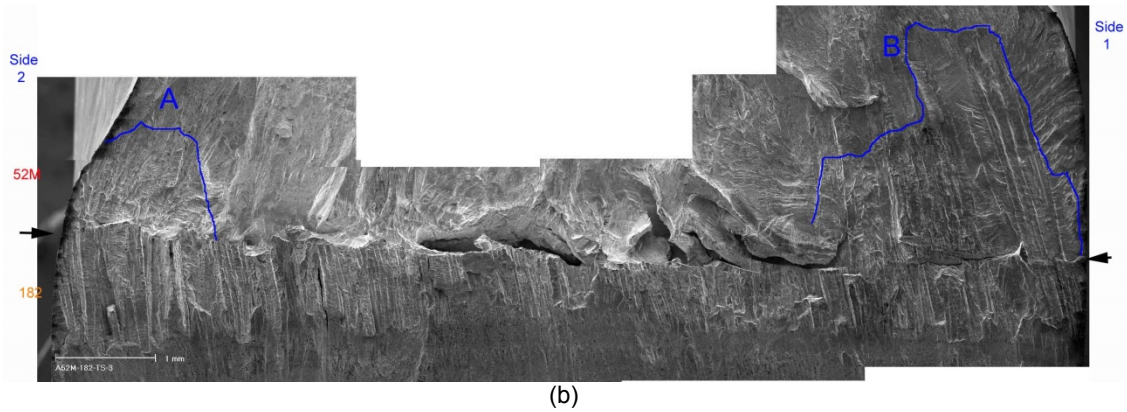


(b)

**Figure 3-12 Fracture surface of Specimen A52M-182-TS-3 (a) photograph, and (b) SEM micrograph. Regions marked "A" and "B" represent the two most prominent regions of IG SCC propagation into the Alloy 52M WOL. Crack propagation is from bottom to top.**

Figure 3-12 also shows that upon reaching the interface, the crack apparently propagated in both the original direction and along the interface between the two welds. While a large portion of the fracture surface is unavailable due to the way this specimen fractured post-test, Fig. 3-12 reveals that approximately 40% of the crack continued in the original direction in a finger-like manner, and maintained the IG fracture characteristics. Propagation at locations A and B in Fig. 3-12b was the most prominent. Figure 3-13 shows additional detail at the interface between the two welds at these locations.

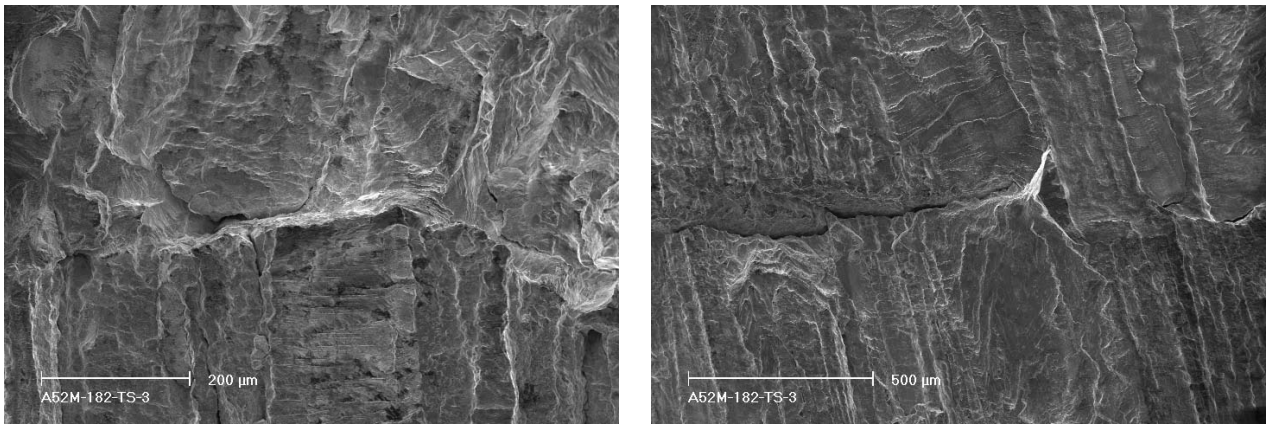


(a) (b)

**Figure 3-13 Crack transition across the Alloy 52M-182 interface at locations (a) A, and (b) in Fig. 3-12b. Crack advance is from bottom to top.**

It is important to note that the amount of IG fracture observed in regions A and B in Fig. 3-12b is equivalent to an average growth of approximately 0.35 mm over the entire width of the specimen. For such cracking to develop over 3000h, the average SCC CGRs must have been approximately $3x10^{-11}$ m/s, and this is consistent with the CGRs measured in periods 19-23 by DC potential. It is also interesting to note that the maximum crack advance in region B is 2.5 mm, corresponding to a maximum SCC CGR of approximately $2x10^{-10}$ m/s.

A precise measurement of the entire extent of crack growth is impossible in this case because the surface needed for the correction of the DC potential data (direction 1b, Fig. 2-3) was not fully revealed after the specimen was fractured. However, the first side surfaces shown in Fig. 3-4 yielded total crack advance measurements of 5.9 mm on one side and 5.2 mm on the other. Given the crack morphology observed past the interface, an uneven crack front was to be expected. Thus, an average of the two side surface measurements was judged to give the best estimate for the full extent of crack advance. That would translate into a correction of 23% for the entire crack length. Nevertheless, the correction for the pre-interface part of the test is likely to be small when compared to that needed for the region tested after the interface cracks developed. As such, given the unevenness of the front, and assuming that the interface cracks had developed by the resumption of fast cycling, the decision was made to apply the entire correction from that point on. Therefore, the needed correction (factor 2.7) was applied to data points resulting from regions 0.35 mm past the interface (test period 26). It is interesting to note that transitioning in Alloy 52M (period 78) as found on the fracture surface (marked with an arrow in Fig. 3-31) occurs approximately 2.6 mm from the Alloy 52M-182 weld interface. As such, the good agreement between the expected fracture mode and the corrected crack length shown in Table 3-1 further substantiates the correction approach described previously.

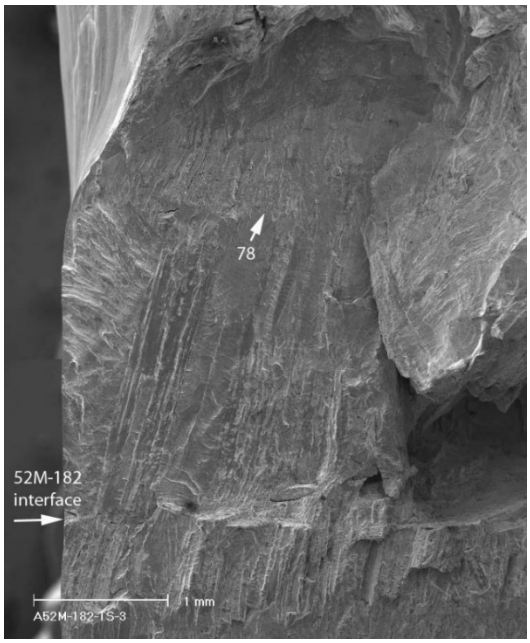


**Figure 3-14 Fracture surface of specimen A52M-182-TS-3. The arrow indicates the beginning of transitioning to IG in Alloy 52M. Crack advance is from bottom to top.**

The evolution of this test can also be inferred from the cyclic rates obtained at the various stages of the test, Fig. 3-15. In all figures, the CGRs measured in the environment are plotted vs. the predicted rates in air under the same loading conditions. The corrosion fatigue curves for Ni-weld alloys are also included. Initially, during test periods precracking–4, the cyclic data was in very good agreement with the data obtained previously on the same Alloy 182 weld, shown in Fig 3-15a. However, as noted previously, the environmental enhancement observed in the subsequent periods begins to diminish, shown in Fig. 3-15b. This figure includes both Alloy 182 data and Alloy 52M data (blue open symbols) from the current specimen, as well as the Alloy 152 data obtained at ANL previously under similar loading conditions (Fig. 2-10a), and Alloy 52 "air line" data from the literature [24-25]. The Alloy 52M data seem consistent with Alloy 152 (red symbols), and are higher than the Alloy 52 "air line". The behavior suggests a high degree of environmental enhancement, and likely propagation in an IG mode. The subsequent data obtained during periods 24-77, shown in Fig. 3-15c, are inconsistent, most likely due to the breaking of ligaments during the overall straightening of the fracture surface. The overall response is lower than expected, perhaps due to a diminished stress intensity factor caused by crack branching at the interface. The baseline – the "air line" for Alloy 52M cyclic rates - cannot be established. By contrast, during test periods 78-93, shown in Fig. 3-15d, the response to fast cycling stabilizes, suggesting that the fracture surface has somewhat straightened. The "air line" for Alloy 52M was established. The cyclic response is much smaller than expected, perhaps due to the lower than measured stress intensity factors caused by crack branching at the interface. It is interesting to note that in order to match the behavior shown by the current specimen, Alloy 52 would have to be loaded at stress intensity factors about half of those shown in Table 3-1. Nevertheless, the specimen response is consistent, and the known R-dependence (Fig. 2-10a) was reproduced. The behavior over a range of load ratios R = 0.3-0.7 seems similar to that observed previously for Alloy 152. This data set also seems to indicate that the optimum loading for environmental enhancement is R = 0.5. Similar to Alloy 152 (see Fig. 2-10a), one observes that by further increasing R to 0.6 the environmental

enhancement begins to diminish. When R is 0.7 and rise time is 1000s, the rate in the environment equals that in air, that is, the environmental enhancement appears to be lost. Interestingly, data obtained at R = 0.3 but with very long rise times (periods 92 and 93) exhibit the highest environmental enhancement.

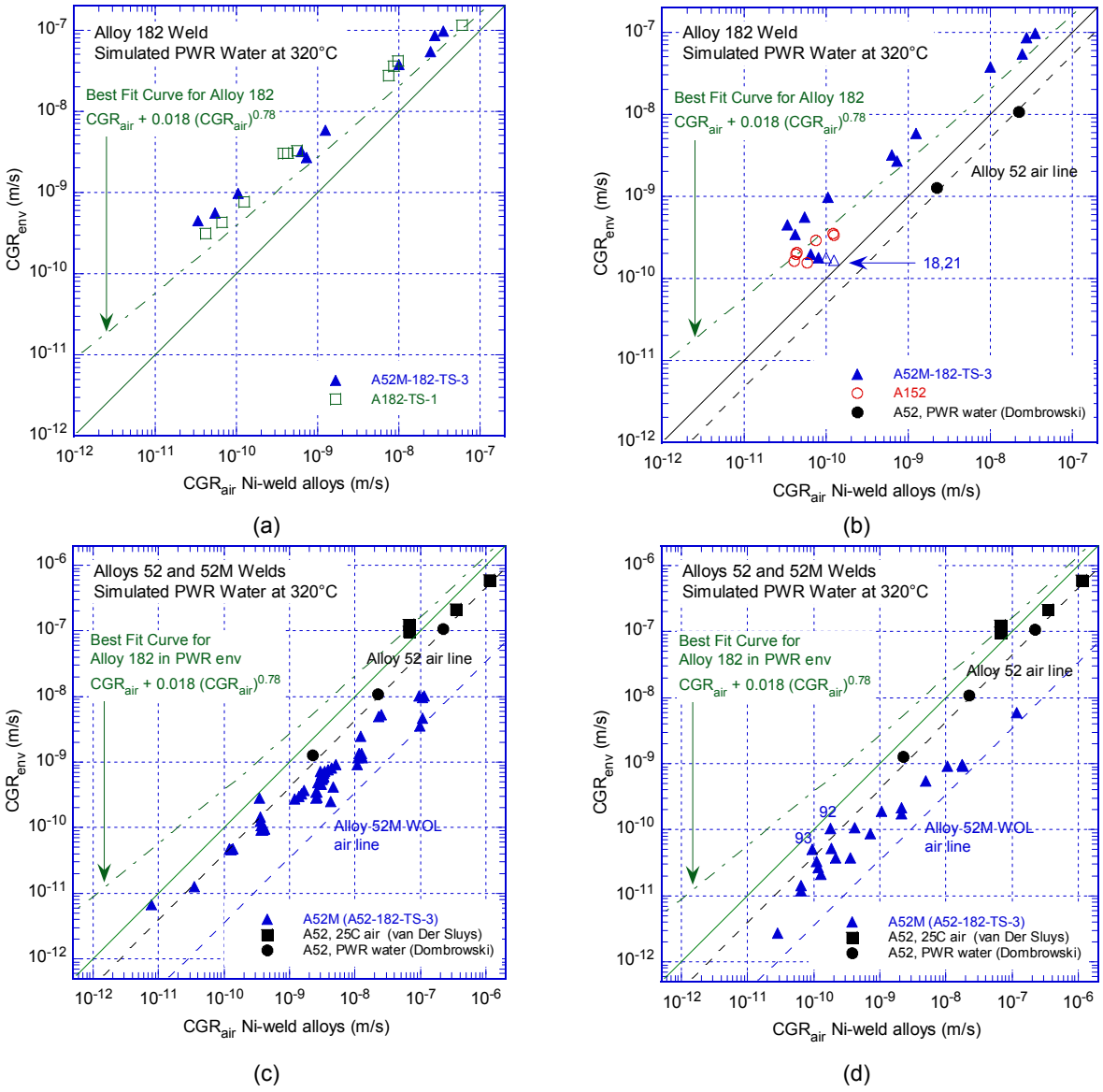


**Figure 3-15 Cyclic CGR data in PWR environment for (a) specimen A52M-182-TS-3 and specimen A182-TS-1 of the same alloy tested previously (without WOL), (b) specimen A52M-182-TS-3 and Alloy 152 specimen A152-TS-4 under similar loading, and Alloy 52 data from the literature [24, 25], (c) Comparison between Alloy 52M data obtained in the current test and Alloy 52 data from the literature [24, 25], (d) Transitioning in Alloy 52M, periods 78-93.**

Table 3-2 provides a summary of the SCC CGR data resulting from this test. These data will be used to illustrate the CGR dependence on the distance to the 52M-182 interface.

**Table 3-2 Summary of SCC CGR and cyclic (control cycle) data for specimen A52M-182-TS-3**

| Test period | K ($MPa \cdot m^{1/2}$) | Distance to interface (mm) | SCC CGR (m/s) | Cyclic CGR (m/s) | Method |
|---|---|---|---|---|---|
| 5 | 26.2 | -1.214 | 1.30E-10 | | CL |
| 10 | 27.4 | -0.914 | 7.51E-11 | | CL + PU |
| 11 | 31.5 | -0.582 | 4.86E-11 | | CL + PU |
| 14 | 33.5 | -0.199 | 3.24E-11 | | CL + PU |
| 17 | 34.7 | 0.030 | 2.69E-11 | | CL + PU |
| 20 | 36.3 | 0.271 | 2.44E-11 | | CL + PU |
| 23 | 38.2 | 0.547 | 1.83E-11 | | CL + PU |
| 97 | 40.3 | 2.457 | 4.04E-12 | | CL + PU |
| 98 | 40.2 | 2.465 | 5.37E-12 | | CL |
| 13 | 32.8 | -0.319 | 4.11E-11 | | est cycle+hold |
| 16 | 34.4 | -0.037 | 2.84E-11 | | est cycle+hold |
| 19 | 36.1 | 0.233 | 2.20E-11 | | est cycle+hold |
| 22 | 38.0 | 0.508 | 1.31E-11 | | est cycle+hold |
| 88 | 35.5 | 2.226 | 5.32E-12 | | est cycle+hold |
| 95 | 40.2 | 2.453 | 5.93E-12 | | est cycle+hold |
| 4 | 26.2 | -1.214 | | 4.47E-10 | |
| 8 | 27.8 | -0.813 | | 3.49E-10 | |
| 12 | 32.4 | -0.384 | | 1.98E-10 | |
| 15 | 34.1 | -0.077 | | 1.80E-10 | |
| 18 | 35.9 | 0.210 | | 1.79E-10 | |
| 21 | 37.8 | 0.476 | | 1.67E-10 | |
| 83 | 34.9 | 2.142 | | 3.31E-11 | |
| 87 | 35.4 | 2.216 | | 2.68E-11 | |
| 91 | 36.3 | 2.323 | | 2.10E-11 | |

To summarize this test, the CGRs shown in Table 3-2 are plotted as a function of the distance to the 52M WOL interface in Fig. 3-16. As described previously, the crack was transitioned to IG SCC in Alloy 182, and the average SCC CGR at 1.2 mm from the interface was $1.3 \times 10^{-10}$ m/s. This CGR is consistent with the CGR measured for the same alloy without the WOL. As the crack approached the interface, the measured CGRs decreased to approximately $2 \times 10^{-11}$ m/s. At the interface, the crack branched. The crack continuing in Alloy 52M along the initial propagation plane grew at a rate of approximately $2 \times 10^{-11}$ m/s. The resulting fracture surface corresponds to regions A+B in Fig. 3-12b, and the average crack advance and CGR estimates based on the fracture surface are consistent with the average growth and rates measured by DC potential. Crack advance resumes in a TG mode after fast cycling is introduced, however, both cyclic and SCC CGRs are retarded beyond this point because of the presumably reduced stress intensity factor. The overall behavior of the SCC CGRs vs. distance is mirrored by the behavior of the control cycle. It should be noted that the rates shown in Fig. 3-16 are not normalized by the stress intensity factor. If that were accomplished, the effect of the interface on the SCC CGRs would perhaps be even more dramatic.

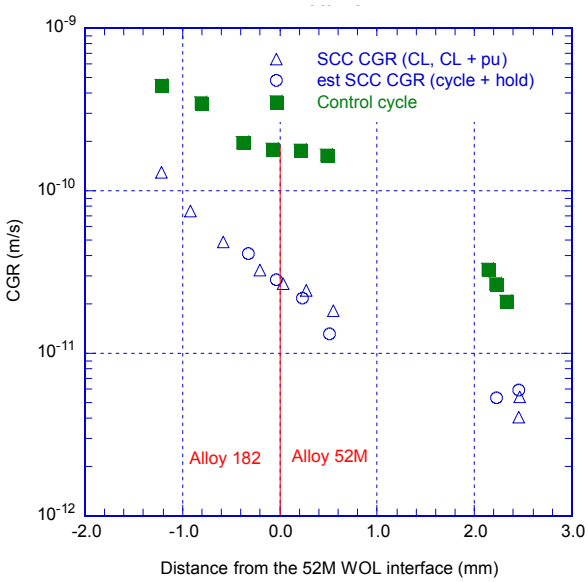


**Figure 3-16 SCC CGR in Specimen A52M-182-TS-3 as a function of distance to the 182/52M interface.**

### 3.1.2 Specimen A52M-182-TS-1

The test on specimen A52M-182-TS-1 (Fig. 2-3) was essentially a repeat of the test described in the previous section, except this specimen was a 1T-CT as a test system that could accommodate the larger specimen size became available. The objective of this test was similar to the first one, i.e. to observe the behavior of a SCC crack propagating from Alloy 182 towards the Alloy 52M WOL. The distance from the notch to the interface was approximately 8 mm.

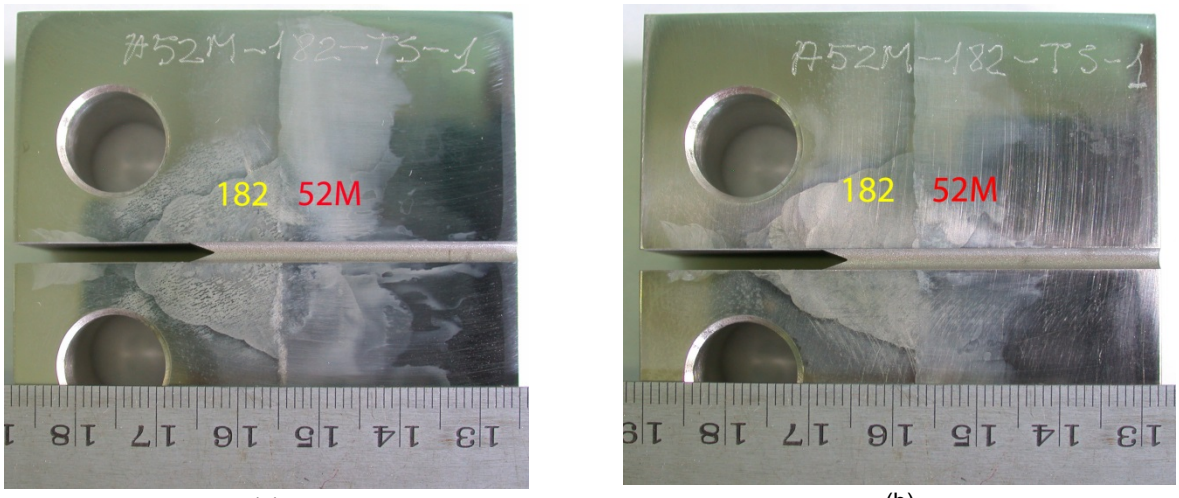


(a) (b)

**Figure 3-17 Photographs of the two sides of the 52M/182 weld overlay specimen A52M-182-TS-1.**

The testing conditions for specimen A52M-182-TS-1 are given in Table 3-3; as with the prior test, the part that took place in Alloy 182 is shaded with gray. The changes in crack length and $K_{max}$ with time are shown in Fig. 3-18. The crack was transitioned in Alloy 182, and a first SCC

CGR was determined in period 7, approximately 4.1 mm from the interface. Next, in order to simulate the conditions from the previous test (IG SCC in Alloy 182 approximately 1 mm from the interface with the WOL), the crack was advanced in fatigue and was transitioned again at a higher stress intensity factor at approximately 1.9 mm from the interface. Both SCC CGRs (periods 7 and 20) are consistent with rates measured previously for this Alloy 182 weld. Next, the crack was advanced towards the interface by a succession of gentle cycling and constant load with periodic unloading. The resulting rate at 1.3 mm from the interface (period 22) was slower than that observed previously, but the trend was expected based on the prior test. The routine was repeated in periods 23-26, 1.2 mm from the interface. Next, the crack was advanced under cyclic loading in period 27; as the rate appeared similar to that measured just prior to the interface in the previous test, the specimen was set at constant load with periodic unloading in period 28, 0.5 mm from the interface. The crack was further advanced until the interface by gentle cycling in period 29, and set at constant load with periodic unloading in test period 30. The CGR was initially slow ($1.5x10^{-11}$ m/s), subsequently appeared to go through slow ($1.5x10^{-11}$ m/–) - fast ($8.0x10^{-11}$ m/s) periods of growth, on average $4.7x10^{-11}$ m/s, Fig. 3-18i. The reason for this behavior is unknown, nevertheless, growth is very different from the "well-behaved" appearance of the previous test periods. As the rate apparently stabilized at $5.3x10^{-11}$ m/s, the specimen was set at constant load. The behavior observed in period 31 suggests that as with the previous specimen, the fracture is complex with perhaps one or several cracks having developed at the interface, and a possible flake shorts the DC potential measurements in the absence of periodic unloading. Periodic unloading was reintroduced in period 32. Growth resumed at the previous (test period 30) rate, then fell into the $10^{-12}$ m/s range, suggesting that the SCC growth has stopped. It was decided to finish the test to assess the fracture surface. Overall, the resulting SCC CGRs vs. distance behavior appears similar to that observed on the previous WOL specimen.

A final set of fatigue measurements were undertaken in periods 33-42. The crack was advanced by a substantial amount (6.5 mm) in order to preserve as much as possible of the the fracture surface at the interface. It is worth noting the jump at the beginning of period 33, Fig. 3-18j, suggesting that some ligaments were broken. Also, it is interesting that overall the fatigue response is approximately an order of magnitude lower than expected for a Ni-base weld (Eqs. 2 and 5). This response is similar to that observed in the prior test (Fig. 3-15d) and suggests that cracking occurred along the interface between the two welds resulting is a reduced stress intensity factor at the crack tip.

## Table 3-3 Crack growth data for WOL specimen A52M-182-TS-1 in PWR water[a,b]

| Test Period | Test Time, h | Temp. °C | Load Ratio R | Rise Time, s | Down Time, s | Hold Time, s | $K_{max}$, MPa·m$^{1/2}$ | $\Delta K$, MPa·m$^{1/2}$ | $CGR_{env}$, m/s | Estimated $CGR_{air}$, m/s | Crack Length, mm |
|---|---|---|---|---|---|---|---|---|---|---|---|
| Pre a | 316 | 320.2 | 0.32 | 0.5 | 0.5 | | 19.5 | 13.3 | 3.07E-08 | 4.35E-08 | 12.665 |
| Pre b | 333 | 320.1 | 0.32 | 50 | 50 | | 19.6 | 13.3 | 1.44E-09 | 4.41E-10 | 12.734 |
| Pre c | 339 | 320.1 | 0.32 | 0.5 | 0.5 | | 20.1 | 13.7 | 4.88E-08 | 4.93E-08 | 13.253 |
| Pre d | 404 | 320.2 | 0.32 | 100 | 100 | | 20.3 | 13.8 | 1.20E-09 | 2.54E-10 | 13.391 |
| Pre e | 410 | 319.8 | 0.32 | 0.5 | 0.5 | | 21.3 | 14.5 | 1.15E-07 | 6.17E-08 | 14.309 |
| Pre f | 428 | 319.8 | 0.32 | 50 | 50 | | 21.4 | 14.5 | 3.88E-09 | 6.31E-10 | 14.426 |
| Pre g | 432 | 319.8 | 0.32 | 2 | 2 | | 21.7 | 14.8 | 4.94E-08 | 1.68E-08 | 14.724 |
| Pre h | 452 | 319.5 | 0.32 | 50 | 50 | | 21.9 | 14.9 | 4.39E-09 | 6.90E-10 | 14.865 |
| Pre i | 457 | 319.9 | 0.32 | 2 | 2 | | 22.7 | 15.4 | 6.21E-08 | 2.00E-08 | 15.561 |
| 1 | 477 | 319.9 | 0.32 | 108 | 12 | | 22.3 | 15.2 | 2.79E-09 | 3.47E-10 | 15.670 |
| 2 | 575 | 319.8 | 0.32 | 650 | 12 | | 22.4 | 15.2 | 5.64E-10 | 5.84E-11 | 15.728 |
| 3 | 597 | 319.8 | 0.49 | 600 | 12 | | 22.6 | 11.5 | 2.90E-10 | 3.19E-11 | 15.880 |
| 4 | 741 | 319.9 | 0.49 | 1000 | 12 | | 22.6 | 11.5 | 1.62E-10 | 1.93E-11 | 15.935 |
| 5 | 791 | 320.0 | 0.49 | 1000 | 12 | | 22.7 | 11.6 | 2.02E-10 | 1.96E-11 | 15.985 |
| 6 | 859 | 319.9 | 0.49 | 1000 | 12 | | 22.7 | 11.6 | 2.30E-10 | 1.96E-11 | 16.003 |
| 7 | 1,220 | 320.3 | 0.49 | 12 | 12 | 7,200 | 22.8 | 11.7 | 5.85E-11 | - | 16.003 |
| 8 | 1,229 | 319.7 | 0.49 | 12 | 12 | | 22.9 | 11.7 | 3.91E-09 | 1.71E-09 | 16.171 |
| 9 | 1,244 | 319.8 | 0.49 | 300 | 12 | | 23.0 | 11.7 | 8.62E-10 | 6.86E-11 | 16.198 |
| 10 | 1,252 | 320.0 | 0.49 | 12 | 12 | | 23.0 | 11.7 | 2.40E-09 | 1.73E-09 | 16.266 |
| 11 | 1,268 | 319.9 | 0.49 | 300 | 12 | | 23.0 | 11.7 | 6.48E-10 | 6.96E-11 | 16.308 |
| 12 | 1,277 | 319.9 | 0.32 | 2 | 2 | | 23.8 | 16.2 | 2.17E-08 | 2.46E-08 | 16.983 |
| 13 | 1,292 | 319.9 | 0.32 | 100 | 100 | | 24.4 | 16.6 | 1.92E-09 | 5.45E-10 | 17.058 |
| 14 | 1,300 | 319.9 | 0.32 | 2 | 2 | | 25.5 | 17.3 | 3.22E-08 | 3.25E-08 | 17.911 |
| 15 | 1,318 | 319.8 | 0.32 | 100 | 100 | | 25.7 | 17.5 | 3.09E-09 | 6.73E-10 | 18.082 |
| 16 | 1,324 | 319.8 | 0.49 | 300 | 12 | | 25.7 | 13.1 | 8.41E-10 | 1.09E-10 | 18.099 |
| 17 | 1,364 | 319.8 | 0.49 | 600 | 12 | | 25.9 | 13.2 | 7.00E-10 | 5.58E-11 | 18.216 |
| 18 | 1,413 | 319.6 | 0.49 | 1000 | 12 | | 26.0 | 13.3 | 1.91E-10 | 3.44E-11 | 18.325 |
| 19 | 1,485 | 319.5 | 0.49 | 1000 | 12 | 7,200 | 26.0 | 13.2 | 1.32E-10 | 4.14E-12 | 18.254 |
| 20 | 2,564 | 320.0 | 0.49 | 12 | 12 | 7,200 | 26.7 | 13.6 | 1.23E-10 | - | 18.743 |
| 21 | 2,950 | 319.6 | 0.49 | 1000 | 12 | | 27.5 | 14.0 | 2.54E-10 | 4.33E-11 | 19.210 |
| 22 | 3,406 | 319.9 | 1.00 | 12 | 12 | 7,200 | 27.9 | 14.2 | 6.80E-11 | - | 19.324 |
| 23 | 3,411 | 319.6 | 0.49 | 50 | 12 | | 27.9 | 14.2 | 3.24E-09 | 9.14E-10 | 19.387 |
| 24 | 3,432 | 319.5 | 0.49 | 300 | 12 | | 28.0 | 14.3 | 7.16E-10 | 1.54E-10 | 19.497 |
| 25 | 3,476 | 319.0 | 0.49 | 1000 | 12 | | 27.9 | 14.2 | 2.57E-10 | 4.55E-11 | 19.409 |
| 26 | 4,725 | 319.6 | 0.49 | 12 | 12 | 7,200 | 28.1 | 14.0 | 3.51E-11 | - | 19.460 |
| 27 | 5,060 | 319.8 | 0.50 | 1000 | 12 | | 28.4 | 14.2 | 1.66E-10 | 4.71E-11 | 19.923 |
| 28 | 6,603 | 319.9 | 0.50 | 12 | 12 | 7,200 | 28.8 | 14.4 | 2.58E-11 | - | 20.088 |
| 29 | 6,905 | 321.1 | 0.50 | 1000 | 12 | | 29.7 | 14.9 | 1.43E-10 | 5.73E-11 | 20.680 |
| 30 | 8,213 | 321.7 | 0.50 | 12 | 12 | 7200 | 30.0 | 15.3 | 5.27E-11 | - | 20.846 |
| 31 | 8,457 | 321.4 | 0.50 | 0 | 0 | | 30.0 | 0.0 | negligible | - | 20.846 |
| 32 | 9,516 | 320.0 | 0.50 | 12 | 12 | 7200 | 30.4 | 15.2 | 1.74E-11 | - | 20.904 |
| 33 | 9,522 | 319.5 | 0.3 | 1 | 1 | | 32.0 | 22.4 | 1.35E-08 | 1.75E-07 | 21.597 |
| 34 | 9,539 | 319.5 | 0.32 | 50 | 50 | | 32.0 | 21.8 | 1.65E-09 | 3.28E-09 | 21.629 |
| 35 | 9,546 | 319.5 | 0.32 | 0.5 | 0.5 | | 33.2 | 22.6 | 2.51E-08 | 3.81E-07 | 22.302 |
| 36 | 9,561 | 319.5 | 0.32 | 50 | 50 | | 33.3 | 22.6 | 2.58E-09 | 3.84E-09 | 22.338 |
| 37 | 9,571 | 319.5 | 0.32 | 0.5 | 0.5 | | 35.3 | 24.0 | 3.36E-08 | 4.88E-07 | 23.379 |
| 38 | 9,585 | 319.5 | 0.32 | 50 | 50 | | 35.4 | 24.1 | 3.55E-09 | 4.98E-09 | 23.471 |
| 39 | 9,594 | 319.5 | 0.32 | 0.5 | 0.5 | | 38.6 | 26.3 | 5.63E-08 | 7.10E-07 | 24.958 |
| 40 | 9,626 | 319.5 | 0.32 | 50 | 50 | | 39.2 | 26.7 | 2.72E-09 | 7.56E-09 | 25.214 |
| 41 | 9,632 | 319.5 | 0.32 | 0.5 | 0.5 | | 45.1 | 30.7 | 1.12E-07 | 1.34E-06 | 27.414 |
| 42 | 9,648 | 319.5 | 0.32 | 50 | 50 | | 45.7 | 31.0 | 3.52E-09 | 1.41E-08 | 27.604 |

[a] Simulated PWR water with 2 ppm Li, 1000 ppm B, and 2 ppm. DO<10 ppb. Conductivity was 21±3 μS/cm, and pH 6.4.

[b] Data was checked against fractography.

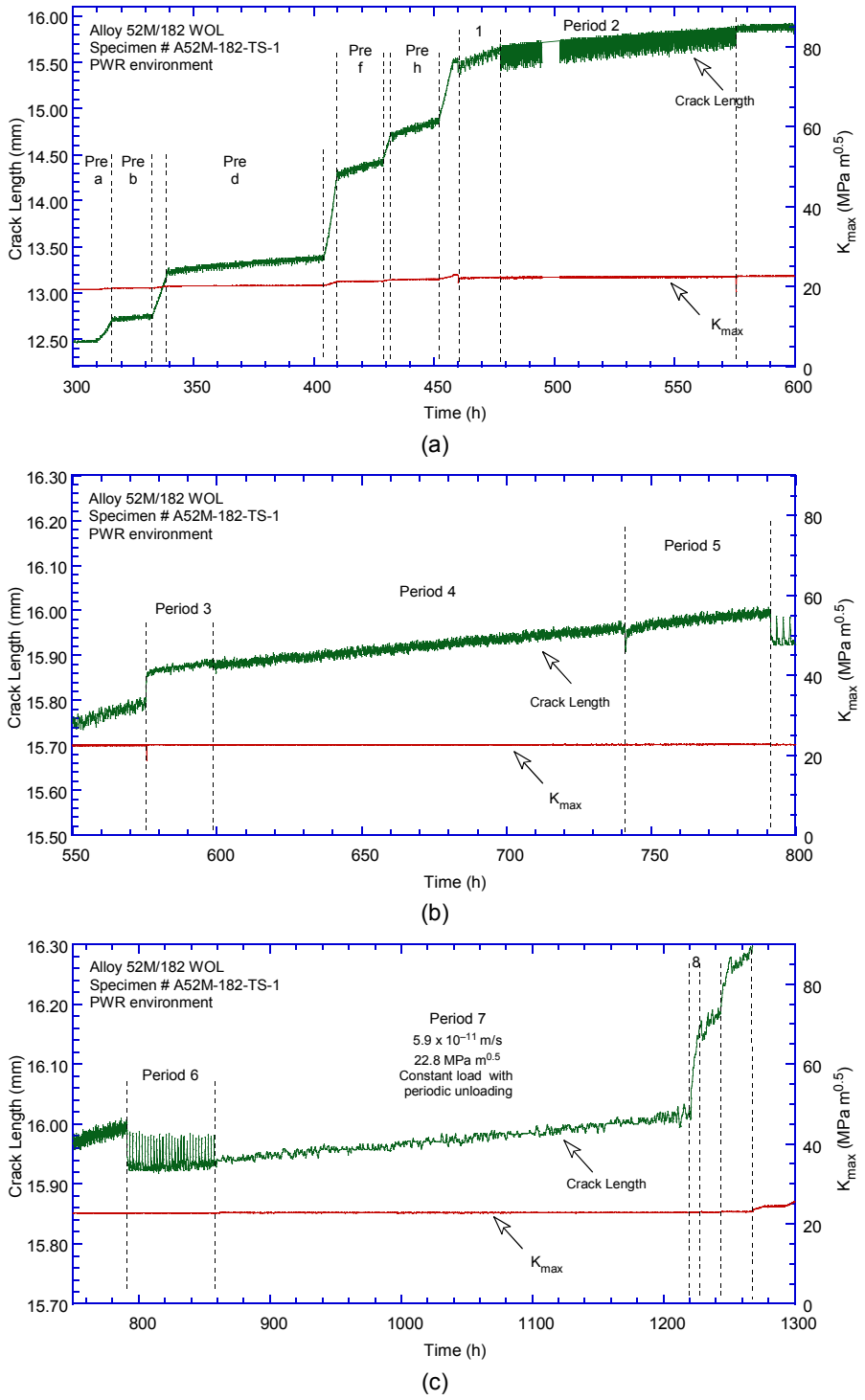


**Figure 3-18 Crack–length–vs.–time for WOL specimen A52M-182-TS-1 in simulated PWR environment during test periods (a) precracking-2, (b) 3-5, (c) 6-11, (d) 12-19, (e) 20-21, (f) 22-25, (g) 26-27, (h) 28, (i) 30, (j) 31-32, (k) 33, and (l) 33-42.**

**Figure 3-18 (Cont.)**

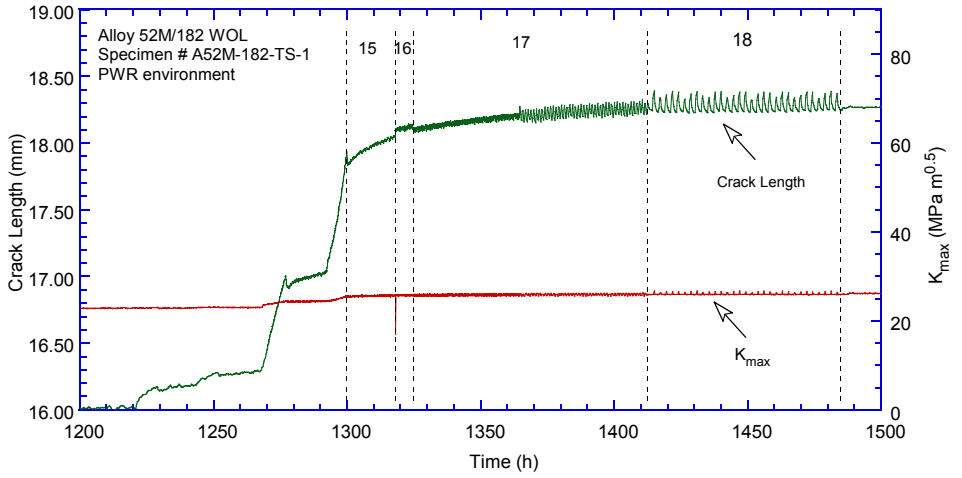


(d)

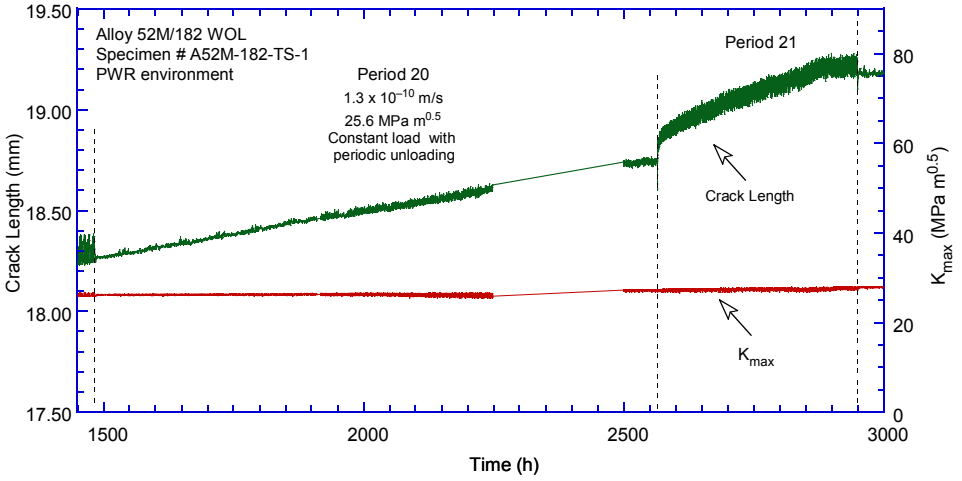


(e)

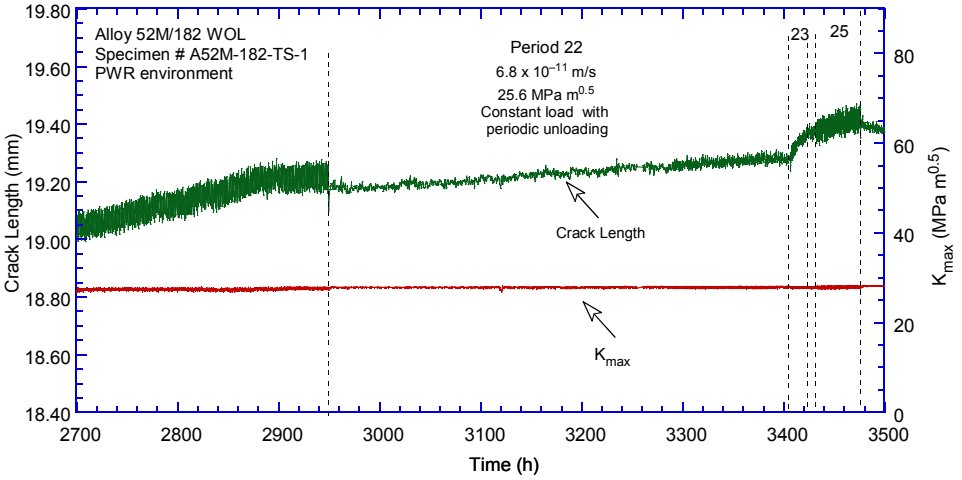


(f)

**Figure 3-18 (Cont.)**

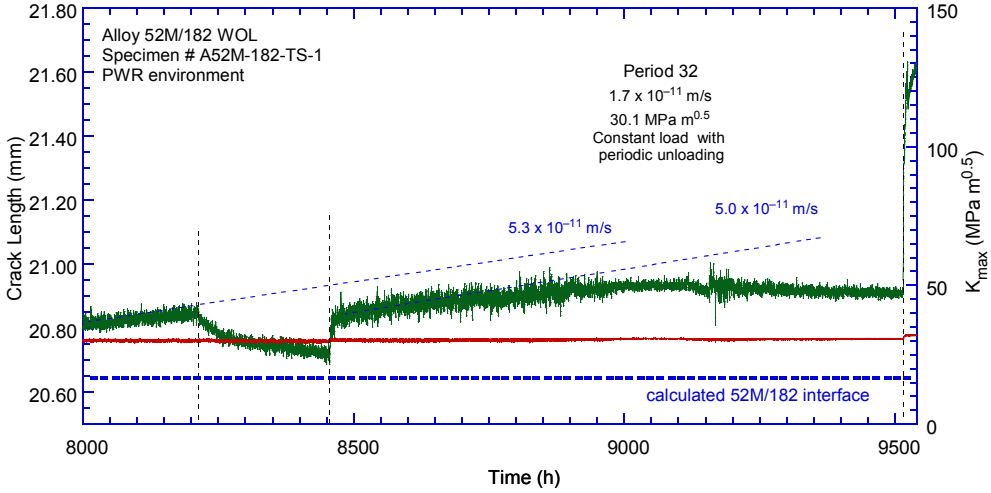


(j)

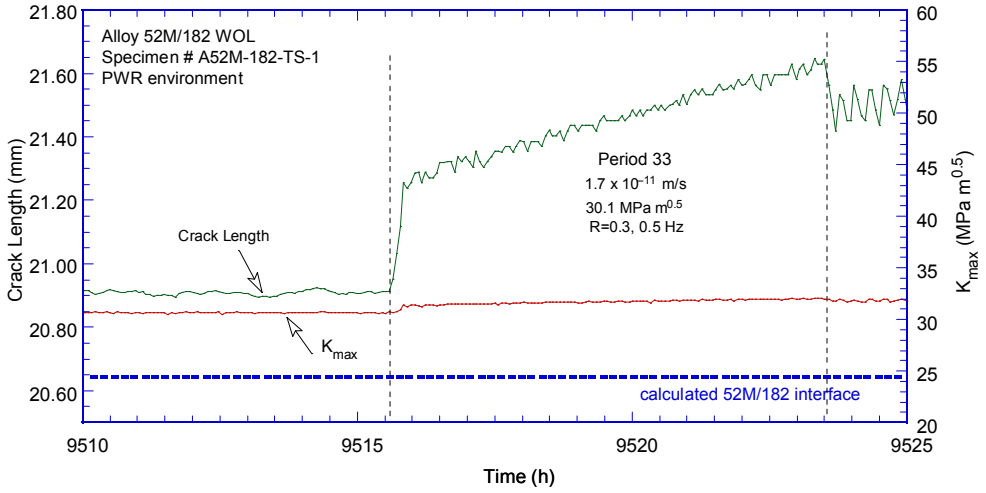


(k)

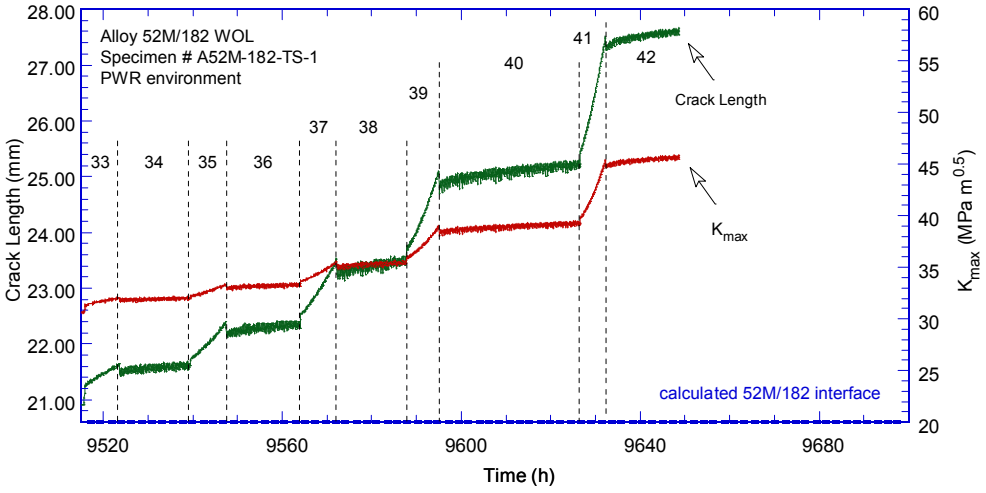


(l)

Following approximately 6.5 mm of crack advance past the interface in fatigue, the test was stopped and the specimen was fractured open, as shown in Fig. 3-19. As was seen in the previous experiment, the fracture surface at the interface was complex, with substantial cracking along the interface along with crack propagation in Alloy 52M along a different plane than the original. Hence, the resulting large ligament observed in the pictures.

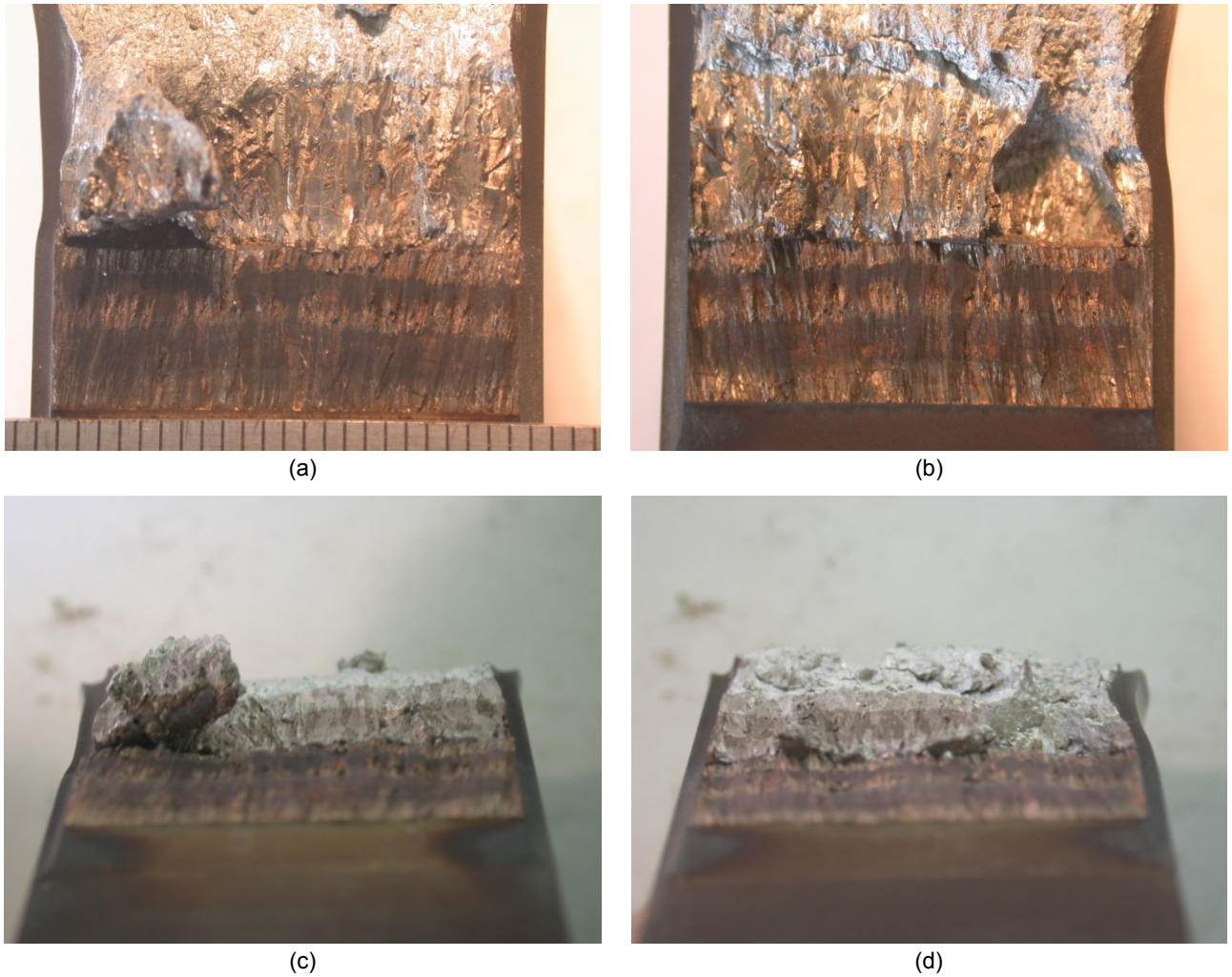


**Figure 3-19 (a, b) The two halves of fractured specimen A52M-182-TS-1. Crack advance is from bottom to top. (c, d) Same fracture surfaces photographed at an angle to show the cracking pattern at the interface.**

The fracture surface of specimen A52M-182-TS-1 was examined by both optical microscopy and SEM. The optical image is shown in Fig. 3-20, and the WOL interface is indicated by black arrows. The various features are in very good agreement with the DC potential measurements: the first IG band (IG-1) starts approximately 4 mm from the interface, the second IG band (IG-2) starts approximately 1.5 mm from the interface, and most importantly, the interaction with the interface occurs after approximately 8 mm of growth as was measured by the DC potential. As such, no correction of the DC potential measurements was needed for this specimen.

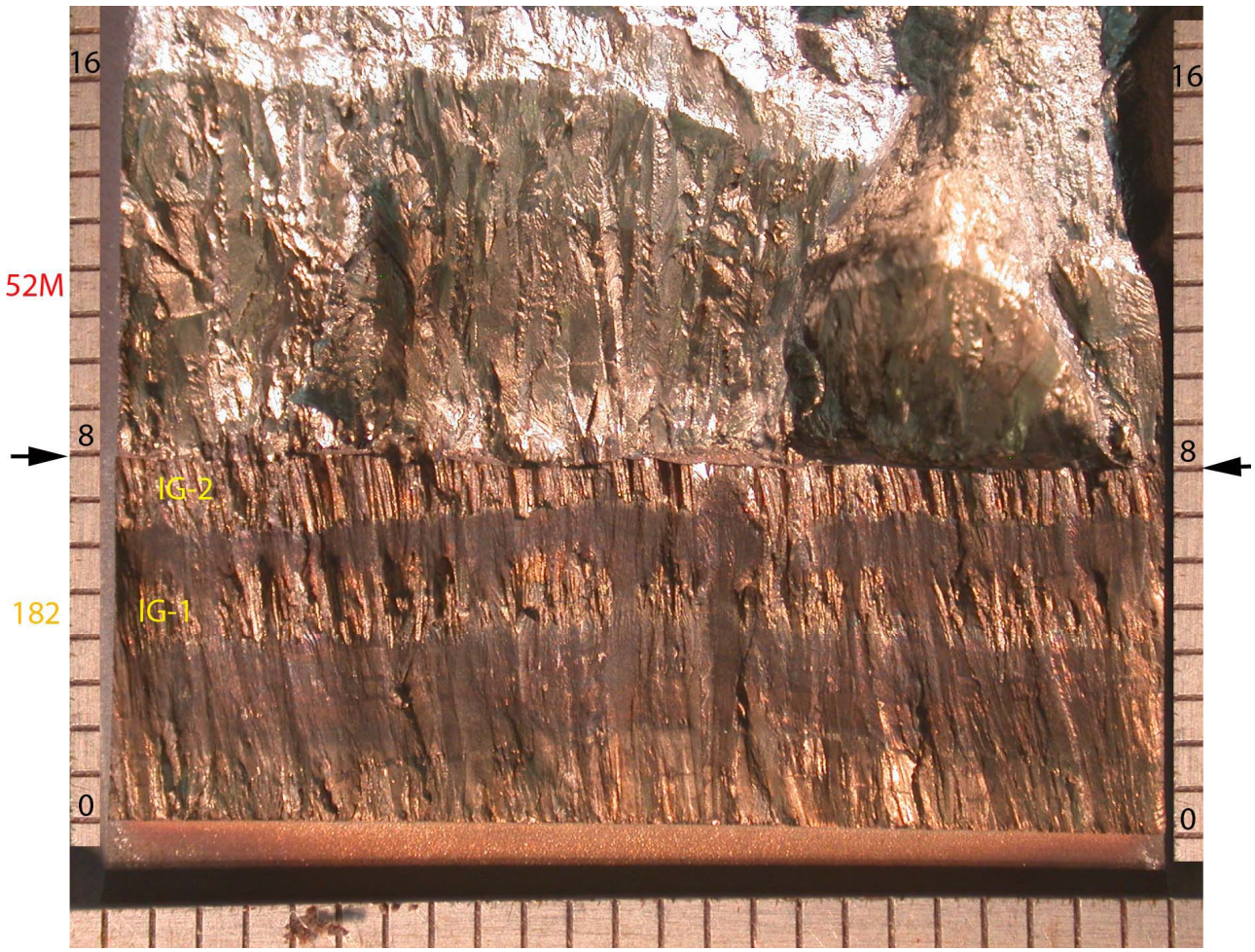


**Figure 3-20** **Fracture surface of specimen A52M-182-TS-1. The interface is indicated by black arrows. Crack advance is from bottom to top. The units of the bottom and side rulers are mm.**

The fracture surface of specimen A52M-182-TS-1 was also examined by SEM with the focus on the interaction of the crack with the WOL interface. Figures 3-21 and 3-22 show detail at select locations on the first half of the fracture surface, and Fig. 3-23 shows additional detail at two locations on the second half. Both Figs. 3-21a and 3-23a shows a straight, fully IG-engaged, SCC front ahead of the interface, just as in the prior specimen. Additional micrographs of features of interest were taken at higher magnifications. As such, Figs. 3-21b, c were taken at locations 1 and 2 in Fig. 3-21a and show cases where the IG crack propagated from Alloy 182 into Alloy 52M along the original direction. Such direct crack propagation through the interface was also observed on the previous specimen. Figures 3-22b, c (locations 3, 4 in Fig. 3-21a) show cases where the crack first propagated along the interface, then into Alloy 52M. Again, propagation along interface and branching into Alloy 52M was also observed in the previous specimen. Figures 3-22b, c (locations 1, 2 in Fig. 3-21a) focus on the region along the large ligament formed past the interface. Figure 3-23b shows IG fracture mode on the side of this ligament. It is likely that such preferential propagation lead to the formation of this ligament in the first place. Fig. 3-23c focuses on the fracture mode at the interface. Interdendritic features are visible suggesting that this was a favorable direction despite being normal to the direction of the dendrites.

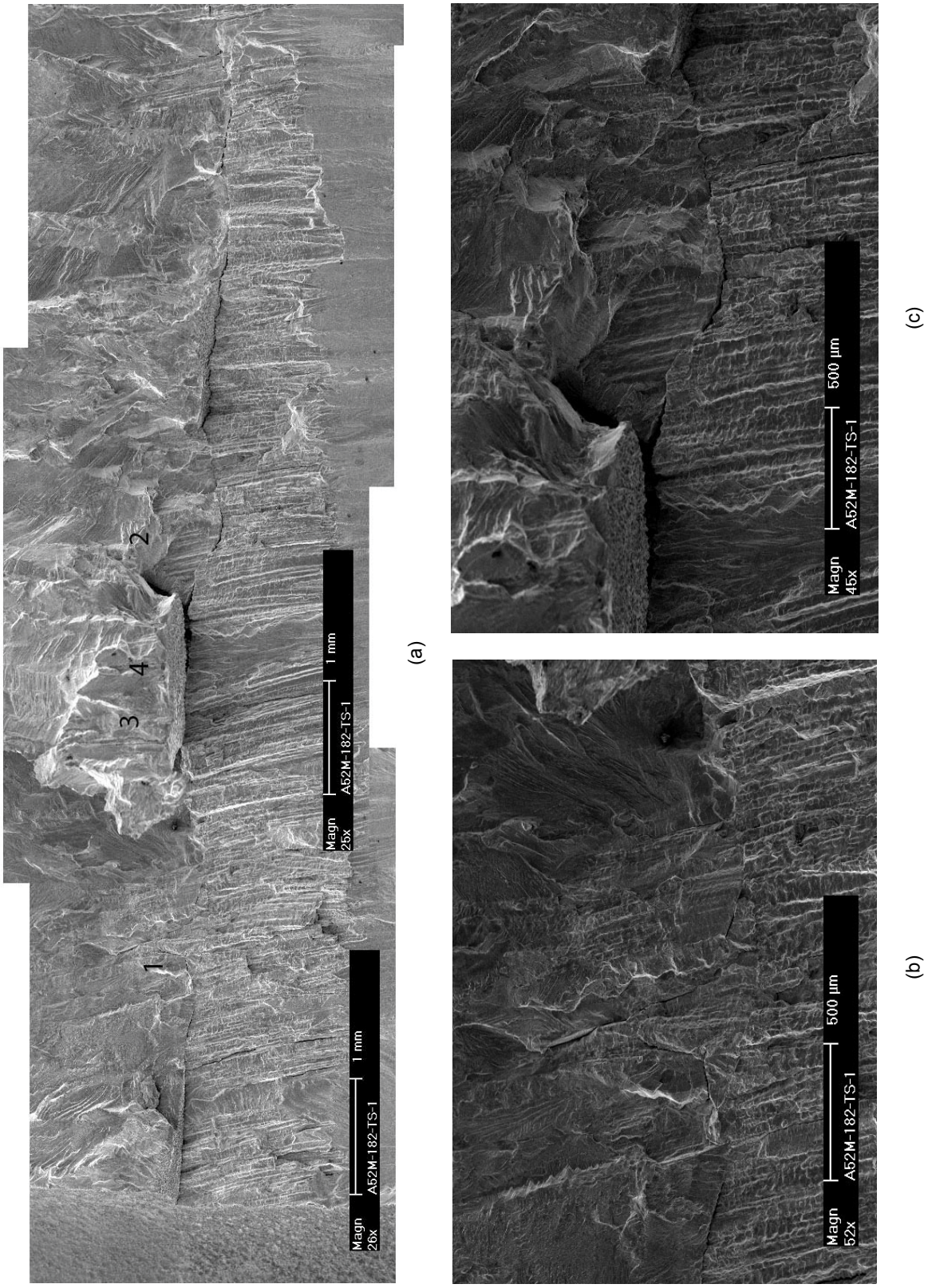


**Figure 3-21 Specimen A52M-182-TS-1: (a) first half of fracture surface, (b) detail at location 1, and (c) detail at location 2. Crack advance is from bottom to top.**

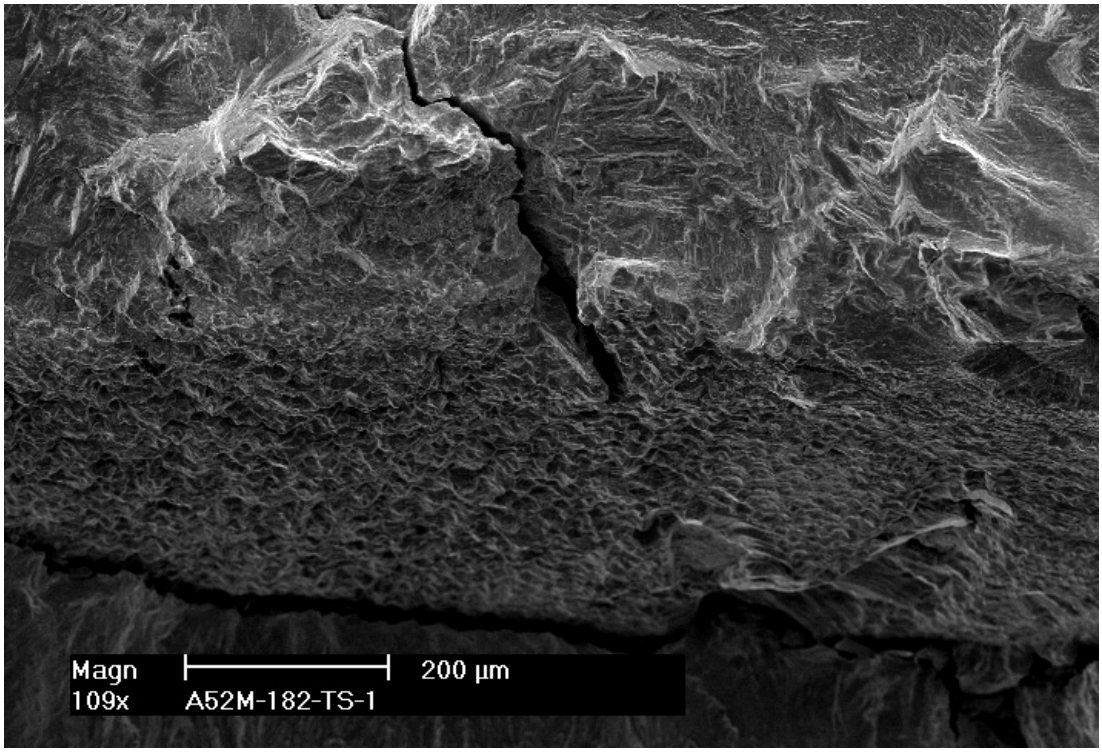


(a)

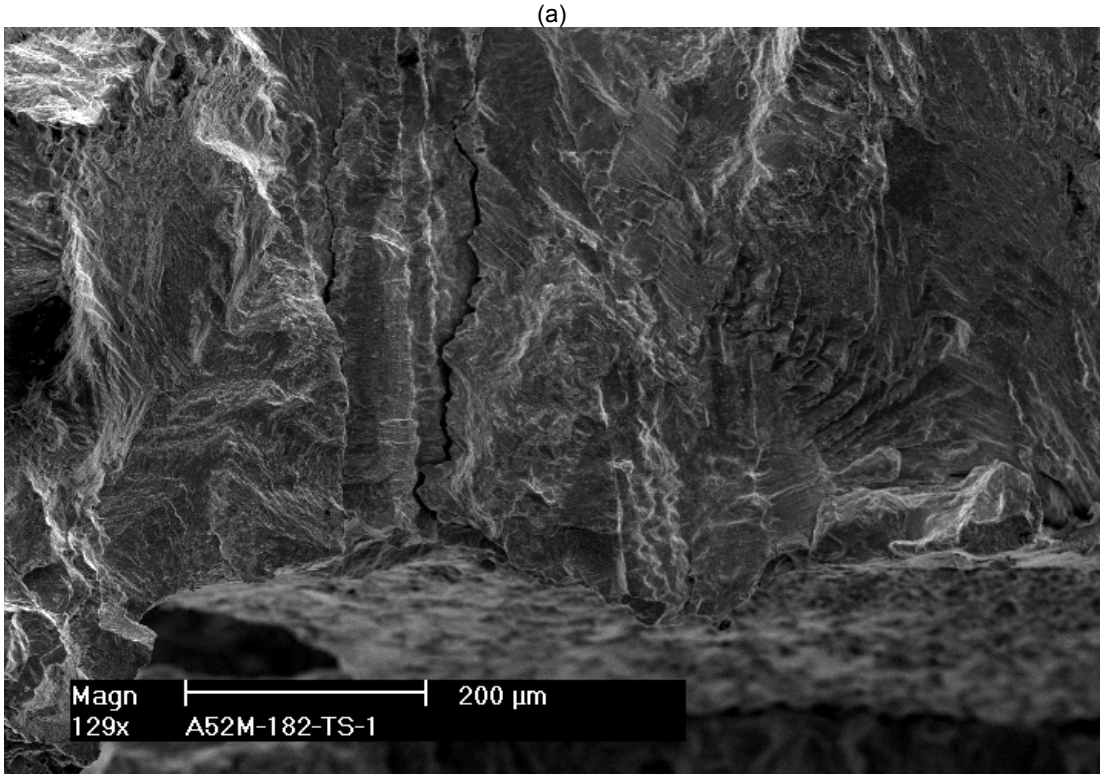


(b)

**Figure 3-22 Specimen A52M-182-TS-1: (a) detail at location 3, and (b) detail at location 4 in Fig. 3-21a. Crack advance is from bottom to top.**

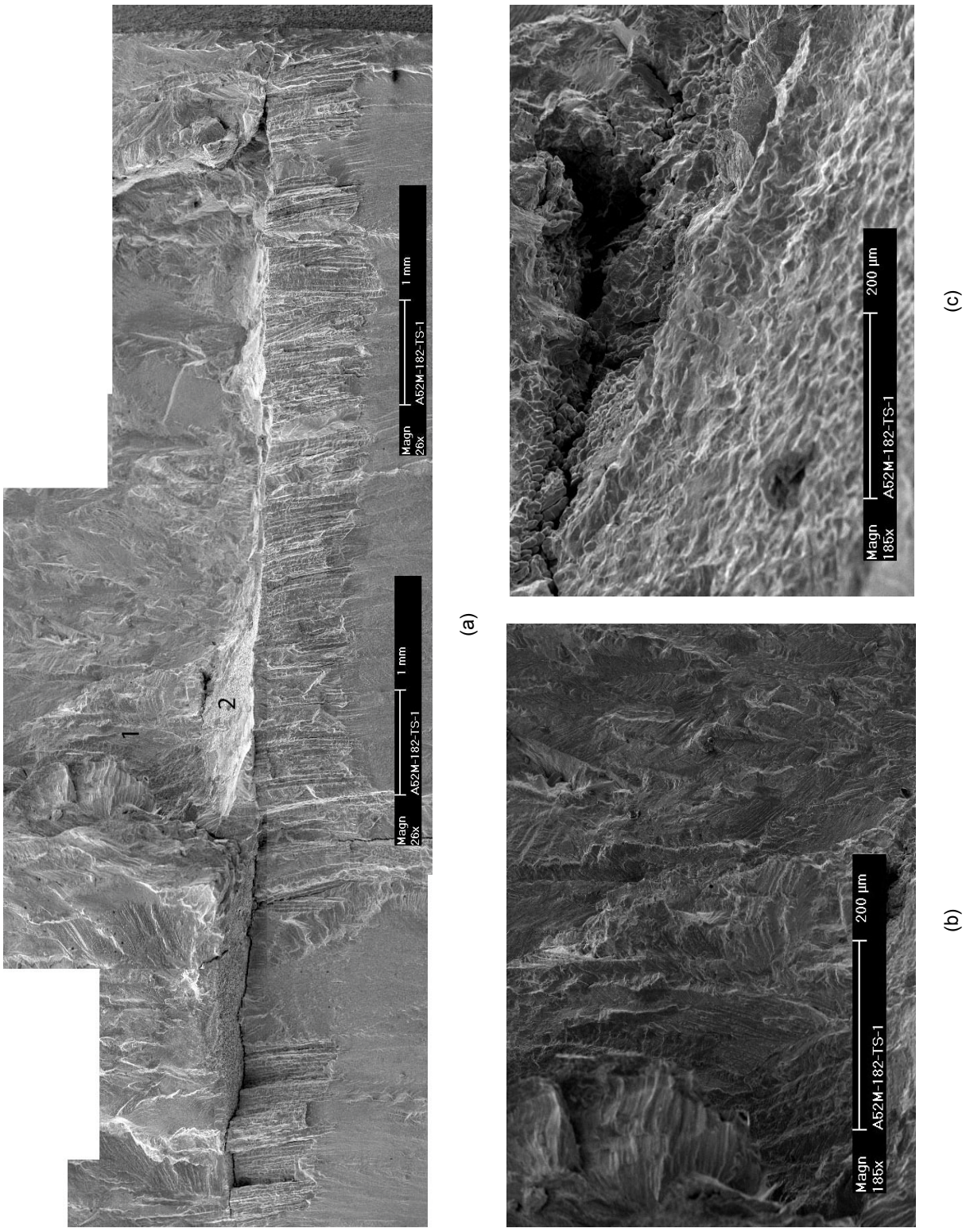


**Figure 3-23 Specimen A52M-182-TS-1: (a) second half of fracture surface, (b) detail at location 1, and (c) detail at location 2. Crack advance is from bottom to top.**

Figure 3-24 summarizes the cyclic CGR data obtained on the WOL specimen A52M-182-TS-1. The corrosion fatigue curve for Alloy 182 is included for comparison. Also included in Fig. 3-24a are data obtained on the 1/2T CT specimen A52M-182-TS-3, and data obtained previously on the same Alloy 182 weld without the WOL. Initially, the cyclic rates from the current specimen appeared to be smaller (Fig. 3-24a) – perhaps due to the fact that the crack is deeper in the weld than it was in the previous tests. However, after approximately 1 mm of advance, the data begins to match the behavior observed previously for this alloy. Figure 3-24b shows the data obtained at the end of the test in Alloy 52M. The fatigue response appears to be approximately one order of magnitude lower than expected. This effect was observed previously in specimen A52M-182-TS-3 (Fig. 3-15d), and was interpreted to have been caused by a decreased stress intensity factor at the crack tip due to the extensive cracking along the interface between the two welds. The fracture shown in Fig. 3-19 exhibits a similar cracking pattern at the interface to that of specimen A52M-182-TS-3 (Fig. 3-18), thus, this similarity supports the previous interpretation.

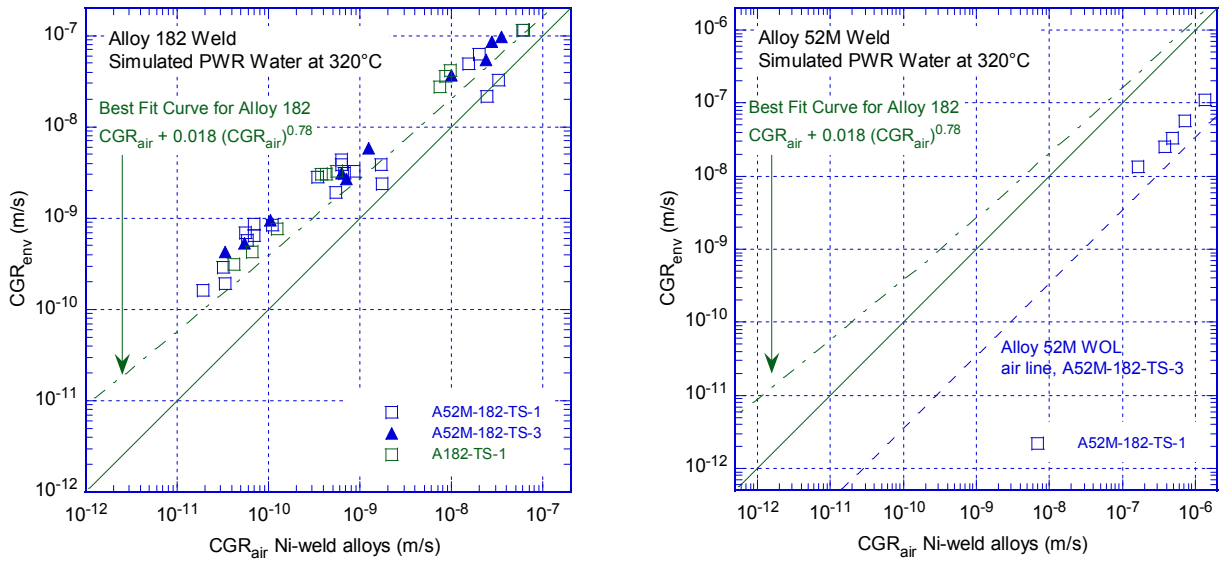


**Figure 3-24 Cyclic CGR data for Alloy 52M WOL specimen A52M-182-TS-1 in simulated PWR environment during (a) precracking and transitioning in Alloy 182, and (b) at the end of the test in Alloy 52M. The dotted blue line shows the "air line" for Alloy 52M obtained in the prior test.**

Figure 3-25 compares the SCC CGR vs. distance data obtained on the two Alloy 52M-182 WOL specimens tested in the TS orientation. The SCC CGR behavior observed in those two specimens seems very similar. In both tests, the SCC CGR data obtained in Alloy 182 with the Alloy 52 WOL at distances larger than 1 mm from the WOL, are similar to the rate obtained in the same weld without the WOL. However, the SCC CGRs decreased by approximately one order of magnitude ahead of the interface. The two higher data points obtained on specimen A52M-182-TS-1 most likely reflect propagation along the interface and/or cracking in Alloy 52M on planes other than the original.

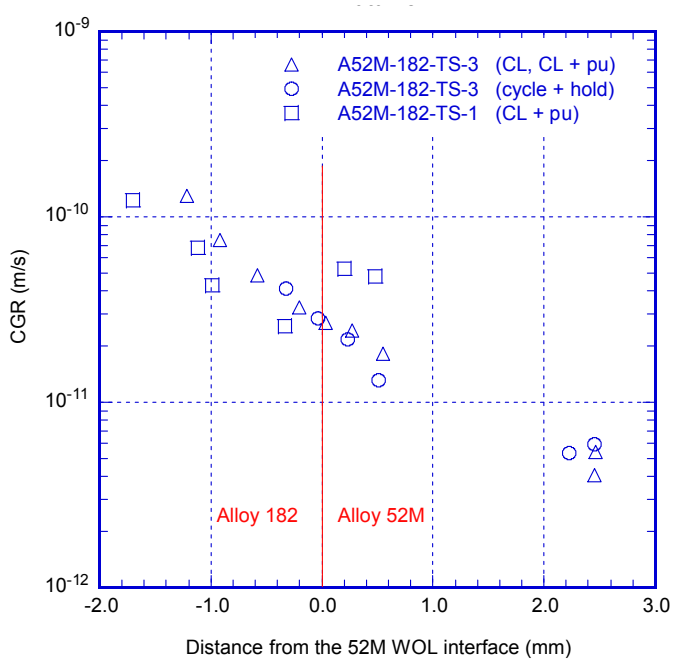


**Figure 3-25 SCC CGR vs. distance for the two Alloy 52M-182 WOL specimens tested in the TS orientation.**

In both TS-oriented specimens, severe cracking was observed along the interface between the two welds as well as in Alloy 52M near the interface. As described previously, estimates based on the fracture surface indicated that the SCC CGRs in the 1st layer of Alloy 52M WOL could be in the $10^{-10}$ m/s range. As such, SCC CGR testing was next undertaken along those planes with the objective of measuring those SCC CGRs directly. In order to accomplish this, the next two tests were conducted on specimens in the ST orientation (Fig. 3-26). In both ST specimens, the test plane was tilted approximately 15º with respect to the Alloy 52M-182 interface. In one case (specimen WOL-ST-1), the crack is growing from Alloy 182 towards the interface with Alloy 52M. In the second case (specimen WOL-ST-2), the crack is initiated in Alloy 52M and grows towards the interface with Alloy 182.

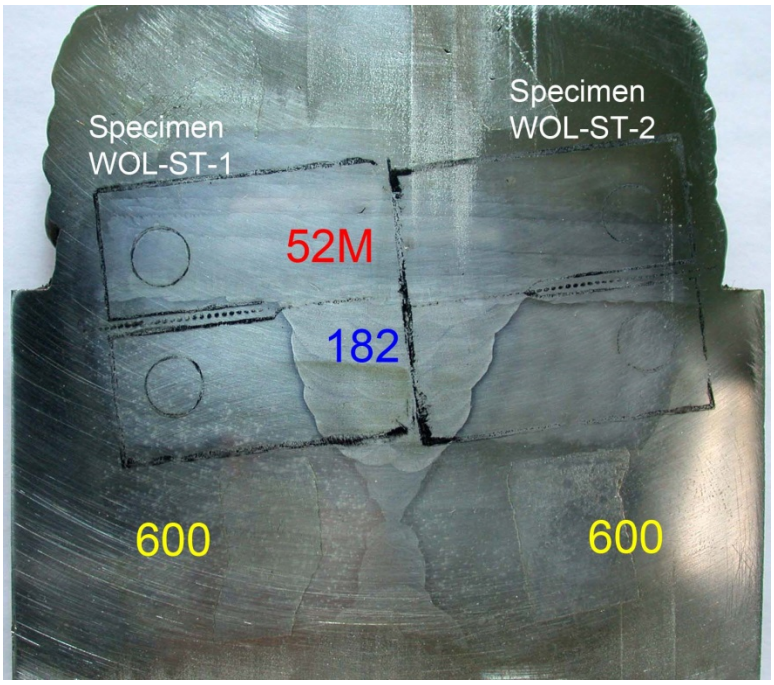


**Figure 3-26 Specimens for SCC CGR testing of Alloy 52M-182 WOL in the ST orientation.**

### 3.1.3 SCC Along the Alloy 52M-182 Interface, Specimen WOL-ST-1

The objective of this test was to measure the SCC CGR along the interface between the Alloy 52M WOL and Alloy 182. In this specimen (Fig. 3-27), the crack was initiated in Alloy 600, was expected to reach the Alloy 182 weld after approximately 1 mm, and then was advanced in Alloy 182 until it reached the Alloy 52M/182 interface. At that point, the specimen was set at constant load to measure the SCC CGR along the interface. The fatigue behaviors of Alloys 600 and 182 are well-known, and were used to manage the test. The testing conditions and CGR responses are given in Table 3-4. These data have been corrected based on fractography.

The specific configuration of specimen WOL-ST-1 (Fig. 3-27) also offered an opportunity to assess the cyclic and SCC behavior in Alloy 600 HAZ. As such, two sets of cyclic and SCC measurements were conducted in the Alloy 600 HAZ. The SCC CGR was first evaluated in test period 3 at approximately 0.7-0.65 mm from the Alloy 182 weld interface. Next, the crack was advanced for approximately 0.45 mm, and the SCC CGR was evaluated again in a region 0.2-0.1 mm from the interface in test period 8.

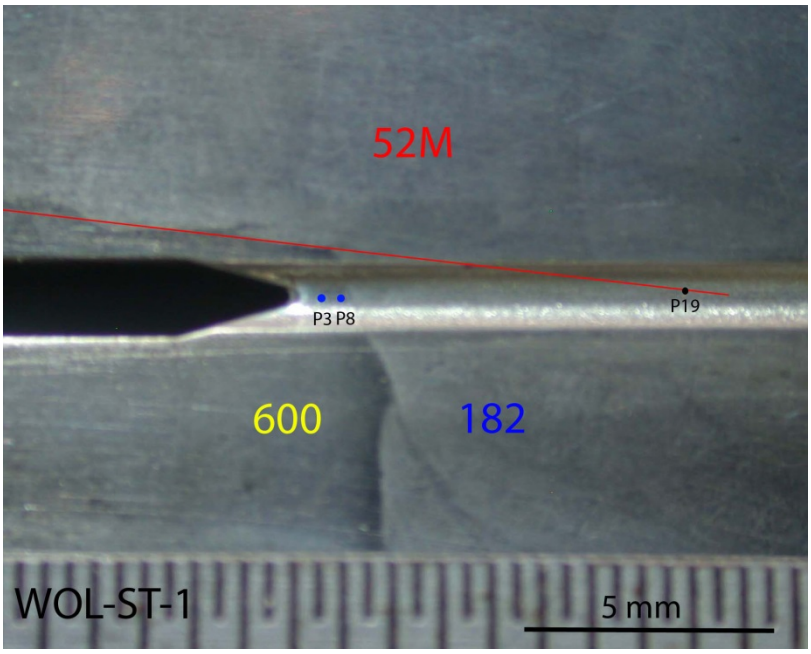


**Figure 3-27 Notch area in specimen WOL-ST-1. P3 and P8 represent the approximate locations where SCC CGR measurements were made in Alloy 600 HAZ, and P19 represents the approximate location where the crack was to intersect the interface with the Alloy 52M.**

Figure 3-28 summarizes the cyclic and SCC CGRs measured in the Alloy 600 HAZ region of specimen WOL-ST-1. Figure 3-28a shows the measured cyclic CGR data vs. the expected CGRs in air under the same loading conditions, and for comparison, the expected curves in air and environment for Alloy 600 (blue) and Ni-base weld (green) are included in the figure. As expected, the cyclic CGRs measured in this stage of the test are consistent with the known response of Alloy 600. The data obtained prior to the first test period at constant load (3, dark blue symbols) seem lower than the data obtained prior to the second test period at constant load (8, light blue symbols). The comparison shown in Fig. 3-28a seems to suggest that the cyclic CGRs of the HAZ increase as the crack approaches the Alloy 182 weld interface. Figure 3-28b shows the SCC CGRs measured for Alloy 600 HAZ in test periods 3 (dark blue symbol) and 8 (light blue symbol), and these also increase as the crack approaches the fusion line. As such, Fig. 3-28 suggests that both cyclic and SCC CGRs appear to increase as the crack advances towards the interface. However, Fig. 3-28b also includes a "reference" SCC CGR obtained from the same heat of Alloy 600 (NX 131031), tested in the same ST orientation separately. The similarity in responses between the "reference" and test period 3 (approximately 0.6 mm from the fusion line) suggests that in this case, the HAZ does not extend more than approximately 0.6 mm from the fusion line. In this test, the effect of the HAZ on the SCC CGR response was approximately a factor of two and was measured approximately 0.1 mm from the weld interface.

## Table 3-4 Crack growth data for specimen WOL-ST-1 in PWR water[a,b]

| Test Period | Test Time, h | Temp. °C | Load Ratio R | Rise Time, s | Down Time, s | Hold Time, s | $K_{max}$, MPa·m$^{1/2}$ | $\Delta K$, MPa·m$^{1/2}$ | $CGR_{env}$, m/s | Estimated $CGR_{air}$, m/s | Crack Length, mm |
|---|---|---|---|---|---|---|---|---|---|---|---|
| Pre a | 173 | 321.6 | 0.30 | 1 | 1 | | 24.8 | 17.4 | 7.15E-09 | 2.05E-08 | 12.015 |
| Pre b | 189 | 321.6 | 0.30 | 50 | 50 | | 24.9 | 17.4 | 4.98E-10 | 4.15E-10 | 12.028 |
| Pre c | 193 | 321.6 | 0.30 | 0.5 | 0.5 | | 25.3 | 17.7 | 1.77E-08 | 4.47E-08 | 12.163 |
| Pre d | 196 | 321.6 | 0.30 | 1 | 1 | | 25.5 | 17.8 | 1.28E-08 | 2.30E-08 | 12.218 |
| Pre e | 213 | 321.6 | 0.30 | 50 | 50 | | 25.6 | 17.9 | 7.77E-10 | 4.66E-10 | 12.242 |
| 1 | 237 | 321.7 | 0.50 | 50 | 12 | | 25.7 | 12.8 | 2.56E-10 | 2.04E-10 | 12.271 |
| 2 | 263 | 321.7 | 0.50 | 300 | 12 | | 25.6 | 12.8 | 9.24E-11 | 3.37E-11 | 12.275 |
| 3 | 406 | 321.7 | 1.00 | 0 | 0 | | 25.7 | 0.0 | 7.93E-11 | - | 12.312 |
| 4 | 408 | 321.9 | 0.20 | 0.5 | 0.5 | | 26.5 | 21.2 | 5.31E-08 | 7.45E-08 | 12.495 |
| 5 | 411 | 321.7 | 0.20 | 0.5 | 0.5 | | 24.6 | 19.7 | 5.72E-08 | 5.47E-08 | 12.704 |
| 6 | 429 | 321.7 | 0.50 | 50 | 12 | | 24.8 | 12.4 | 3.89E-10 | 1.78E-10 | 12.771 |
| 7 | 433 | 321.8 | 0.50 | 300 | 12 | | 24.8 | 12.4 | 2.04E-10 | 2.98E-11 | 12.779 |
| 8 | 668 | 321.6 | 1.00 | 0 | 0 | | 25.2 | 0.0 | 1.63E-10 | - | 12.885 |
| 9 | 671 | 321.6 | 0.20 | 0.5 | 0.5 | | 26.8 | 21.4 | 5.29E-08 | 7.76E-08 | 13.345 |
| 10 | 676 | 321.6 | 0.20 | 0.5 | 0.5 | | 23.0 | 18.4 | 2.01E-08 | 1.27E-07 | 13.451 |
| 11 | 692 | 321.6 | 0.20 | 50 | 50 | | 23.0 | 18.4 | 1.41E-09 | 1.28E-09 | 13.464 |
| 12 | 701 | 321.8 | 0.20 | 1 | 1 | | 23.2 | 18.6 | 3.40E-10 | 6.69E-08 | 13.528 |
| 13 | 717 | 321.6 | 0.20 | 50 | 50 | | 23.3 | 18.6 | 1.00E-09 | 1.34E-09 | 13.528 |
| 14 | 724 | 321.7 | 0.20 | 0.5 | 0.5 | | 23.8 | 19.1 | 1.64E-08 | 1.49E-07 | 13.719 |
| 15 | 741 | 321.6 | 0.20 | 50 | 50 | | 24.0 | 19.2 | 2.38E-09 | 1.53E-09 | 13.770 |
| 16 | 748 | 321.7 | 0.20 | 0.5 | 0.5 | | 25.0 | 20.0 | 7.73E-08 | 1.79E-07 | 14.013 |
| 17 | 764 | 321.7 | 0.50 | 50 | 12 | | 26.3 | 13.2 | 9.22E-10 | 6.98E-10 | 14.379 |
| 18 | 837 | 321.7 | 0.50 | 300 | 12 | | 26.7 | 13.4 | 2.68E-10 | 1.24E-10 | 14.446 |
| 19 | 6,472 | 321.3 | 1.00 | 0 | 0 | | 46.6 | 0.0 | 1.30E-10 | - | 17.265 |

[a] Simulated PWR water with 2 ppm Li, 1000 ppm B, and 2 ppm. DO<10 ppb. Conductivity was 21±3 □S/cm, and pH 6.4.
[b] Data was corrected using fractography.

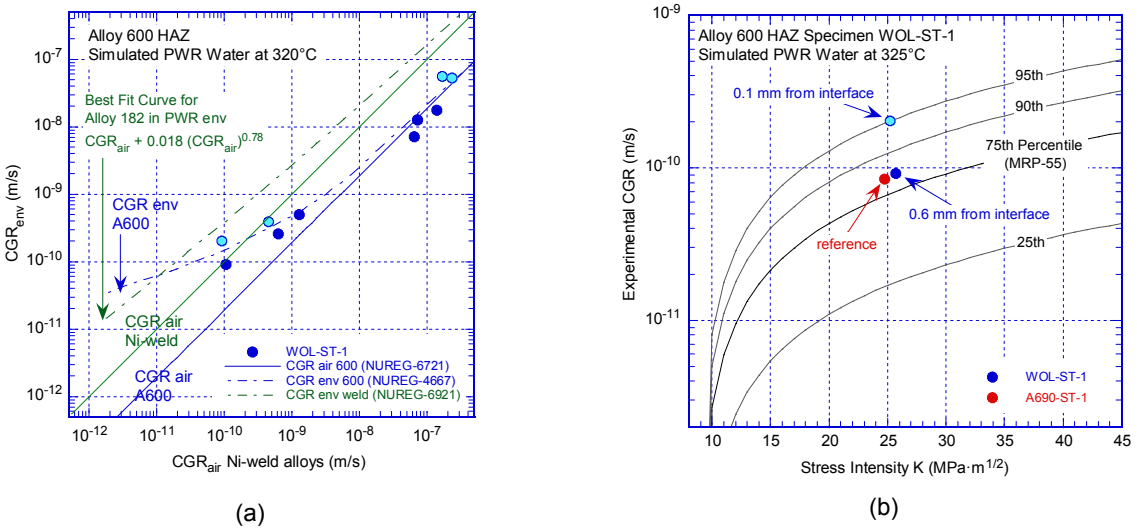


**Figure 3-28 (a) Cyclic CGR data for the Alloy 600 (HAZ) region of specimen WOL-ST-1 in simulated PWR environment; (b) SCC CGR data for the Alloy 600 (HAZ) region of specimen WOL-ST-1 and MRP-55 disposition curve for Alloy 600 [11]. The data obtained prior to the first test period at constant load (3) is shown with dark blue symbols, and the data obtained prior to the second test period at constant load (8) is shown with light blue symbols).**

Next, the crack was advanced in fatigue across the Alloy 600-182 interface into Alloy 182, and Fig. 3-29 shows the cyclic response in Alloy 182. For comparison, the expected curves in air and environment and for Alloy 600 (blue) and Ni-base weld (green) are included in the figure. The response seems lower than expected, and this was interpreted as an off-plane advance. As such, it was estimated that the crack turned towards the interface with Alloy 52M, hence, the specimen was set at constant load in what was estimated to be the vicinity of the Alloy 52M-182 interface in test period 19.

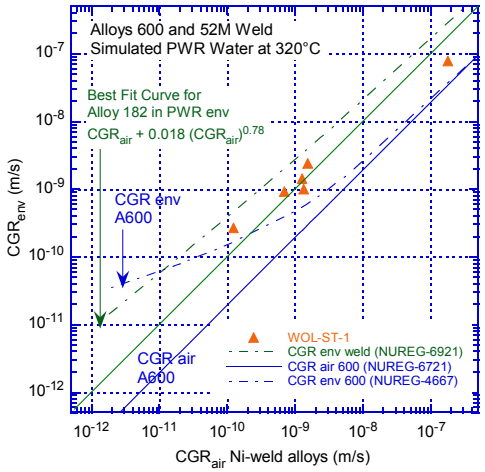


**Figure 3-29 Cyclic CGR data for the Alloy 182 region of specimen WOL-ST-1 in simulated PWR environment.**

Figure 3-30 shows the changes in crack length and $K_{max}$ with time for the entire test, and Fig. 3-30g shows the constant load SCC response of the Alloy 182-Alloy 52M interface. The initial SCC CGR of $2.8 \times 10^{-10}$ m/s (up to approximately 1240h) was unexpectedly high given the orientation of the crack front with respect to the dendrites, then began to diminish and continued at the diminished rate of approximately $1.3 \times 0^{-10}$ m/s for the remainder of the test. The calculated $K_{max}$ appears to increase from approximately 27 MPa $m^{1/2}$ to approximately 47 MPa $m^{1/2}$, primarily as a result of the factor 8.2 correction (Fig. 3-30g). However, the SCC CGR does not increase accordingly. As such, it appears that the unbroken ligaments responsible for the correction prevented the actual $K_{max}$ from reaching the calculated values. Also, small "jumps" have been observed and these are indicated by arrows in the figure. It was verified that these jumps are neither the result of some errant loading nor an electrical artifact. In fact, they are regions of fast growth ($10^{-8}$ m/s) that occur over short periods of time (15-20 min). The cause of the "jumps" is unknown, however, as it will be shown during the next test, they are a signature of SCC propagation along an interface between the two welds.

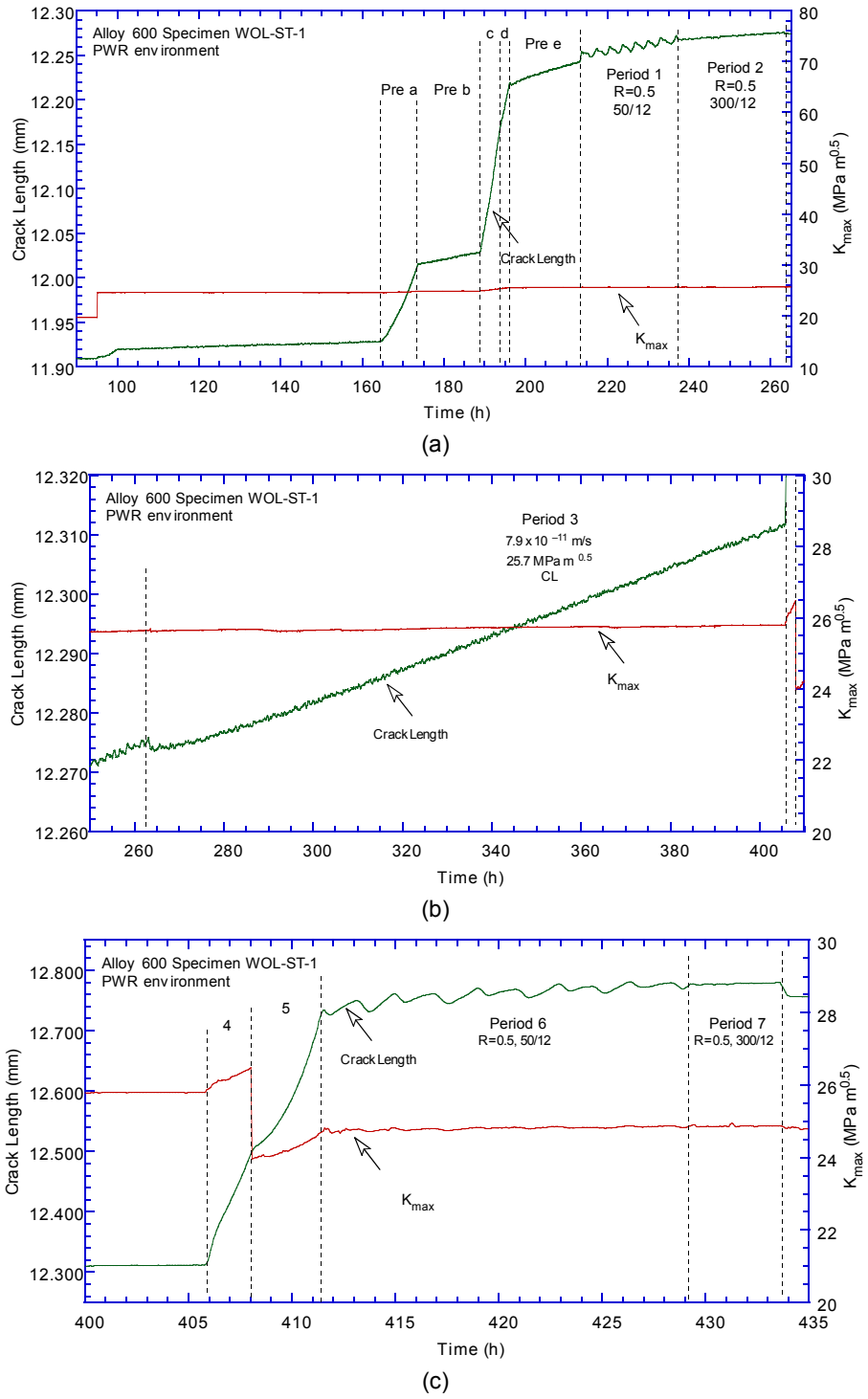


**Figure 3-30 Crack–length–vs.–time for specimen WOL-ST-1 in simulated PWR environment during (a) precracking-2, (b) 3, (c) 4-7, (d) 8, (e) 9, (f) 10-18, and (g) 19.**

**Figure 3-30 (Cont.)**

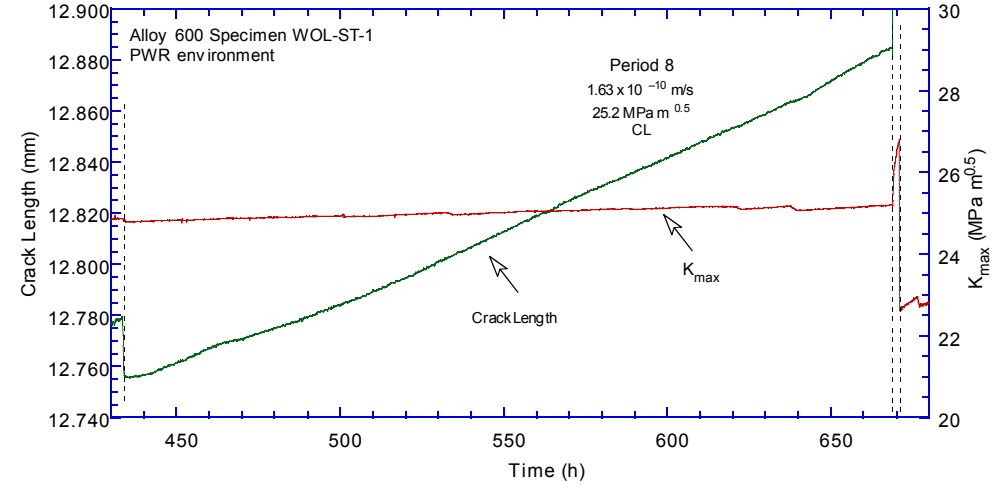


(d)

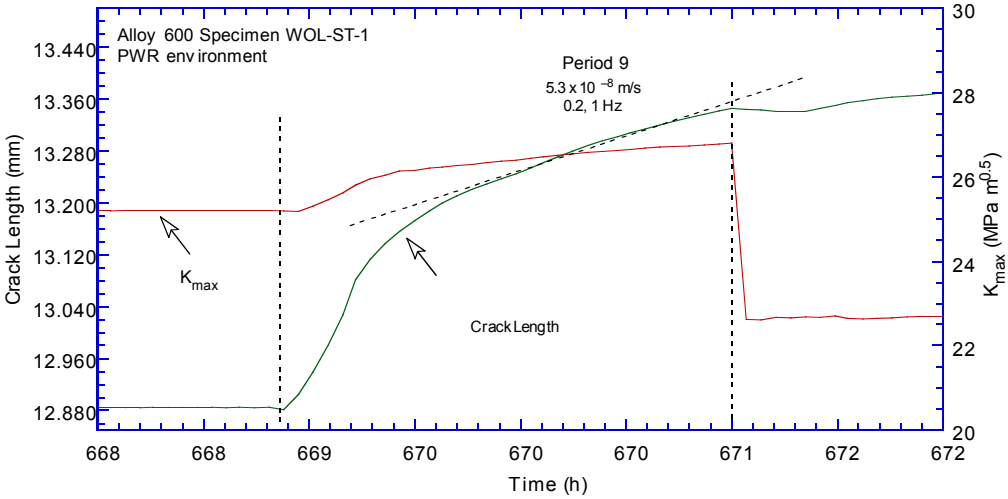


(e)

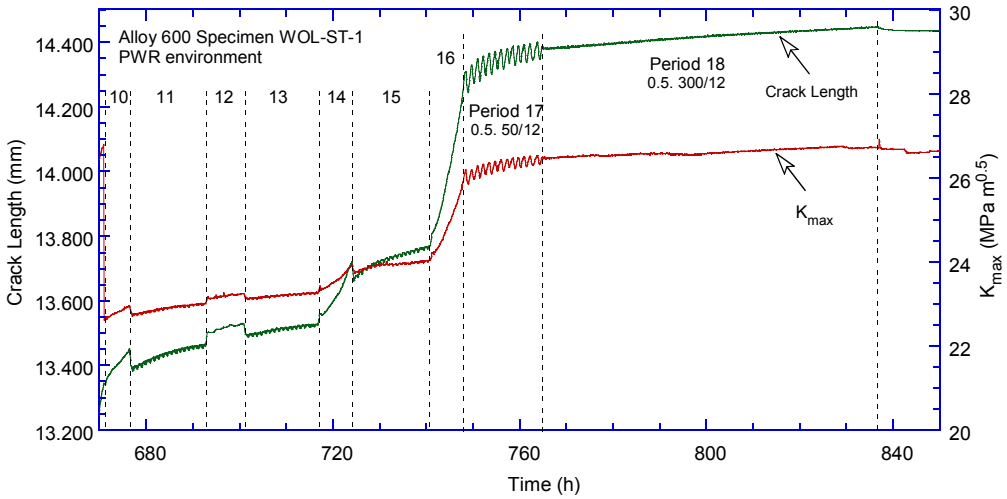


(f)

**Figure 3-30 (Cont.)**

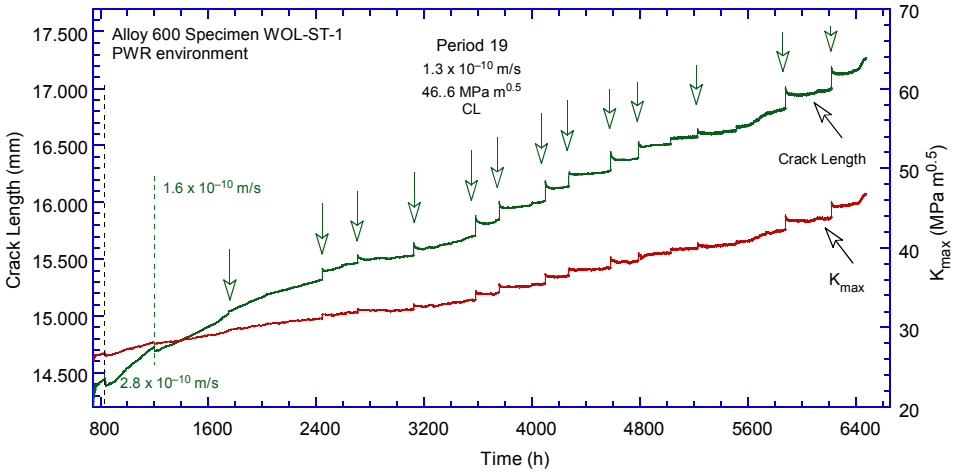


(g)

The post test-examination of this specimen involved both the side surfaces and that of the fracture surface.

In order to show the side cross sections, the side surfaces were ground to eliminate the side grooves, polished and electrochemically etched in a nital solution. The two side surfaces (Fig. 3-31) show that the test progressed largely as anticipated (Fig. 3-27), and confirm that cracking initiated in Alloy 600, transitioned into Alloy 182 weld, and then along the Alloy 182/52M interface.

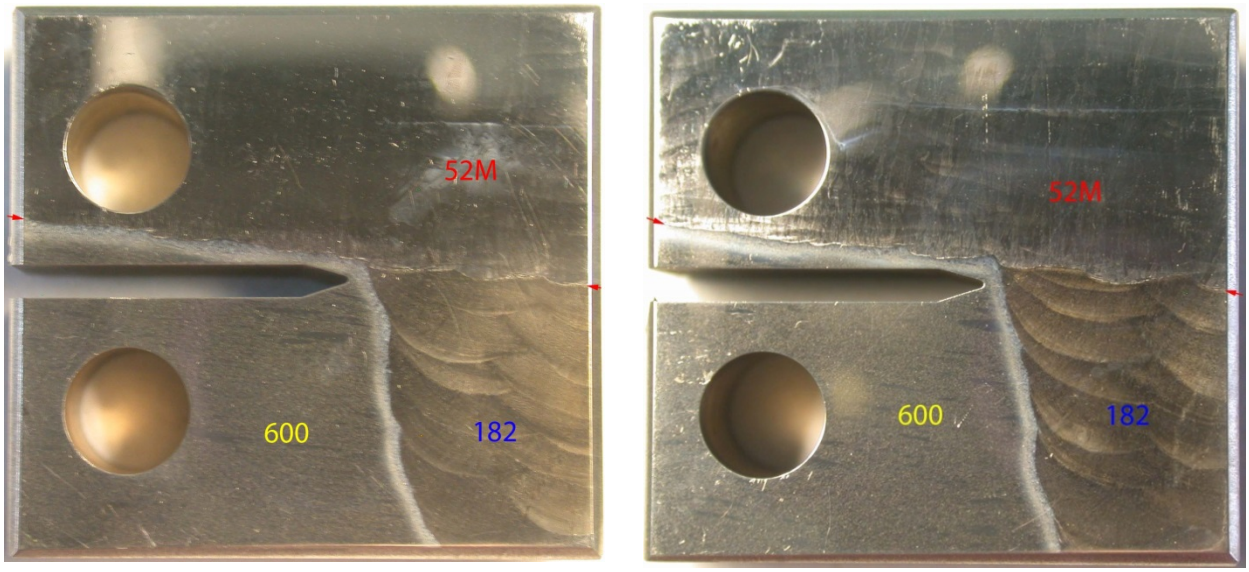


(a) (b)

**Figure 3-31 Post-test specimen WOL-ST-1 seen from both sides: (a) side 1, and (b) side 2. The red arrows indicate the Alloy 52M WOL interface. Crack advance is from left to right.**

The two side surfaces were further examined by optical microscopy, as shown in Fig. 3-32. The blue arrows indicate the Alloy 600/182 interface, and the red arrows indicate the Alloy 182-52M interface. Both cross sections show that after passing through the Alloy 600-182 interface, the crack turns towards the Alloy 52M WOL interface. This off-plane cracking caused the Alloy 182 cyclic data to appear less than expected, Fig. 3-29. The two cross sections show that the crack was driven in the vicinity of the Alloy 182-52M WOL as anticipated: on one surface (side 1), the crack under cyclic loading overshoots slightly the WOL interface, while on the second surface (side 2), the crack ends up slightly below the interface. Overall, the two images shown in Fig. 3-32 demonstrate that the specimen was set at constant load in the vicinity of the Alloy 182-52M WOL interface, and, hence, test period 19 represents cracking along the interface.

Figure 3-33 provides additional detail on the crack path. Figure 3-33a was taken at location 1A in Fig. 3-32a, the area where the crack overshot the WOL interface. The fracture appears TG, consistent with the fatigue loading. Figure 3-33b was taken at location 1B in Fig. 3-32a, at the end of the test. EDX analysis show that the preferred crack path was through a region with an average Cr concentration of 18%. Figures 3-33c and 3-33d were taken at locations 2A and 2B in Fig. 3-32b, and the EDX analysis shows that the preferred crack path was through a region with an average Cr concentration of 18-20%. In addition, Figs. 3-33b and 3-33c show that the dilution of Cr on the Alloy 52M WOL side within 20-30 μm from the interface is significant. Nevertheless, the EDX analysis shows that in this test, cracking occurred preferentially along the Alloy 182-52M WOL interface with Cr concentrations of 18-20%.

Following the examination of the side surfaces, the specimen was fatigued in air at room temperature to break some of the remaining ligaments, and was fractured after cooling in liquid nitrogen. The fracture surface was photographed (Fig. 3-34) and was examined in the SEM (Fig. 3-35).

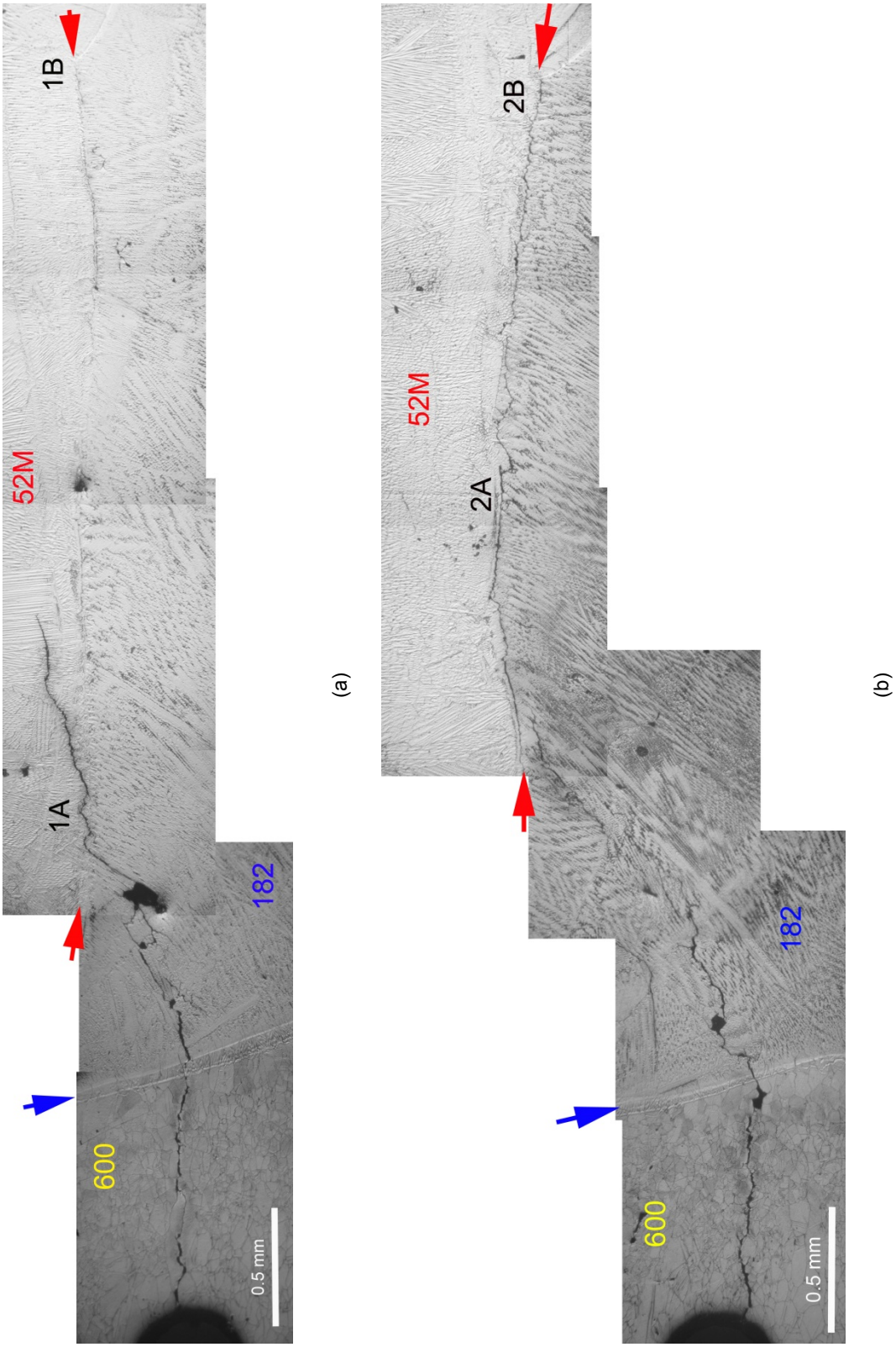


**Figure 3-32** **Cross sections of specimen WOL-ST-1: (a) side 1, and (b) side 2. Blue arrows indicate the Alloy 600/182 interface and the red arrows indicate the Alloy 182-52M interface. Crack advance is from left.**

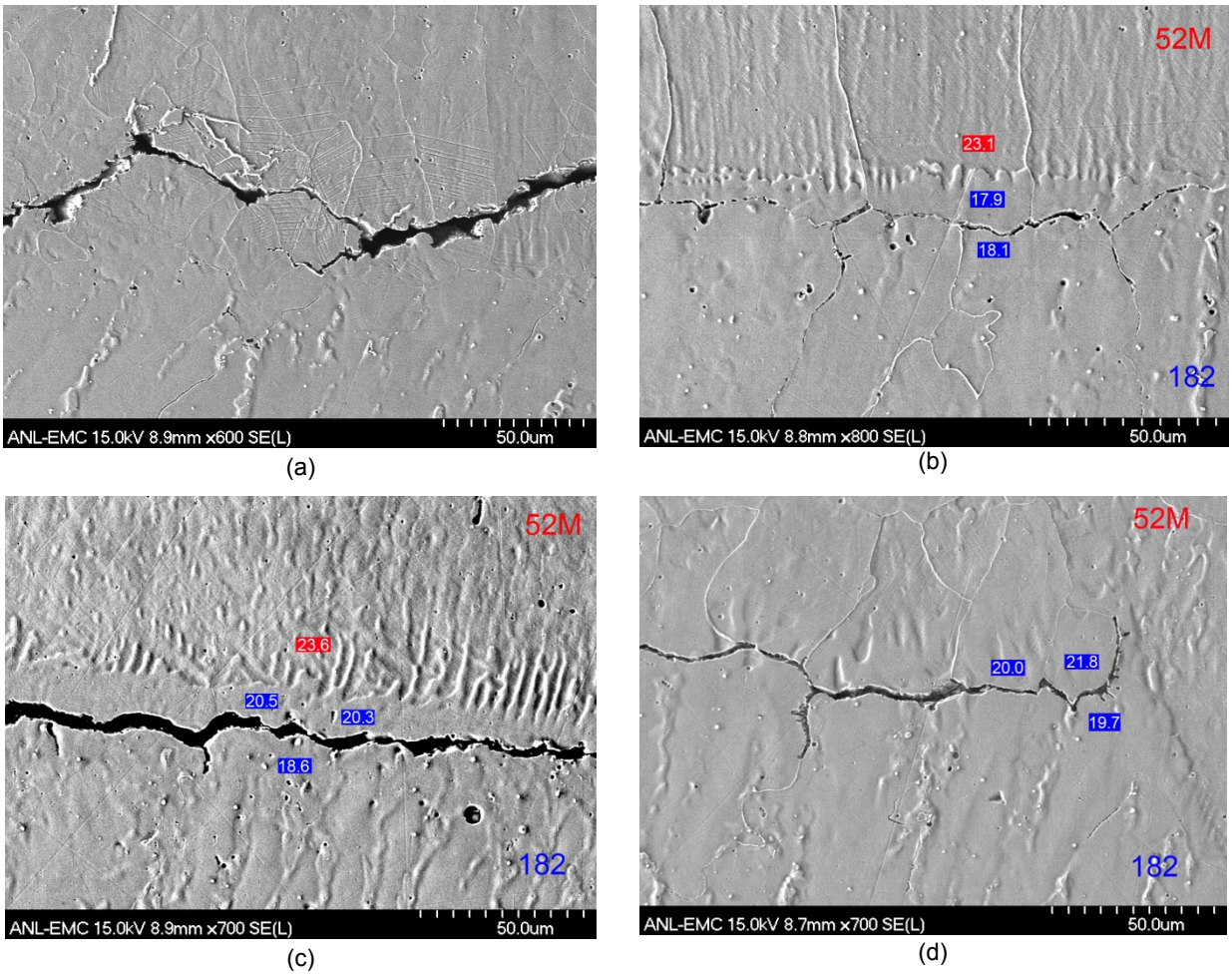


**Figure 3-33 Micrographs on the cross section of specimen WOL-ST-1 on: side 1 taken at location (a) 1A, and (b) 1B in Fig. 3-32a, and side 2 taken at location (c) 2A and (d) 2B in Fig. 3-32b. Inserts show the local Cr concentrations (wt. %). Crack advance is from left to right.**

The photograph, Fig. 3-34, provides a good visual contrast between the various alloys that were tested. Blue arrows indicate the Alloy 600-Alloy 182 interface, green arrows indicate the Alloy 182-Alloy 52M interface, and the red arrows and line mark the end of the test. The locations of the two test periods in Alloy 600 (P3 and P8) and along the Alloy 52M-182 interface (P19) are indicated in the figure. Measurements show that the Alloy 600-182 interface is 1.06 mm from the notch, in good agreement (5%) with expectations. The crack reached the Alloy 52M-Alloy 182 interface after 2.61 mm, again in good agreement (2%) with the distance measured by DC potential through test period 18, Table 3-4, which was 2.54 mm. The end of the test is 5.50 mm from the specimen notch, hence, the crack extension under constant load in test period 19 is 2.89 mm, a factor of 8.2 higher than the 0.339 mm extension measured by DC potential. The final crack extension was re-measured on the SEM image (Fig. 3-35) and was found to be in very good agreement (7%) with the determination based on Fig. 3-34. As such, test period 19 was corrected by a factor 8.2, and the corrected outcome was already shown in Fig. 3-30g. Table 3-4 also already reflects the corrected rate.

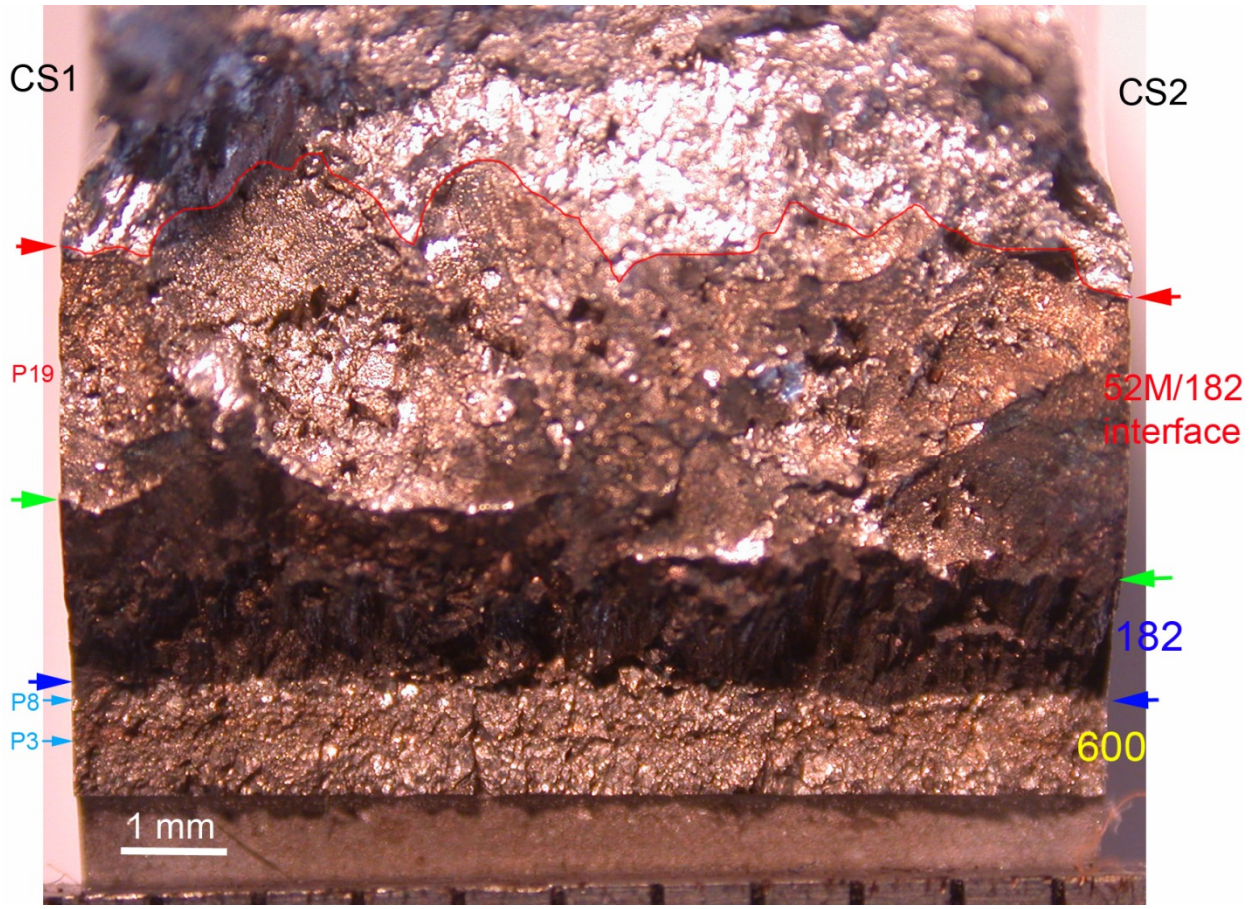


**Figure 3-34** **Fracture surface of specimen WOL-ST-1. Blue arrows indicate the Alloy 600-Alloy 182 interface, green arrows indicate the Alloy 182-Alloy 52M interface, and the red arrows and line mark the end of the test. The locations of the two test periods in Alloy 600 (P3 and P8) and along the Alloy 52M-182 interface (P19) are indicated in the figure. Crack advance is from bottom to top.**

The SEM examination allowed for a closer inspection of the fracture features. Several areas of interest are marked in Fig. 3-35, and will be presented next.

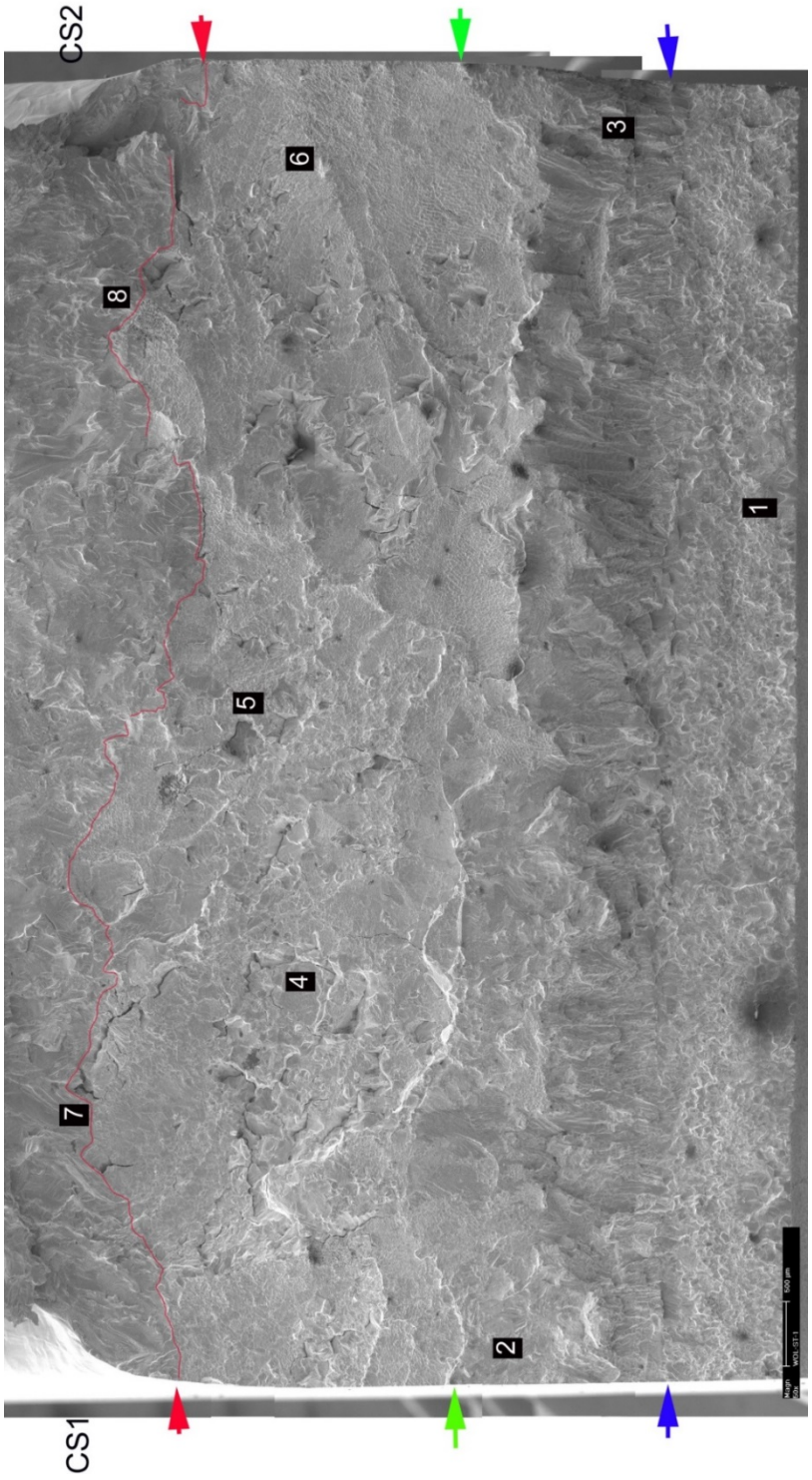


**Figure 3-35** **Fracture surface of specimen WOL-ST-1. Blue arrows indicate the Alloy 600-Alloy 182 interface, green arrows indicate the Alloy 182-Alloy 52M interface, and the red arrows and line mark the end of the test. Crack advance is from bottom to top.**

Figure 3-36 is an image taken at location 1 in Fig. 3-35 and focuses on the Alloy 600 region. Given the short distance to the interface, the specimen was transitioned to IG and set at constant load relatively quickly. The blue arrows designate the intersection with the Alloy 182 weld, and the white arrows show areas of TG obtained most likely during fast cycling in at the beginning of test period 9, Table 3-4. Overall, the fracture surface is predominantly IG despite the fact that fast cycling was also used in test periods 4-5 to separate the two constant load test periods conducted in Alloy 690. This behavior suggests that this Alloy 600 HAZ is rather susceptible to SCC, and the rather high SCC rates that were measured (Fig. 3-28b) reflect that.

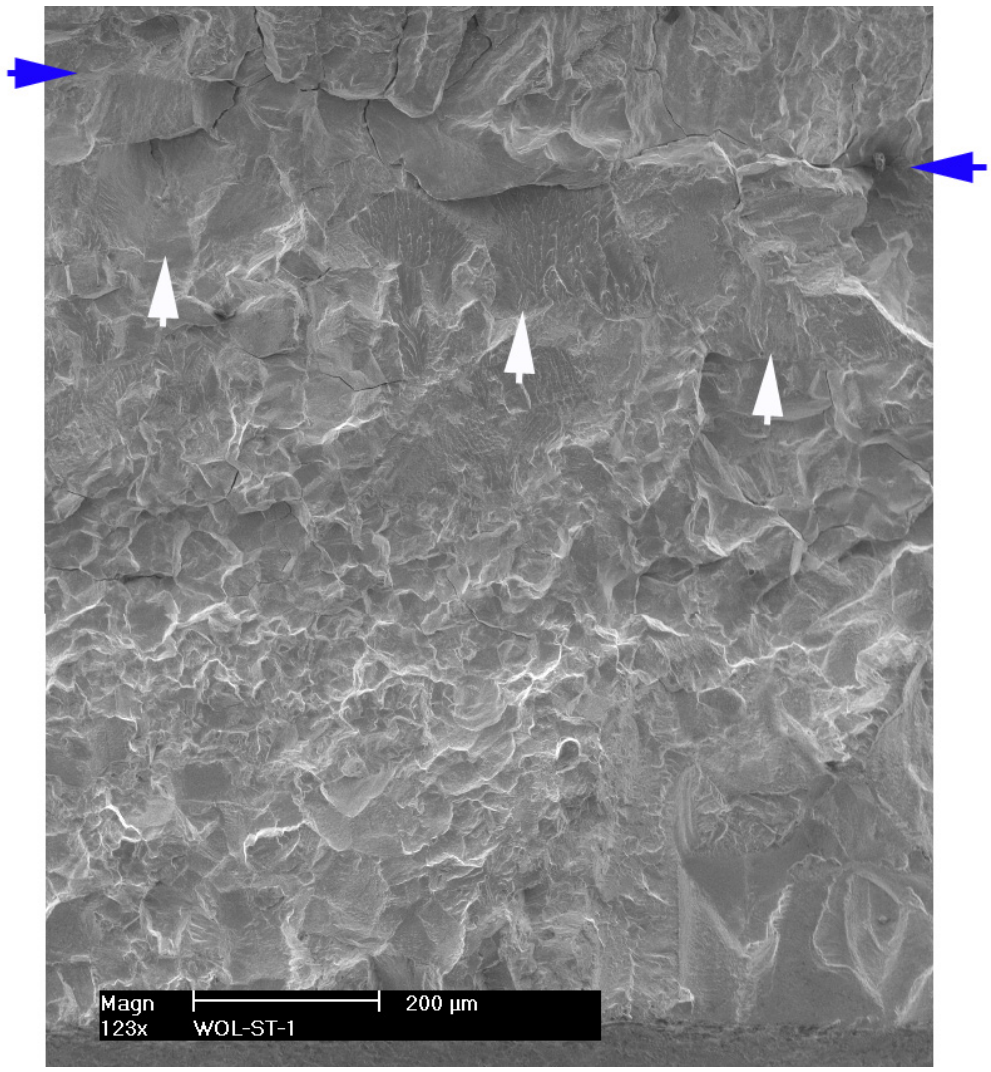


**Figure 3-36 Fracture surface of specimen WOL-ST-1 at location 1 in Fig. 3-35. The blue arrows designate the intersection with the Alloy 182 weld, and the white arrows show areas of TG obtained most likely during fast cycling in at the beginning of test period 9, Table 3-4. Crack advance is from bottom to top.**

Figures 3-37 and 3-38 are images taken at locations 2 and 3 in Fig. 3-35, and focus on the Alloy 182-Alloy 52M transition. The blue arrows in Fig. 3-37 indicate the onset of cracking in Alloy 182, and the image seems to show that occasional TG features (white arrows) occurred prior to transitioning into Alloy 52M. These correspond to location 1A in Fig. 3-32a where the crack,

under fatigue loading, overshot the WOL interface. Nevertheless, the crack seems to have eventually transitioned to IG, and one of the early occurrences is indicated with a green arrow. At the opposite end of the fracture surface, Fig. 3-38 shows that in that area the transition occurred more readily. The green arrows indicate the region where the fracture mode changes its appearance from TS to ST, i.e., from parallel to normal to the direction of dendrites.

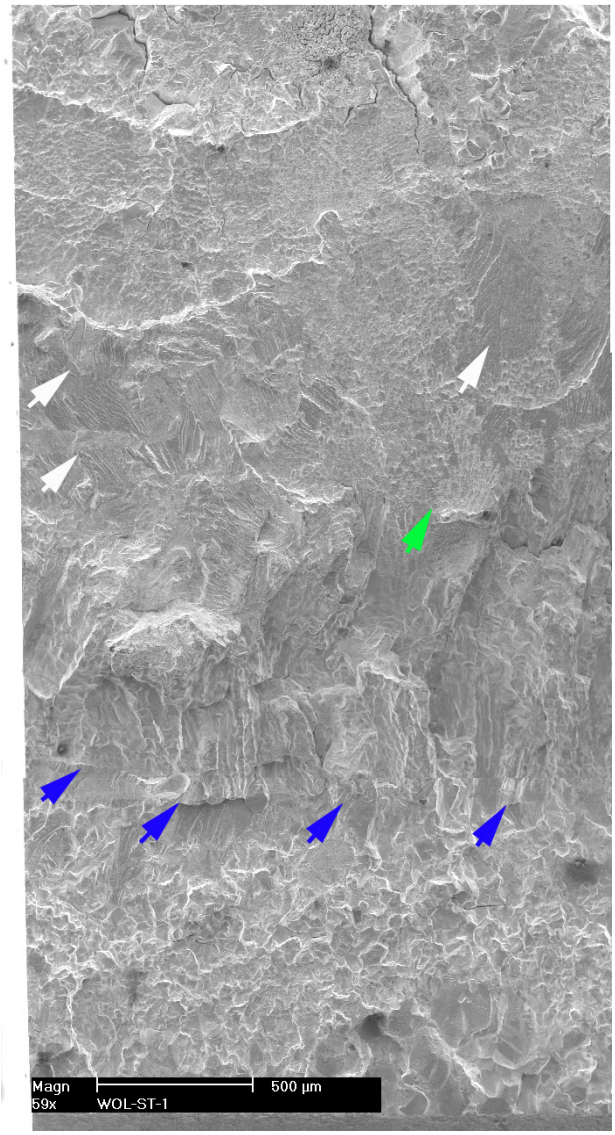


**Figure 3-37 Fracture surface of specimen WOL-ST-1 at location 2 in Fig. 3-35. The blue arrows indicate the onset of cracking in Alloy 182, and white arrows indicate the occasional TG fracture that occurred prior to transitioning into Alloy 52M. An early occurrence of IG is indicated with a green arrow. Crack advance is from bottom to top.**

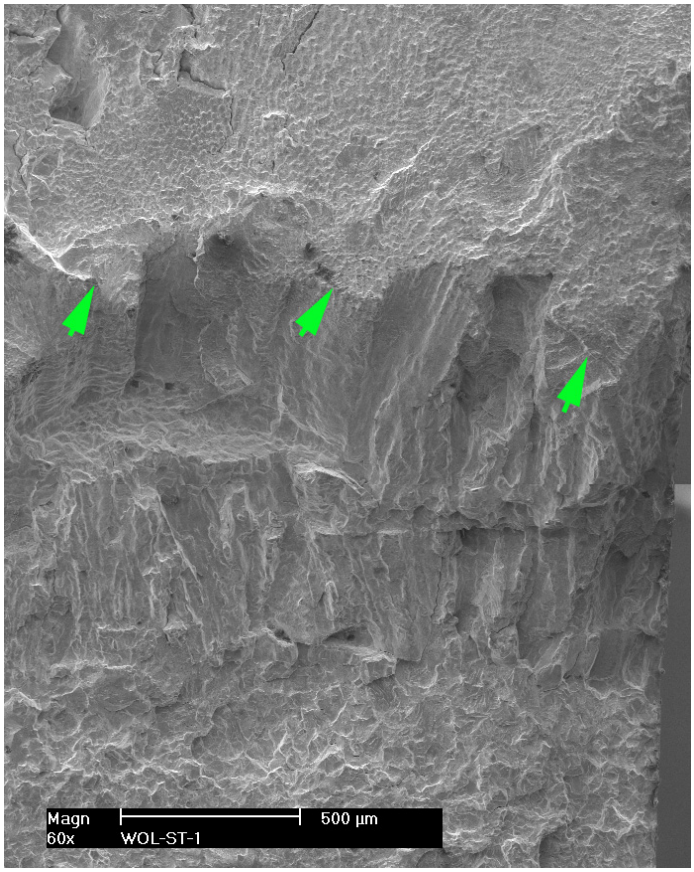


**Figure 3-38 Fracture surface of specimen WOL-ST-1 at location 3 in Fig. 3-35. The green arrows indicate the onset of IG along the interface. Crack advance is from bottom to top.**

Figures 3-39 and 3-40 shows images taken at locations 4, 5 and 6 in Fig. 3-35, and illustrate the fracture mode obtained under constant load in this specimen. Out-of-plane cracking was observed at several locations but this did not appear to be a predominant feature. The lack of out-of-plane cracking suggests that the interface was indeed the most susceptible microstructure for crack propagation. Figure 3-40a shows an area with less out of plane cracking, and Fig. 3-40b provides a higher magnification image of the fracture mode at the location indicated by the arrow in Fig. 3-40a. Overall, the general aspect of the fracture mode was as expected from the geometry of this specimen, i.e., with the dendrites normal to the plane of the figure. Figure 3-41 shows images from locations 7 and 8 in Fig. 3-35, and focus on areas at the end of the test. In both images the IG fracture mode at the end of the test is indicated by red arrows.

In summary, this section has documented the crack path from Alloy 600 to Alloy 182 and onto the Alloy 52M-Alloy 182 interface. SCC under constant load occurred along the interface in an IG/interdendritic fracture mode. The overall appearance – with minimal crack branching and off-plane cracking – suggests that the interface was the preferred crack path.

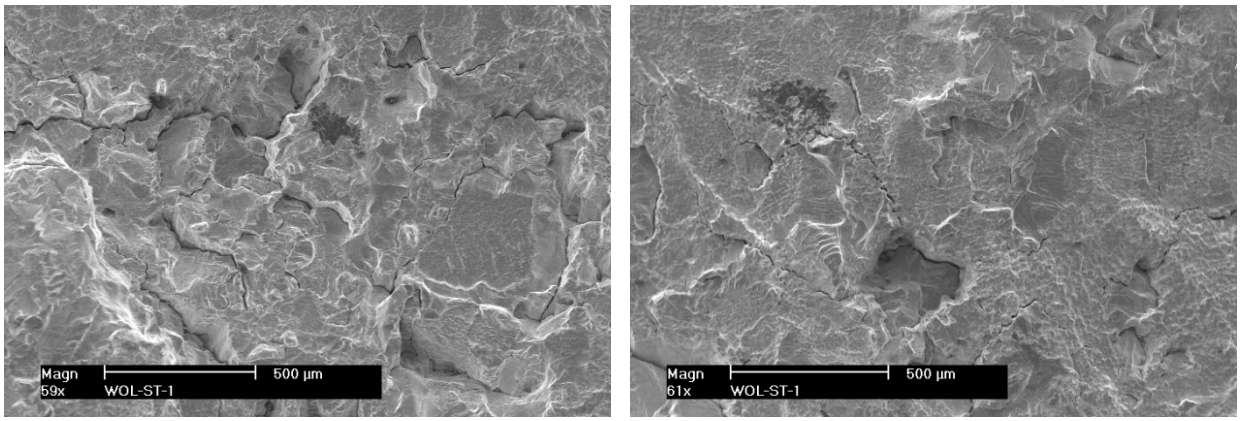


(a) (b)

**Figure 3-39 Fracture surface of specimen WOL-ST-1 at (a) location 4, and (b) location 5 in Fig. 3-35. Crack advance is from bottom to top.**

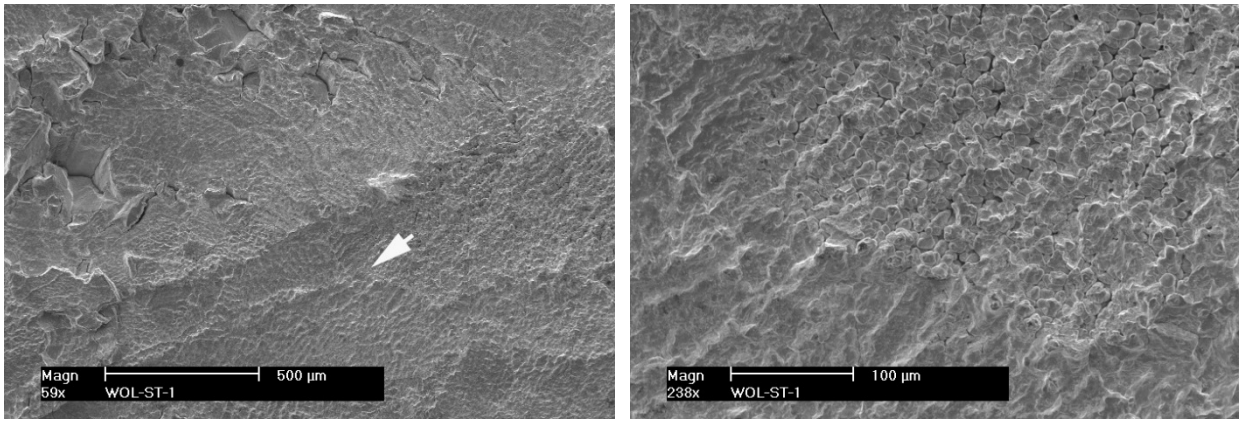


(a) (b)

**Figure 3-40 Fracture surface of specimen WOL-ST-1 at (a) locations 6 in Fig. 3-35, and (b) detail at the white arrow in (a). Crack advance is from bottom to top.**

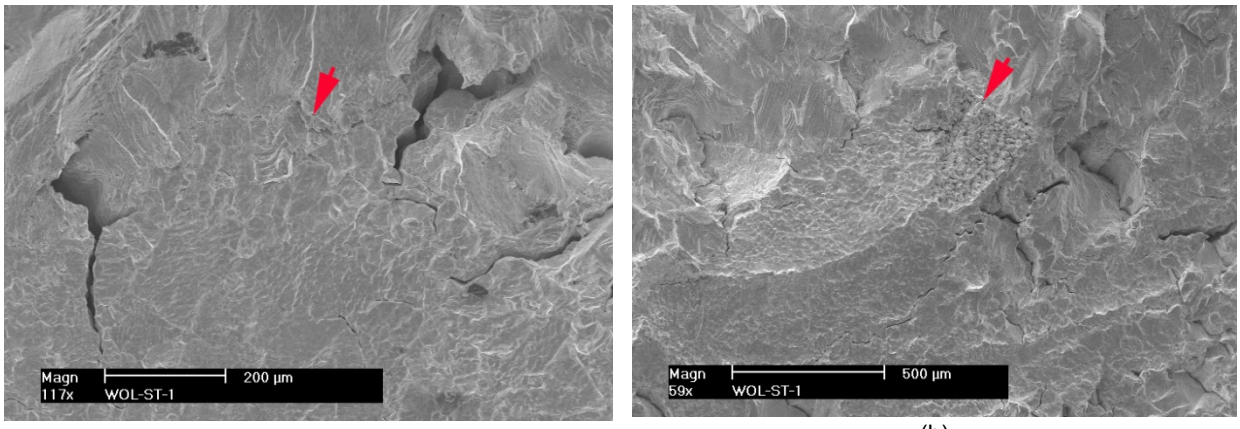


(a) (b)

**Figure 3-41 Fracture surface of specimen WOL-ST-1 at (a) location 7, and (b) location 8 in Fig. 3-35. The red arrows indicate IG fracture mode at the end of the test. Crack advance is from bottom to top.**

### 3.1.4 SCC in Alloy 52M Near the Interface with Alloy 182, Specimen WOL-ST-2

The objective of the test on Specimen WOL-ST-2 was to measure the SCC CGR in Alloy 52M near the interface with Alloy 182. In this specimen the crack was initiated in Alloy 52M and was expected to reach the Alloy 182 weld after approximately 6 mm of growth, Fig. 3-42. Based on prior observations and SCC CGR estimates (Fig. 3-12), the expectation for this test was for the crack to find a highly SCC-susceptible region in Alloy 52M near the interface, then continue on the interface between the two welds as the prior WOL-ST-1 test showed that that is the most susceptible path; moreover, prior testing (Fig. 3-25) showed that Alloy 182 near the WOL was relatively resistant.

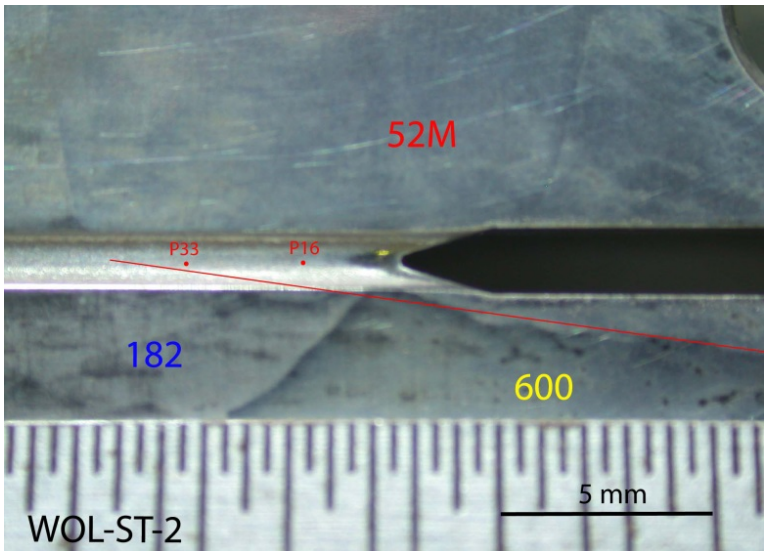


**Figure 3-42 Notch area in specimen WOL-ST-2. P16 and P33 represent the approximate locations where SCC CGR measurements were made in this specimen.**

The testing conditions and CGR responses are given in Table 3-5, and these data have been corrected based on fractography. The test was initiated with precracking in the PWR

environment (as usual), and this was followed by transitioning steps, and the known [24, 25] fatigue and corrosion fatigue behavior for the Ni-base weld were reproduced (Fig. 3-43). Early attempts at measuring an SCC CGR yielded very low SCC rates ($10^{-12}$ m/s), and it is not clear whether the unfavorable orientation with respect to the dendritic grains played a role or not. Nevertheless, regions of high SCC susceptibility were known to exist from the earlier TS tests (Fig. 3-12), hence it was decided to advance the crack while closely monitoring the environmental enhancement of the cyclic rates. This was accomplished in test periods 20-31. When the cyclic response in test period 31 was believed to be indicative of a microstructure susceptible to SCC based on Alloy 152 experience (see Figs. 3-44 and 2-10), the SCC CGR component was verified briefly by superposition in test period 32, and the specimen was set at constant load in test period 33.

## Table 3-5 Crack growth data for 52M specimen WOL-ST-2 in PWR water[a,b]

| Test Period | Test Time, h | Temp. °C | Load Ratio R | Rise Time, s | Down Time, s | Hold Time, s | $K_{max}$, MPa·m$^{1/2}$ | ΔK, MPa·m$^{1/2}$ | $CGR_{env}$, m/s | Estimated $CGR_{air}$, m/s | Crack Length, mm |
|---|---|---|---|---|---|---|---|---|---|---|---|
| Pre a | 196 | 319.5 | 0.31 | 0.5 | 0.5 | | 20.0 | 13.8 | 1.20E-08 | 4.94E-08 | 11.229 |
| Pre b | 214 | 319.4 | 0.31 | 50 | 50 | | 20.2 | 13.9 | 4.63E-10 | 5.12E-10 | 11.241 |
| Pre c | 216 | 319.5 | 0.31 | 0.5 | 0.5 | | 20.2 | 14.0 | 1.07E-08 | 5.20E-08 | 11.260 |
| Pre d | 221 | 319.5 | 0.31 | 1 | 1 | | 20.4 | 14.1 | 6.12E-09 | 2.67E-08 | 11.314 |
| Pre e | 237 | 319.5 | 0.31 | 50 | 50 | | 20.4 | 14.1 | 4.52E-10 | 5.35E-10 | 11.324 |
| Pre f | 241 | 319.5 | 0.31 | 1 | 1 | | 20.5 | 14.2 | 9.34E-09 | 2.76E-08 | 11.395 |
| Pre g | 298 | 319.5 | 0.31 | 100 | 100 | | 20.7 | 14.2 | 3.79E-10 | 2.82E-10 | 11.432 |
| Pre h | 302 | 319.4 | 0.31 | 1 | 1 | | 20.9 | 14.4 | 1.12E-08 | 2.95E-08 | 11.523 |
| Pre i | 416 | 319.1 | 0.31 | 50 | 50 | | 21.1 | 14.6 | 5.67E-10 | 6.19E-10 | 11.611 |
| Pre j | 420 | 318.7 | 0.31 | 1 | 1 | | 21.6 | 14.9 | 2.45E-08 | 3.36E-08 | 11.764 |
| Pre k | 423 | 318.7 | 0.31 | 2 | 2 | | 21.8 | 15.0 | 1.41E-08 | 1.74E-08 | 11.828 |
| Pre l | 462 | 318.9 | 0.31 | 50 | 50 | | 22.0 | 15.2 | 1.30E-09 | 7.29E-10 | 11.921 |
| Pre m | 467 | 319.3 | 0.31 | 1 | 1 | | 23.2 | 16.0 | 4.07E-08 | 4.50E-08 | 12.307 |
| Pre n | 469 | 319.5 | 0.31 | 2 | 2 | | 23.3 | 16.1 | 2.65E-08 | 2.33E-08 | 12.365 |
| 1 | 533 | 319.1 | 0.49 | 300 | 12 | | 27.1 | 13.8 | 3.76E-10 | 1.33E-10 | 12.465 |
| 2 | 804 | 319.9 | 0.49 | 600 | 12 | | 27.6 | 14.1 | 1.58E-10 | 7.28E-11 | 12.618 |
| 3 | 870 | 319.9 | 0.49 | 600 | 12 | 7200 | 27.7 | 14.1 | 2.86E-11 | 5.72E-12 | 12.621 |
| 4 | 999 | 319.1 | 1.00 | 0 | 0 | | 27.7 | 0.0 | 3.69E-12 | | 12.621 |
| 5 | 1,060 | 319.4 | 0.49 | 600 | 12 | 7200 | 27.6 | 14.1 | 1.95E-11 | 5.59E-12 | 12.627 |
| 6 | 1,099 | 320.2 | 0.49 | 600 | 12 | | 27.1 | 13.8 | 1.05E-10 | 6.77E-11 | 12.645 |
| 7 | 1,516 | 320.2 | 0.49 | 600 | 12 | 7200 | 27.7 | 14.1 | 1.76E-11 | 5.68E-12 | 12.673 |
| 8 | 1,607 | 320.4 | 0.49 | 600 | 12 | | 28.4 | 14.5 | 1.28E-10 | 8.24E-11 | 12.711 |
| 9 | 2,191 | 320.4 | 0.49 | 600 | 12 | 7,200 | 28.6 | 14.6 | 1.47E-11 | 6.55E-12 | 12.743 |
| 10 | 2,383 | 320.6 | 0.49 | 600 | 12 | | 29.1 | 14.8 | 1.10E-10 | 9.15E-11 | 12.817 |
| 11 | 2,815 | 320.7 | 0.49 | 600 | 12 | 7,200 | 29.0 | 14.8 | 1.29E-11 | 6.97E-12 | 12.838 |
| 12 | 3,157 | 320.2 | 0.49 | 600 | 12 | | 29.4 | 15.0 | 1.25E-10 | 9.37E-11 | 12.970 |
| 13 | 3,415 | 320.2 | 0.49 | 120 | 12 | | 29.8 | 15.2 | 6.61E-10 | 5.03E-10 | 13.380 |
| 14 | 3,487 | 320.8 | 0.49 | 600 | 12 | | 29.6 | 15.1 | 2.05E-10 | 9.85E-11 | 13.432 |
| 15 | 3,487 | 320.8 | 0.49 | 600 | 12 | 7,200 | 29.7 | 15.1 | 2.63E-11 | 7.58E-12 | 13.442 |
| 16 | 4,308 | 320.6 | 1.00 | 0 | 0 | | 29.9 | 0.0 | 2.75E-12 | | 13.450 |
| 17 | 4,408 | 319.9 | 0.49 | 120 | 12 | | 28.8 | 14.7 | 8.14E-10 | 4.32E-10 | 13.629 |
| 18 | 4,477 | 320.0 | 0.49 | 600 | 12 | | 29.3 | 14.9 | 2.18E-10 | 9.33E-11 | 13.679 |
| 19 | 4,992 | 320.6 | 0.49 | 600 | 12 | 7,200 | 29.5 | 15.0 | 2.33E-11 | 7.40E-12 | 13.718 |
| 20 | 5,051 | 320.1 | 0.49 | 120 | 12 | | 29.3 | 14.9 | 7.31E-10 | 4.65E-10 | 13.866 |
| 21 | 5,214 | 320.3 | 0.44 | 120 | 12 | | 26.4 | 14.8 | 6.39E-10 | 3.86E-10 | 14.101 |
| 22 | 5,285 | 320.4 | 0.42 | 600 | 12 | | 26.2 | 15.2 | 1.87E-10 | 8.18E-11 | 14.149 |
| 23 | 5,454 | 320.4 | 0.43 | 120 | 12 | | 28.4 | 16.2 | 8.39E-10 | 5.51E-10 | 14.563 |
| 24 | 5,549 | 320.1 | 0.49 | 120 | 12 | | 29.2 | 14.9 | 7.70E-10 | 4.61E-10 | 14.788 |
| 25 | 5,617 | 319.9 | 0.49 | 600 | 12 | | 29.4 | 15.0 | 2.28E-10 | 9.46E-11 | 14.836 |
| 26 | 5,687 | 319.7 | 0.49 | 120 | 12 | | 30.7 | 15.7 | 9.11E-10 | 5.65E-10 | 15.035 |
| 27 | 5,806 | 319.6 | 0.47 | 120 | 12 | | 30.5 | 16.1 | 1.10E-09 | 6.02E-10 | 15.372 |
| 28 | 5,977 | 319.9 | 0.48 | 120 | 12 | | 30.8 | 16.0 | 9.49E-10 | 6.06E-10 | 15.815 |
| 29 | 5,996 | 319.9 | 0.48 | 600 | 12 | | 30.8 | 16.0 | 2.68E-10 | 1.20E-10 | 15.830 |
| 30 | 6,144 | 318.9 | 0.50 | 120 | 12 | | 31.3 | 15.7 | 8.81E-10 | 5.78E-10 | 16.172 |
| 31 | 6,210 | 319.6 | 0.50 | 600 | 12 | | 31.4 | 15.7 | 4.38E-10 | 1.18E-10 | 16.244 |
| 32 | 6,282 | 320.4 | 0.50 | 600 | 12 | 7,200 | 32.8 | 16.4 | 5.32E-10 | 1.09E-11 | 16.371 |
| 33 | 7,867 | 319.2 | 1.00 | 0 | 0 | | 44.2 | 0.0 | 2.97E-10 | - | 17.815 |
| 34 | 7,986 | 319.4 | 1.00 | 0 | 0 | | 31.1 | 0.0 | 5.88E-11 | - | 17.818 |

[a] Simulated PWR water with 2 ppm Li, 1000 ppm B, and 2 ppm. DO<10 ppb. Conductivity was 21±3 □S/cm, and pH 6.4.
[b] Data was corrected using fractography.

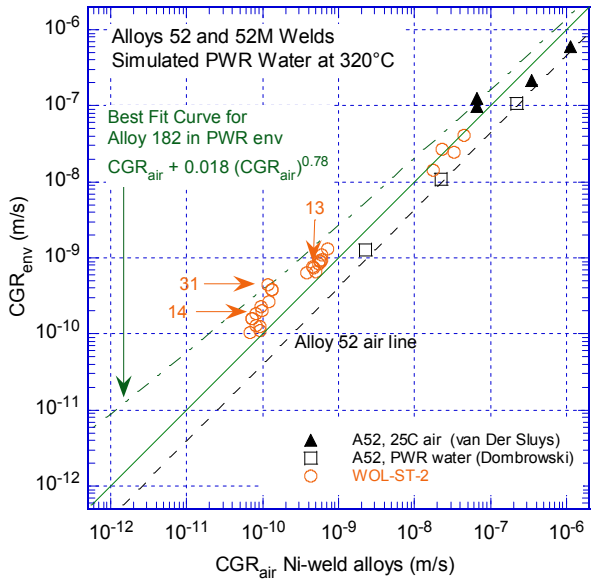


**Figure 3-43 Cyclic CGRs for Alloy 52M specimen WOL-ST-2 in simulated PWR environment. Also included are Alloy 52 data from the literature [24, 25] obtained in air at room temperature and in PWR environment.**

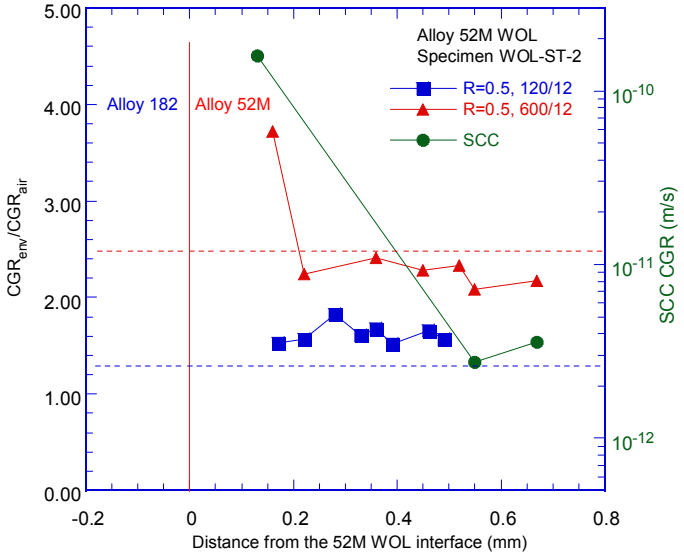


**Figure 3-44 Environmental enhancement of two control test conditions vs. calculated distance to the interface. Crack propagation is from right to left (see also Fig. 3-25 for guidance).**

Figure 3-45 shows the changes in crack length and $K_{max}$ with time for the entire test, and Fig. 3-45l shows the response under constant load conditions in test period 33. The initial SCC CGR of $1.6 \times 10^{-10}$ m/s ($K_{max}$ = 32.3 MPa $m^{1/2}$) was maintained until approximately 7,100h for the first 0.46 mm of growth, and this rate will be reported for the first layer of Alloy 52M as the post-test examination will establish unequivocally that the growth occurred in the Alloy 52M WOL. Next, the rate appeared to increase, and the SCC CCR was on average approximately double, $3.8 \times 0^{-10}$ m/s. It is interesting to note that in the latter part of this test period (7,700 h,

Fig. 3-45n), 5-10 μm "jumps" similar to those seen in specimen WOL-ST-1 (Fig. 3-30g) were observed; given that in the WOL-ST-1 specimen the SCC growth was along the Alloy 52M-182 interface, the "jumps" in the current test likely suggest that the crack reached the interface with Alloy 182. Towards the end of the test period, the SCC CGR reached $1.4 \times 10^{-9}$ m/s (after 7,855h). The calculated $K_{max}$ also appears to increase from 32.3 MPa $m^{1/2}$ to approximately 44.2 MPa $m^{1/2}$, primarily as a result of the factor 4.2 correction (Fig. 3-30g). Nevertheless, in the latter part of the test it is uncertain whether the SCC CGR increases because of the larger stress intensity factor or because of the faster SCC path along the interface between the two welds. Finally, the specimen was unloaded and it is interesting to note that although the unload at the end of test period 33 was intended to stop the growth (and effectively end the test), the crack continued to grow at a substantial rate even after the stress intensity factor was drastically decreased. Hence, this last period received its own designation, test period 34 in Table 3-5. Post-test measurements on three cross sections (the two sides of the specimen and one additional cross section in the middle of the specimen, as presented later in this section, confirmed that the SCC crack initiated in Alloy 52M, at least 0.8 mm from the interface with Alloy 182. The early response shown in Fig. 3-45l confirms the previous SCC CGR estimate based on fractgraphy of specimen A52M-182-TS-3 (Fig. 3-12).

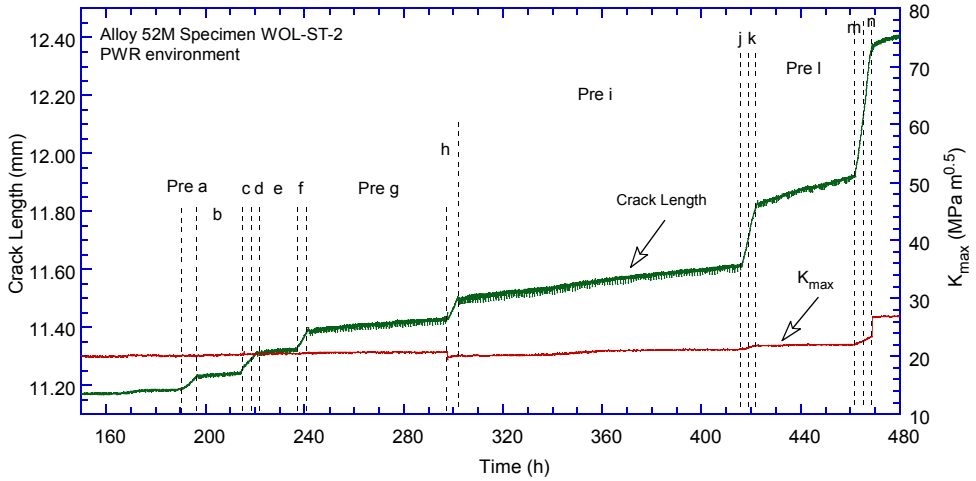


(a)

**Figure 3-45 Crack–length–vs.–time for Alloy 52M specimen WOL-ST-2 in simulated PWR environment during test periods (a) precracking, (b) 1-3, (c) 4-7, (d) 8-9, (e) 10-12, (f) 13-15, (g) 16, (h) 17-19, (i) 20-27, (j) 28-32, (k) 31, (l) 33, (m) detail in the first part of test period 33, (n) detail in the second part of test period 33, and (o) 34.**

**Figure 3-45 (Cont.)**

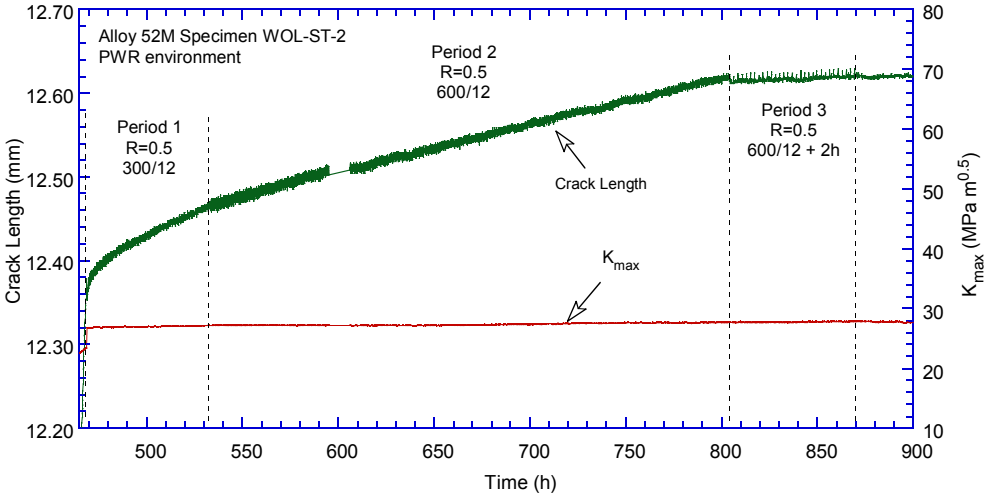


(b)

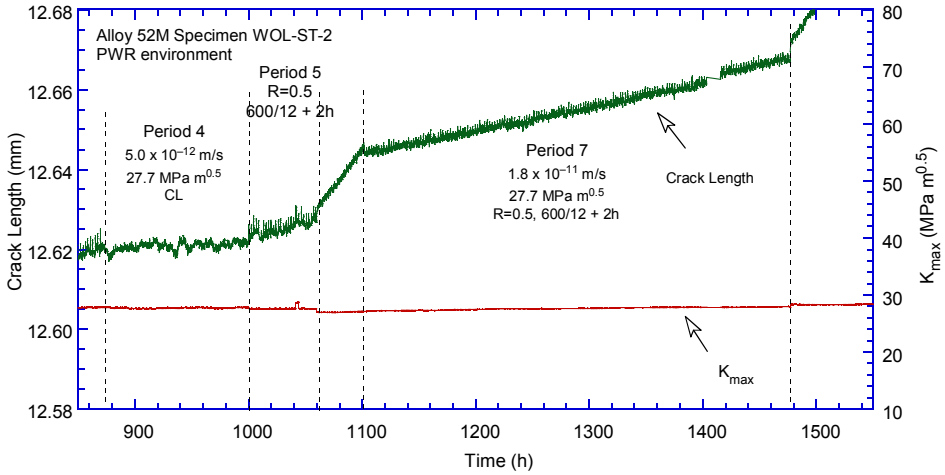


(c)

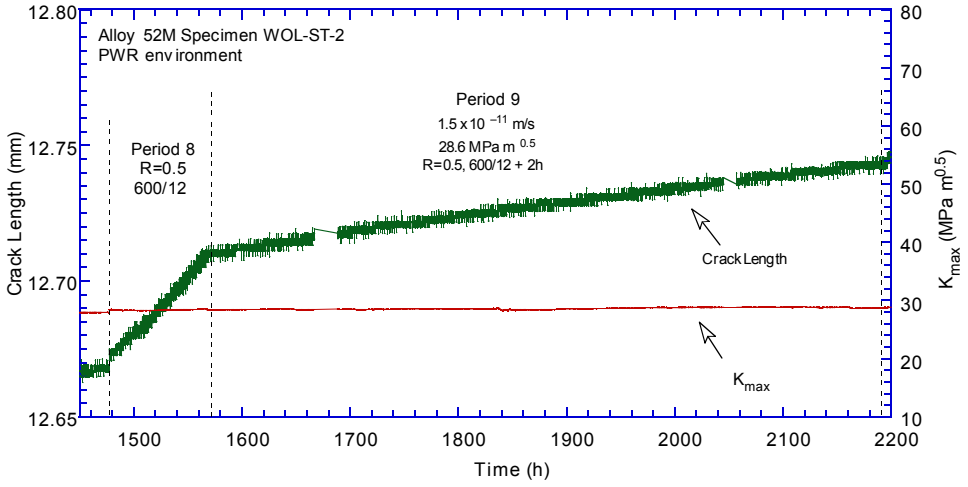


(d)

**Figure 3-45 (Cont.)**

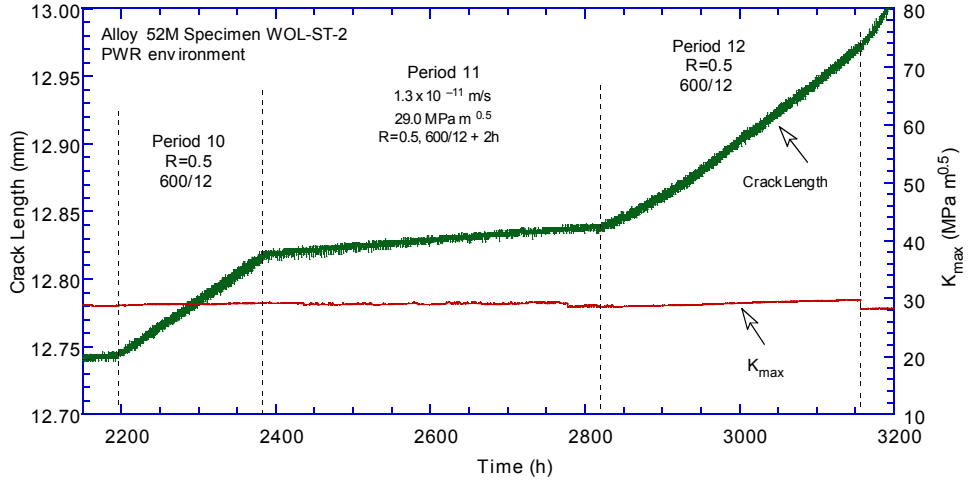


(e)

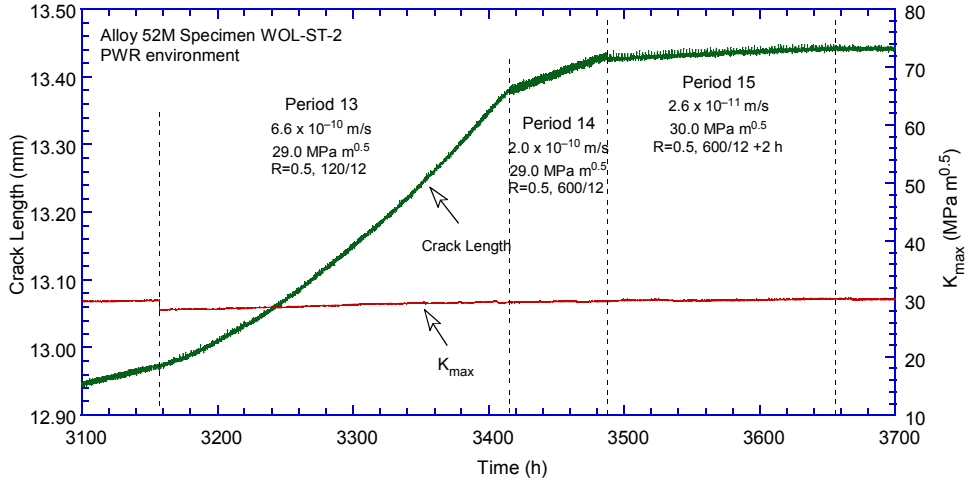


(f)

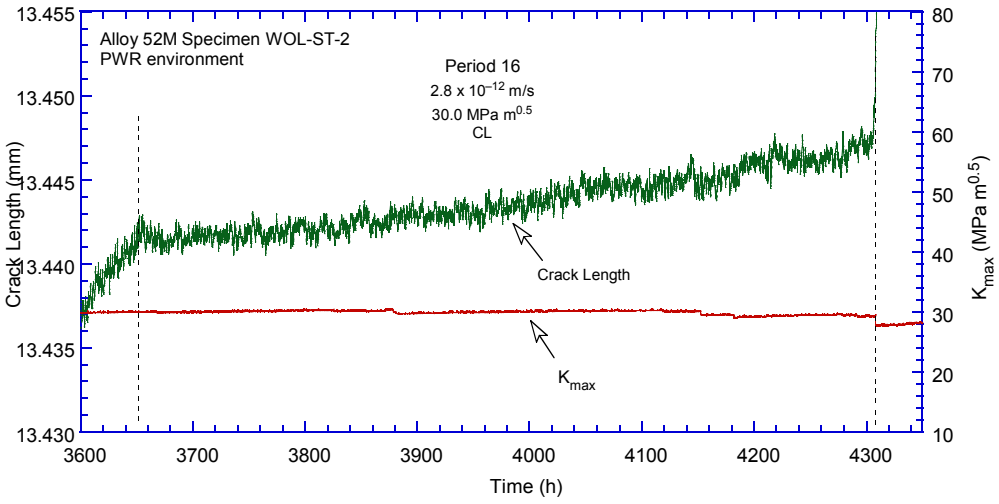


(g)

**Figure 3-45 (Cont.)**

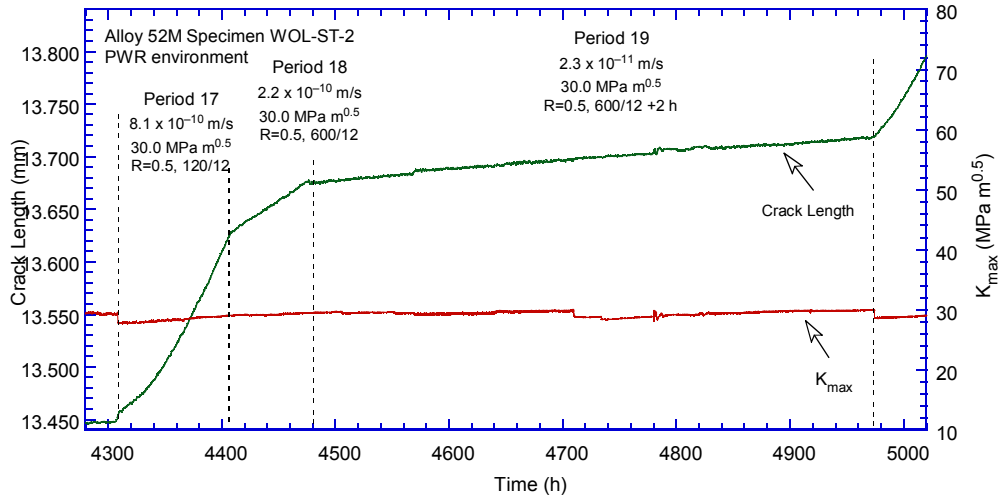


(h)

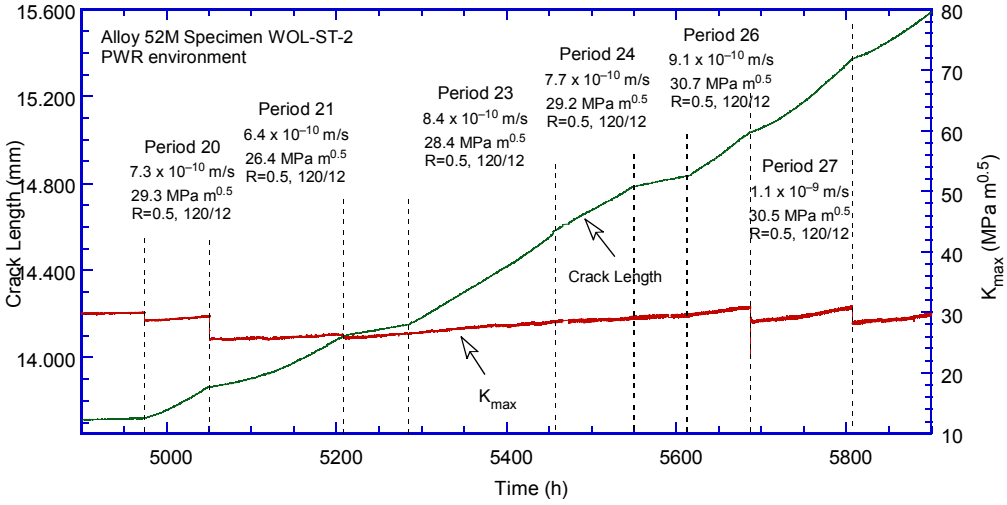


(i)

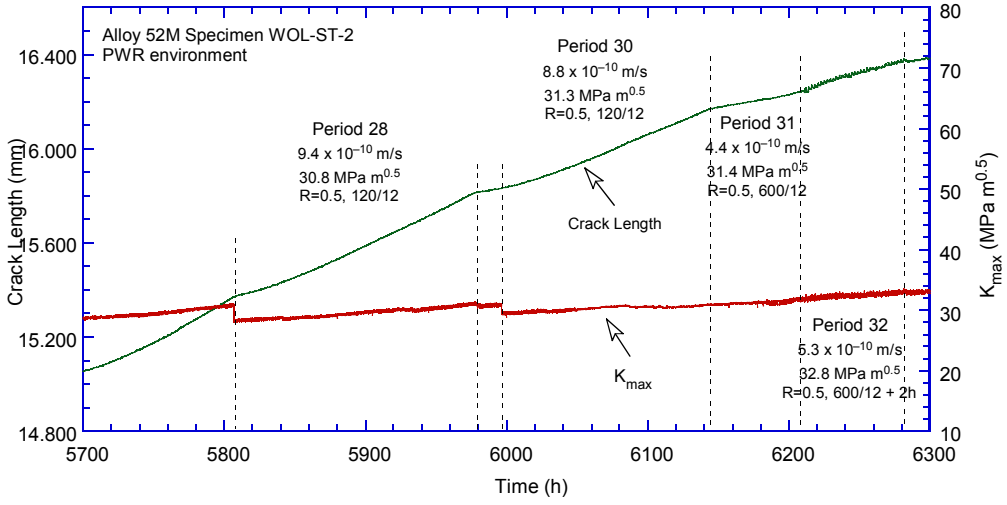


(j)

**Figure 3-45 (Cont.)**

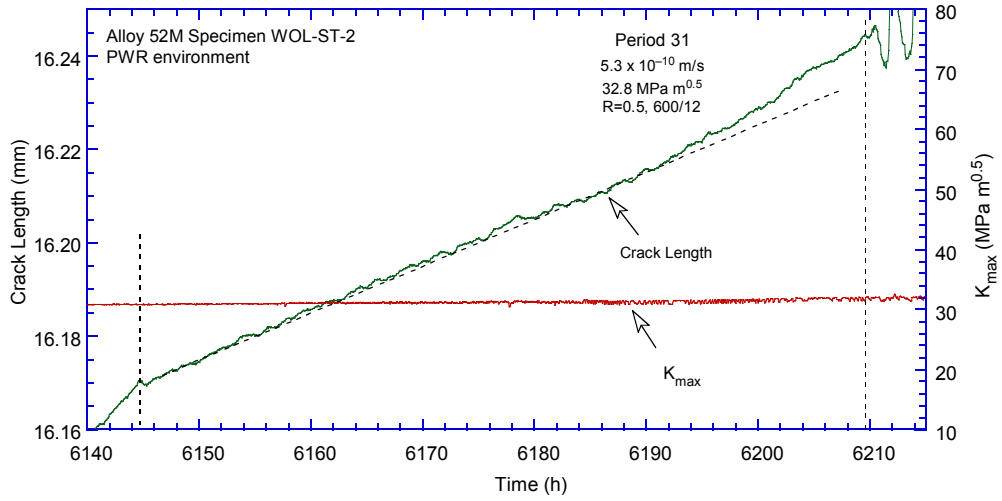


(k)

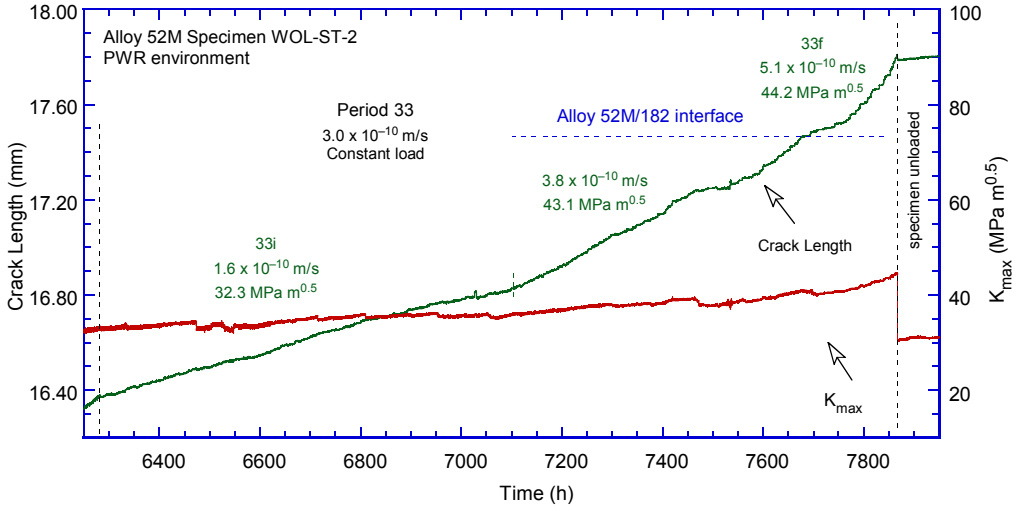


(l)

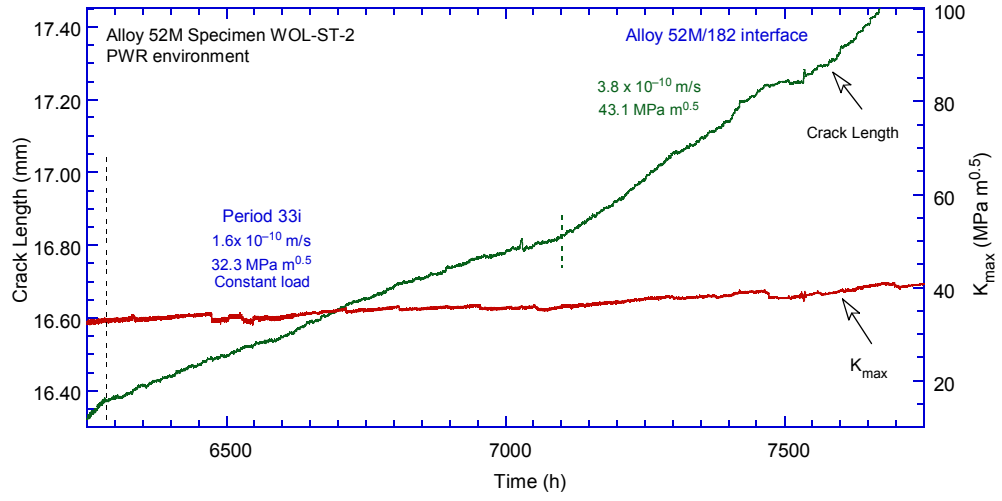


(m)

**Figure 3-45 (Cont.)**

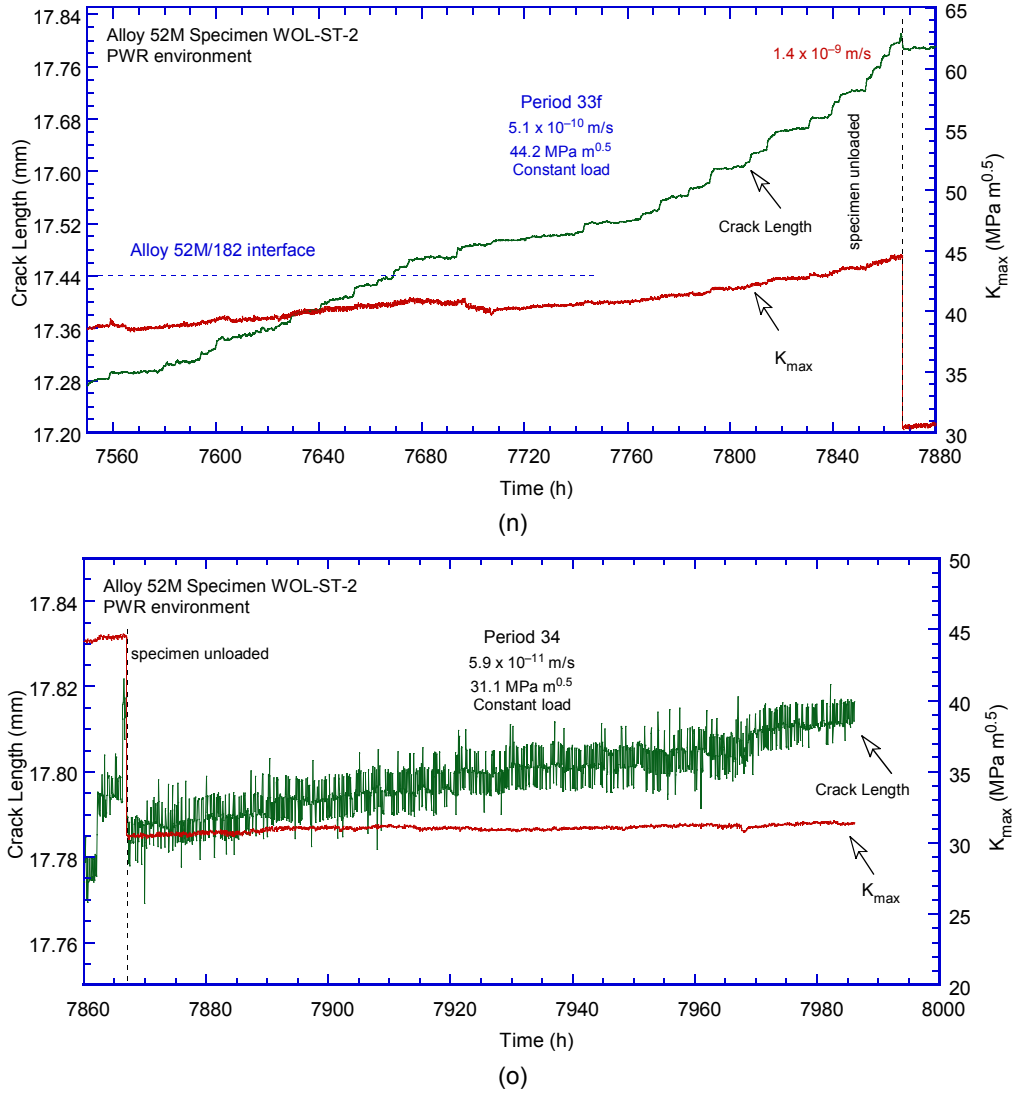


The post test-examination of this specimen involved the examination of the side surfaces (cross sections) as well as that of the fracture surface.

For this test, the examination of the side surfaces was essential for determining the crack path. For this purpose, the side surfaces of the specimen were ground to eliminate the side grooves, polished and electrochemically etched in a nital solution. The two side surfaces (Fig. 3-46) show that the test progressed as anticipated, and confirm that the test took place in the Alloy 52M dilution – interface area, as was intended.

The two side surfaces were further examined by optical microscopy, Fig. 3-47. The crack advance was straight, and the large opening suggests a TG fracture mode for the most part of the test. The average TG advance measured on the two side surfaces is 5.01 mm, a value which corresponds to test period 31 (Table 3-5). This finding suggests that the onset of high environmental enhancement in test period 31 corresponds to a change in fracture mode from TG to IG.

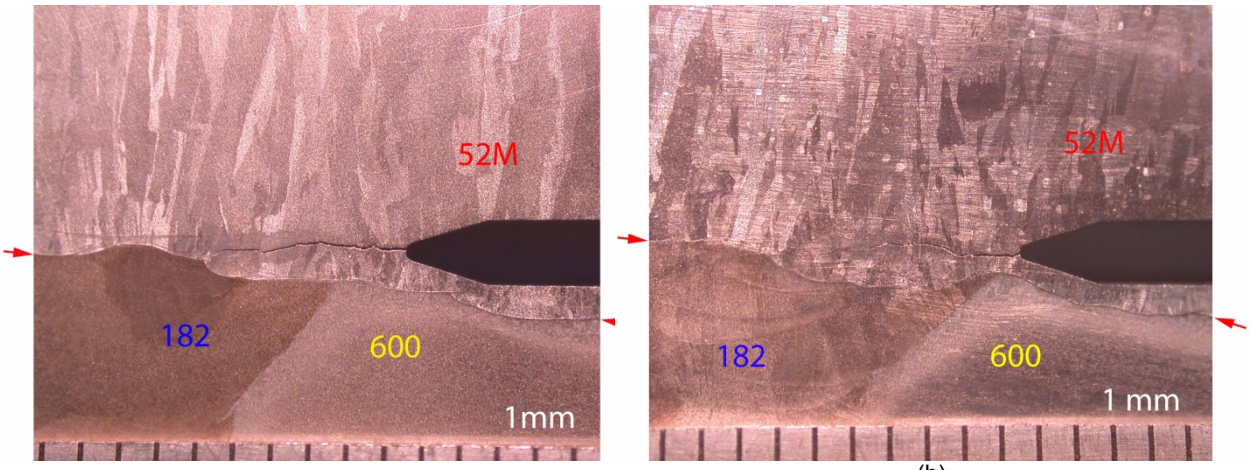


(a) (b)

**Figure 3-46 Notch area post-test in specimen WOL-ST-2 seen from both sides: (a) side 1, and (b) side 2. The red arrows indicate the WOL interface. Crack advance is from right to left.**

The IG regions initiating in the areas marked 1A and 2A in Figs. 3-47a and 3-47b, respectively, were further examined in the SEM. Figure 3-48 shows the IG region on side 1 of the specimen. Chemical composition measurements show that Cr levels were on average 25.5 wt. % along the IG crack path, and no Cr gradient seems present. By contrast, Cr levels at location 1B – corresponding to test period 16 with no SCC growth – were 27.1 wt. %. The figure also reveals that the IG crack appears to have taken a more favorable orientation towards the interface, but the clear path seems to be obstructed by a ligament. Nevertheless, cracking along the interface seems extensive, 1.6 mm from the end of the TG region. Secondary cracking in Alloy 182 is also visible. Figure 3-49 shows the IG region on side 2 of the specimen (beginning at location marked 2A in Fig. 3-47b). Chemical composition measurements at the TG-IG transition area show that Cr levels were on average 26.6 wt. %, however, the crack did not seem to propagate much. For comparison, Cr levels at location 2B in Fig. 3-47b –corresponding to test period 16 with no SCC growth – were 28.1 wt. %. Nevertheless, the crack appears to have taken a more favorable orientation towards the interface, and it resurfaces at the interface with Alloy 182, 0.9 mm away. As with the previous cross section, cracking along the interface seems extensive, and ends 1.2 mm from the TG region. Extensive secondary cracking in Alloy 182 is also visible.

In order to gain additional information regarding the crack propagation in the Cr dilution zone of Alloy 52M, an additional cross section was created by sectioning the specimen in the middle. This middle cross section (side M) is shown in Fig. 3-50. As with the two side surfaces, the crack advance was straight with a large opening suggesting a largely TG fracture mode. Nevertheless, Fig. 3-50 shows that following the TG growth, the crack propagated in an IG fashion towards the interface, perhaps along a more favorable weld orientation. Figure 3-51 (taken at location A in Fig. 3-50) shows that the average Cr content along the crack path was 24.2 wt. %. By contrast, Cr levels at location B in Fig. 3-50 – corresponding to test period 16 with no SCC growth – were on average 27.1 wt. %. As with the previous two examples, cracking along the interface seems extensive, 2.2 mm from the end of the TG region. Extensive secondary cracking in Alloy 182 is also visible.

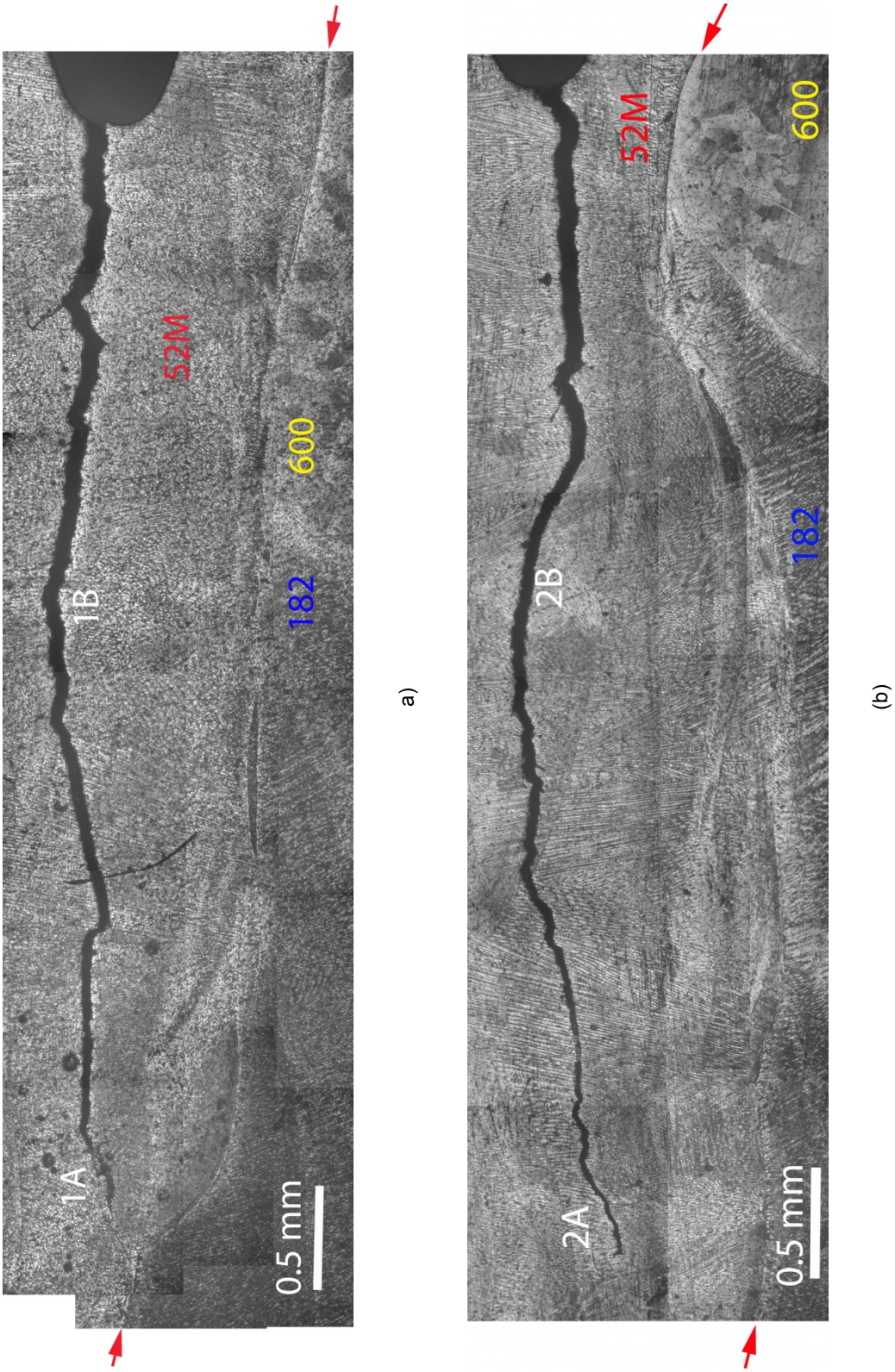


**Figure 3-47** **Cross section of specimen WOL-ST-2: (a) side 1, and (b) side 2. Crack advance is from right to left. The red arrows indicate the WOL interface.**

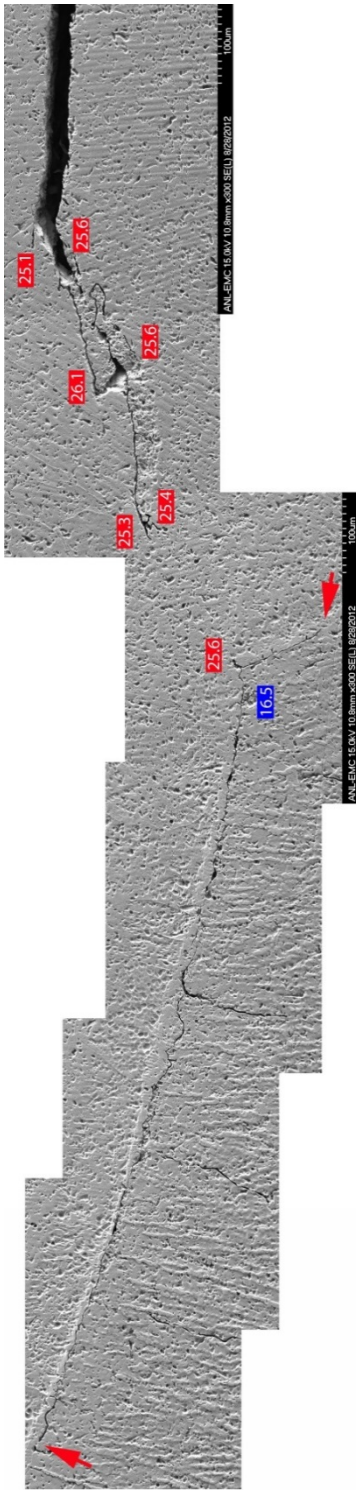


**Figure 3-48** **Crack tip region on the first side surface of specimen WOL-ST-2 (side 1, location 1A in Fig. 3-47a). Crack advance is from right to left. Cr concentration at select locations is indicated in the figure. The red arrows indicate the WOL interface.**

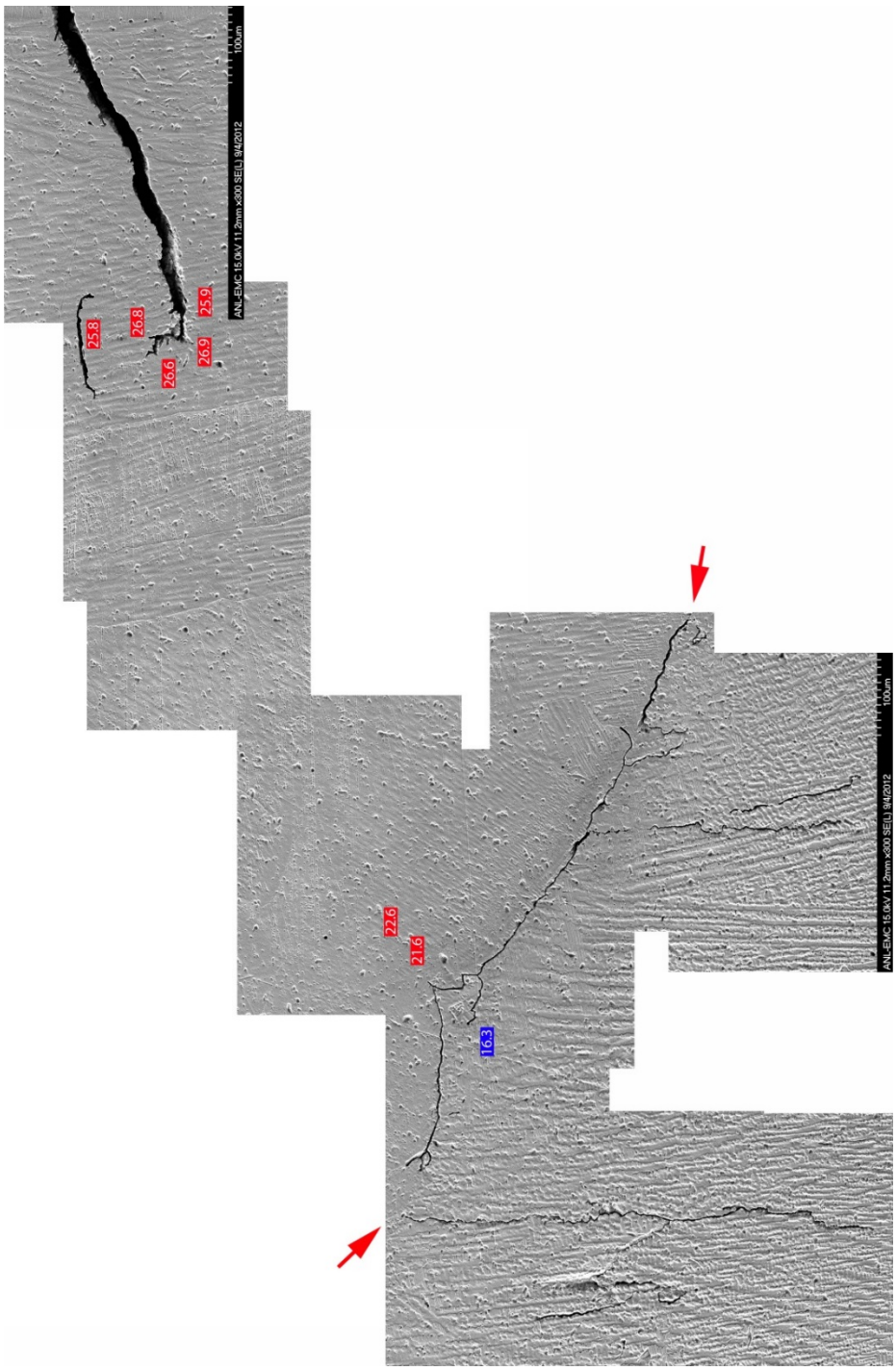


**Figure 3-49** **Crack tip regions on the second side surface of specimen WOL-ST-2 (side 2, location 2A in Fig. 3-47b). Crack advance is from right to left. Cr concentration at select locations is indicated in the figure. The red arrow indicates the WOL interface.**

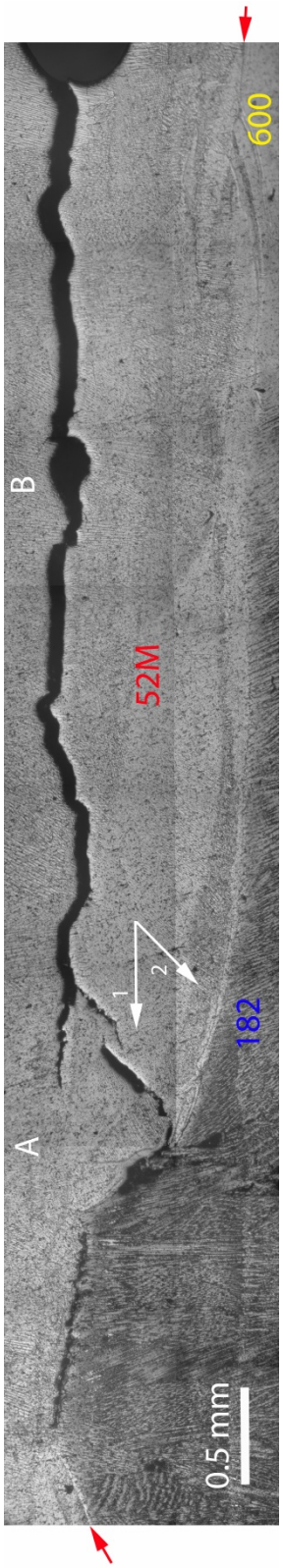


**Figure 3-50** Cross section of specimen WOL-ST-2: taken in the middle of the specimen (side M). Crack advance is from right to left. The red arrows indicate the WOL interface.

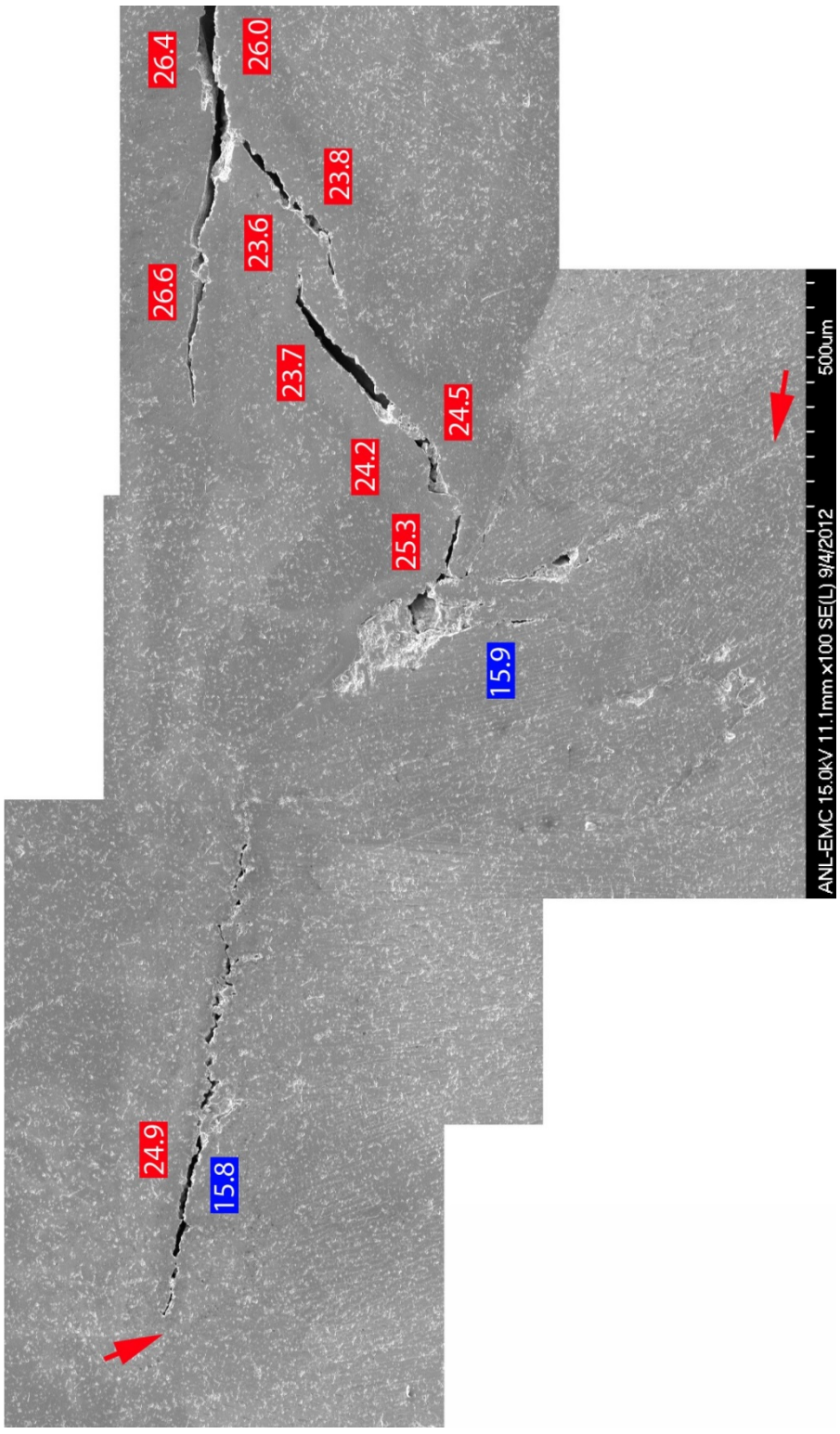


**Figure 3-51** **Crack tip regions on the second side surface of specimen WOL-ST-2 (side M, location A in Fig. 3-50). Crack advance is from right to left. Cr concentration at select locations is indicated in the figure. The red arrow indicates the WOL interface.**

In summary, the examination of three cross sections revealed that the test evolved as planned: the crack was transitioned to IG in the diluted area of Alloy 52M WOL, was allowed to propagate towards the interface, and towards the end of the test it reached and propagated along the interface. SCC cracking at constant load seemed to span three regions: Cr diluted Alloy 52M WOL in the beginning, Alloy 52M-182 interface at the end, and most likely a combination of the two in the middle. This sequence seems to describe the evolution observed during test period 33 in Fig. 3-45l.

The Cr content of the diluted Alloy 52M WOL seems to play a role: SCC occurred in regions with a Cr content which was on average 25.4 wt. %, and did not occur in regions with Cr content of 27.1 wt. %. Also, qualitatively, cracking appeared to be the most extensive in the middle cross section (24.2 wt. %), followed by side 1 (25.5 wt. %); side 2 (26.6 wt. %) showed the least amount of propagation.

After the cross sections were examined, the two halves of the specimen were fractured apart after cooling in liquid nitrogen. Both appeared to have fractured along the initial direction of the crack front, i.e., along the direction labeled “1” in Fig. 3-50. This outcome was somewhat unexpected, as cracking along direction “2” (along the dendrites) seemed to feature prominently in at least two of the three cross sections examined.

The fracture surface of specimen WOL-ST-2 is shown in Fig. 3-52. With respect to the CT specimen geometry, the fracture surface shown corresponds to the bottom part of the specimen as shown in Fig. 3-42, i.e., the Alloy 182 weld is below the plane of the crack. The yellow arrows indicate the beginning of SCC growth, the red arrows show the end of the test, and the green arrows indicate the region where the crack would have intersected the interface. The relative location of each cross section, side 1 (CS 1), side 2 (CS 2), and the middle cross section (CS M) described previously is indicated in the figure. Crack advance measurements on the fracture surface and the DC potential measurements are in excellent agreement (4%) for the precracking and transitioning stage. However, the crack advance under constant load was approximately 4.2 times higher than the determination by DC potential. The disparity between the DC potential and the actual measurements is not surprising given the complicated crack pattern and the large unbroken ligaments that have been observed on the cross sections. As such, a correction factor of 4.2 was applied uniformly to test periods 32-34. Table 3-5 and Fig. 3-45l-o already reflect that correction.

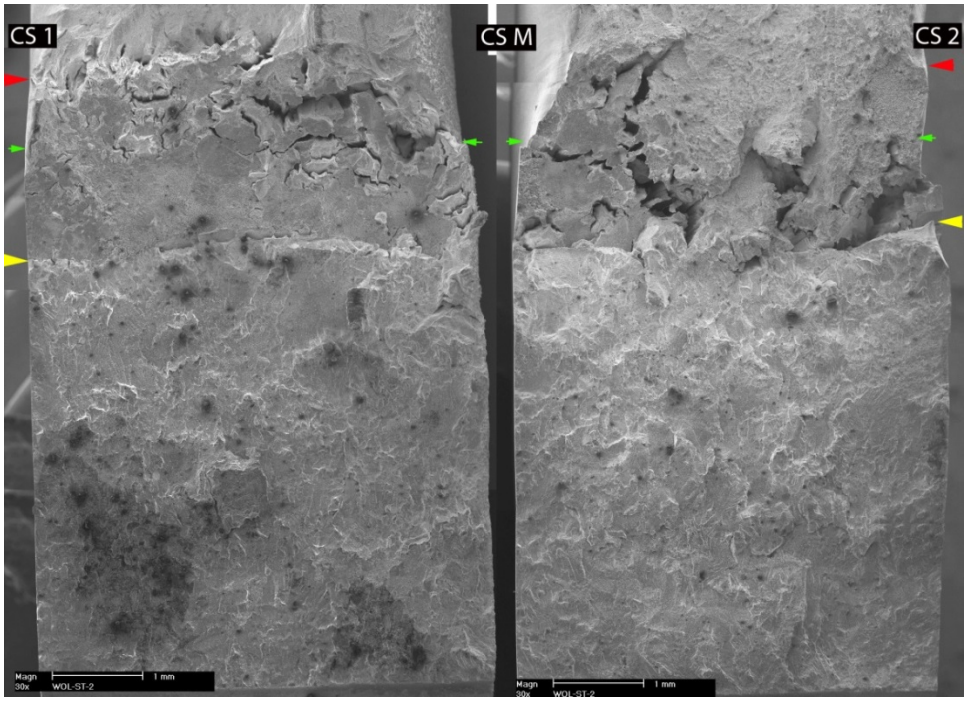


**Figure 3-52 Fracture surface of specimen WOL-ST-2. The yellow arrows indicate the beginning of SCC growth, the red arrows show the end of the test, and the green arrows indicate the region where the crack would have intersected the interface. Crack advance is from bottom to top.**

Figure 3-53 shows the first half of the fracture surface, and focuses on the region at constant load. As before, the yellow arrows indicate the beginning of SCC growth, the red arrows show the end of the test, and the green arrows indicate the region where the crack would have intersected the interface. Several locations of interest are identified in the figure. For the most part, the crack transitioned readily to an IG/interdendritic fracture mode, as observed at locations 1 and 2 (Figs. 3-53b, c). The morphology is consistent with an ST orientation (perpendicular to the direction of dendrites, i.e., along direction 1 in Fig. 3-50), and several secondary cracks can be observed. Further along, more prominent secondary cracks seem to develop, most likely along direction 2 in Fig. 3-50, Figs. 3-53d.

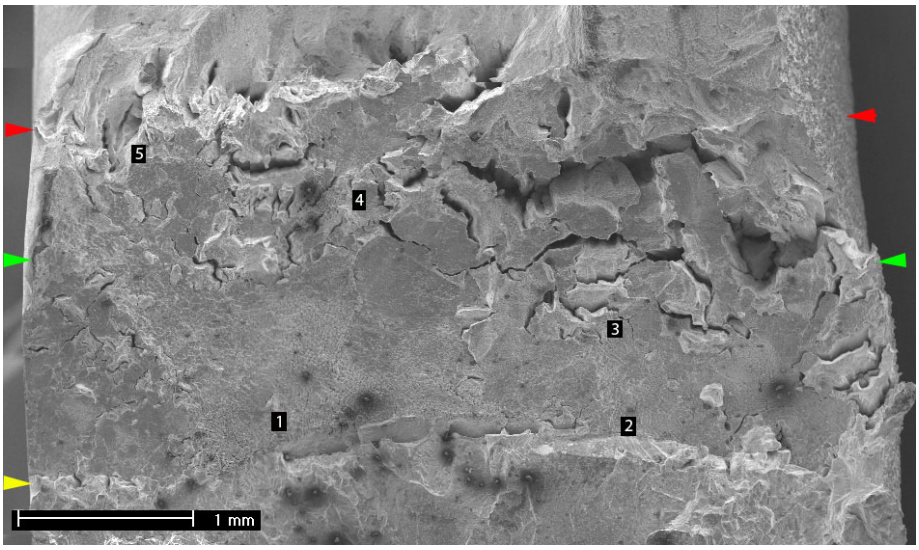


(a)

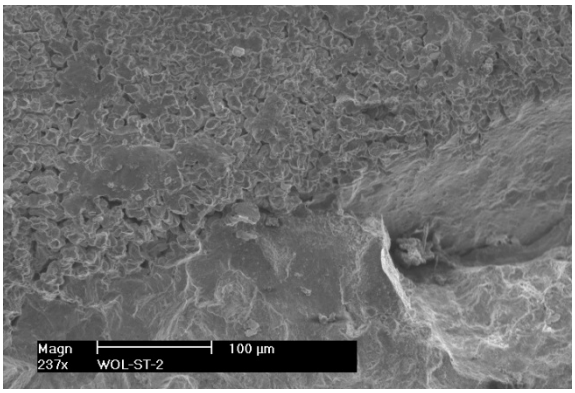


(b)

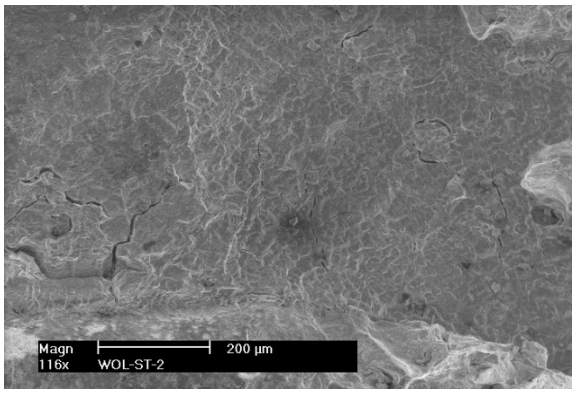


(c)

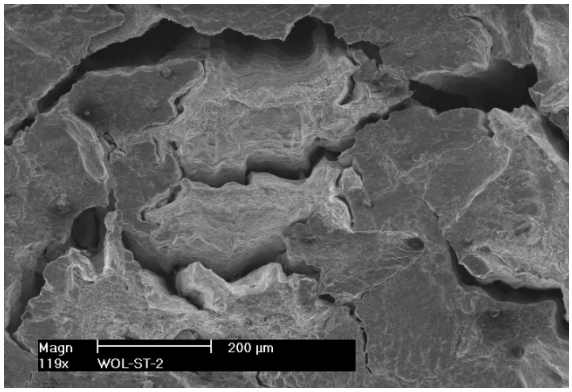


(d)

**Figure 3-53** **(a) First half (right hand side of Fig. 3-52a) of the fracture surface of specimen WOL-ST-2 obtained under constant load in simulated primary water. (b) location 1, (c) location 2, and (d) location 3. Crack advance is from bottom to top.**

Figure 3-54 focuses on the later part of the test. Figure 3-54a (location 4 in Fig. 3-53a) shows a combination of fracture modes: IG/interdendritic with secondary cracks, ductile rupture (white arrow) – most likely a ligament, and in the upper left hand corner, a fracture mode that seems consistent with that of the interface. Figure 3-54b (location 5 in Figs. 3-53a) shows the fracture surface at the end of the test. This exhibits an IG/interdendritic fracture mode as well as secondary IG cracks.

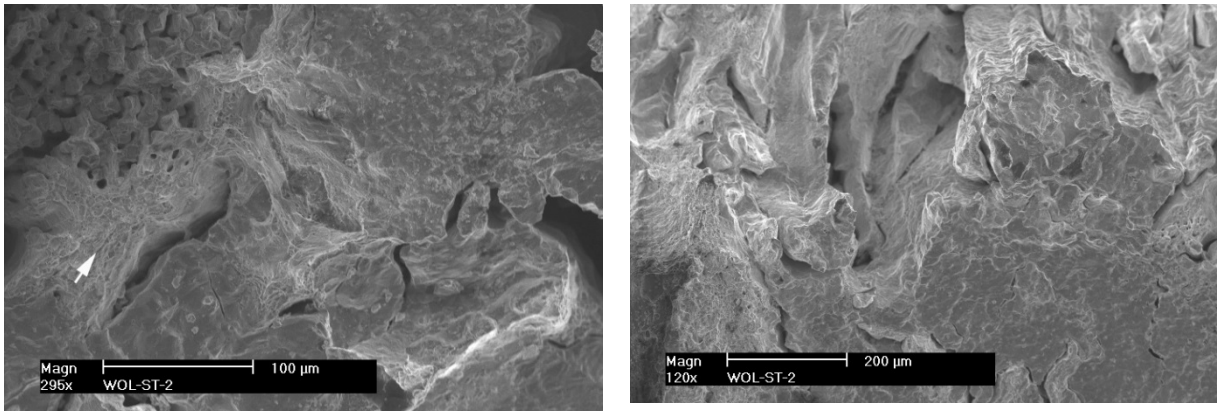


(a) (b)

**Figure 3-54 Fracture surface of specimen WOL-ST-2 at (a) location 4, and (b) location 5 in Fig. 3-53a. The white arrow indicates an unbroken ligament. Crack advance is from bottom to top.**

Figure 3-55 shows the second half of the fracture surface in the constant load region. The yellow arrows indicate the beginning of SCC growth, the red arrows show the end of the test, and the green arrows indicate the region where the crack would have intersected the interface. Several locations of interest are identified in the figure. For approximately 1/3 of the fracture surface, the appearance is similar to that shown in Fig. 3-53a. However, out of plane cracking – most likely along direction 2 (along the dendritic grains) in Fig. 3-50 – seems dominant. On this half of the specimen, cracking along the dendrites occurred early, Fig. 3-55b, and seems to have also been extensive. Figure 3-55c shows a region displaying what appears to be deep secondary cracking. Fracture morphology consistent with the weld interface (white arrow) also seems to be present.

The right hand side of Fig. 3-55a corresponds to the cross section shown in Fig. 3-49. In this particular case, the crack path was obstructed by a large ligament (Figure 3-49 suggested it was also off plane), but resurfaced along the weld interface. Fig. 3-55a provides confirmation for that initial inference, and pictures taken at location 3 provide the fracture morphology of the cracked weld interface. These images are shown in Fig. 3-56.

In summary the examination of the fracture surface confirmed the earlier observations on the cross sections. The crack transitioned readily to an IG/interdendritic fracture mode, and propagated in the Cr diluted area of Alloy 52M along two main directions, labeled 1 and 2 in Fig. 3-50. Direction 1 (normal to the dendrites) appeared to be the dominant direction, and the secondary cracking observed on the fracture surface was mostly due to of propagation along direction 2. Upon reaching the interface, IG/interdendritic fracture mode continued.

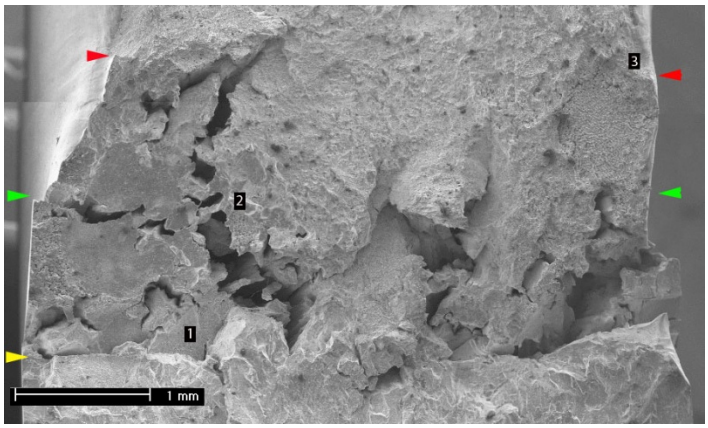


(a)

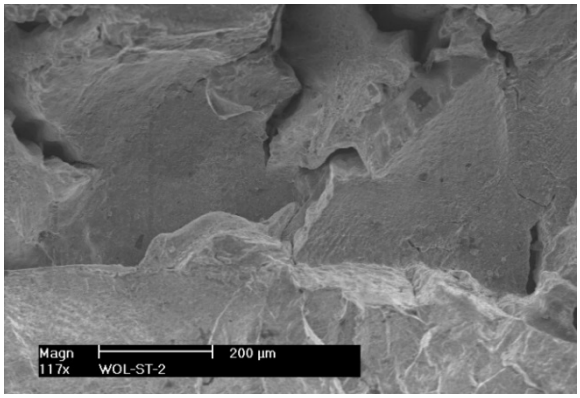


(b)

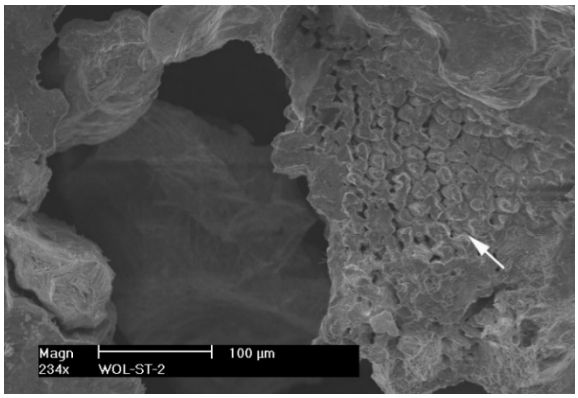


(c)

**Figure 3-55** **Second half (left hand side of Fig. 3-52a) of the fracture surface of specimen WOL-ST-2 obtained under constant load in simulated primary water. (b) location 1, and (c) location 2. Crack advance is from bottom to top.**

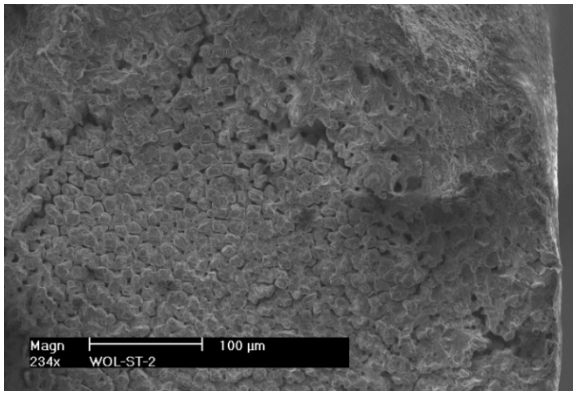


(a)

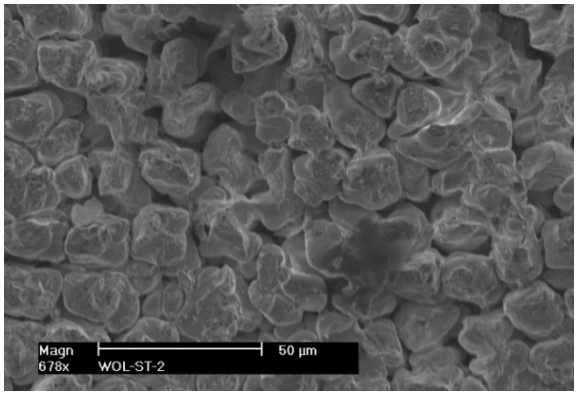


(b)

**Figure 3-56** **Fracture surface of specimen WOL-ST-2 at location 3 in Fig. 3-55a. Crack advance is from bottom to top.**

## 3.2 SCC CGR Testing of Alloy 152-LAS 1st Dilution Layer

Two tests were completed on Alloy 152 in a first layer configuration (Fig. 3-57), and the results will be presented in this section. There was no microstructural characterization conducted prior to machining the specimens. The only requirement for the specimens – produced at ANL Central Shops - was that they be aligned in the first weld layer, hence, the specimens sampled random locations in that first layer. The microstructural characterization (with a special attention to Cr concentration) was conducted post-test, along the actual crack path.

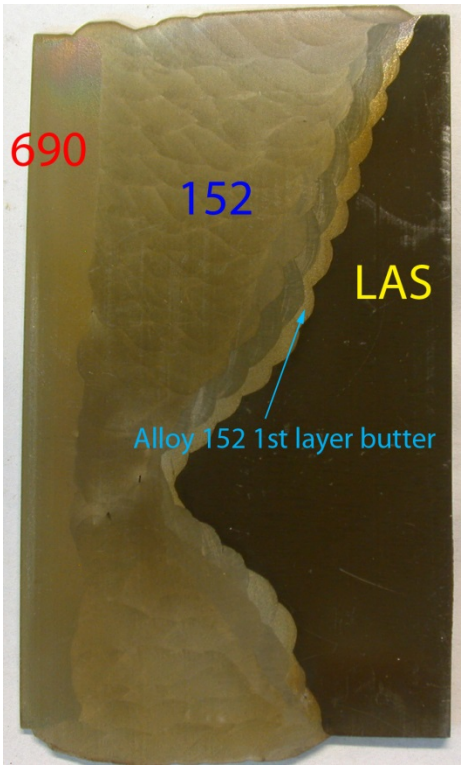


**Figure 3-57 Photograph of the Alloy 152 weld joining Alloy 690 and Alloy 533 LAS. SCC CGR test specimens were aligned in the 1st layer of Alloy 152 butter.**

### 3.2.1 SCC CGR Test on 1st layer Alloy 152 Weld Butter Specimen N152-LAS-1

Specimen N152-LAS-1 was a 1T CT specimen aligned along the first layer of the Alloy 152 butter, with the notch located approximately at the end of the blue arrow shown in Fig. 3-57. Figure 3-58 shows both sides of that specimen prior to the SCC CGR test. Pictures taken before and after machining the notch have been overlapped to show alignment. The alignment was aimed at the outer region of the Alloy 152, as close to the LAS as was possibly achievable. Both sides of this specimen seem to indicate that one lobe of the butter weld is ahead of the crack tip.

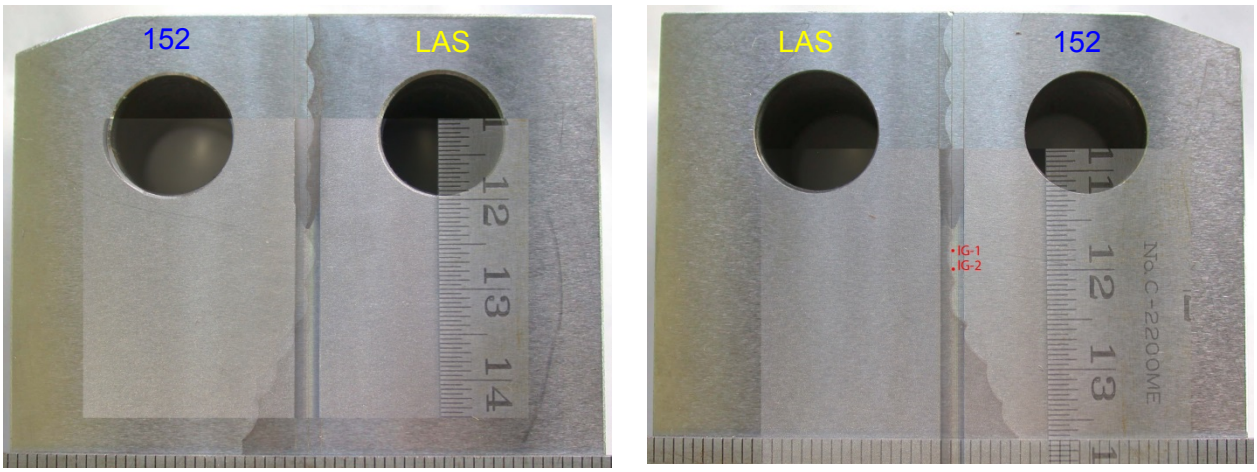


(a) (b)

**Figure 3-58 Specimen N152-LAS-1, overlapped images before and after the specimen notch was machined: (a) side 1, and (b) side 2. Units of the rulers are mm.**

The testing conditions for specimen N152-LAS-1 are given in Table 3-6 (data has been corrected based of fractography). The crack was advanced approximately 1.65 mm in fatigue, slightly into the first weld lobe, and transitioning steps were undertaken. The SCC CGR component was first calculated by superposition in test period 4 to be approximately $1.9 \times 10^{-11}$ m/s, and this rate suggested that the fracture mode was IG. However, it became clear rather quickly that the preferred crack path is off-plane, hence a correct SCC CGR will be difficult to measure by DC potential. To illustrate this point, a visual representation of the test in the approach described previously in Section 2.5. and applied successfully in a previous test (Fig. 3-44) is shown in Fig. 3-59. The plots tracks the environmental enhancement of two loading conditions – rise 50s and rise 600s, R = 0.5 – vs. crack advance from the notch. The purpose of the fast cycle is to advance the crack, and the purpose of the slow cycle is to probe for environmental enhancement. The dotted red and blue horizontal lines represent the enhancement levels of a forward advancing IG crack based on the Alloy 152 experience (Fig. 2-10). The large scatter observed in the cyclic response was judged to be indicative of primarily off-plane crack propagation. Overall, Fig. 3-59 also provides the SCC CGRs and shows that such measurements were attempted mainly at two locations in the specimen where the "conditions" were judged to be optimal from an experimental standpoint.

## Table 3-6 Crack growth data for dilution specimen N152-LAS-1 in PWR water[a,b,c]

| Test Period | Test Time, h | Temp. °C | Load Ratio R | Rise Time, s | Down Time, s | Hold Time, s | $K_{max}$, MPa·m$^{1/2}$ | $\Delta K$, MPa·m$^{1/2}$ | $CGR_{env}$, m/s | Estimated $CGR_{air}$, m/s | Crack Length, mm |
|---|---|---|---|---|---|---|---|---|---|---|---|
| Pre a | 145 | 321.3 | 0.2 | 0.5 | 0.5 | | 21.7 | 17.4 | 4.48E-08 | 1.02E-07 | 10.480 |
| Pre b | 160 | 321.2 | 0.2 | 50 | 50 | | 21.8 | 17.4 | 1.06E-09 | 1.02E-09 | 10.515 |
| Pre c | 169 | 321.1 | 0.2 | 0.5 | 0.5 | | 23.1 | 18.5 | 9.06E-08 | 1.30E-07 | 11.430 |
| Pre d | 184 | 321.2 | 0.2 | 50 | 50 | | 23.3 | 18.6 | 1.15E-09 | 1.34E-09 | 11.534 |
| Pre e | 189 | 321.1 | 0.2 | 0.5 | 0.5 | | 24.3 | 19.4 | 9.01E-08 | 1.59E-07 | 12.196 |
| Pre f | 193 | 321.1 | 0.2 | 1 | 1 | | 24.7 | 19.7 | 3.60E-08 | 8.48E-08 | 12.466 |
| Pre g | 208 | 321.2 | 0.2 | 50 | 50 | | 24.7 | 19.8 | 2.26E-09 | 1.72E-09 | 12.506 |
| Pre h | 214 | 321.3 | 0.2 | 1 | 1 | | 25.3 | 20.3 | 3.56E-08 | 9.50E-08 | 12.885 |
| 1 | 234 | 321.2 | 0.5 | 50 | 12 | | 25.4 | 12.7 | 1.12E-09 | 6.04E-10 | 12.966 |
| 2 | 305 | 321.7 | 0.5 | 300 | 12 | | 25.5 | 12.8 | 2.66E-10 | 1.03E-10 | 13.039 |
| 3 | 575 | 320.0 | 0.5 | 600 | 12 | | 25.8 | 12.9 | 1.32E-10 | 5.25E-11 | 13.133 |
| 4 | 976 | 320.4 | 0.5 | 600 | 12 | 7,200 | 25.8 | 12.9 | 4.16E-11 | 4.09E-12 | 13.171 |
| 5 | 1,742 | 320.3 | 1.0 | 0 | 0 | | 25.8 | 0.0 | 1.99E-11 | - | 13.201 |
| 6 | 2,421 | 319.4 | 0.5 | 12 | 12 | 7,200 | 26.0 | 13.0 | 1.98E-11 | 4.47E-12 | 13.262 |
| 7 | 2,680 | 320.5 | 1.0 | 0 | 0 | | 26.0 | 0.0 | 1.47E-11 | - | 13.279 |
| 8 | 2,917 | 320.9 | 0.49 | 600 | 12 | | 25.9 | 13.2 | 7.49E-11 | 5.72E-11 | 13.358 |
| 9 | 3,024 | 321.1 | 0.49 | 50 | 12 | | 26.1 | 13.3 | 6.36E-10 | 7.07E-10 | 13.541 |
| 10 | 3,454 | 320.9 | 0.49 | 600 | 12 | | 26.2 | 13.4 | 4.57E-11 | 6.01E-11 | 13.628 |
| 11 | 3,862 | 320.5 | 0.49 | 50 | 12 | | 27.8 | 14.2 | 8.37E-10 | 9.04E-10 | 14.530 |
| 12 | 3,934 | 320.1 | 0.49 | 600 | 12 | | 27.8 | 14.2 | 1.17E-10 | 7.54E-11 | 14.545 |
| 13 | 4,151 | 320.0 | 0.49 | 50 | 12 | | 29.3 | 14.9 | 1.49E-09 | 1.12E-09 | 15.366 |
| 14 | 4,294 | 320.1 | 0.49 | 600 | 12 | | 29.5 | 15.0 | 2.13E-10 | 9.55E-11 | 15.474 |
| 15 | 4,318 | 320.0 | 0.49 | 50 | 12 | | 29.6 | 15.1 | 1.53E-09 | 1.18E-09 | 15.565 |
| 16 | 4,367 | 320.0 | 0.49 | 600 | 12 | | 29.8 | 15.2 | 2.48E-10 | 9.95E-11 | 15.605 |
| 17 | 4,534 | 320.0 | 0.49 | 600 | 12 | 7,200 | 29.9 | 15.3 | 1.12E-10 | 7.82E-12 | 15.693 |
| 18 | 6,879 | 319.6 | 1.0 | 0 | 0 | | 30.1 | 0.0 | 1.82E-11 | - | 15.839 |
| 19 | 7,026 | 319.1 | 0.49 | 600 | 12 | | 30.3 | 15.5 | 2.48E-10 | 1.06E-10 | 16.034 |
| 20 | 7,237 | 319.5 | 0.49 | 600 | 12 | 7,200 | 30.2 | 15.4 | 5.46E-11 | 8.12E-12 | 16.073 |
| 21 | 7,977 | 318.7 | 1.00 | 0 | | | 30.2 | 0.0 | no growth | - | 16.073 |
| 22 | 9,701 | 318.8 | 0.49 | 12 | 12 | 28,800 | 30.6 | 15.6 | 9.90E-12 | 2.29E-12 | 16.115 |
| 23 | 11,411 | 318.7 | 0.49 | 12 | 12 | 7,200 | 30.7 | 15.6 | 1.44E-11 | 9.25E-12 | 16.211 |
| 24 | 13,060 | 318.3 | 1.0 | 0 | 0 | | 30.7 | 0.0 | no growth | - | 16.211 |
| 25 | 13,068 | 27.3 | 0.2 | 1 | 1 | | 32.3 | 25.8 | 2.80E-08 | 7.88E-08 | 16.961 |

[a] Simulated PWR water with 2 ppm Li, 1000 ppm B, and 2 ppm. DO<10 ppb. Conductivity was 21±3 □S/cm, and pH 6.4.

[b] CGR rates in air are calculated assuming typical behavior for a Ni-base weld. The 152-LAS rates are approximately a factor of two lower.

[c] Data was corrected using fractography.

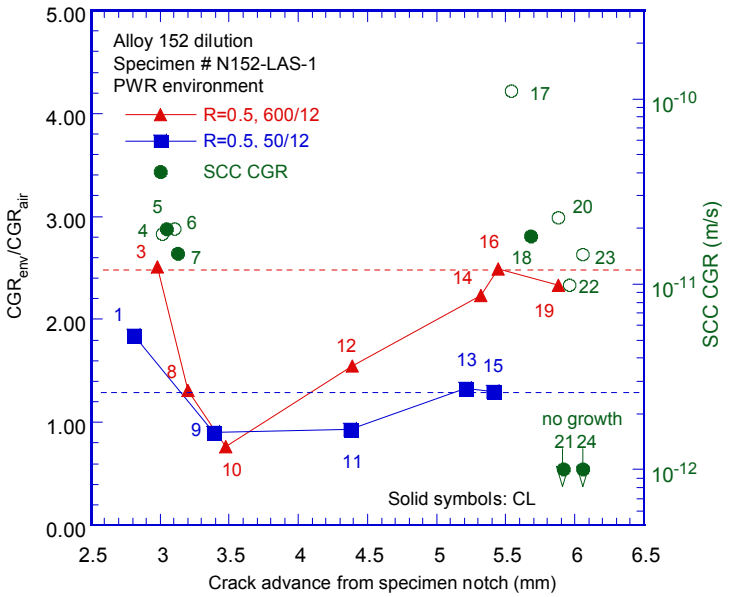


**Figure 3-59 Environmental enhancement of two control test conditions and SCC CGRs vs. distance from the specimen notch for Specimen N152-LAS-1. Test periods are indicated in the figure.**

The changes in crack length and $K_{max}$ vs. time are shown in Fig. 3-60. As described previously, the SCC CGR component was first calculated by superposition in test period 4 to be approximately $1.9 \times 10^{-11}$ m/s, and this rate is substantiated by the rate measured in the subsequent test period at constant load only if the jump observed when cyclic is re-introduced is considered an unbroken ligament and in taken into account in the rate calculation, as shown in Fig. 3-60c. Nevertheless, the rates measured during the following test periods 6 and 7 seem to substantiate these early SCC CGR determinations. However, the rates measured in test period 8 under cyclic loading is approximately half of that measured under similar conditions in test period 3, suggesting that the preferred crack path is off-plane. Some of the challenges posed by off-plane cracking will be highlighted next. After a favorable location was identified in test periods 14 and 16, and an approximately $2 \times 10^{-10}$ m/s SCC CGR component was estimated by superposition in test period 17 (Fig. 3-59), the specimen was set at constant load in period 18 (Fig. 3-60g). The resulting SCC CGR was approximately $1.8 \times 10^{-11}$ m/s for the first 1000h of this test period, then diminished to approximately $7 \times 10^{-13}$ m/s. At that stage, cycling was reintroduced in test period 19, and it is interesting to note that under cyclic loading the initial measured CGR of $1.2 \times 10^{-9}$ m/s decreases by a factor 5 by the end of the test period (Fig. 3-60h), suggesting that the ligaments that that had formed during the constant load test period were being broken. If the rate of growth in test period 18 is assumed to have been $1.8 \times 10^{-11}$ m/s for the entire test period, the subsequent (remaining) growth in test period 19 still displays a pronounced curvature (Fig. 3-60h), and this shape is atypical of corrosion fatigue growth. Hence, a more conservative approach would have been to assume that growth in test period 18 ended where the CGR in test period 19 stabilizes and reaches the expected value of $2.4 \times 10^{-10}$ m/s, making it consistent with test period 16. In this latter case, the conservative SCC CGR for test period 18 is estimated to be $3.7 \times 10^{-11}$ m/s.

An additional example of SCC growth determination is shown in Fig. 3-60j. As the measured SCC CGR under constant load conditions in the preceding test period 21 was very small,

periodic unloading (8h hold, $CGR_{air} \approx 1x10^{-12}$ m/s) was introduced in test period 22 to investigate whether unbroken ligaments are present or not. The SCC CGR measured initially (first 1,000h) in test period 22 was approximately $9.9x10^{-12}$ m/s, then the growth appeared to stop. In order to re-activate the growth, a somewhat more aggressive loading (2h hold, $CGR_{air} \approx 5x10^{-12}$ m/s) was introduced in test period 23 and the response was similar to that observed at the beginning of test period 22. The fact that a similar rate was measured under two different hold times (8h in period 22, and 2h in period 23) confirms that fatigue is not the dominating driving force for crack growth in this specimen. After another "no growth" measurement under constant load conditions in test period (24), the test in water ended, and that was followed by a final fatigue test period in room temperature air.

It is important to note that while the above seemingly "benign" SCC CGR determinations were made by DC potential, massive SCC was taking place off-plane, in a direction almost normal to the test plane.

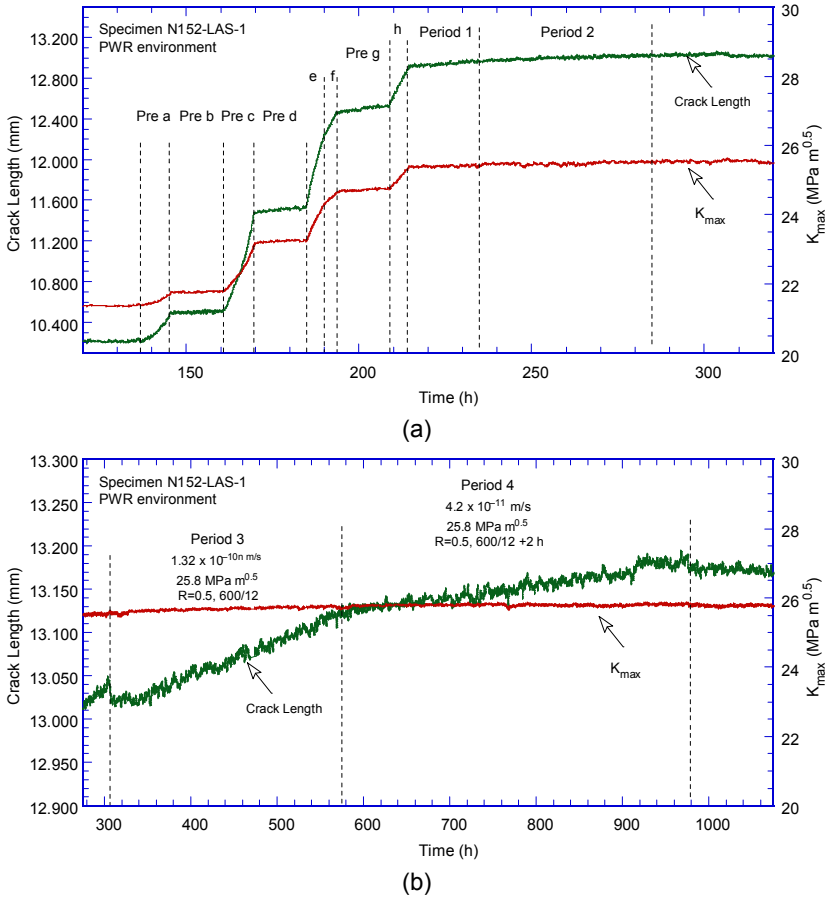


**Figure 3-60 Crack–length–vs.–time for dilution specimen N152-LAS-1 in simulated PWR environment during test periods (a) precracking-2, (b) 3-4, (c) 5, (d)6, (e) 7-10, (f) 11-17, (g) 18, (h) 19-20, (i) 21, (j) 22-23, and (k) 24.**

**Figure 3-60 (Cont.)**

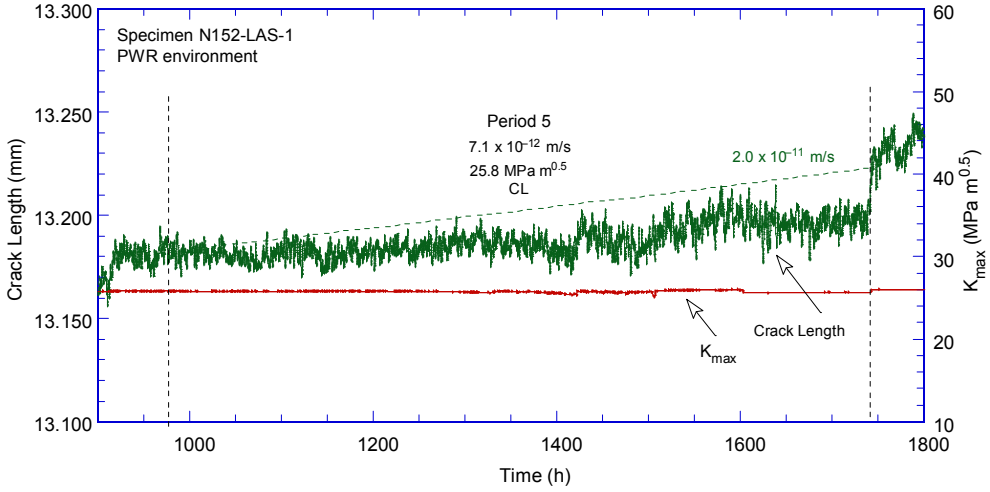


(c)

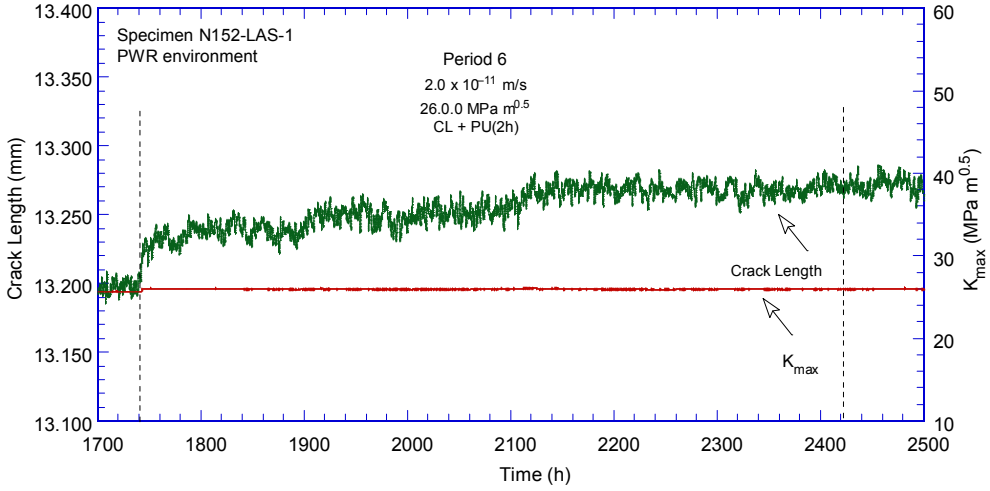


(d)

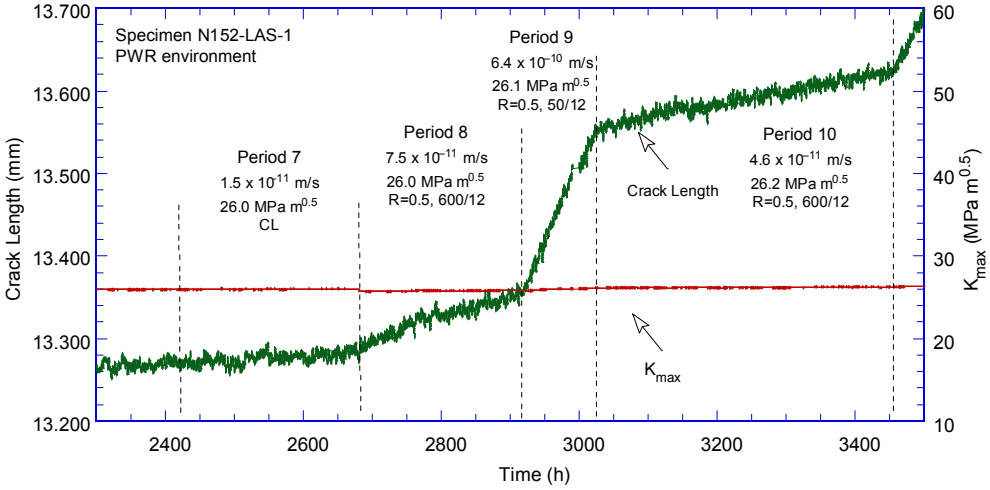


(e)

**Figure 3-60 (Cont.)**

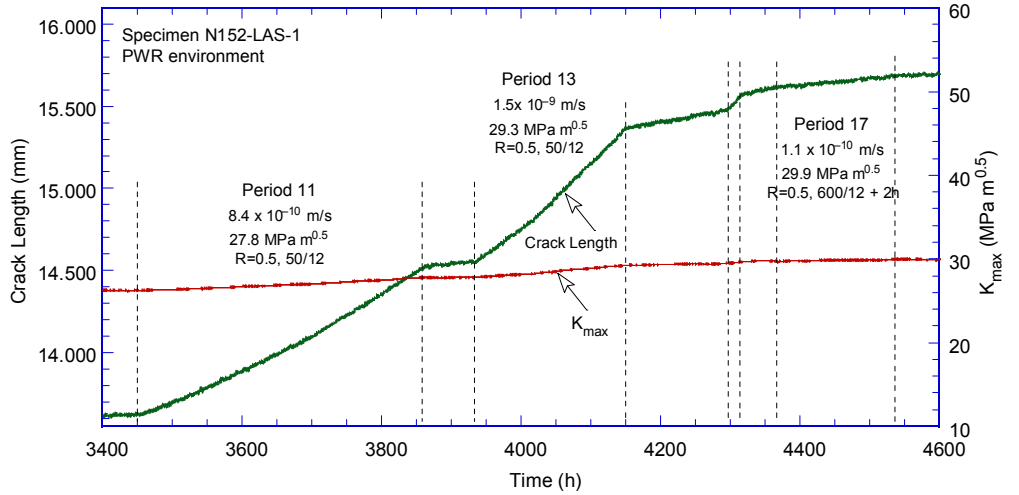


(f)

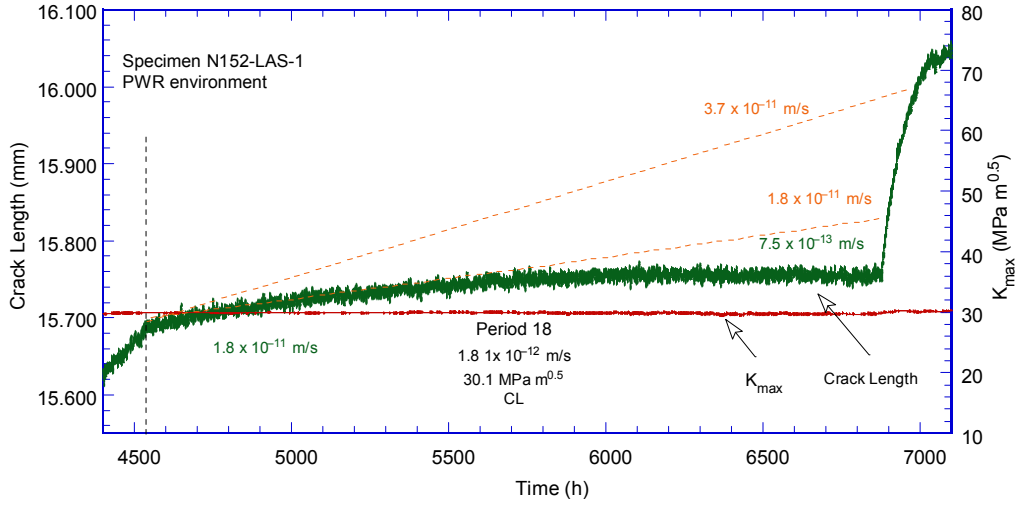


(g)

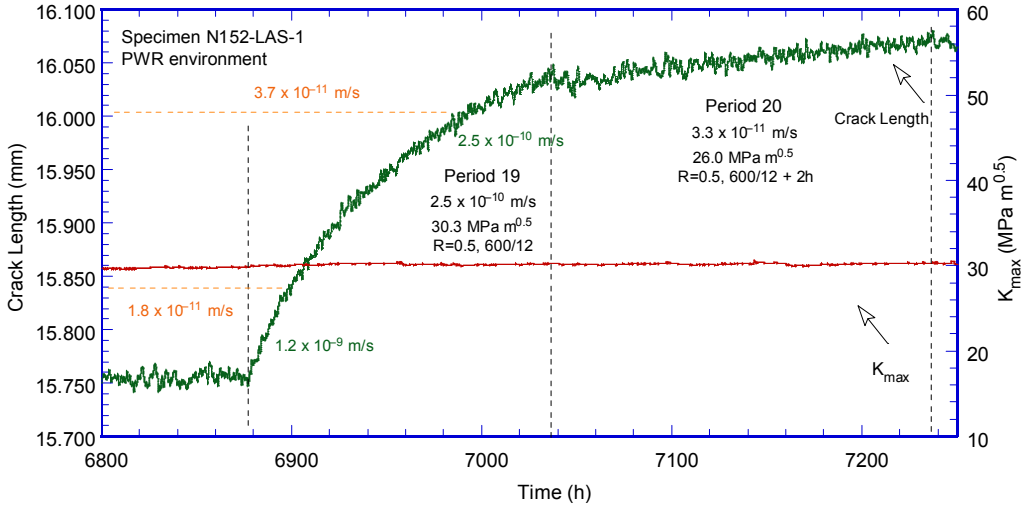


(h)

**Figure 3-60 (Cont.)**

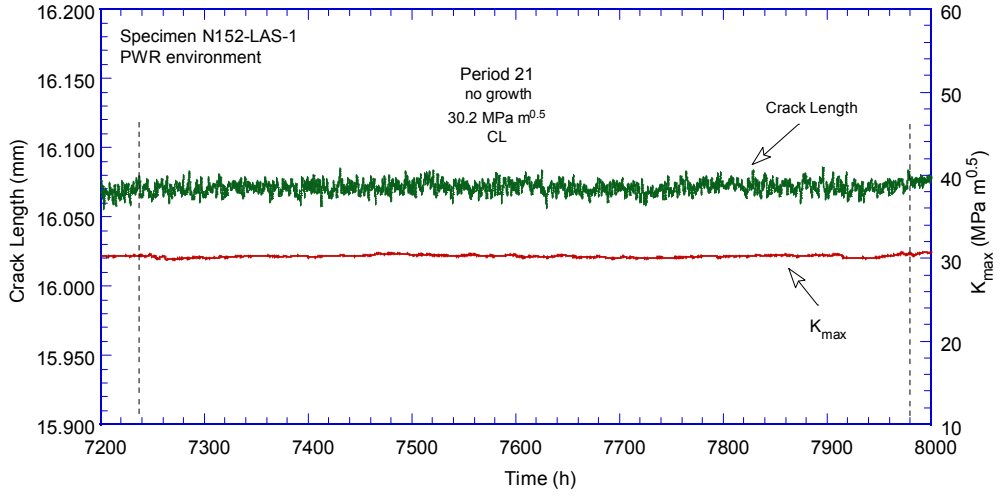


(i)

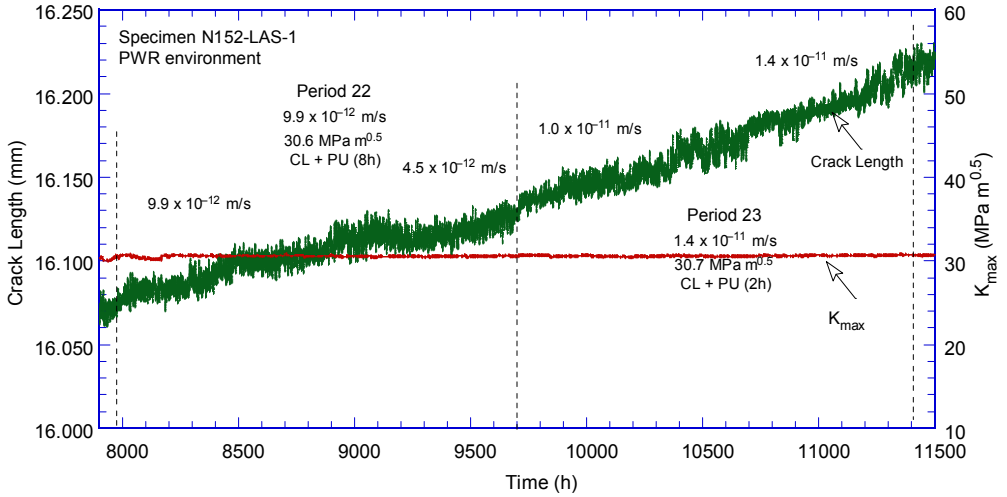


(j)

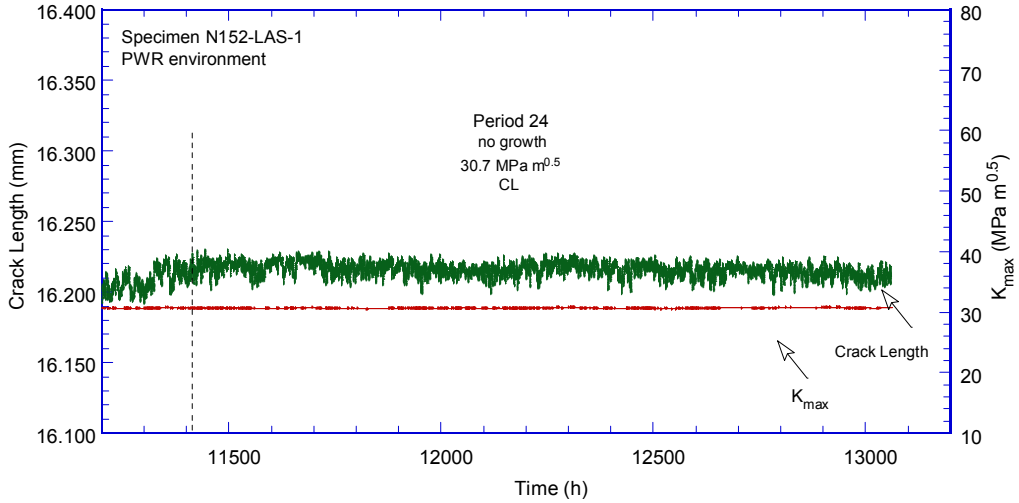


(k)

**Figure 3-60 (Cont.)**

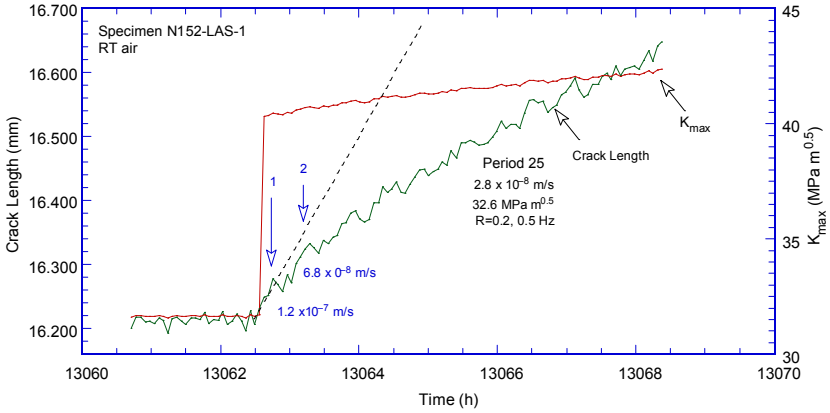


(l)

The post-test examination of specimen N152-LAS-1 involved the examination of both the side surfaces and that of the fracture surface. For the examination of the side surfaces, the side-grooved sections of the specimens were removed by wire cutting, and the resulting flat surfaces were polished and etched electrochemically in a 10% nital solution. Following this exposure, the resulting weld surface was still shiny while the LAS surface became dull. Nevertheless, the outcome (Fig. 3-61) shows that the test went largely as planned (see for comparison Fig. 3-58).

Figures 3-62 and 3-63 are SEM images of the side surfaces. Areas of interest are shown at higher magnification in each figure. As described previously, the crack started from the notch in the LAS, then, upon reaching the Alloy 152 interface, it continued along the interface. Eventually, in both cases, the crack made its way into the weld. The crack hit the LAS interface once more towards the end of the test. This location is marked LAS-i in Fig. 3-62.

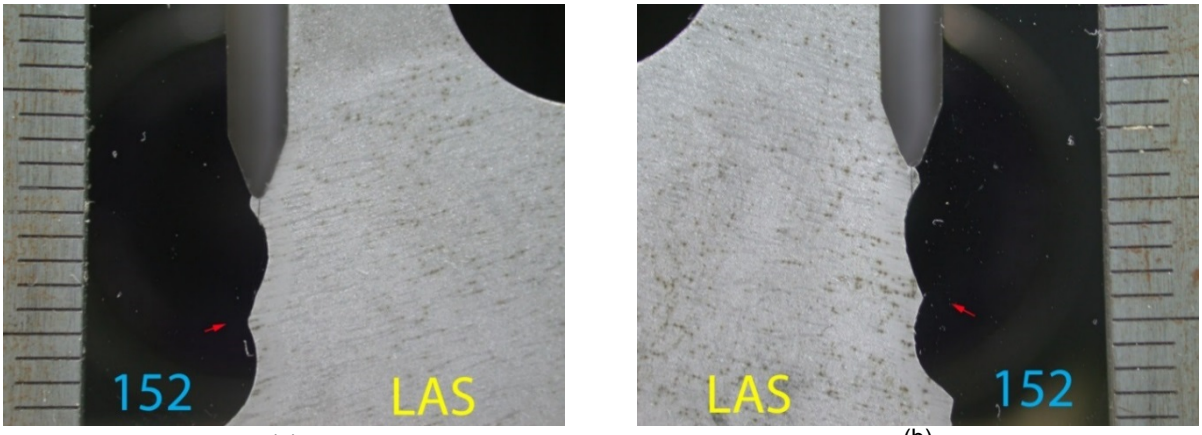


(a) (b)

**Figure 3-61 The two sides of the dilution specimen N152-LAS-1 after testing in primary water: (a) side 1, and (b) side 2. The red arrows indicate the approximate location of the end of the test as determined on the fracture surface. Units of the side rulers are mm.**

As the fracture surface will show later, Figure 3-62 is the best illustration of the evolution of this test. After advancing in the LAS and along the LAS-Alloy 152 interface in fatigue, the crack

turned into the weld, and the first attempts at an SCC CGR measurement were made at location 1 in Fig. 3-62a. The crack appears to follow the direction of the interdendritic grains rather than that of the test plane. The first set of chemical composition measurements were conducted at this location by SEM EDX and yielded an average 27 Cr - 21.4 Fe – 51.5 Ni (Fig. 3-62b). Next, the crack advanced into the weld, intersected the LAS interface one more time (location marked LAS-i), then turned decisively into the weld, and propagated along the direction of the dendritic grains, normal to the original crack direction, shown in Fig. 3-62c. Chemical composition measurements were conducted in this region and yielded an average 24.1 Cr - 31.4 Fe – 43.5 Ni (Fig. 3-62c). The latter measurements confirm that Cr dilution in the first weld layer at least 0.1 mm from the interface with the LAS.

Figure 3-63 shows that on second side, after the initial advance in the LAS and the subsequent propagation in fatigue along the interface, the crack appears to stay mostly on the interface, and enters the LAS at the end of the test during fatigue in room temperature air. The micrograph shown in Fig. 3-63b illustrates crack propagation along the interface under cyclic loading. However, as with the first side surface, the first attempts at an SCC CGR measurement resulted in IG growth into the weld, in a direction normal to the test plane (Fig. 3-63c).

In summary, the two cross sections show that while the LAS-Alloy 152 interface is a preferred path for fatigue crack propagation, it appears to be highly resistant to IG SCC. In fact, in this test, the crack had ample opportunity to propagate along the interface, but turned towards the weld each time transitioning to IG SCC was attempted. These observations are consistent with those generated within a co-operative research program between the Fracture & Reliability Research Institute (FRI) at Tohoku University and Paul Scherrer Institute (PSI) [26, 27]. In that program, the objective was to determine whether a fast growing IG SCC crack in the highly susceptible Alloy 182 weld metal can easily cross the fusion line and significantly propagate into the adjacent low-alloy RPV steel. The outcome of that research was that in high-purity or sulphate-containing oxygenated water under constant or periodic partial unloading conditions, IG SCC growth was arrested whenever it reached the LAS fusion line. The authors further speculated that a similar outcome was to be expected in PWR water because of the very low SCC and moderate corrosion fatigue susceptibilities of LAS at low ECP. While the results from the current test already seem to confirm that expectation, they will be substantiated further during the examination of the fracture surface.

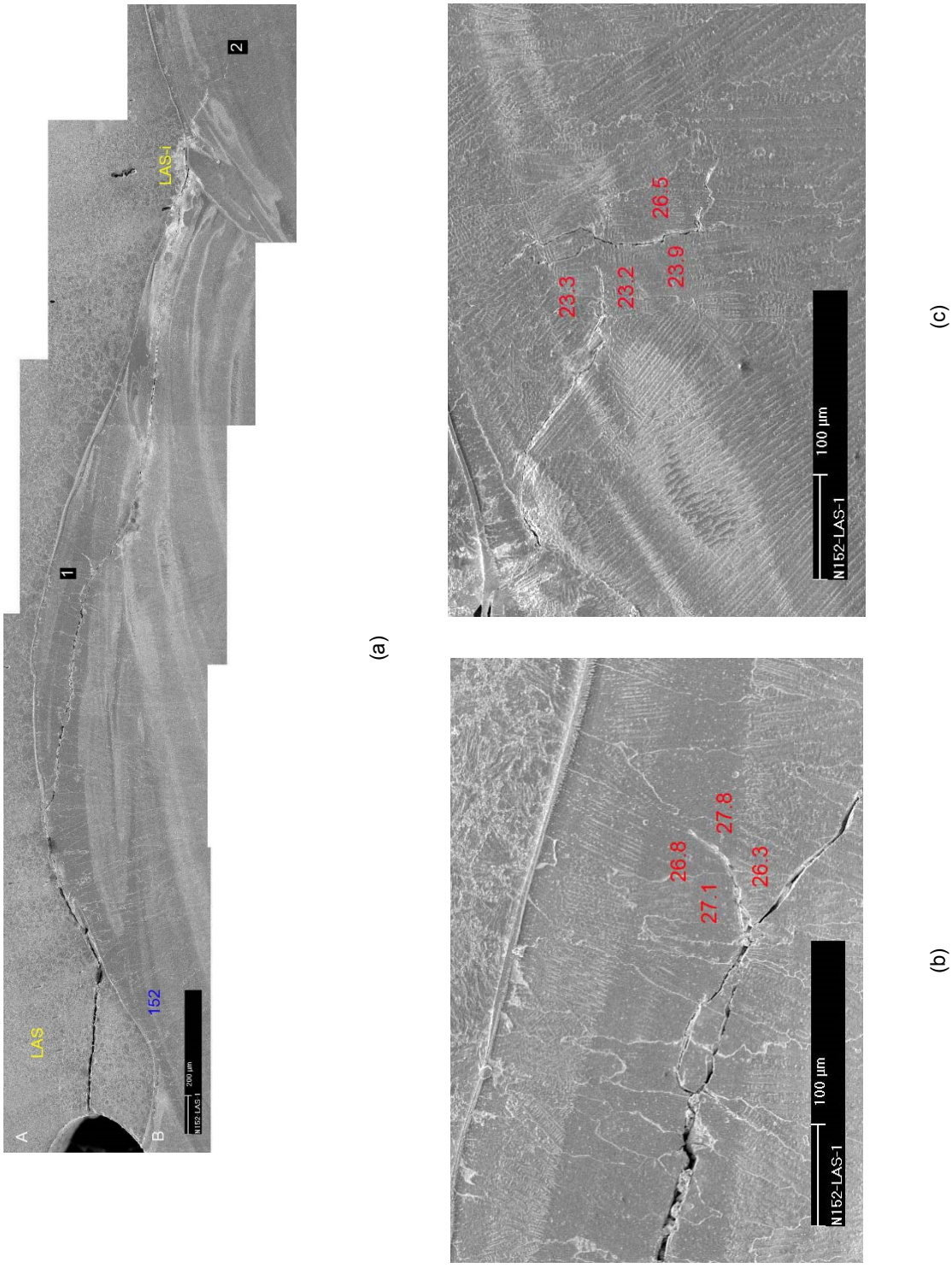


**Figure 3-62** **(a) Cross section 1 of Specimen N152-LAS-1, (b) detail at location 1 in (a), and (c) detail at location 2 in (a). The local Cr concentration is shown in red. Crack advance is from left to right.**

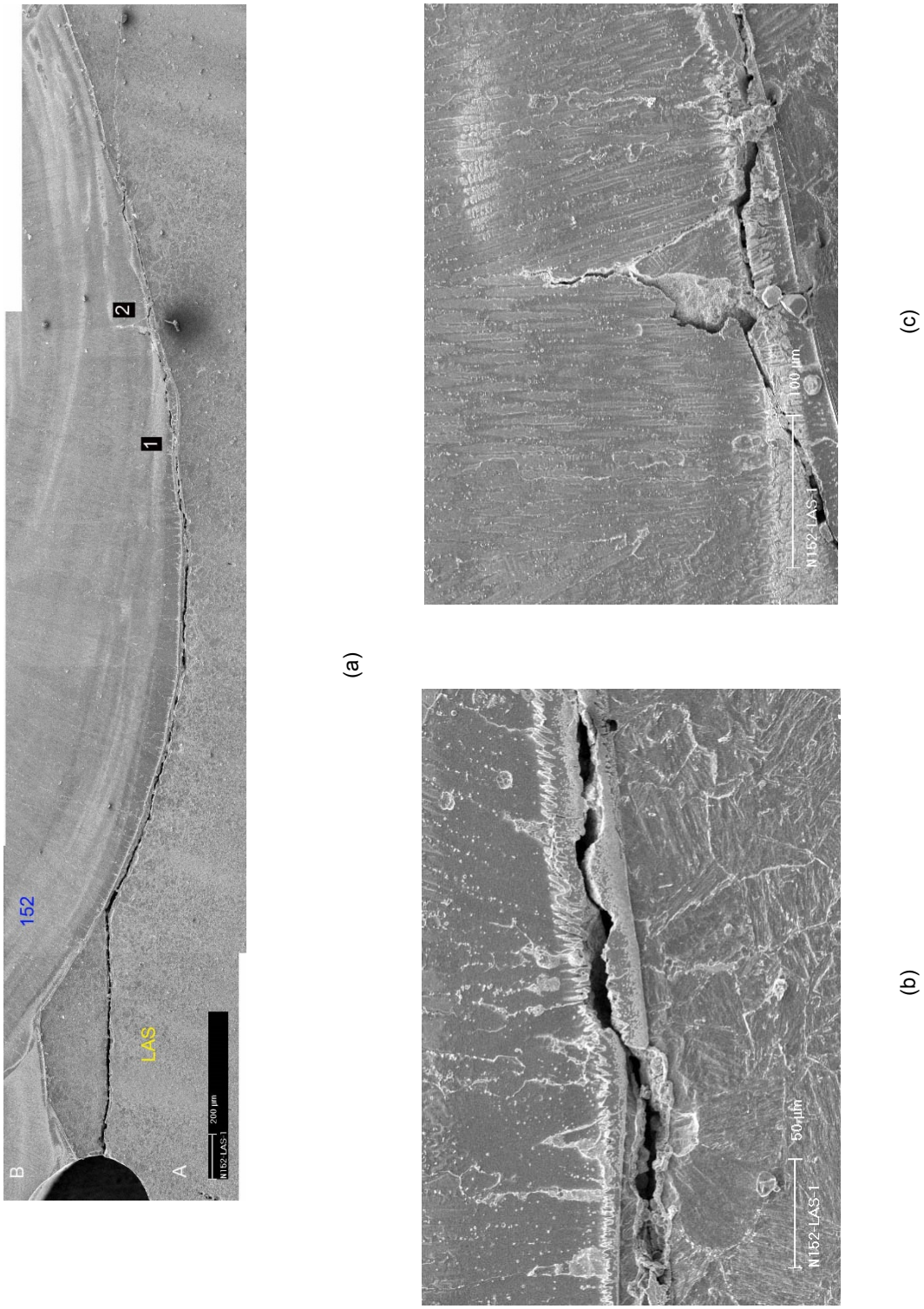


**Figure 3-63 (a) Cross section 2 of Specimen N152-LAS-1, (b) detail at location 1 in (a), and (c) detail at location 2 in (a). Crack advance is from left to right.**

Next, the specimen was broken open to allow for the examination of the fracture surface. This is shown in Fig. 3-64, and the major landmarks of the test are indicated in the figure. As described previously (Fig. 3-62), the crack started in the LAS, propagated along the interface and into the weld (note that there is no difference in appearance between the interface and the weld), and the first set of SCC CGR determination were made at location IG-1. Then, the crack was advanced through the weld, transitioned to IG SCC, hit the LAS interface again at location marked LAS-i, then continued its advance in an IG/interdendritic mode in the weld, IG-2. Rather large ligaments were observed on the left hand side of the fracture surface that developed during fatigue and corrosion fatigue propagation through the weld. It should be noted that in Fig. 3-64, the fracture surface was photographed slightly tilted to show the full extent of IG-2 and ligaments (marked with red arrows) that developed in that region.

Measurements performed on the un-tilted the fracture surface yielded an overall crack advance measurement error of 39%, and because ligaments have been observed in all stages of the test, this correction was applied uniformly along the DC potential data set. However, it is important to observe that especially in the tilted photograph (Fig. 3-64), the extent of IG-2 appears to be approximately 5 times higher than the crack advance of 0.3 mm measured by DC potential for this region where the crack propagated off-plane. Hence, one conservative way to evaluate the SCC CGR for this entire region would be to simply divide the full extent of the crack by the time, and obtain approximately $5 \times 10^{-11}$ m/s.

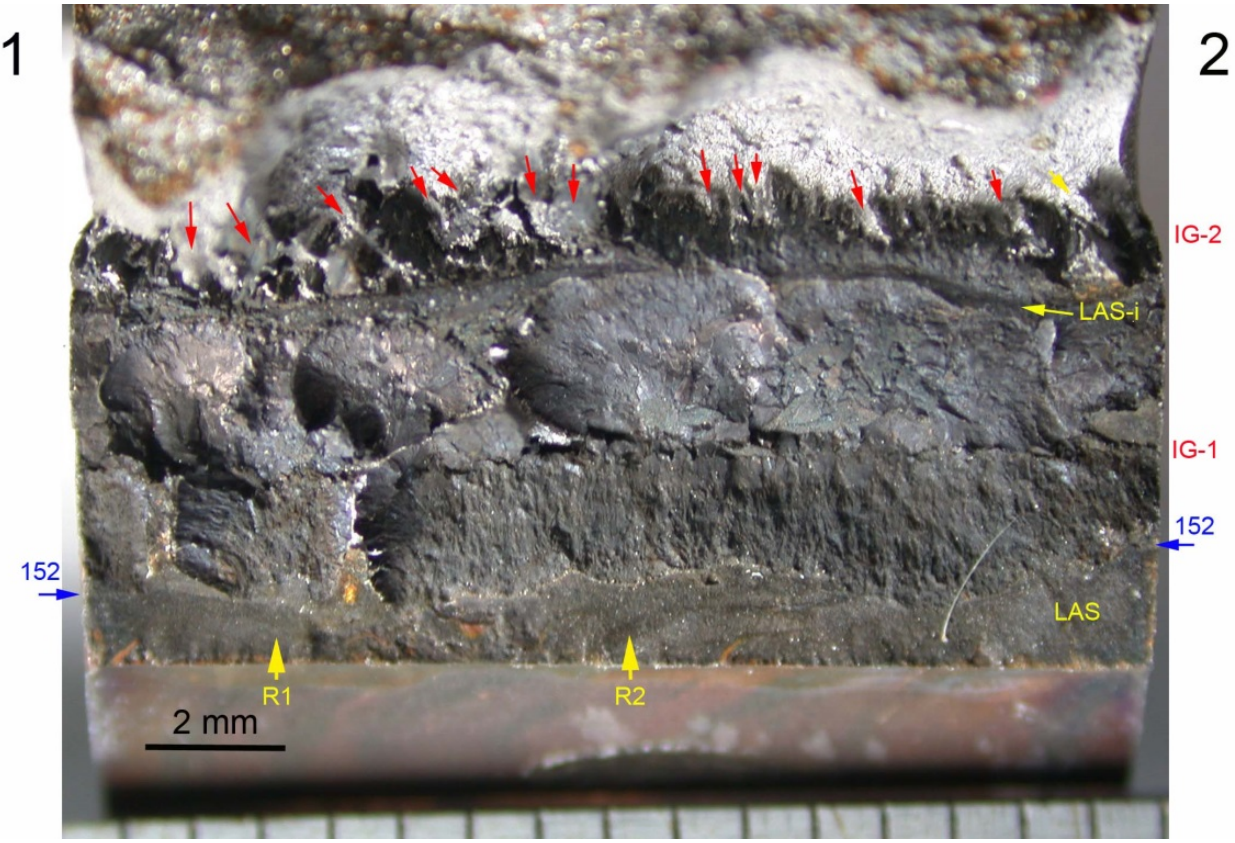


**Figure 3-64 Fracture surface (A, Fig. 3-63) of specimen N152-LAS-1 tilted to show the final IG region. Two regions of interest, R1 and R2 are marked in the figure. Crack advance is from bottom to top.**

Figure 3-64 identifies two areas of interest, R1 and R2, and these will be discussed next. Figure 3-65 shows the image obtained in region R1 of Fig. 3-64. This image shows the ligaments that developed in the weld, in the close proximity to the LAS interface during the fatigue and corrosion fatigue stages of the test. Two additional locations of interest are further identified: IG-1 (location 1) and the second intersection of the crack with the LAS interface (location 2), labeled LAS-i. These are shown at higher magnification in Fig. 3-66. In region IG-1, the crack propagated mostly off-plane – and it appears mostly like a line in Fig. 3-64. At location 1 in Fig. 3-65, the geometry is further complicated by the presence of the weld ligaments. Nevertheless, Fig. 3-66a shows a mixed IG and TG fracture mode with quite prevalent secondary IG cracking. It is important to note that wherever the IG cracking is in the plane of the test, the dendritic features are normal to it. Figure 3-66b focuses on the crack intersection with the LAS at location 2 in Fig. 3-65. One observes that what appears to be a fully engaged IG crack in the weld does not propagate into the LAS, and somehow manages to continue as an IG crack in the weld only after it reaches the weld material again at the top of the picture.

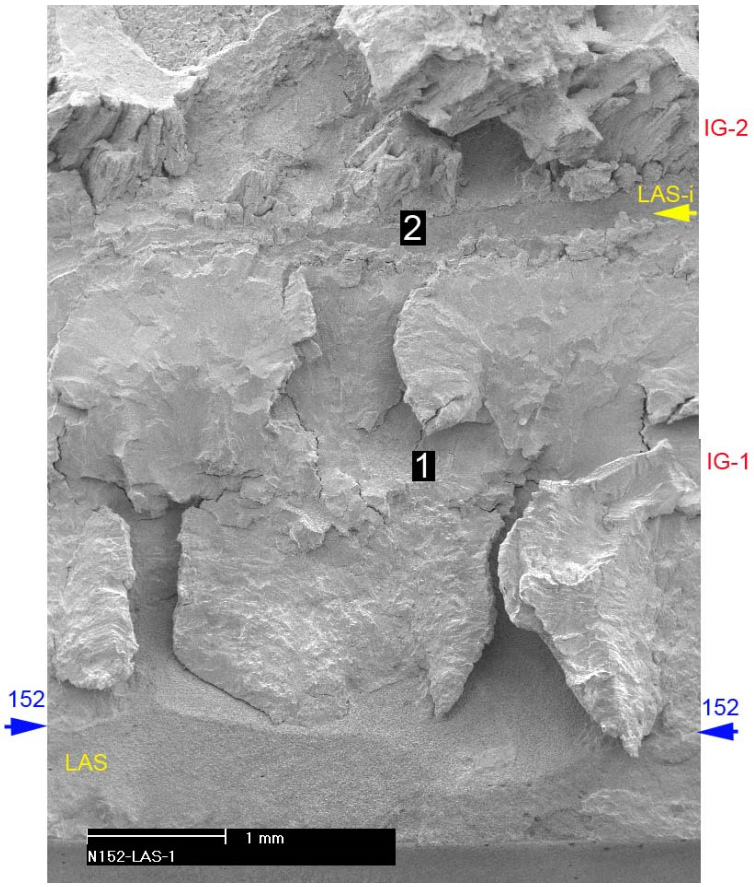


**Figure 3-65 Region R1 on the fracture surface A of specimen N152-LAS-1 (Fig. 3-64). Blue arrows indicate the transition from LAS to Alloy 152, and two additional locations of interest: IG-1 (location 1) and the second intersection of the crack with the LAS interface (location 2), labelled LAS-i. Crack advance is from bottom to top.**

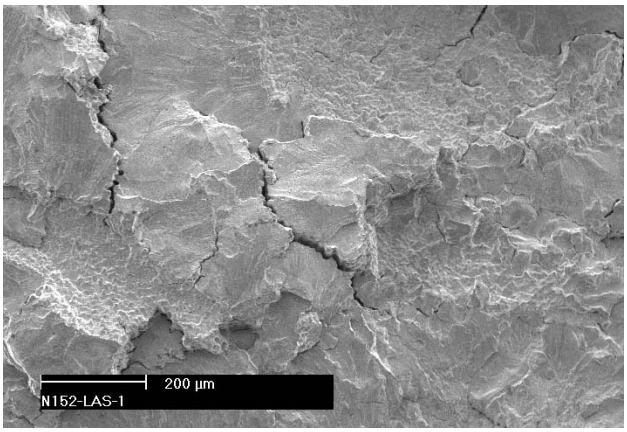


(a)

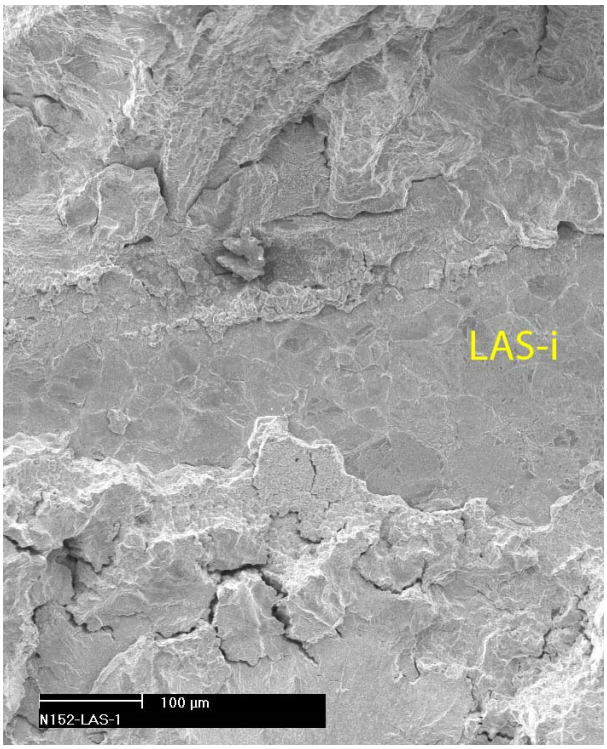


(b)

**Figure 3-66 Fracture surface of specimen N152-LAS-1, locations: (a) 1, and (b) 2 in region R1, Fig. 3-65. Crack advance is from bottom to top.**

Figure 3-67 shows an image obtained in region R2 of Fig. 3-64. Unlike region R1 (Fig. 3-65), the weld ligaments formed during the fatigue and corrosion fatigue stages of the test are less prominent. Two additional locations of interest, IG-1 (location 1) and the second intersection of the crack with the LAS interface (location 2), labeled LAS-i, are indicated in the picture. These locations are shown at higher magnification in Fig. 3-68. In region IG-1, while the crack propagated mostly off-plane, secondary cracks as well as a somewhat uniform IG/interdentritic mode can be observed, Fig. 3-68a. Again, it is important to note that the dendritic features are normal to the test plane. Figure 3-68b focuses on the intersection with the LAS at location 2 in Fig. 3-67. Again, one observes that what appears to be a fully engaged IG crack in the weld is essentially arrested at the LAS, and continues as an IG crack in the weld after it reaches the weld again at the top of the picture. Such areas would have likely remained as un-broken ligaments if the crack was not advanced under gentle cyclic loading.

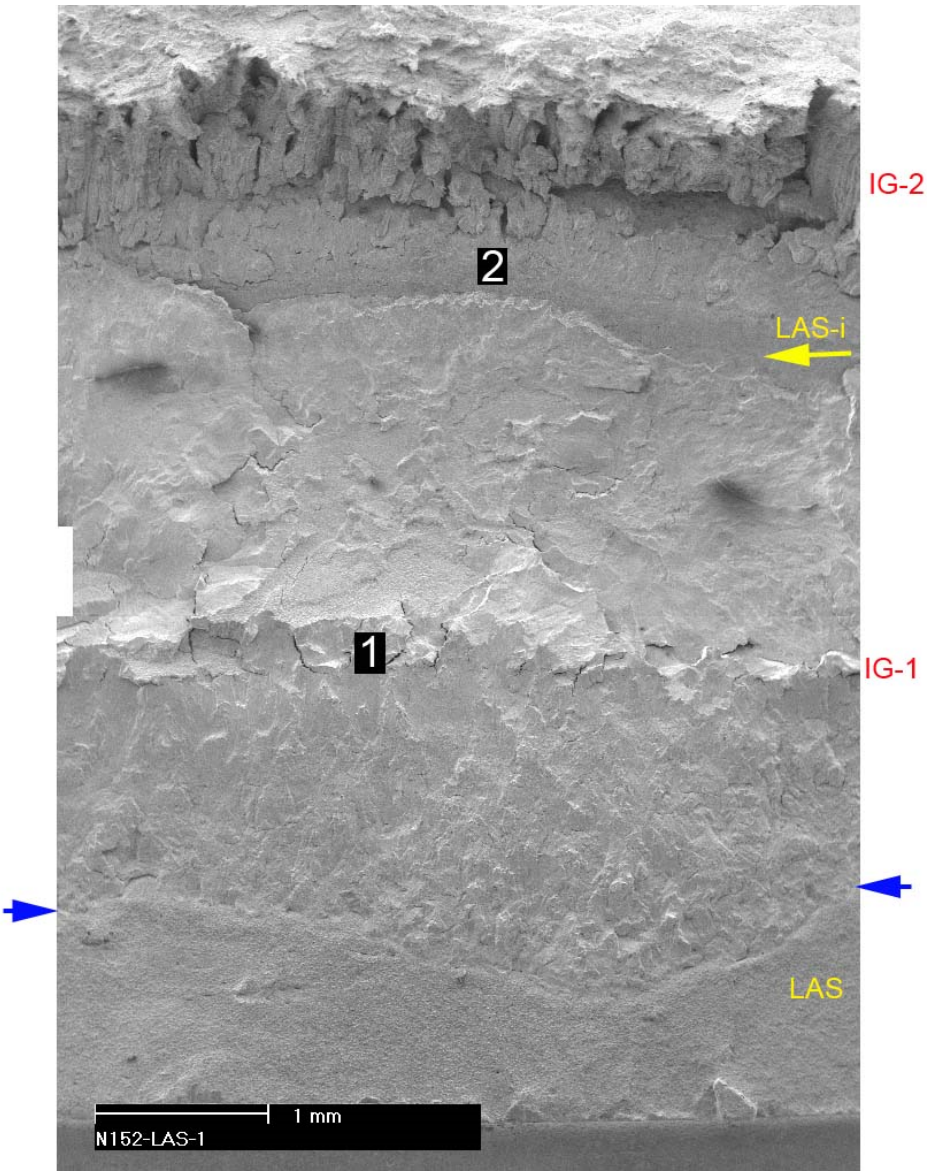


**Figure 3-67** **Region R2 on the fracture surface A of specimen N152-LAS-1 (Fig. 3-64). Blue arrows indicate the transition from LAS to Alloy 152, and two additional locations of interest: IG-1 (location 1) and the second intersection of the crack with the LAS interface (location 2), labelled LAS-i. Crack advance is from bottom to top.**

Figures 3-69 and 3-70 focus on region IG-2 (Fig. 3-64), and in order to show some detail, the fracture surface was broken down into two halves. Areas of interest are identified in both pictures. As such, Fig. 3-69b shows the IG interdendritic cracking observed at location 1 in Fig. 3-69a, and Fig. 3-69c focuses on a large ligament observed at location 2, also in Fig. 3-69a. Figure 3-69a also indicates the interaction between the crack and the LAS interface, e.g., L1 and L2. As noted previously, one observes that what appears to be a fully engaged IG crack in the weld does not propagate into the LAS, but manages to continue as an IG crack in the weld after it reaches the

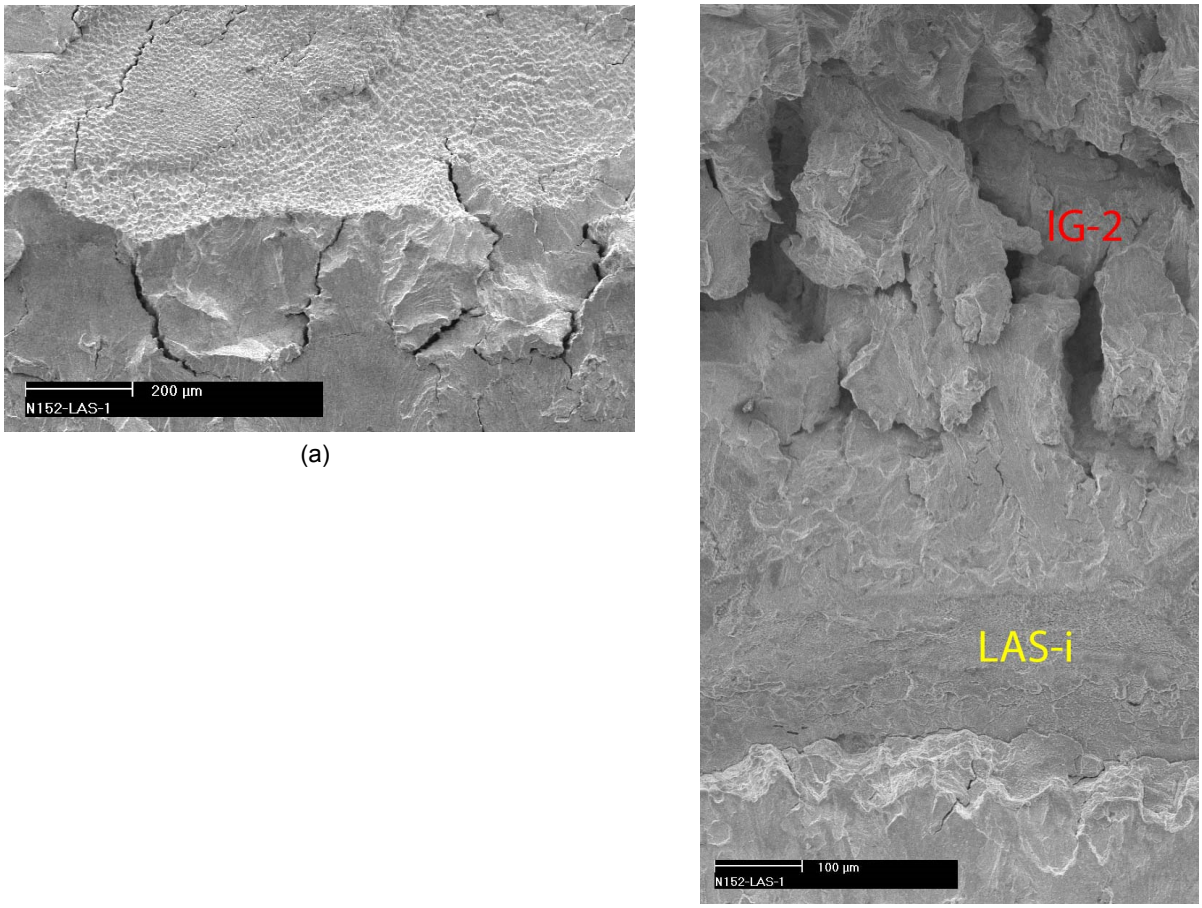


(a) (b)

**Figure 3-68 Fracture surface of specimen N152-LAS-1, locations: (a) 1, and (b) 2 in region R2, Fig. 3-67. Crack advance is from bottom to top.**

weld again at the top of the picture. As described previously, it is likely that this area would have remained as an un-broken ligament if not for the cyclic loading. Likewise, Fig. 3-70 shows the second half of region IG-2 (Fig. 3-64). Figure 3-70b shows the IG interdendritic cracking observed at location 3 in Fig. 3-70a, and Fig. 3-70c focuses on a large ligament and surrounding IG cracking observed at location 4 in Fig. 3-70a. Overall, the fracture mode in the IG-2 region was almost completely IG. However, as noted previously, the direction of propagation was off-plane, and, hence, there should be no surprise that the DC potential recorded very low or "no growth" SCC CGRs.

In summary, the conclusions and, more importantly, the "lessons learned" from the first test are as follows: the Cr-diluted Alloy 152 butter is susceptible to SCC, the IG fracture mode was found to occur readily, and the measured SCC rates are high enough to warrant further investigation. However, cracking tends to occur off-plane, hence, constant load should follow quickly once a "susceptible" region is identified. This could be accomplished by eliminating the test periods with a hold. Also, consistent with similar observations from the literature [26, 27], the LAS and LAS-weld interface appears to be resistant to IG SCC as no evidence of IG cracking was found at the LAS interface or in the LAS despite ample opportunity. As such, in order to avoid crack arrest at the LAS-152 interface, future specimens should be aligned further away from the Alloy 152-LAS interface.

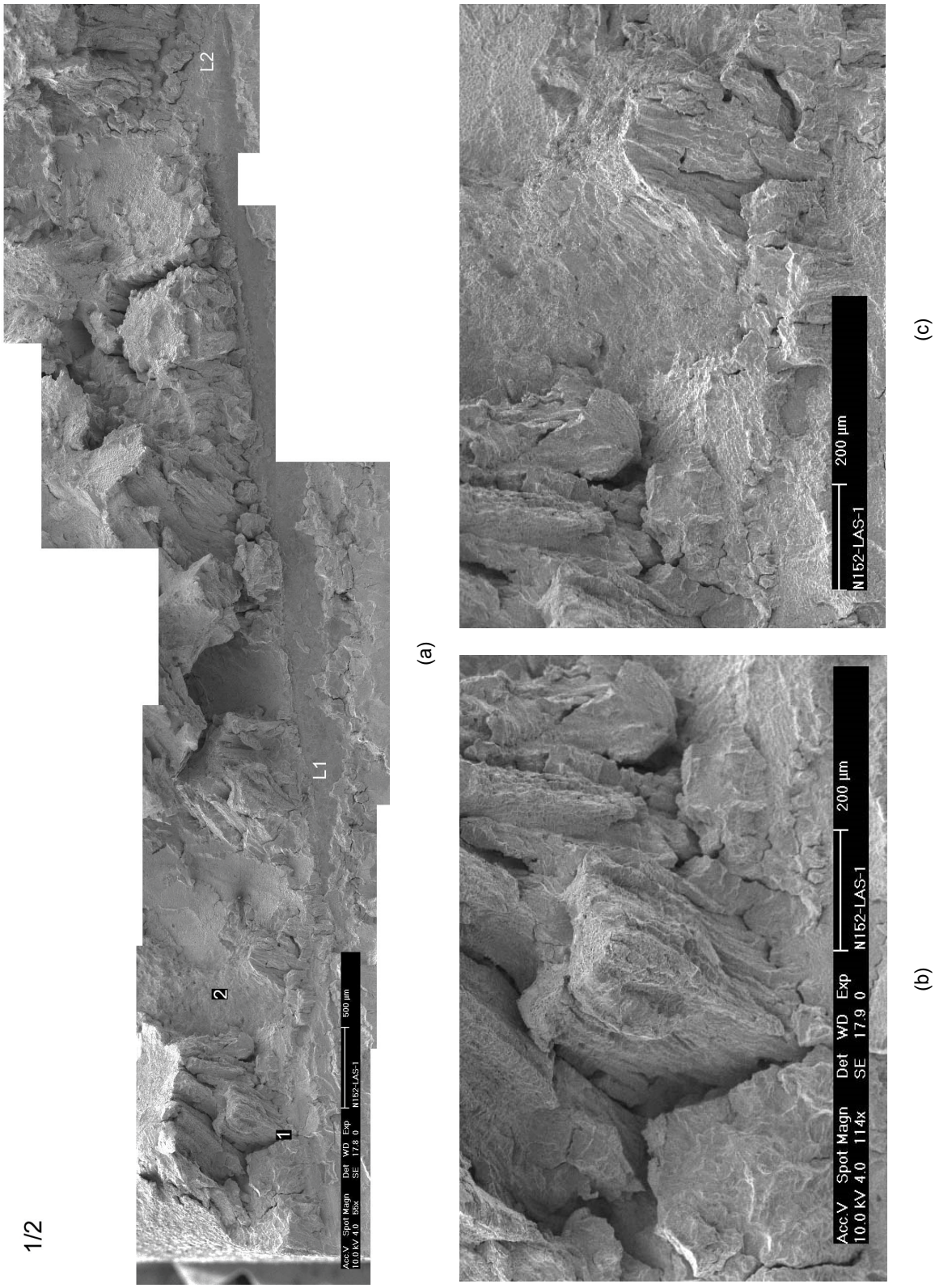


**Figure 3-69** **Fracture surface of N152-LAS-1, region IG-2 (Fig. 3-64): (a) first half of the fracture surface, (b) detail at location 1, and (c) detail at location 2. Crack advance is from bottom to top.**

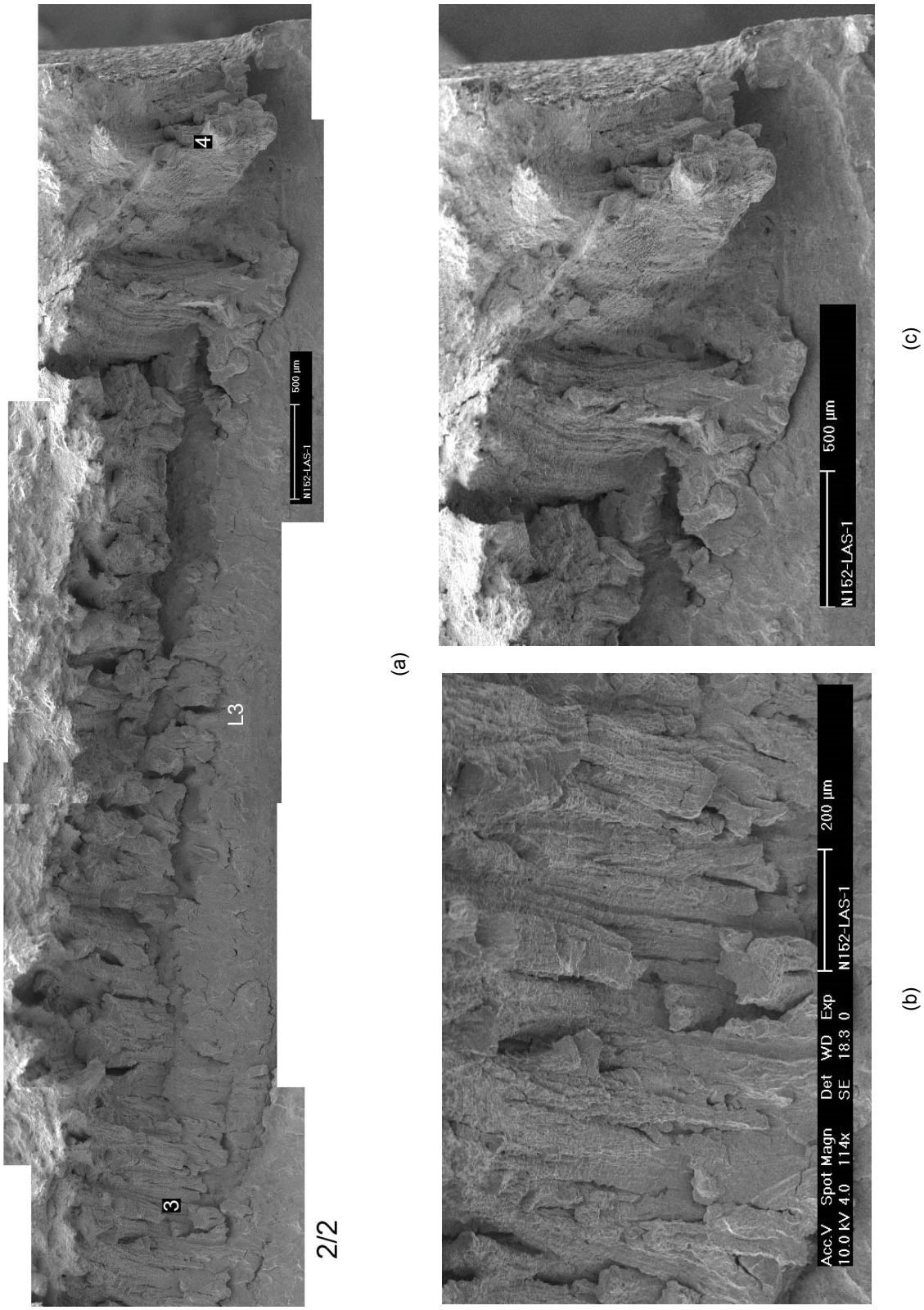


**Figure 3-70** **Fracture surface of N152-LAS-1, region IG-2 (Fig. 3-64): (a) second half of the fracture surface, (b) detail at location 3, and (c) detail at location 4. Crack advance is from bottom to top.**

### 3.2.2 SCC CGR Test on 1st Layer Alloy 152 Weld Butter Specimen N152-LAS-11

Specimen N152-LAS-11 was cut from the same general area as the prior specimen, and the notch location was perhaps two weld beads removed from that of specimen N152-LAS-1, Fig. 3-71. The specimen arrangement shown in Fig. 3-71 was chosen because it allowed for two test specimens to be machined from the same piece of material. However, the positioning of the N152-LAS-11 specimen with respect to the weld-LAS interface benefitted from the "lessons learned" in the first test. As such, in order to avoid crack interaction and arrest at the Alloy 152-LAS interface, the notch of Specimen N152-LAS-11 was still machined in the 1st layer of Alloy 152 weld, but further away from the interface with the LAS, Fig. 3-72.

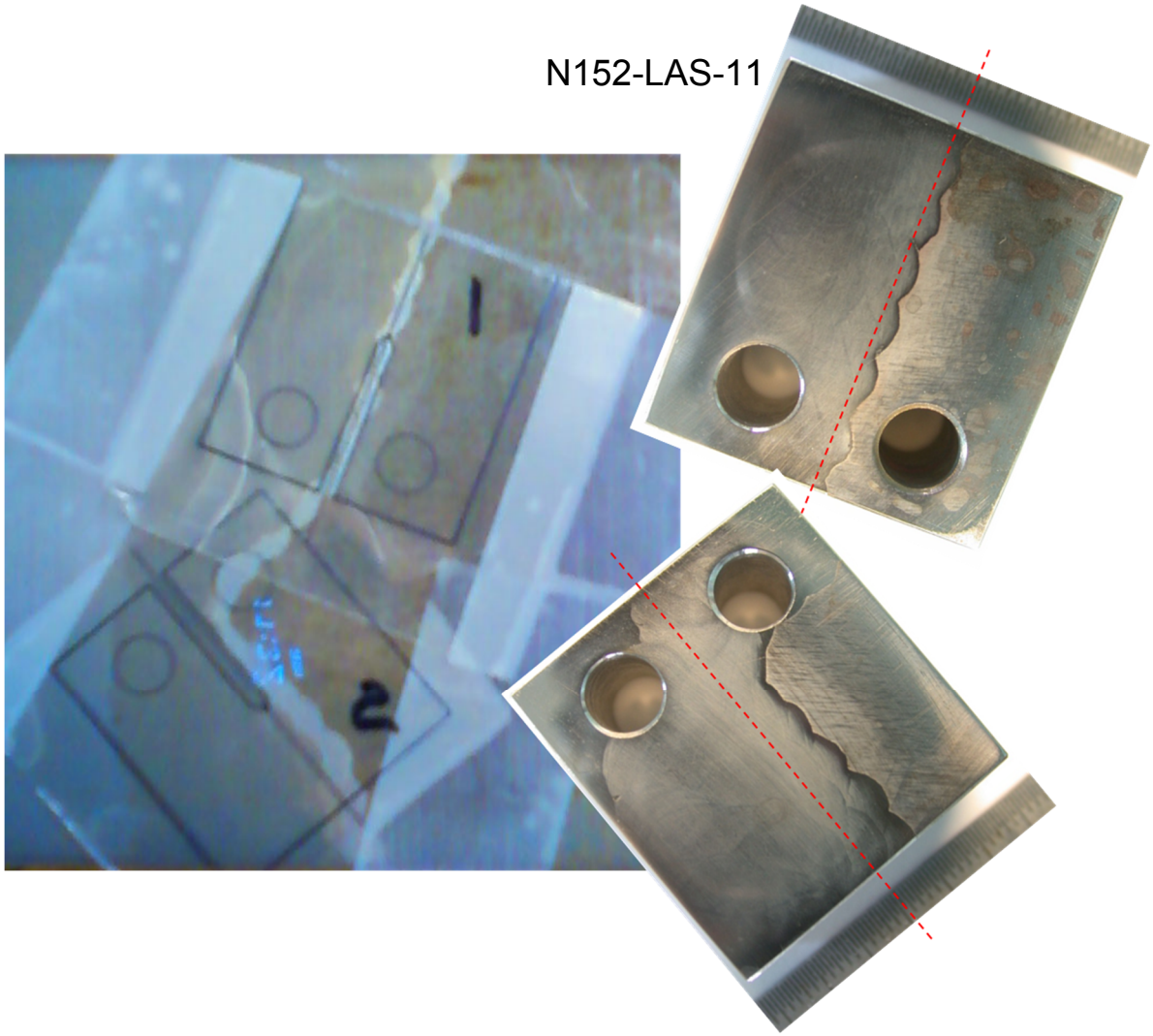


**Figure 3-71 Approximate locations of the CT specimen blanks for first layer and second layer weld butter SCC CGR testing. The specimen blank that will later become CT test specimen N152-LAS-11 is indicated in the figure.**

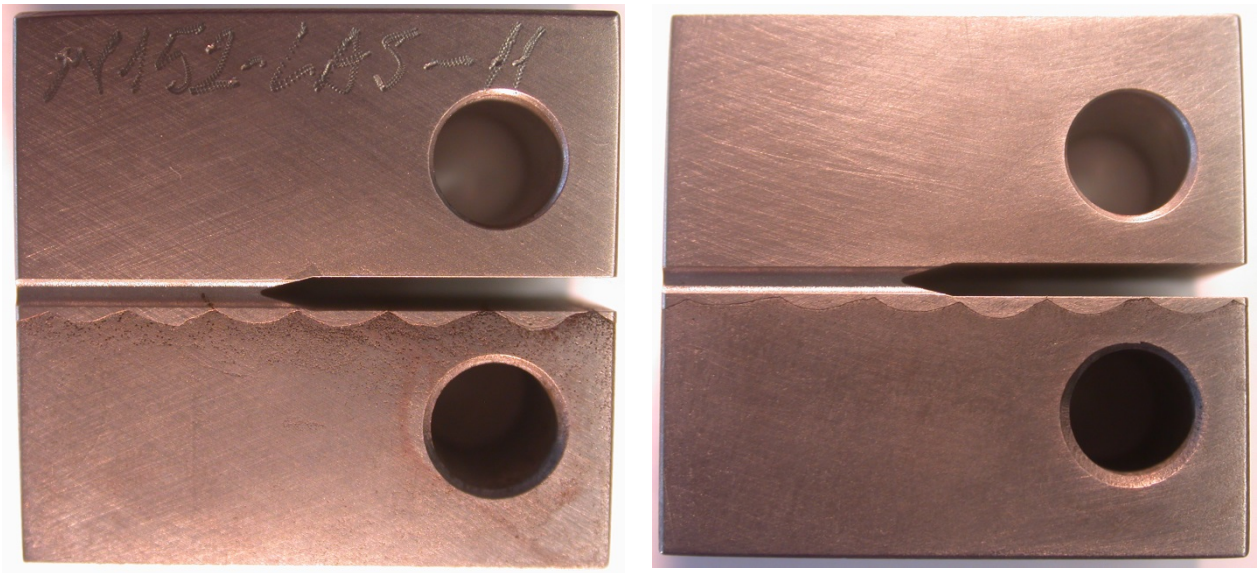

(a) (b)

**Figure 3-72 The two sides of specimen N152-LAS-11 prior to the SSC test: (a) side 1, and (b) side 2. Alloy 152 is in the top half, and the LAS is in the bottom half of both pictures.**

The test on specimen N152-LAS-11 was initiated with precracking in the PWR environment, followed by transitioning. The testing conditions are given in Table 3-7, and a visual representation of the test in the framework described previously is shown in Fig. 3-73. As before, the plots tracks the environmental enhancement of two loading conditions – rise 50s and rise 600s, R = 0.5 – vs. crack advance from the notch. The purpose of the fast cycle is to advance the crack, and the purpose of the slow cycle is to probe for environmental enhancement. The dotted red and blue horizontal lines represent the enhancement levels of a forward advancing crack based on the prior Alloy 152 experience (Fig. 2-10). The changes in crack length and $K_{max}$ vs. time are shown in Fig. 3-74.

Early data (Fig. 3-73) seem to show an environmental enhancement exceeding the highest that was observed in the N152-LAS-1 specimen (and in the Alloy 152 tested previously, Fig. 2-10), hence, the current specimen was set at constant load fairly early in test period 4. Upon measuring a small SCC CGR, the cyclic routine was repeated, allowing more time in test period 6 to assess the SCC CGR component. Based on superposition in test periods 5 and 6, this was calculated to be $1.7 \times 10^{-12}$ m/s. The rate was next measured at constant load in test period 7 and was found to be indeed very small, $1.4 \times 10^{-12}$ m/s. Subsequent cycling in test period 8 found significantly less environmental enhancement (Fig. 3-73). The dramatic drop in cyclic response suggests that SCC occurred off-plane, and the SCC CGR measurements conducted in the interim are perhaps of little significance.

Next, the crack was advanced incrementally using the fast/slow loading conditions described previously, monitoring the environmental enhancement in an attempt to identify another “SCC-susceptible” microstructure. A condition yielding comparable enhancement to that resulting in a $1.81 \times 10^{-11}$ m/s SCC CGR in the prior test was identified in test period 27. Next, the test was converted directly to constant load in test period 28, assuming that the more susceptible material was at that point still ahead of the crack. The test ended after approximately 2,700h in this condition resulting in approximately 1.4 mm of growth (after a factor 10 correction based on

the fracture surface was applied to the DC potential data). One notes that following this large correction factor applied uniformly, the $K_{max}$ for test period 18 became almost 38 MPa $m^{0.5}$. This is likely highly overestimated because - as the fractography will later show – large unbroken ligaments "shielded" the crack tip. While the average SCC CGR was approximately $1.4x10^{-10}$ m/s, the rate was observed to accelerate locally to rates as high as $3.1x10^{-10}$ m/s, and slow down to rates as low as $4.0x10^{-11}$ m/s, Fig. 3-74i. In summary, there are two regions in this specimen (test periods 7-14 and 28) with SCC CGRs differing by a factor 100, and the subsequent post-test examination will have to elucidate the reason for the difference.

**Table 3-7 Crack growth data for Alloy 152 dilution specimen N152-LAS-11 in PWR water[a,b,c]**

| Test Period | Test Time, h | Temp. °C | Load Ratio R | Rise Time, s | Down Time, s | Hold Time, s | $K_{max}$, MPa·$m^{1/2}$ | ΔK, MPa·$m^{1/2}$ | $CGR_{env}$, m/s | Estimated $CGR_{air}$,[b] m/s | Crack Length, mm |
|---|---|---|---|---|---|---|---|---|---|---|---|
| Pre a | 55 | 320.0 | 0.30 | 1 | 0.5 | | 22.8 | 15.9 | 2.26E-08 | 8.75E-08 | 11.784 |
| Pre b | 71 | 320.0 | 0.30 | 50 | 50 | | 22.9 | 16.0 | 1.24E-09 | 8.98E-10 | 11.819 |
| Pre c | 74 | 319.8 | 0.30 | 1 | 0.5 | | 23.5 | 16.5 | 5.17E-08 | 1.00E-07 | 12.029 |
| 1 | 78 | 320.5 | 0.50 | 50 | 12 | | 23.5 | 11.7 | 8.74E-10 | 4.33E-10 | 12.043 |
| 2 | 143 | 319.9 | 0.50 | 600 | 12 | | 23.6 | 11.8 | 1.41E-10 | 3.66E-11 | 12.076 |
| 3 | 176 | 319.9 | 0.50 | 600 | 12 | 7,200 | 23.6 | 11.8 | 2.43E-11 | 2.83E-12 | 12.084 |
| 4 | 493 | 320.0 | 1.00 | 0 | 0 | | 23.7 | 0.0 | 5.34E-12 | - | 12.095 |
| 5 | 504 | 320.1 | 0.50 | 600 | 12 | | 23.8 | 11.9 | 1.60E-10 | 3.76E-11 | 12.104 |
| 6 | 912 | 320.1 | 0.50 | 600 | 12 | 7,200 | 23.8 | 11.9 | 1.89E-11 | 2.92E-12 | 12.131 |
| 7 | 1,442 | 320.1 | 1.00 | 0 | 0 | | 23.7 | 0.0 | 1.47E-12 | - | 12.131 |
| 8 | 1,488 | 320.1 | 0.50 | 600 | 12 | | 23.6 | 11.8 | 9.78E-11 | 3.65E-11 | 12.145 |
| 9 | 2,067 | 320.1 | 0.50 | 600 | 12 | 7,200 | 23.5 | 11.8 | 1.42E-11 | 2.78E-12 | 12.181 |
| 10 | 3,026 | 320.1 | 1.00 | 0 | 0 | | 23.8 | 0.0 | 1.25E-12 | - | 12.189 |
| 11 | 3,864 | 320.0 | 0.50 | 12 | 12 | 14,400 | 24.0 | 12.0 | 3.67E-12 | 1.64E-12 | 12.204 |
| 12 | 3,888 | 320.1 | 0.50 | 600 | 12 | | 26.9 | 13.4 | 1.68E-10 | 6.26E-11 | 12.216 |
| 13 | 4,009 | 320.2 | 0.50 | 600 | 12 | 7,200 | 27.0 | 13.5 | 2.81E-11 | 4.90E-12 | 12.233 |
| 14 | 5,713 | 320.1 | 0.50 | 12 | 12 | 28,800 | 27.3 | 13.6 | 4.87E-12 | 1.38E-12 | 12.265 |
| 15 | 6,025 | 320.2 | 0.50 | 600 | 12 | - | 27.6 | 13.8 | 1.20E-10 | 6.98E-11 | 12.374 |
| 16 | 6,049 | 320.1 | 0.50 | 50 | 12 | | 27.8 | 13.9 | 1.23E-09 | 8.63E-10 | 12.458 |
| 17 | 6,239 | 320.2 | 0.50 | 600 | 12 | | 28.3 | 14.2 | 1.50E-10 | 7.76E-11 | 12.560 |
| 18 | 6,287 | 320.2 | 0.50 | 50 | 12 | | 27.9 | 14.0 | 1.13E-09 | 8.77E-10 | 12.700 |
| 19 | 6,365 | 320.3 | 0.50 | 600 | 12 | | 28.2 | 14.1 | 1.53E-10 | 7.61E-11 | 12.742 |
| 20 | 6,408 | 320.1 | 0.50 | 50 | 12 | | 28.2 | 14.1 | 1.54E-09 | 9.08E-10 | 12.901 |
| 21 | 6,528 | 320.2 | 0.50 | 600 | 12 | | 28.7 | 14.3 | 1.84E-10 | 8.13E-11 | 12.982 |
| 22 | 6,550 | 320.3 | 0.50 | 50 | 12 | | 29.0 | 14.5 | 1.41E-09 | 1.03E-09 | 13.073 |
| 23 | 6,597 | 320.2 | 0.50 | 600 | 12 | | 29.3 | 14.6 | 1.90E-10 | 8.84E-11 | 13.106 |
| 24 | 6,621 | 320.3 | 0.50 | 50 | 12 | | 29.8 | 14.9 | 1.48E-09 | 1.15E-09 | 13.208 |
| 25 | 6,699 | 320.1 | 0.50 | 600 | 12 | | 30.1 | 15.1 | 2.35E-10 | 9.97E-11 | 13.273 |
| 26 | 6,718 | 320.1 | 0.50 | 50 | 12 | | 30.4 | 15.2 | 1.76E-09 | 1.23E-09 | 13.362 |
| 27 | 6,743 | 320.0 | 0.50 | 600 | 12 | | 30.7 | 15.3 | 2.79E-10 | 1.07E-10 | 13.374 |
| 28 | 9,417 | 320.2 | 1.00 | 0 | 0 | | 37.9 | 0.0 | 1.42E-10 | - | 14.728 |

[a] Simulated PWR water with 2 ppm Li, 1000 ppm B, and 2 ppm. DO<10 ppb. Conductivity was 21±3 □S/cm, and pH 6.4.
[b] CGR rates in air are calculated assuming typical behavior for a Ni-base weld. The 152-LAS rates are approximately a factor of two lower.
[c] Data was corrected using fractography.

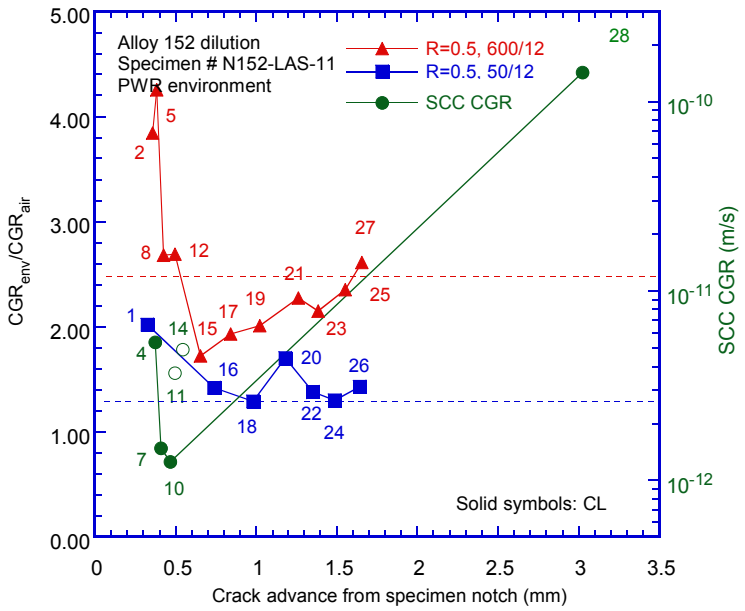


**Figure 3-73 Environmental enhancement of two control test conditions and SCC CGRs vs. distance from the specimen notch for Specimen N152-LAS-11. Test periods are indicated in the figure.**

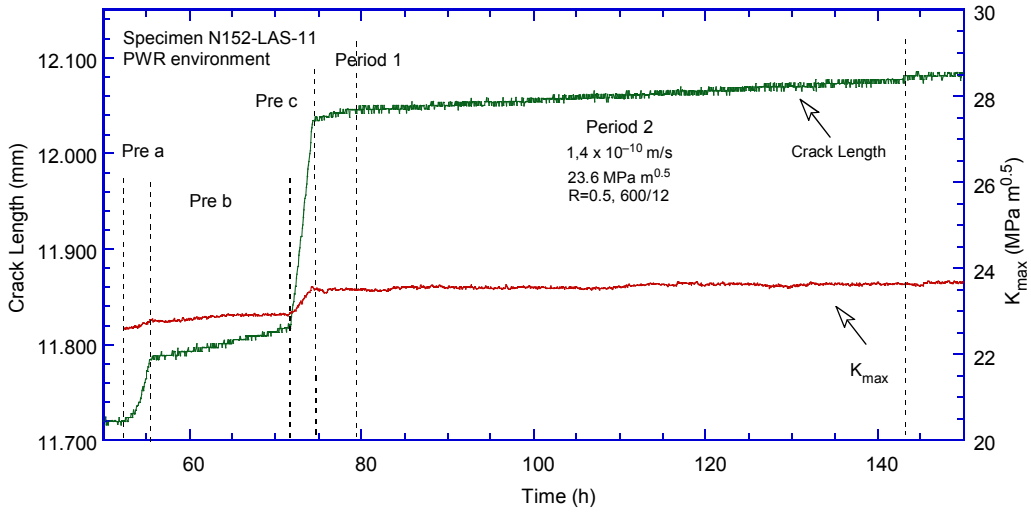


(a)

**Figure 3-74 Crack–length–vs.–time for dilution specimen N152-LAS-11 in simulated PWR environment during test periods (a) precracking-2, (b) 3-5, (c) 6, (d) 7 9, (e) 10, (f) 11-13, (g) 14-15, (h) 16-27, and (i) 28.**

**Figure 3-74 (Cont.)**

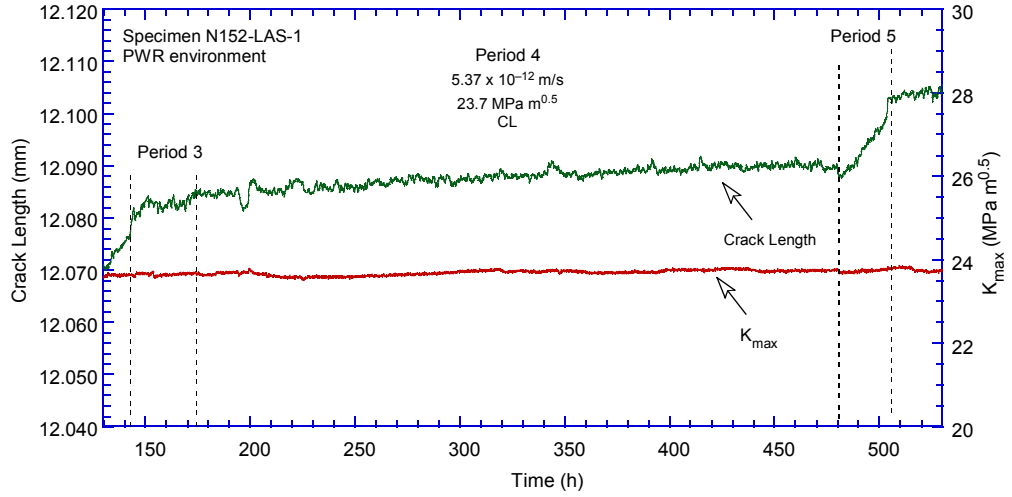


(b)

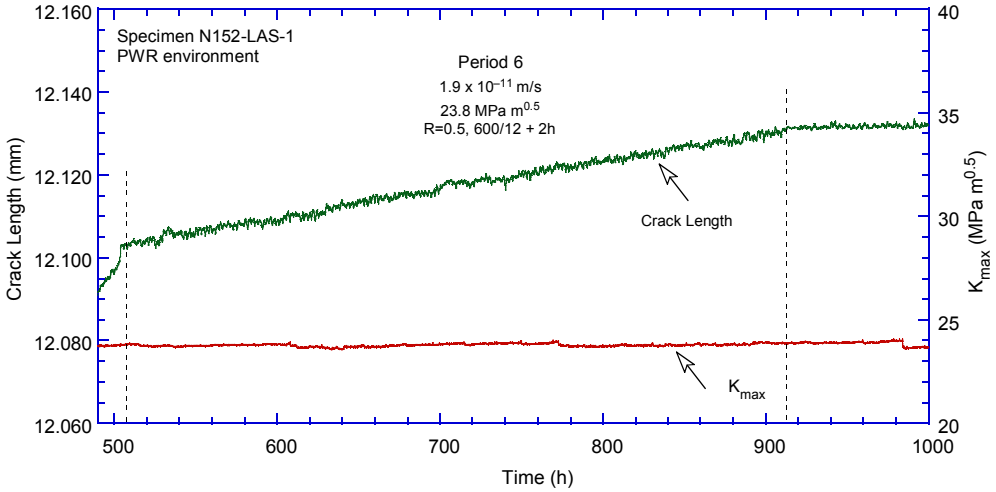


(c)

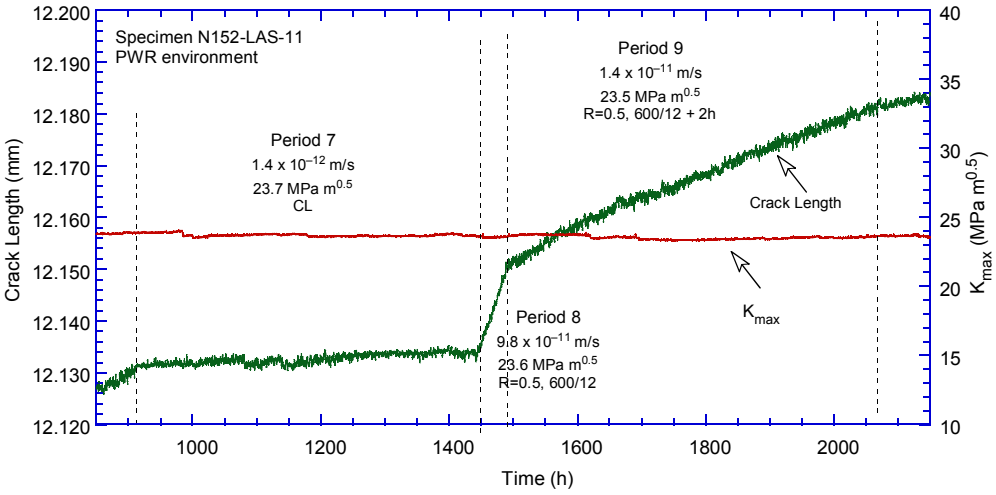


(d)

**Figure 3-74 (Cont.)**

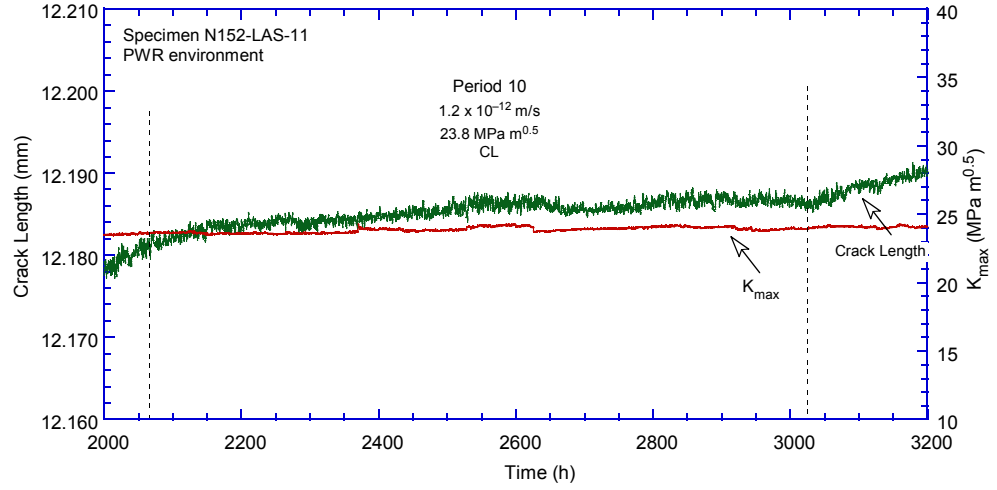


(e)

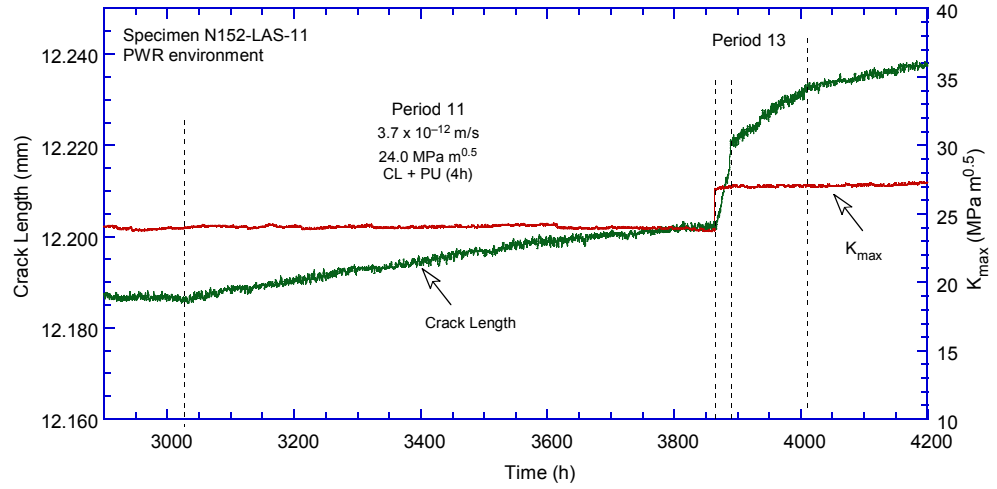


(f)

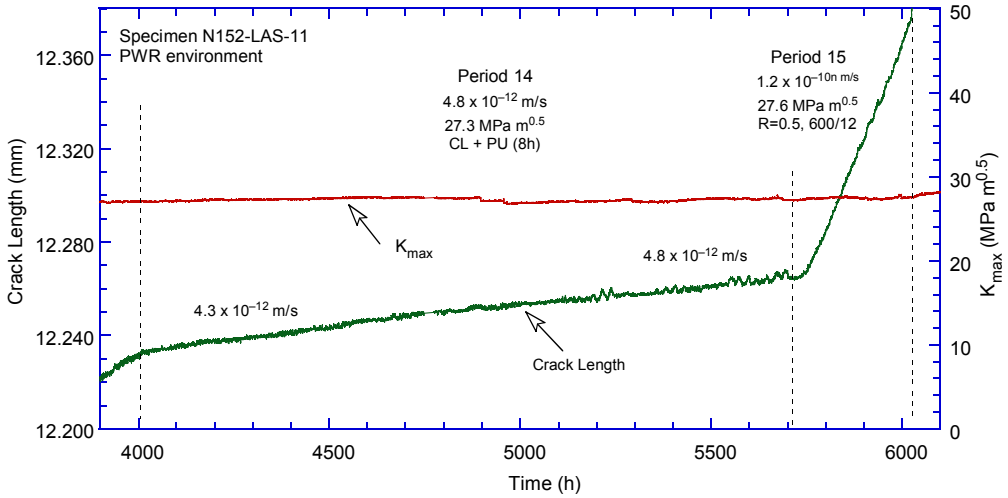


(g)

**Figure 3-74 (Cont.)**

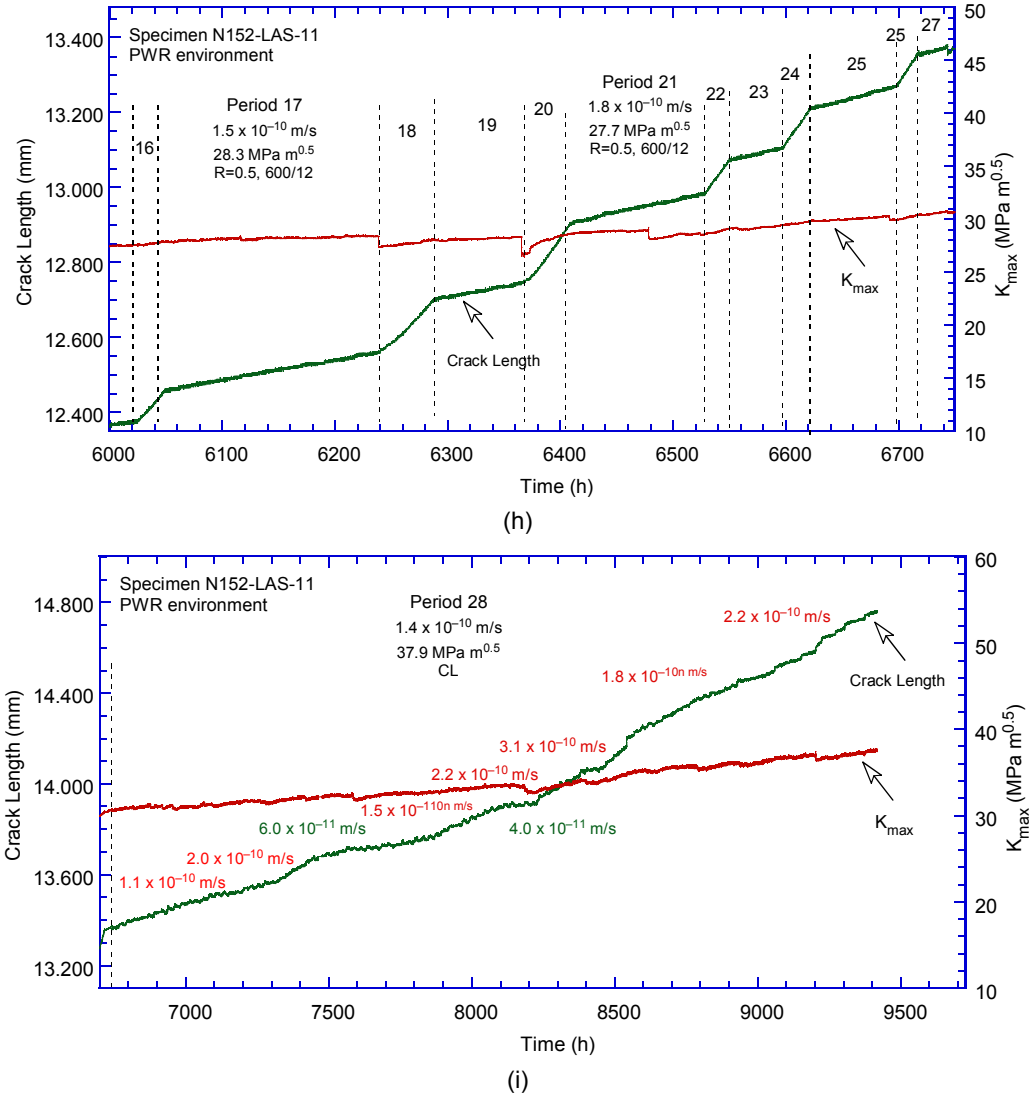


After the test was completed, the sample was removed from the autoclave and the side surfaces were ground to remove the side grooves. No fatigue in air was done immediately following the completion of the test in water in order to be able to establish precisely on the side surfaces where the test ended. The images shown in Fig. 3-75 seem to indicate that the test started and ended in the 1st layer of Alloy 152.

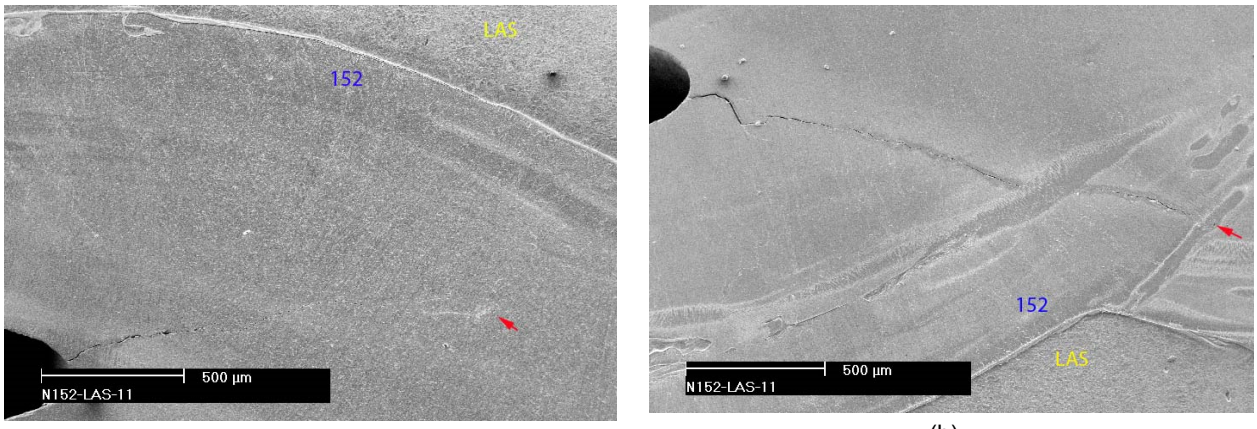


(a) (b)

**Figure 3-75 SEM images of the two sides of the dilution specimen N152-LAS-11 after the test: (a) side 1, and (b) side 2. Alloy 152 and the LAS are as marked in each picture. The red arrows mark the end of the test.**

The side surfaces were examined in the SEM to investigate the difference in cracking between the regions in this specimen with SCC CGR differing by a factor 100, namely between test periods 7-14 and 28. Side surface 1, Fig. 3-75a, does not seem to provide much revealing information. By contrast, side surface 2, Fig. 3-75b, appears to shows some detail at the locations of interest. As such, Fig. 3-76 identifies the regions of low SCC CGR (location 1) and high SCC CGR (location 3). The average composition (wt. %) at location 1 (Fig. 3-76b) is 26.1 Cr-24.4 Fe-49.5 Ni, and the average composition (wt. %) at location 3 (Fig. 3-76c) is nearly identical, 25.4 Cr–26.6 Fe–48.0 Ni. Hence, the chemical composition does not seem to account for the apparent factor 100 difference in SCC CGRs measured at the two locations. However, SCC at location 1 (Fig. 3-76b) is clearly off-plane; hence, the low SCC CGRs measured by DC potential at this location could be due to off-plane cracking.

Of high interest was also the interaction of the crack front with the two “swirls” shown at locations 2 and 3 in Fig.3-76 a. The “swirls” appear in the form of equiaxed dendrites composed of partly melted base metal that is diluted with Ni-base filler metal, and at closer inspection, Fig. 3-77, they seem to either slow (location 2) or arrest (location 3) the crack advance. The average composition (wt. %) for the “swirls” was 19 Cr–44 Fe–36 Ni, hence, a low Cr concentration does not seem to necessarily translate into an increased SCC-susceptibility.

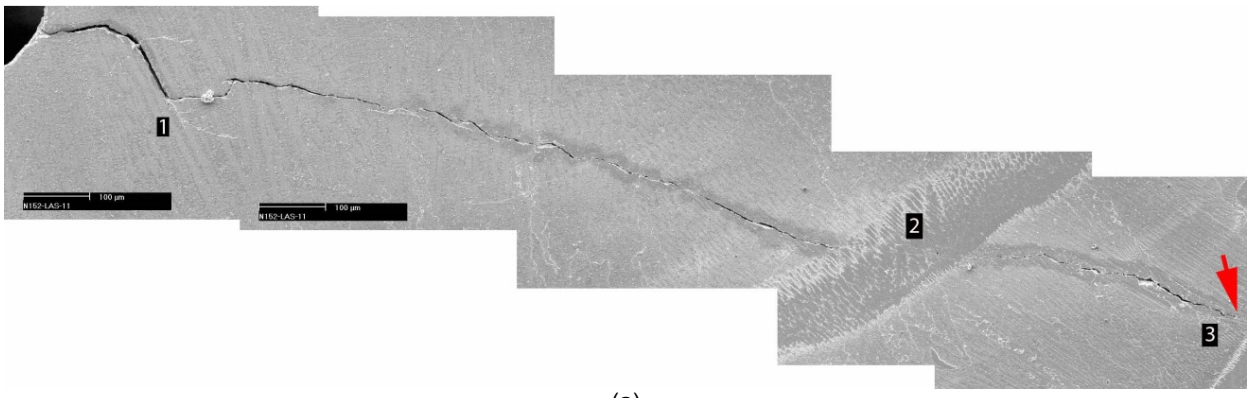


(a)

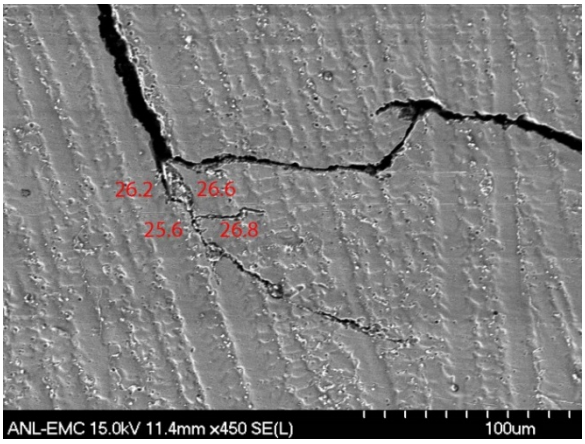


(b)

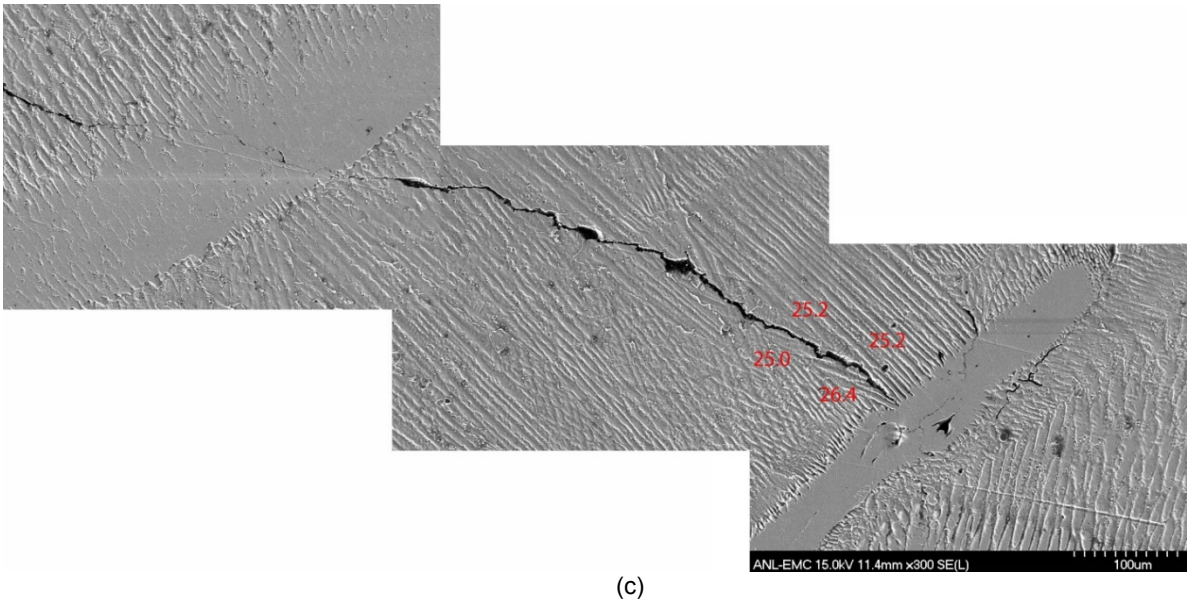


(c)

**Figure 3-76** **(a) Side surface 2 of Specimen N152-LAS-11; Regions with low (b) and high (c) SCC CGRs as observed on the side surface "2" at locations 1 and 3. Local Cr concentration (wt. %) measurements are indicated with red in each figure. Crack propagation is from left to right.**

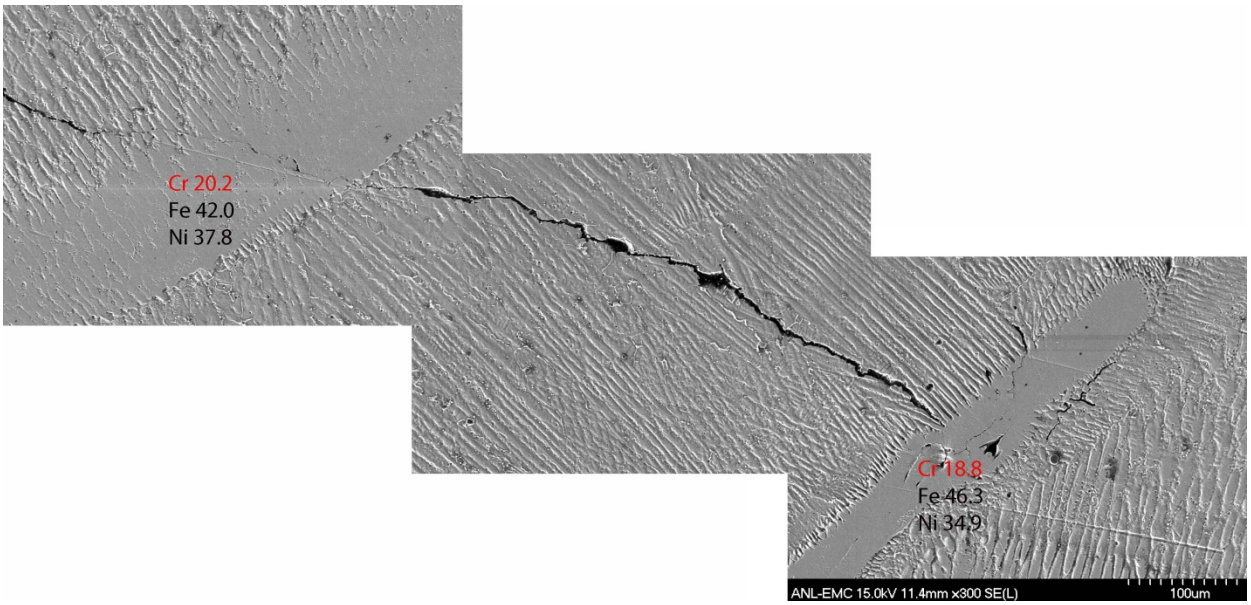


**Figure 3-77 "Swirls" appearing to slow down/arrest crack propagation observed on the side surface 2 in specimen N152-LAS-11 (locations 2 and 3 in Fig. 2-9b). Measured Cr concentration (wt. %) for each "swirl" is indicated with red in the figure. Crack propagation is from left to right.**

After the examination of the side surfaces, the specimen was fatigued in air for an additional 2 mm, and then broken open to examine the fracture surface, Fig. 3-78. The milestones of the test are indicated in the figure: the specimen was set at constant load fairly early in the test (IG-1), then the crack was advanced by cyclic loading (test periods 15-27, Table 3-7), and finally the specimen was set at constant load in test period 28. Advance under cyclic loading produces a relatively straight fracture surface with no ligaments, and this is especially true for test period 27 which reproduced the expected CGR for Alloy 152 (Fig. 2-10). Hence, the red lateral arrows in Fig. 3-78 indicate the end of cyclic loading (including test period 27). Finally, the last test period 28 produced the region labeled IG-2. This region was measured to be on average 10 times higher than the DC potential measurement of 0.140 mm, and hence, the correction for the DC potential data in test period 28 was a factor 10. The general appearance in the later part of the test – with several unbroken ligaments – was unexpected, and these areas were investigated further as it will be documented later in this section.

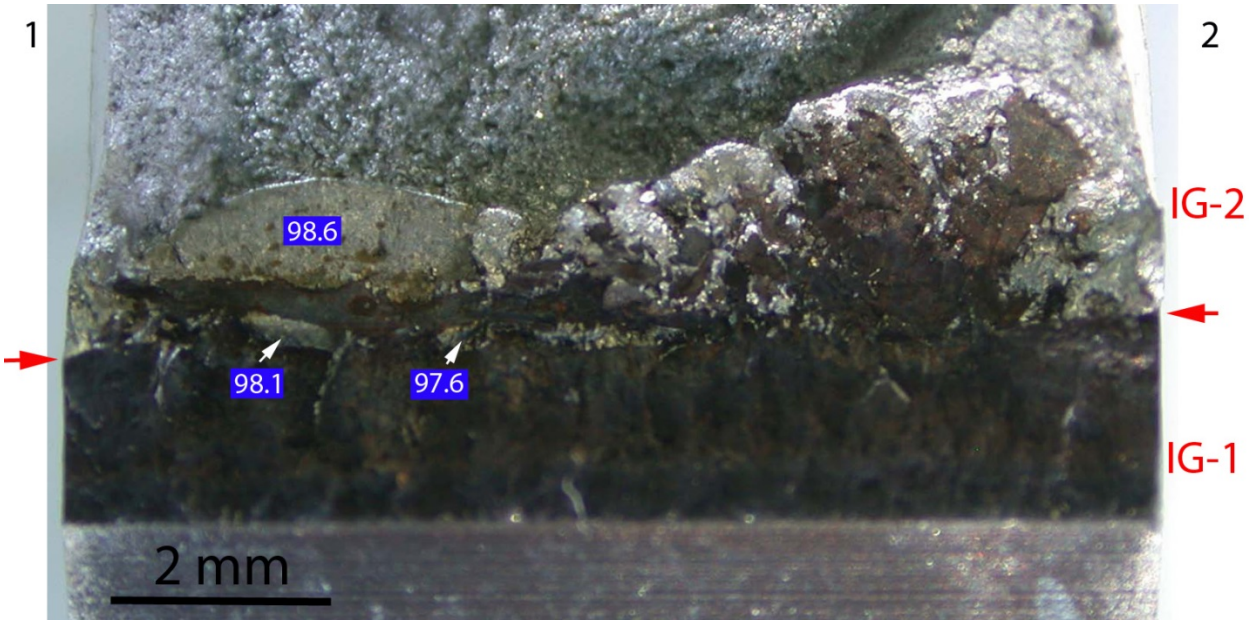


**Figure 3-78 Fracture surface of specimen N152-LAS-11. The red lateral arrows indicate the end of cyclic loading and the beginning of the final constant load test period. Measured Fe concentration (wt. %) for at several locations is indicated on a blue background in the figure. Crack advance is from bottom to top.**

Figure 3-78 also shows the local Fe concentrations of several of the unbroken ligament regions, confirming that these regions are the result of crack interaction with the SCC-resistant Alloy 152-LAS interface. These resistant regions were not suspected initially to be LAS because the post-test examination of the side surfaces (Fig. 3-75) suggested that the crack was contained in the Alloy 152 weld. Nevertheless, it appears that, unlike the previous specimen (N152-LAS-1) where the crack was advanced with gentle cycle + hold and constant load with periodic unloading and overcame the LAS regions, in the current specimen under constant load the areas where the crack interacted with the LAS remained as unbroken ligaments. However, it seems that the crack found a path around those regions, and appeared to propagate as long as there was weld metal available. Overall, the fracture surface suggests that the crack was eventually arrested at the intersection with the LAS on the left side, but propagated quite extensively in the weld on the right side. Given the extent of the unbroken ligaments, the large correction factor was not surprising.

Figure 3-79 shows the entire fracture surface of specimen examined in the SEM. Additional images at areas of interest were acquired and will be discussed next.

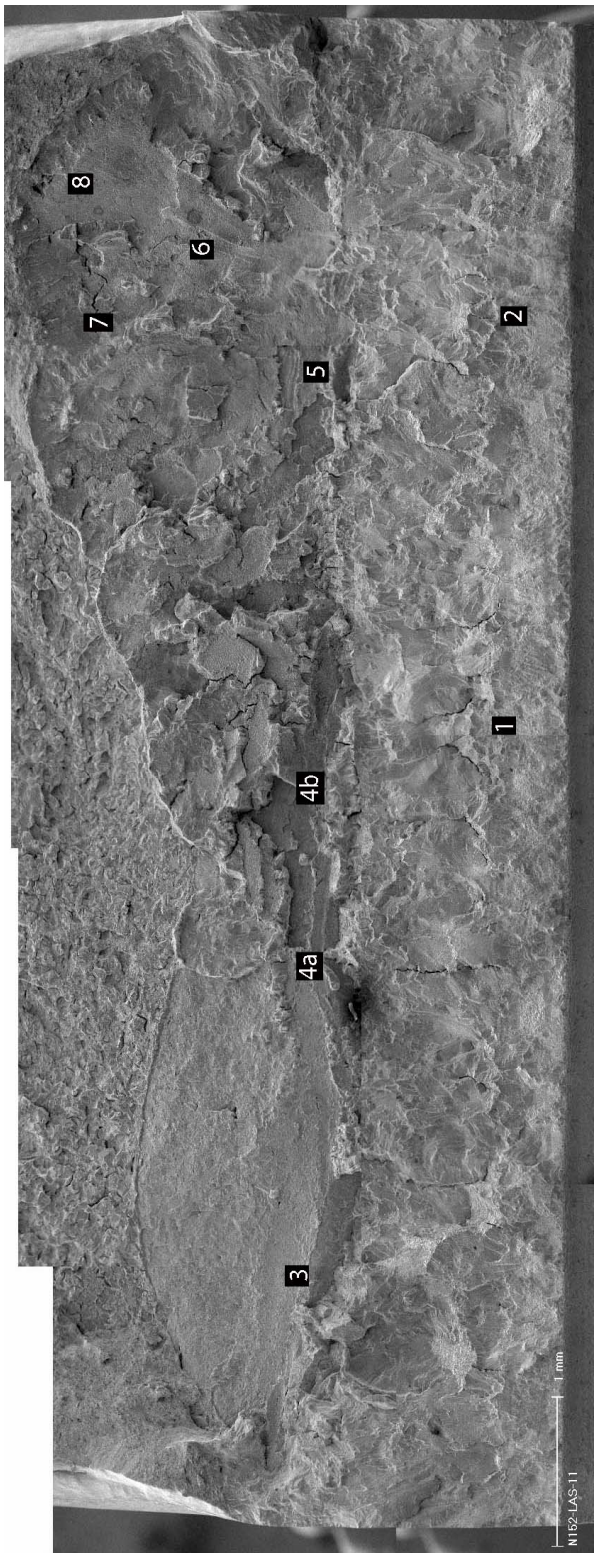


**Figure 3-79 Fracture surface of specimen N152-LAS-11. Crack advance is from bottom to top.**

Figure 3-80 focuses on what was believed to be (based on the DC potential measurement) the SCC-resistant region IG-1, locations 1 and 2 in Fig. 3-79. The presence of IG fracture very early in the test explains the high environmental enhancement observed in test periods 2 and 5 (Fig. 3-73). Eventually, the environmental enhancement is lost as the preferred crack direction is off-plane. The fracture mode for this region appears on the fracture surface as mixed IG-TG mode, with extensive secondary (off-plane) cracking.

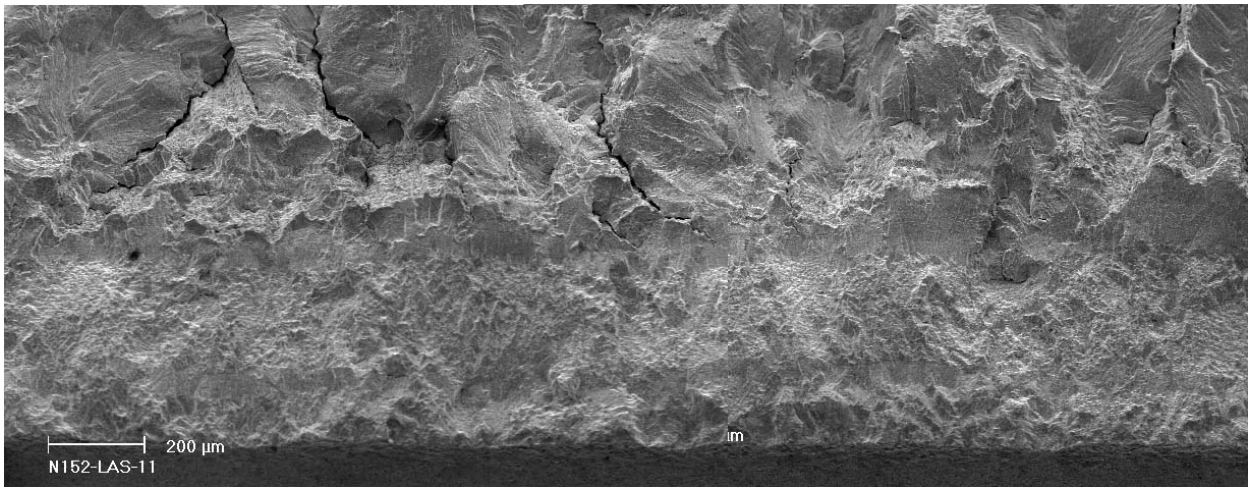


(a)

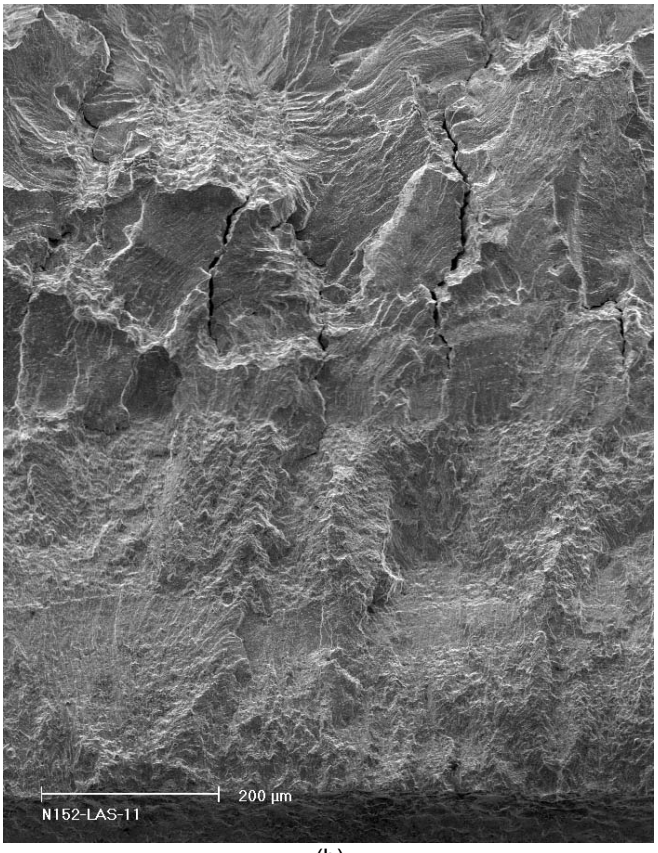


(b)

**Figure 3-80 Fracture surface of specimen N152-LAS-11 at locations (a) 1, and (b) 2 in Fig. 3-79. Crack advance is from bottom to top.**

Figure 3-81 illustrates the interaction of the crack front with the LAS, locations 3 and 4b in Fig. 3-79. As described previously in the context of discussing Fig. 3-78, these regions are resistant to SCC, and remained as un-broken ligaments on the fracture surface under constant load conditions. The crack eventually found a path around them and propagated as long as there was weld metal available. Figure 3-82 obtained at location 4a in Fig. 3-79 presents a similar situation.

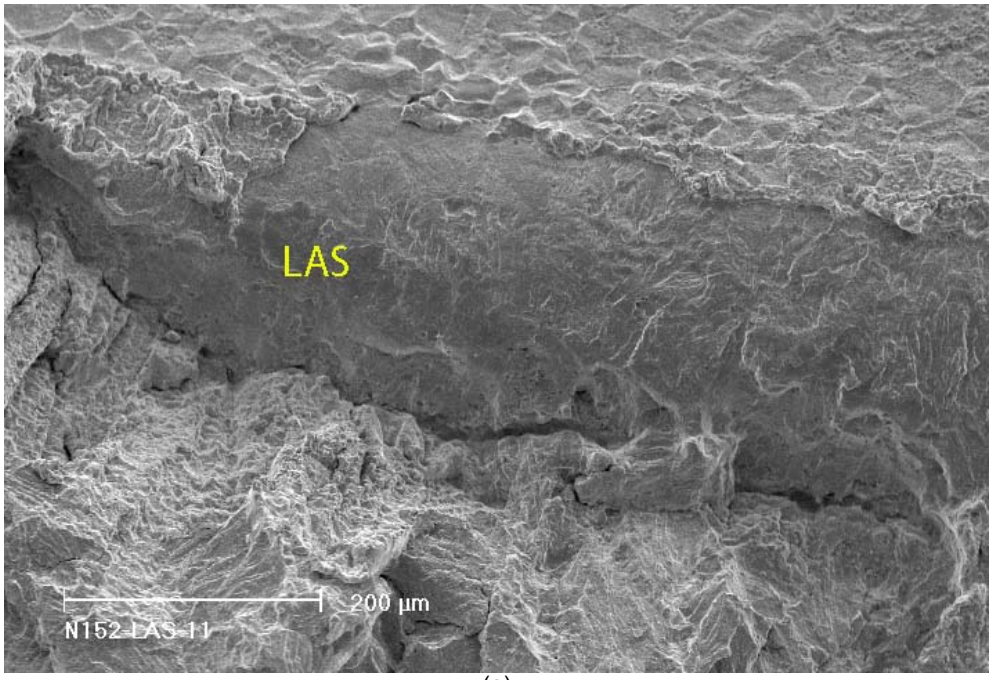


(a)

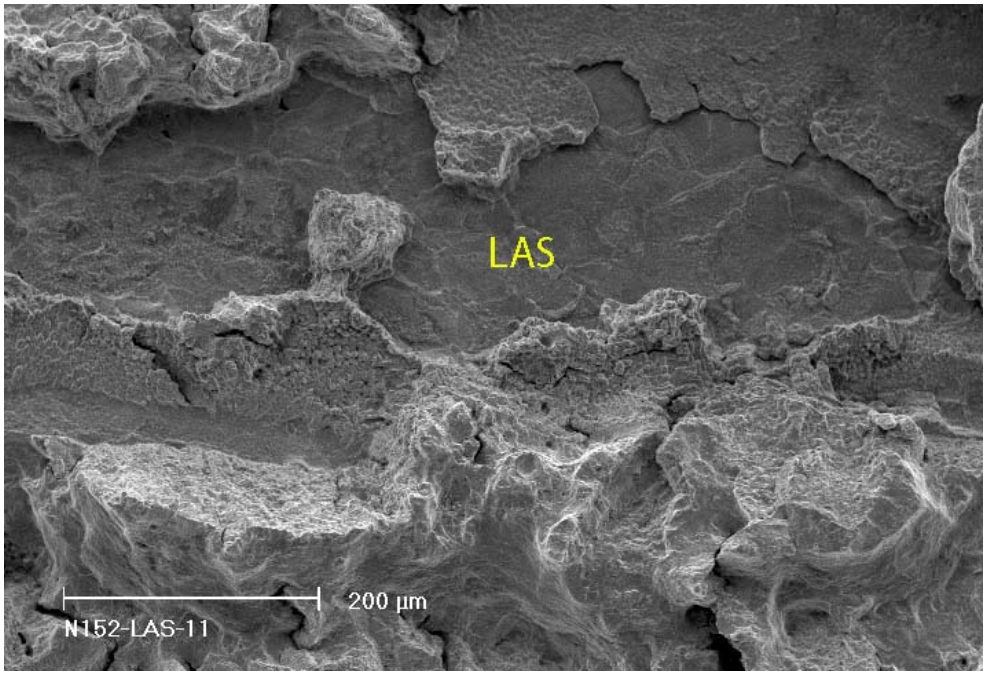


(b)

**Figure 3-81 Fracture surface of specimen N152-LAS-11 at location: (a) 3, and (b) 4b in Fig. 3-79. Crack advance is from bottom to top.**

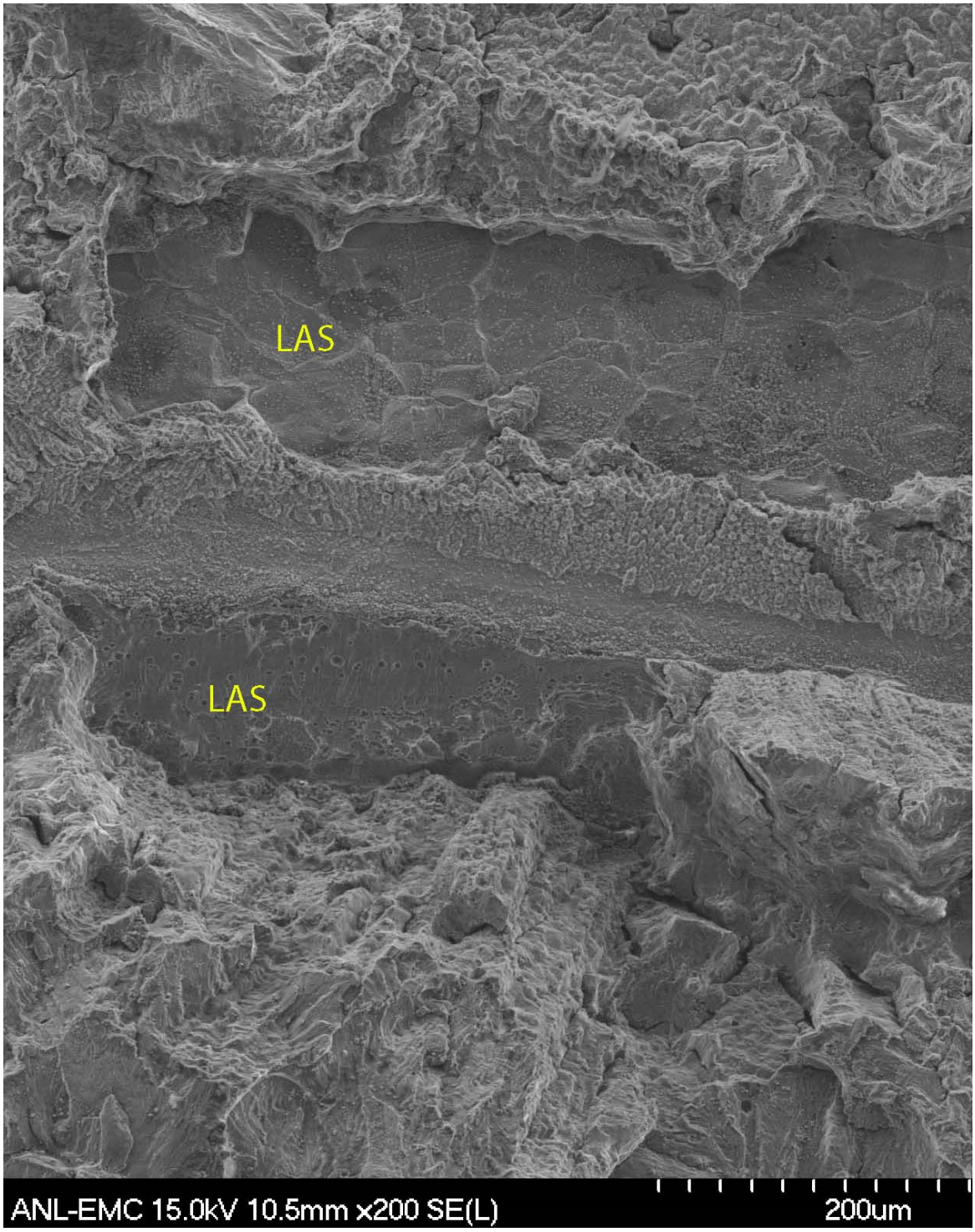


**Figure 3-82 Fracture surface of specimen N152-LAS-11 at location 4a in Fig. 3-79. Crack advance is from bottom to top.**

Figure 3-83 provides additional detail at locations 5 and 6 in Fig. 3-79. At location 5 (Fig. 3-83a), several IG SCC directions appear visible – both along and normal to the dendritic grains. Past the LAS (unbroken ligament), the crack seems to settle along a direction normal to the dendritic grains, and the crack plane appears to be flat. This type of fracture appears almost exclusively by the time the crack reaches location 6, Fig. 3-83b.

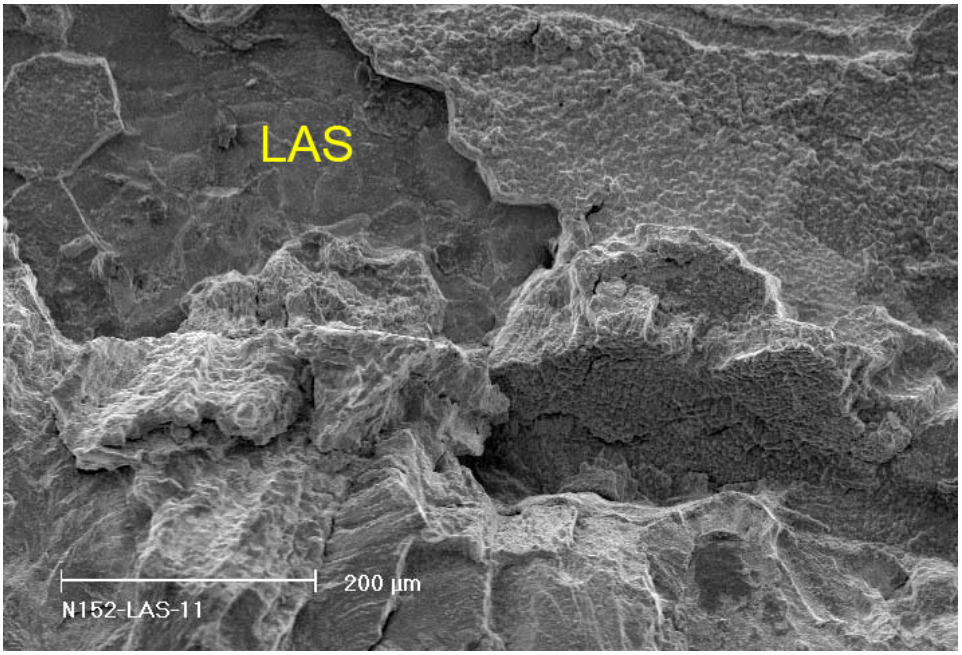


(a)

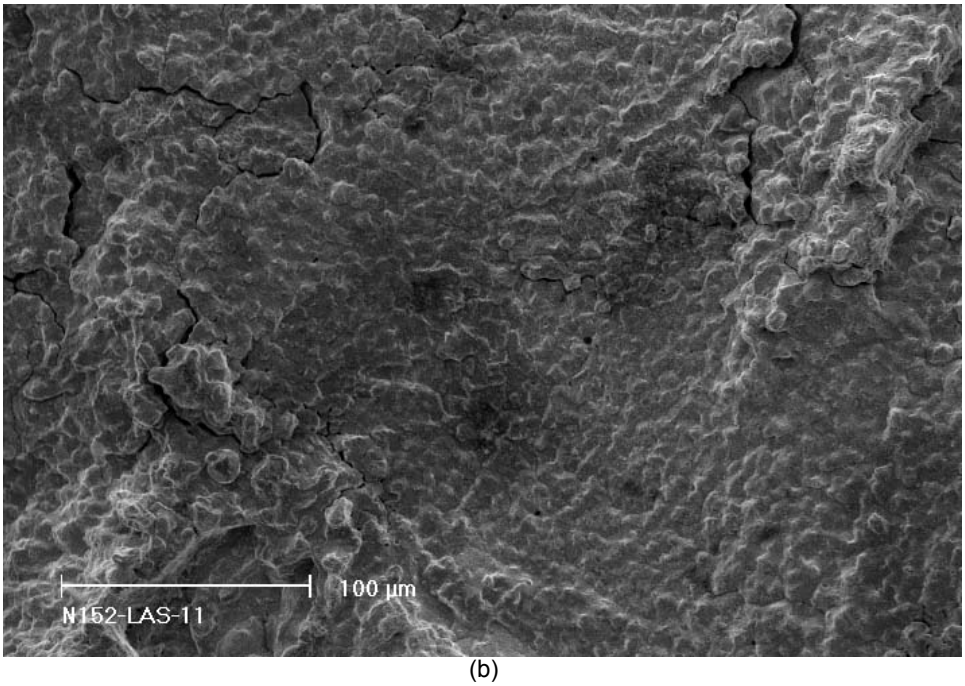


(b)

**Figure 3-83 Fracture surface of specimen N152-LAS-11 at location: (a) 5, and (b) 6 in Fig. 3-79. Crack advance is from bottom to top.**

Figure 3-84 shows two locations from final part of the test (7 and 8 in Fig. 3-79). Propagation is flat, in an IG mode, in a direction perpendicular to the direction of the dendrites, and in a finger-like manner that leaves unbroken ligaments behind. Overall, a similar fracture mode was observed in the first layer of Alloy 52M deposited on an Alloy 182 interface.

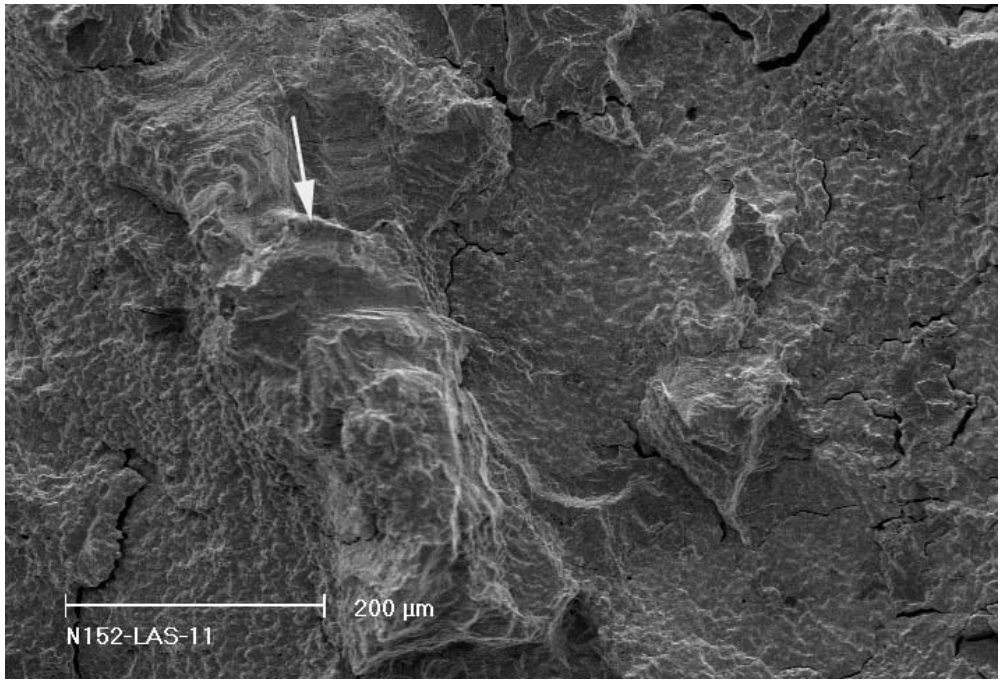


(a)

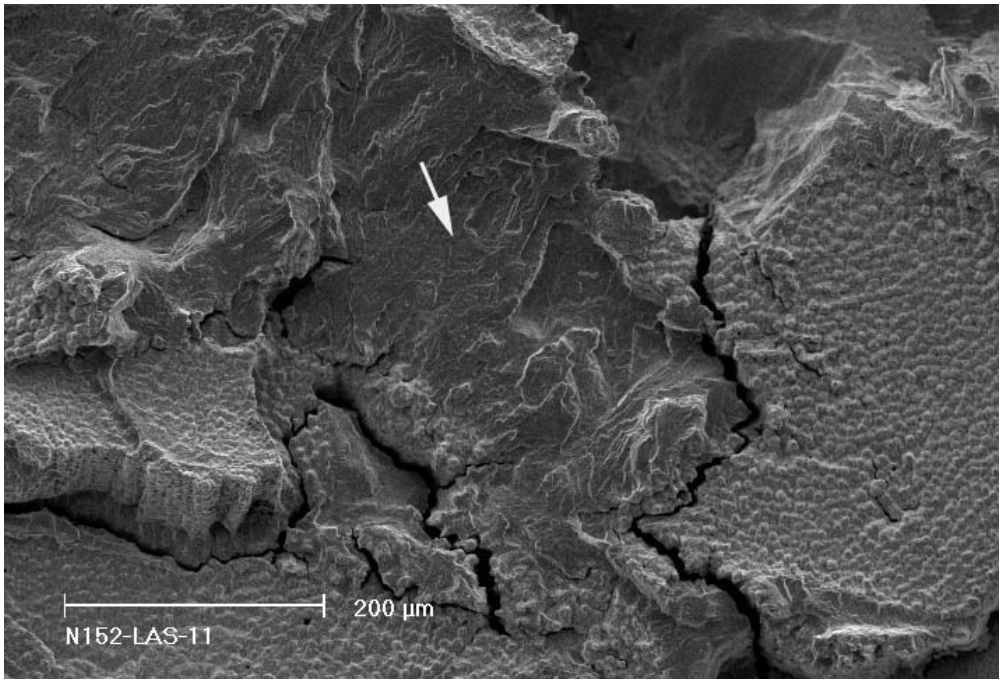


(b)

**Figure 3-84 Fracture surface of specimen N152-LAS-11 at location: (a) 7, and (b) 8 in Fig. 3-79. Arrows indicate unbroken ligaments. Crack advance is from bottom to top.**

Finally, in order to obtain additional confirmation on the crack path, the test specimen was further sectioned along directions “11” and “22”, as shown schematically in Fig. 3-85. Cross section “11” was chosen in an area where the crack was arrested at the LAS, and cross section “22” was chosen in an area where the crack propagated over several millimeters. Figure 3-85b indicates that the crack observed on cross section “11” was indeed arrested at the interaction with the LAS and, along with Fig. 3-81a, demonstrates that the crack continued to propagate as long as there was some weld metal available. Figure 3-85c demonstrates that the crack observed on cross section “22” propagated freely into the Alloy 152 weld with no interference from the LAS interface. This behavior is similar to that observed for specimen N152-LAS-1 where the SCC crack front was also found to propagate away from the interface (Fig. 3-62c).

The type of SCC fracture (flat, and in a direction normal to the dendritic grains) that was occasionally observed in these first layer Alloy 152 weld specimens, as well as the resulting fast propagation rates have generated interest in the SCC community. As such, the current specimen was made available to other laboratories for additional investigations. Figure 3-86 shows SEM and Electron Backscatter Diffraction (EBSD) maps obtained at Pacific Northwest National Laboratory (PNNL) on cross section “22” (Fig. 3-85c). The EBSD inverse pole figure (IPF) map set to only display FCC structure shows a grain boundary ~125 μm from the fusion boundary as indicated by the yellow arrow [28]. This boundary is aligned to the target cracking direction, and the PNNL investigators have proposed that such a boundary could explain the flat appearance and overall the crack path in this test. An additional, similar EBSD investigation was conducted at Tohoku University [29] on side surface 2 (Figs. 3-75b and 3-76), and the resulting SEM and EBSD images are shown in Fig. 3-87. On that side surface, the SCC propagation was more “traditional”, i.e. along the dendritic grains, and similar to that observed in the first N152-LAS-1 specimen. However, as indicated by the blue arrows in Fig. 3-87, two sets of flat boundaries would have been readily available in the next weld bead should those boundaries prove themselves to be particularly prone to SCC propagation.

Other researchers [30] have suggested that the feature identified by the yellow arrow in Fig. 3-86 could be a Type II boundary. Type II boundaries require a ferrite/austenite phase boundary at elevated temperatures to form, i.e., the weld metal solidifies in the austenite mode despite the dilution from the base metal, while the LAS solidifies as delta ferrite which then undergoes a transformation first to austenite and then to ferrite/bainite/martensite [31]. Type II boundaries exist parallel to the fusion boundary and are located in the chromium dilution zone, as illustrated in Fig. 3-87b. They have been identified in the literature as prone to SCC [26], owing to the large stress concentrations in their vicinity. However, as indicated by the large variation in crystal orientations above and below the boundary shown in Fig. 3-86, this appears to be simply a collection of high angle boundaries. Figure 3-87 shows that, in fact, both type II and flat high angle boundaries were present in this butter weldment. Moreover, a similar fracture mode – flat and normal to the dendritic grains – was observed for Alloy 52M WOL deposited on Alloy 182 (Figs. 3-52 - 3-56) – which is not a ferrite/austenite phase boundary, hence Type II boundaries do not occur in that material. Thus, it appears that Type II boundaries cannot explain the observed cracking in first layer Alloy 52M and 152 weldments. Additional analysis may be needed to better understand how the weld microstructure affects the crack growth behavior.

In summary, the test on specimen N152-LAS-11 confirmed the prior observations on specimen N152-LAS-1. The first layer of the Alloy 152-LAS weld is susceptible, extensive IG SCC was observed in both specimens, and in this test, in a favorable orientation, a SCC CGR in the $10^{-10}$ m/s range was measured.

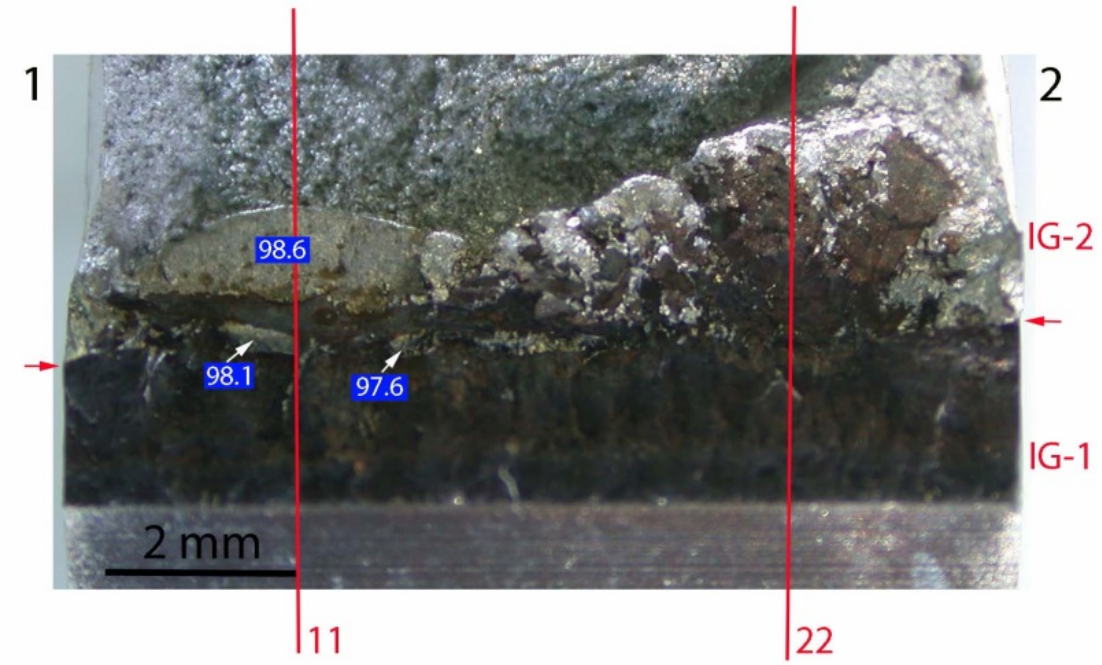


(a)

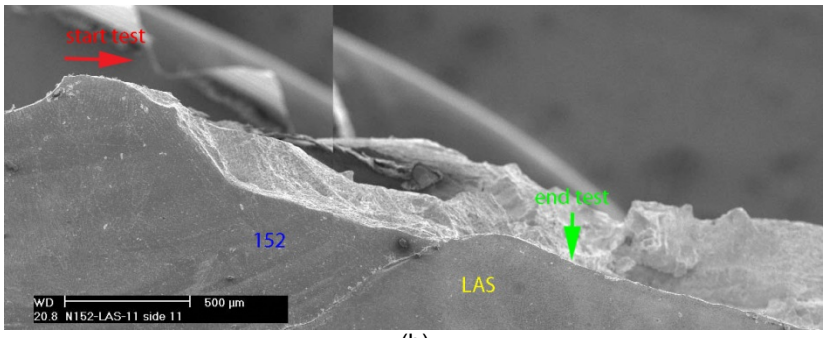


(b)

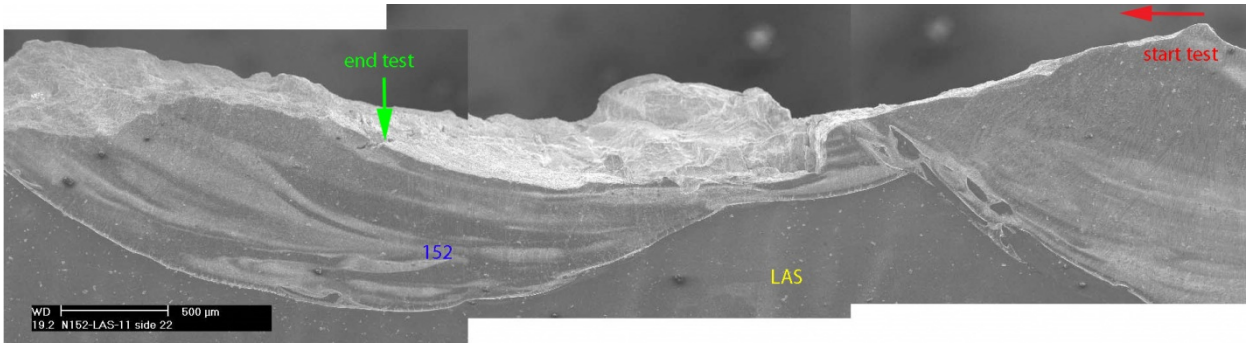


(c)

**Figure 3-85** **(a) Fracture surface of specimen N152-LAS-11. Additional cross sections were obtained along directions "11" (a), and "22" (b). Red arrows are placed at the specimen notch and indicate the direction of propagation. Green arrows indicate the end of the test.**

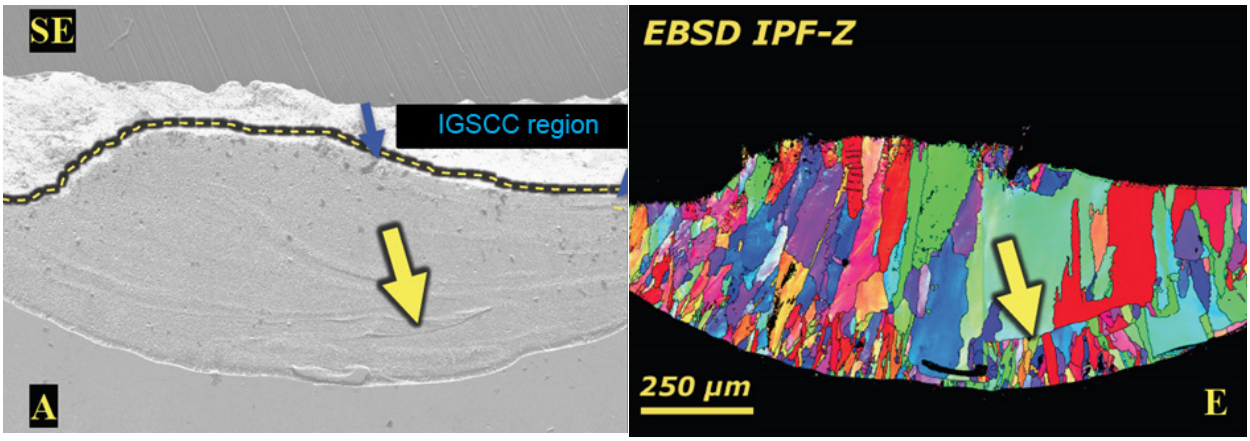


(a) (b)

**Figure 3-86** **SEM (a) and EBSD (b) map obtained on cross section "22" (Fig. 3-85) of Specimen N152-LAS-11. The yellow arrow points to a set of aligned boundaries that could plausibly explain the crack path in this test [28]. Crack propagation is from right to left.**

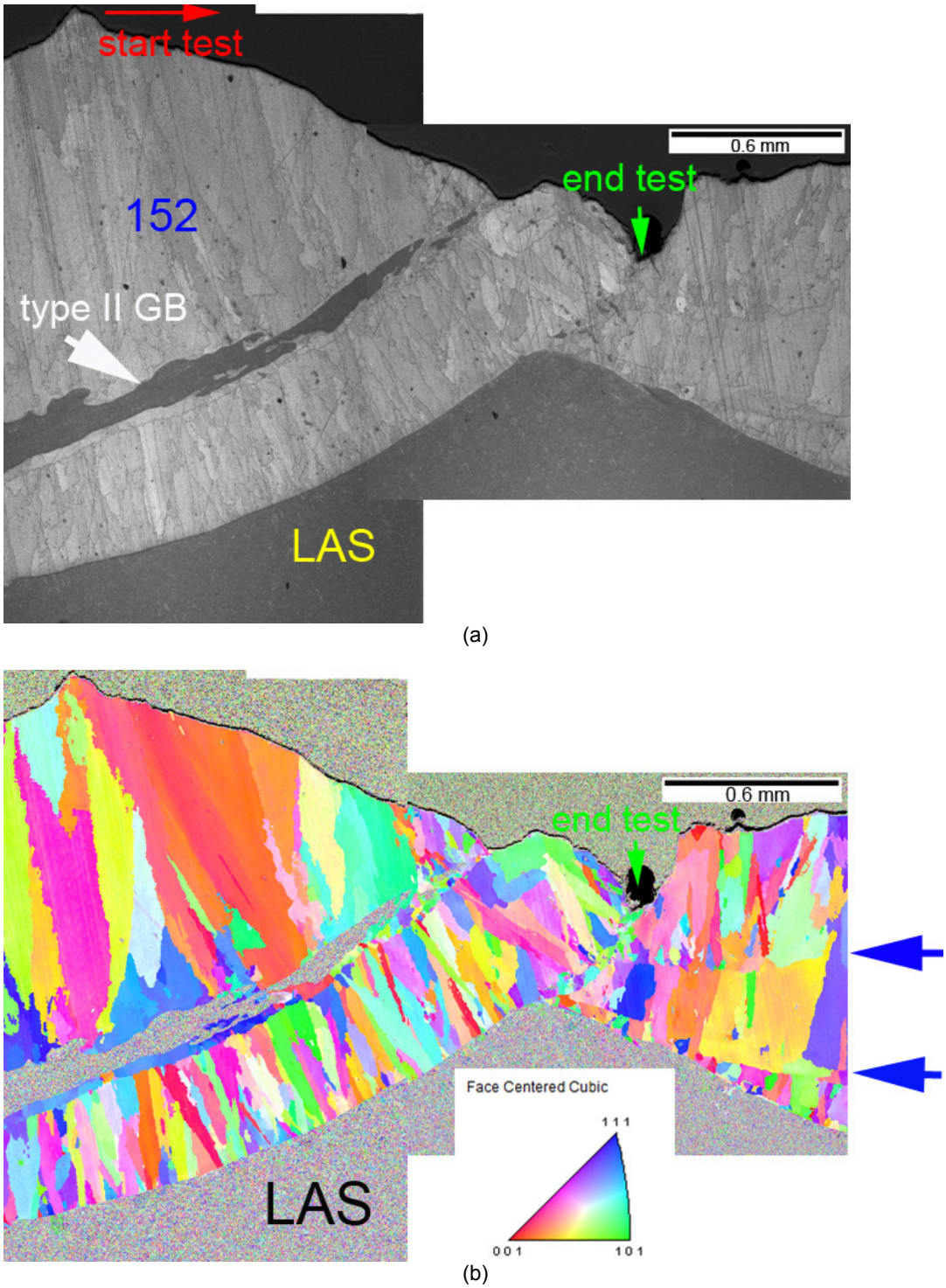


**Figure 3-87** **SEM (a) and EBSD (b) map obtained on side surface 2 (Figs. 3-75b and 3-76) of specimen N152-LAS-11. The blue arrows point to sets of aligned boundaries in the next weld bead [29]. Red arrows are placed at the specimen notch and indicate the direction of propagation. Green arrows indicate the end of the test. Crack propagation is from left to right.**

# 4 DISCUSSION

The section summarizes the cyclic and SCC CGR results obtained on the Alloy 52M-182 WOL and Alloy 152–LAS butter specimens. A comparison of outcomes is made, and the role of the microchemistry and that of the substrate are discussed.

## 4.1 SCC CGR Response of Alloy 52M WOL

SCC CGR testing on the Alloy 52M-182 WOL was conducted in two orientations: TS and ST. Figure 4-1 illustrates these orientations and the SCC CGRs that were measured in each orientation. As described previously, the SCC CGRs in Alloy 182 are unaffected by the Alloy 52M WOL at distances larger than 1-1.5 mm from the WOL interface. However, as those cracks approached the interface in the TS orientation, the SCC CGRs in Alloy 182 were found to decrease by approximately one order of magnitude in the 1 mm leading up to the interface. The reason for the decrease is unknown, however, it may be due to the compressive stress exerted by the WOL. In both TS-oriented tests, significant cracking was found to develop at the interface between the two welds, and this prevented an unambiguous measurement of the SCC CGRs in Alloy 52M past the interface. Nevertheless, estimates based on fractography (Fig. 2-12) suggested that the maximum SCC CGR in the first layer of Alloy 52M can be relatively high. As such, additional testing was undertaken in the ST orientation to measure the SCC CGRs at the interface between the two welds and the first layer of Alloy 52M directly. Both the Alloy 52M-182 interface and the first layer of Alloy 52M were found to be highly susceptible. Given the long crack extensions for these measurements, and the fact that the SCC region was readily identifiable on the fracture surface, these SCC CGRs are thought to be highly reliable.

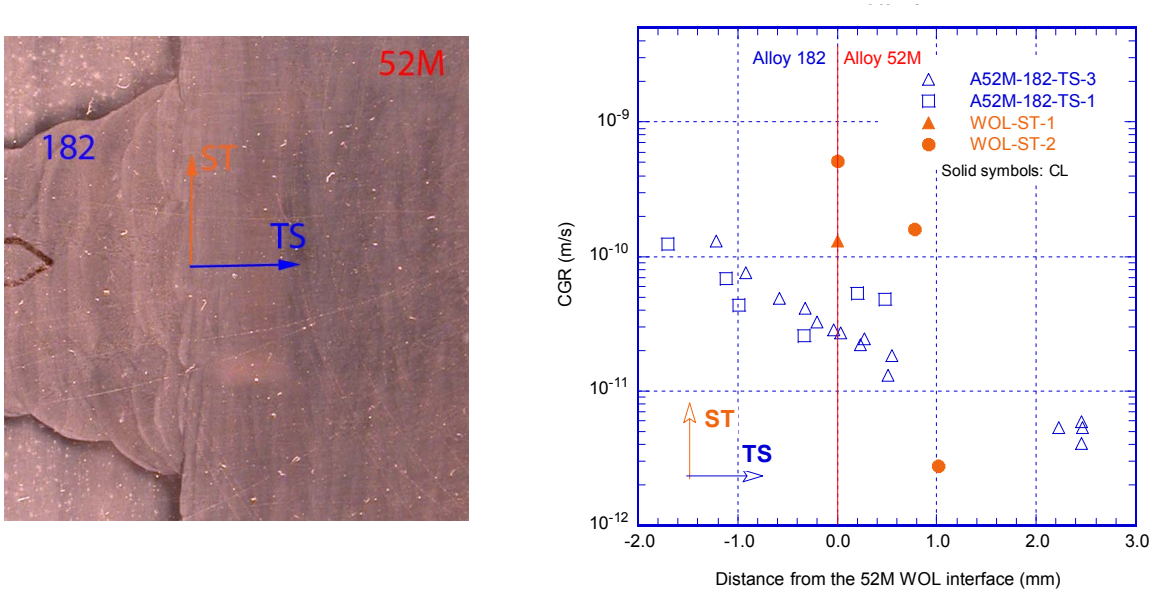


(a) (b)

**Figure 4-1 SCC CGRs in an Alloy 52M-182 overlay: (a) Schematic showing the test specimen orientations with respect to the Alloy 52M-182 WOL, and (b) SCC CGRs vs. distance to the Alloy 52M-182 interface.**

In order to put the Alloy 52M WOL data into perspective, Figure 4-2 summarizes the SCC CGR data obtained from the two ST-oriented specimens presented in this report, along with data for Alloy 152 heat WC04F6 (28.7 wt. %) tested previously at ANL [22, 23]. Also included for comparison is the MRP-115 75$^{th}$ percentile curve [1]. The local Cr concentration that was measured in close proximity of each crack is also included.

Figure 4-2 suggests that the SCC CGRs along the interface between the two welds can be as high as the MRP-115 75$^{th}$ percentile curve [1]. The Cr concentration for the Alloy 52M-182 interface was measured to be approximately 20 wt. %. For Alloy 52M (Fig. 4-2b), the Cr concentration seems to be playing a role. The SCC CGR in a region with 27.4 wt. % Cr was low, however, the unfavorable orientation of the crack with respect to the dendritic grains could have also played a role. Additionally, in the first layer of Alloy 52M weld, in a region with an average Cr concentration of 25.4 wt. %, the SCC CGR was relatively high (factor of two lower than the MRP-115 75$^{th}$ percentile curve [1]) despite the unfavorable orientation with the dendritic grains. Nevertheless, it is important to note that the SCC CGR measured in the latter case in the unfavorable orientation matches almost exactly the maximum SCC CGR estimated on the fracture surface in a case where propagation was along the "traditional" direction, i.e., along the dendritic grains (see Fig. 2-12). Hence, it is not clear at this stage whether crack orientation with respect to the dendrites plays a major role in the case at hand.

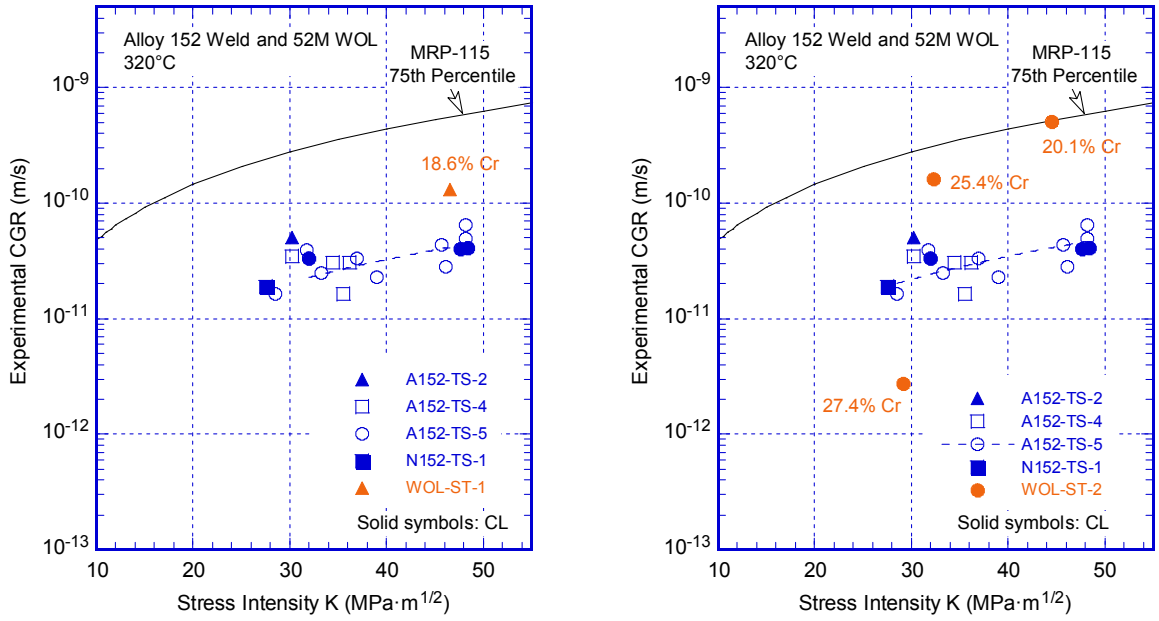


**Figure 4-2 SCC CGRs in the Alloy 52M-182 overlay: (a) along the Alloy 52-182 interface in specimen WOL-ST-1, and (b) as a function of average Cr content in specimen WOL-ST-2. Also included are Alloy 152 data generated at ANL [22, 23] and the MRP-115 disposition curve for Alloys 82/182 [1].**

## 4.2 1st Layer Alloy 152-LAS Cyclic and SCC CGR Response

The cyclic and SCC CGRs generated in the two first layer Alloy 152-LAS specimens are shown as a function of crack advance in Fig. 4-3. Overall, the cyclic data for the two specimens is in excellent agreement, and the approach based on measuring the local environmental enhancement was instrumental for identifying the locations where an SCC CGR could be measured by DC potential.

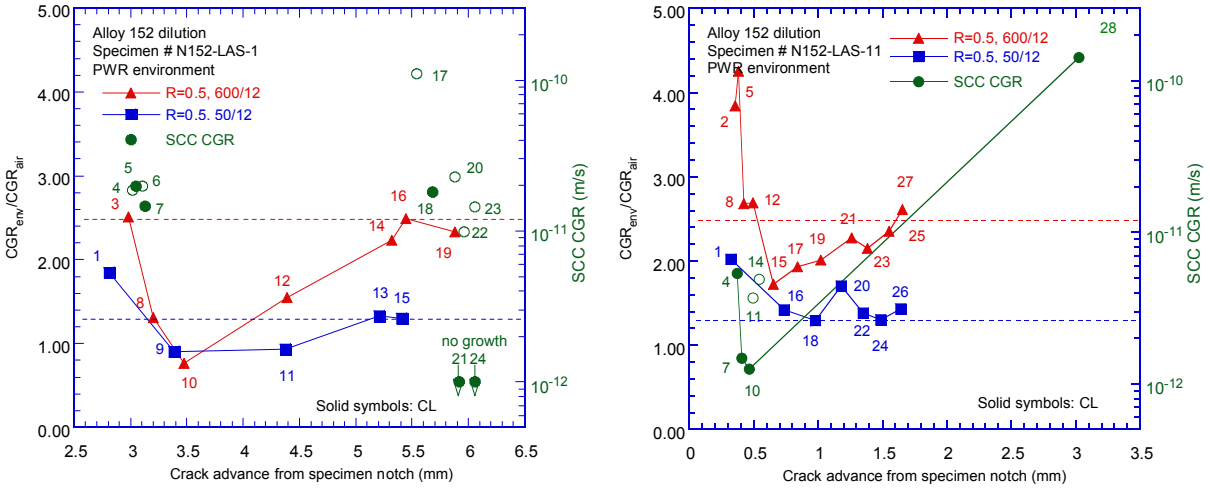


**Figure 4-3 Environmental enhancement of two control test conditions and SCC CGRs vs. distance from the specimen notch for (a) N152-LAS-1, and (b) N152-LAS-11. Crack propagation is from left to right.**

Figure 4-4 shows the SCC CGR data measured for the two first layer Alloy 152-LAS specimens along with the Alloy 152 data obtained previously on a double-J symmetrical Alloy 152 weld [22, 23]. Despite the un-favorable orientation with respect the weld dendrites, some locations of these first layer Alloy 152-LAS dilution welds yielded SCC CGRs higher than those measured for bulk Alloy 152. These SCC CGRs show a factor 100 variation depending on the location in the specimen where they were measured, as was already illustrated in Fig. 4-3. Nevertheless, the crack direction versus test plane and the ability of the DC potential to measure correctly the SCC CGRs in those directions emerge as major contributors to the scatter. While the Alloy 52M results discussed in the previous section suggest that the test plane versus grain orientation can yield similar SCC CGRs, the situation for the Alloy 152-LAS specimens is less clear. As described in this report, extensive SCC was observed in directions both parallel (specimen N152-LAS-1) and normal (specimen N152-LAS-11) to the dendritic grains, yet only the normal direction coincided with the test plane where the CGRs were readily measurable by DC potential. As such, the SCC propagation normal to the dendrites in specimen N152-LAS-11 may appear at first sight to be faster than that along the dendrites in specimen N152-LAS-1, yet a lone data point in the latter specimen (as seen in test period 17, Figs. 4-3a and 4-4) seems to suggest that the SCC CGRs in the two orientations may in fact be similar, just as was the case with Alloy 52M WOL. Nevertheless, given the severe off-plane crack direction in specimen N152-LAS-1, the lone observation in test period 17 could not be later substantiated by subsequent determinations in the same test. By contrast, with an SCC crack propagating favorably in the test plane, specimen N152-LAS-11 yielded one SCC CGR that was within a factor of two of the 75th percentile MRP-115 disposition curve for Alloys 82/182 [1], and was

based on a crack advance larger than 1 mm. Because of the size of this crack, and the fact that it was readily identifiable on the fracture surface, this SCC CGR is deemed by the authors of this report to be highly reliable. However, as discussed previously, it is not clear at this stage whether or how the crystallographic orientation affects the magnitude of the measured SCC CGRs in those first layer weldments.

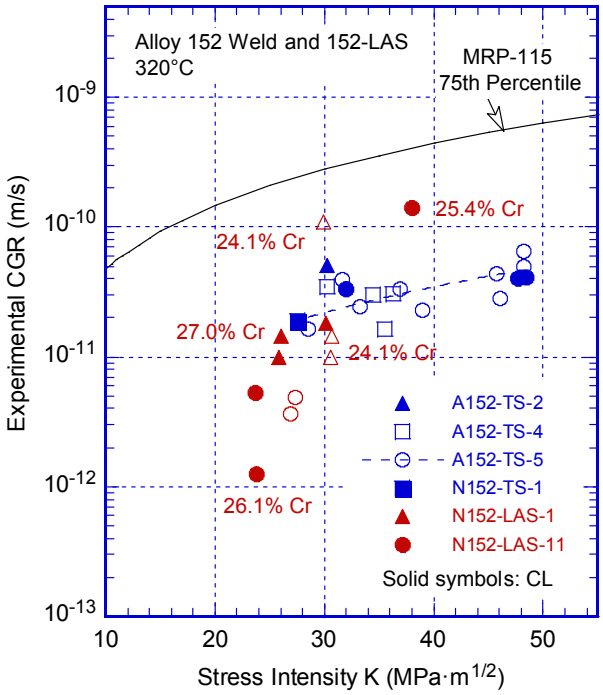


**Figure 4-4 SCC CGRs in and 1st layer Alloy 152-LAS specimens. Also included are Alloy 152 data generated at ANL [22, 23] and the 75th percentile MRP-115 disposition curve for Alloys 82/182 [1].**

## 4.3 Comparison of Cyclic and SCC CGR Responses in 1st Layer Alloy 152-LAS and 1st Layer Alloy 52M-182 WOL

In order to put the first layer Alloy 52M-182 and Alloy 152-LAS data into perspective, Fig. 4-5 provides a side-by-side comparison of the cyclic and SCC CGR data obtained on the two welds. The two sets of cyclic and SCC responses are in excellent agreement with each other, with no apparent effect from the nature of the substrate or the interface. In both cases, the environmental enhancement was a good predictor for the SCC response. Also, in both cases, as discussed previously (Figs. 4-2 and 4-4), in the most favorable orientations, the SCC CGRs were within a factor of two of the MRP-115 75th percentile curve [1]. It is also interesting to note that in both first layer welds, the fastest measured SCC propagation occurred in a direction normal to the dendrites, as shown in Fig. 4-6. While it is not clear whether this propagation mode even exists in Alloy 182 or it is specific to those high-Cr weld layers near an interface, favorable crystallographic planes allowing such propagation were identified for the Alloy 152-LAS weldment, shown in Figs. 3-86 and 3-87. However, as discussed in the prior section, it is not clear at this stage whether SCC growth along such planes is faster or not than that occurring along more “traditional” directions, i.e., along the dendritic grains.

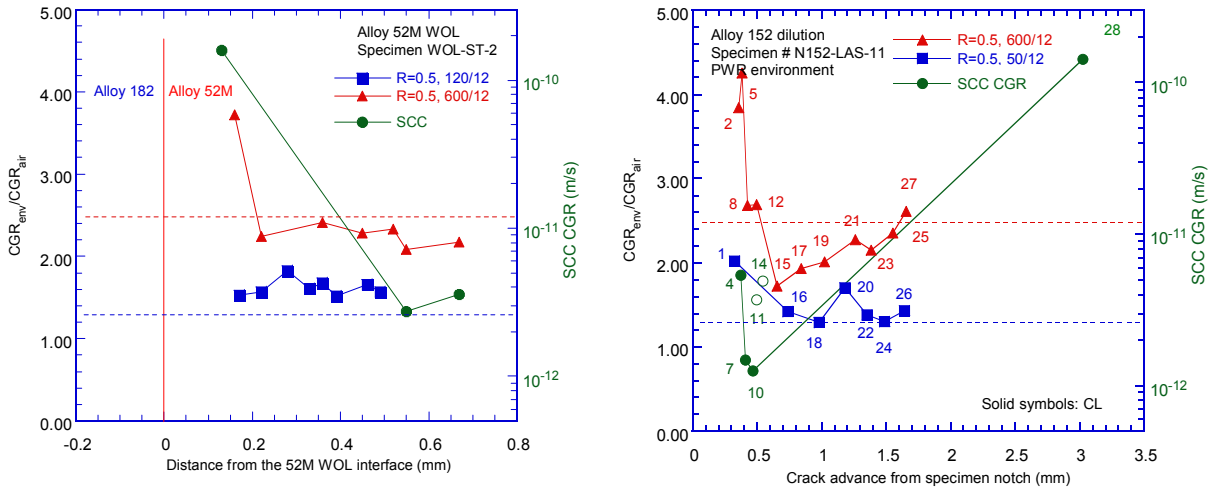


(a) (b)

**Figure 4-5 Environmental enhancement of two control test conditions and SCC CGRs vs. distance from the specimen notch for 1st layer (a) Alloy 52-182 specimen WOL-ST-2, and (b) Alloy 152-LAS specimen N152-LAS-11.**

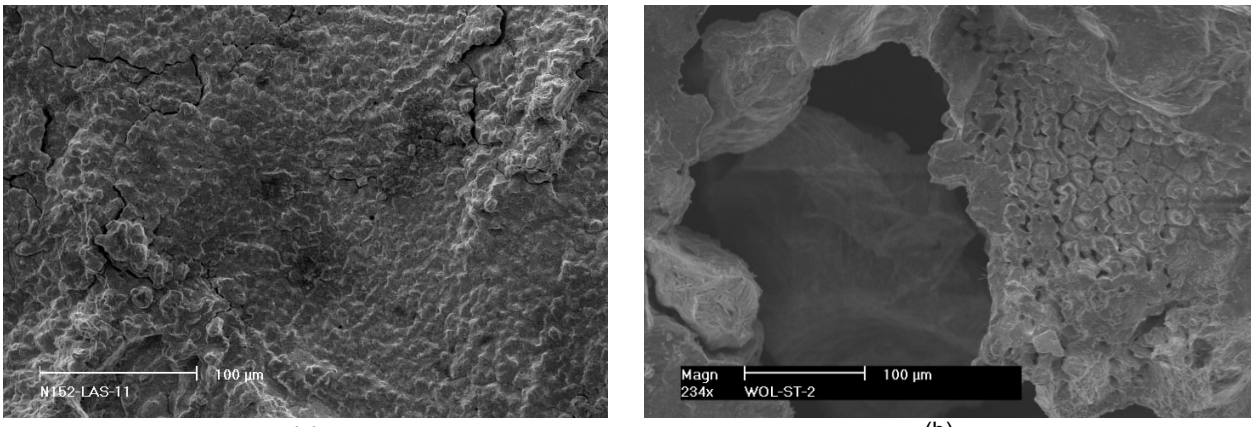


(a) (b)

**Figure 4-6 SCC fracture modes the regions near the interface in (a) Alloy 152 – LAS, and (b) Alloy 52M WOL specimens tested in simulated primary water environment. SCC propagation is from bottom to top.**

## 4.4 The Effect of Local Cr Concentration and that of the Substrate on the Cyclic and SCC CGR Response of a Cr-Depleted 1st Layer High Cr Ni-Base Weldment

The effect of the local elemental concentration of Cr is unclear. While the Alloy 52M WOL SCC CGR data (Fig. 4-2) appears to show a trend, the Alloy 152-LAS SCC CGR data (Fig. 4-4) shows a large scatter, and no clear Cr effect. The plausible reasons for the scatter are off-plane cracking as well as possible differences in the local microstructure and Cr concentration. Off-plane cracking was well-documented in these tests, hence the inability of the DC potential method to measure the SCC CGRs correctly in such cases may be partly responsible for the data scatter. However, it is important to note that relatively fast SCC in the first layer of Alloy 152-LAS (approximately 25 wt. % Cr) was observed in both weld directions, along and normal to

the dendritic grains (Fig. 3-64, IG-2 and Fig. 3-78, IG-2). The mechanism that triggers one fracture mode over the other is not at all understood. Further complicating the analysis is the fact that microstructures having even less Cr (approximately 20 wt. % Cr, see for example the "swirls" in Fig. 3-77) appeared to slow down/arrest crack propagation. Moreover, the cross sections shown in Figs. 3-62 and 3-85c does not suggest that SCC tends to propagate towards the interface with the LAS, or along an expected Cr gradient as one would expect if Cr content were to play a dominant role in the SCC at hand. In fact, for both Alloy 152-LAS specimens that were tested, the SCC propagation was away from the interface with the LAS. In summary, it appears that the elemental concentration of Cr, in itself, does not fully predict the (local) SCC susceptibility.

Despite the lack of clear trends in the SCC CGR data or an understanding of the mechanism(s) at work, the SCC in the first layer of Alloy 52M-182 WOL and Alloy 152-LAS (approximately 25 wt. % Cr) was found to occur in similar fracture modes (Fig. 4-6) and have equivalent SCC CGRs (Figs. 4-2 and 4-4). Moreover, the cyclic responses were found to be similar (Figs. 4-3 and 4-5), and overall consistent with those expected for a Ni-base weld. As such it appears that the type of material on which the weld is deposited, either Alloy 182 or Alloy 533 LAS, does not affect the cyclic and SCC CGR response in those first layer welds. The only difference was found to occur in cases where the cracks intersected the interface with the substrate: at the Alloy 52M-182 interface, the SCC CGR is even faster than in the first layer of Alloy 52M, while SCC is arrested at the intersection with the Alloy 152-LAS interface. The latter observation is consistent with those from the literature [26, 27]. As such, attempts to transition SCC cracks in high-purity or sulphate-containing oxygenated water under constant or periodic partial unloading conditions from Alloy 182 into LAS were unsuccessful, and were found to slow down and arrest [27] or blunt at the LAS interface [26].

# 5 CONCLUSIONS

This report summarizes testing performed at ANL to investigate the SCC susceptibility at or near the interface between the high Cr weld metals, Alloys 52 and 152, and low Cr weld metals or steel, where localized Cr dilution could affect the cracking behavior. The tests were performed using two mockups. The first was a WOL mockup of Alloy 52M to Alloy 182, and the second was a butt weld mockup of Alloy 152 to LAS.

SCC testing on the Alloy 52M-182 WOL was conducted in two orientations, TS (weld interface is perpendicular to the crack growth direction) and ST (crack growth direction is parallel to the weld interface). SCC CGRs were measured as a function of orientation and distance from the interface between the two materials. It was found that in the TS orientation, as SCC cracks in Alloy 182 approached within 1 mm of the interface with Alloy 52M, the CGRs decreased by approximately one order of magnitude. When the crack intersected the interface, branches extended along the boundary between Alloy 52M and 182, even as the leading crack front advanced into the Alloy 52M. Testing was undertaken in the ST orientation to measure the SCC CGRs at the interface between the two welds and in first layer of Alloy 52M weld beads within the WOL. The SCC CGRs along the interface between the two welds was measured to be as high as the MRP-115 75$^{th}$ percentile curve for Alloys 82/182 [1]. The SCC CGR in the first layer of Alloy 52M weld beads was a factor of two lower than the MRP-115 75$^{th}$ percentile curve [1], though the dendritic grains were not favorably oriented for cracking.

SCC CGR testing on the butt weld mockup was conducted on two specimens aligned in the first layer of Alloy 152 weld beads adjacent to LAS. The environmental enhancement of the fatigue CGR was found to be a good predictor for the SCC response. Both fatigue and SCC CGR responses were similar to those observed in the first layer of Alloy 52M weld beads within the WOL. In both cases, in the most favorable orientations, the SCC CGRs were within a factor of two of the MRP-115 75$^{th}$ percentile curve [1]. Material compositional analyses taken along the crack path indicated that locations with the highest measured crack growth did not necessarily correlate with the lowest chromium content. This suggests that microstructural factors, in addition to the chromium content, could affect the SCC susceptibility near the interface. EBSD analyses identified apparent grain or dendrite packet boundaries in the Alloy 152 weld metal that are oriented parallel to the Alloy 152-LAS interface and in the direction of the crack growth. These may be preferential crack paths that contribute to the relatively fast growth, but it will require analysis of additional welds to confirm this hypothesis.

The fatigue and SCC growth rates near the interfaces were similar in the Alloy 52M-182 WOL and the Alloy 152-LAS butt weld mockups, respectively, as were the fracture modes. As such, it appears that the type of material on which the weld is deposited, whether Alloy 182 or Alloy 533 LAS, does not uniquely affect the SCC susceptibility in the adjacent high-Cr weld metal. The only difference was found to occur when the crack actually intersected the interface. At the Alloy 52M-182 interface, the SCC CGR is even faster than in the first layer of Alloy 52M weld beads, while SCC is arrested when in intersects the Alloy 152-LAS interface.

These data suggest that safety evaluations to determine the appropriate in-service inspection requirements for components that could be affected by SCC, should consider the potential for preferential cracking along weld interfaces. However, additional testing is needed to further assess the mechanistic cause of this behavior and to understand whether this would manifest in welds in actual plant service, where the geometries, fabrication methods, and other properties may differ from those of the welds described in this report.

# 6 REFERENCES


1. Materials Reliability Program: Crack Growth Rates for Evaluating Primary Water Stress Corrosion Cracking (PWSCC) of Alloy 82, 182, and 132 Welds (MRP-115), EPRI, Palo Alto, CA: 2004. 1006696.

2. Materials Reliability Program: Resistance of Alloys 690, 52 and 152 to Primary Water Stress Corrosion Cracking (MRP-237, Rev. 1): Summary of Findings From Completed and Ongoing Test Programs Since 2004. EPRI, Palo Alto, CA: 2008. 1018130.

3. Materials Reliability Program: Resistance of Alloys 690, 152, and 52 to Primary Water Stress Corrosion Cracking (MRP-237, Rev.2): Summary of Findings Between 2008 and 2012 from Completed and Ongoing Test Programs. EPRI, Palo Alto, CA: 2013. 3002000190

4. Materials Reliability Program: Resistance to Primary Water Stress Corrosion Cracking of Alloy 690 in Pressurized Water Reactors (MRP-258). EPRI, Palo Alto, CA: 2009. 1019086.

5. Dunn, D., Alexandreanu, B., Toter, W., “Shielded Metal Arc Welding Parameters for Primary Water Stress Corrosion Cracking Test Materials,” Technical Letter Report ML13171A113, June 2013.

6. Alexandreanu, B., O. K. Chopra, and W. J. Shack, “Crack Growth Rates and Metallographic Examinations of Alloy 600 and Alloy 82/182 from Field Components and Laboratory Materials Tested in PWR Environments,” NUREG/CR–6964, ANL–07/12, May 2008.

7. Material Documentation Report for Consumers Power Midland (620-0012-51) and TMI-2 (620-0006-51) Reactor Vessel Lower Head Material, The Babcock & Wilcox Company, BAW-2071, January 1989.

8. American Society for Testing and Materials, “Standard Test Method for Measurement of Fatigue Crack Growth Rates,” ASTM E647-08, DOI 10.1520/E0647-08, West Conshohocken, PA, 2008.

9. American Society for Testing and Materials, “Standard Test Method for Determining a Threshold Stress Intensity Factor for Environment-Assisted Cracking of Metallic Materials,” ASTM E1681-03, DOI 10.1520/E1681-03R08, West Conshohocken, PA, 2008.

10. Electric Power Research Institute, “PWR Primary Water Chemistry Guidelines,” Volume 1, Revision 4, EPRI, Palo Alto, CA, 1999.

11. Electric Power Research Institute, “Materials Reliability Program (MRP) Crack Growth Rates for Evaluating Primary Water Stress Corrosion Cracking (PWSCC) of Thick-Wall Alloy 600 Materials (MRP-55),” Revision 1, 1006695, Palo Alto, CA, 2002.

12. Ruther, W. E., W. K. Soppet, and T. F. Kassner, “Corrosion Fatigue of Alloys 600 and 690 in Simulated LWR Environments,” NUREG/CR-6383, ANL-95/37, April 1996.

13. Ruther, W. E., W. K. Soppet, T. F. Kassner, and W. J. Shack, “Environmentally Assisted Cracking of Alloys 600 and 690 in Simulated LWR Water,” in Environmentally Assisted Cracking in Light Water Reactors, Semiannual Report, January 1998-July 1998, NUREG/CR-4667, Vol. 26, ANL-98/30, pp. 25-32, March 1999.

14. Chopra, O. K., W. K. Soppet, and W. J. Shack, “Effects of Alloy Chemistry, Cold Work, and Water Chemistry on Corrosion Fatigue and Stress Corrosion Cracking of Nickel Alloys and Welds,” NUREG/CR-6721, ANL-01/07, April 2001.

15. Cassagne, T. B., and A. Gelpi, “Crack Growth Rate Measurements on Alloy 600 Steam Generator Tubes in Steam and Primary Water,” Proc. of the Fifth Intl. Symp. on Environmental Degradation of Materials in Nuclear Power Systems--Water Reactors, American Nuclear Society, La Grange Park, IL, pp. 518-524, 1991.

16. Foster, J. P., W. H. Bamford, and R. S. Pathania, “Initial Results of Alloy 600 Crack Growth Rate Testing in a PWR Environment,” Proc. of the Seventh Intl. Symp. on Environmental Degradation of Materials in Nuclear Power Systems-Water Reactors, NACE International, Houston, TX, pp. 25-39, 1995.

17. Magdowski, R., F. Vaillant, C. Amzallag, and M. O. Speidel, “Stress Corrosion Crack Growth Rates of Alloy 600 in Simulated PWR Coolant,” Proc. of the 8th Intl. Symp. on Environmental Degradation of Materials in Nuclear Power Systems--Water Reactors, S. M. Bruemmer, ed., American Nuclear Society, La Grange Park, IL, pp. 333-338, 1997.

18. Le Hong, S., C. Amzallag, and A. Gelpi, “Modeling of Stress Corrosion Crack Initiation on Alloy 600 in Primary Water of PWRs,” Proc. of the Ninth Intl. Symp. on Environmental Degradation of Materials in Nuclear Power Systems--Water Reactors, F. P. Ford, S. M. Bruemmer, and G. S. Was, eds., Minerals, Metals, and Materials Society, Warrendale, PA, pp. 115-122, 1999.

19. Raquet, O., and G. Santarini, “Stress Corrosion Crack Propagation Rate of Alloy 600 in the Primary Water of PWR Influence of a Cold Worked Layer,” Proc. of the Ninth Intl. Symp. on Environmental Degradation of Materials in Nuclear Power Systems--Water Reactors, F. P. Ford, S. M. Bruemmer, and G. S. Was, eds., Minerals, Metals, and Materials Society, Warrendale, PA, pp. 207-213, 1999.

20. Alexandreanu, B., O. K. Chopra, and W. J. Shack, “Crack Growth Rates of Nickel Alloys from the Davis-Besse and V. C. Summer Power Plants in a PWR Environment,” NUREG/CR–6921, ANL–05/55, November 2006.

21. Alexandreanu, B., O. K. Chopra, and W. J. Shack, “Crack Growth Rates of Nickel Alloy Welds in a PWR Environment,” NUREG/CR–6907, ANL–04/3, May 2006.

22. Alexandreanu, B., Chen, Y., Natesan, K., and Shack, W. J., SCC Behavior of Alloy 152 Weld in a PWR Environment, 15th International Conference on Environmental Degradation of Materials in Nuclear Power Systems – Water Reactors, Cheyenne Mountain Resort, Colorado Springs, Colorado, August 7-11, 2011.

23. Alexandreanu, B., Y. Yang, Y. Chen, and W. J. Shack, “Stress Corrosion Cracking in Nickel-Base Alloys 690 and 152 Weld in Simulated PWR Environment - 2009,” NUREG/CR–7137, ANL–10/36, June 2012.

24. Van Der Sluys, W. A., B. A. Young, and D. Doyle, “Corrosion Fatigue Properties on Alloy 690 and some Nickel–Based Weld Metals,” Assessment Methodologies for Preventing Failure: Service Experience and Environmental Considerations, PVP Vol. 410-2, ed., R. Mohan, American Society of Mechanical Engineers, New York, pp. 85–91, 2000.

25. Psaila–Dombrowski, M. J., C. S. Wade, J. M. Sarver, W. A. Van Der Sluys, and P. E. Doherty, “Evaluation of Weld Metals 82, 152, 52, and Alloy 690 Stress Corrosion Cracking and Corrosion Fatigue Susceptibility,” Proc. of the 8th Intl. Symp. on Environmental Degradation of Materials in Nuclear Power Systems-Water Reactors, S. M. Bruemmer, ed., American Nuclear Society, La Grange Park, IL, pp. 412–421, 1997.

26. Hou, J., Peng, Q., Takeda Y., Jiro, K., Shoji, T., Microstructure and stress corrosion cracking of the fusion boundary region, in an alloy 182-A533B low alloy steel dissimilar weld joint, Corrosion Science 52 (2010) 3949–3954.

27. Seifert, H.P., Ritter, S., Shoji, T., Peng, Q.J., Takeda, Y., Lu, Z.P., Environmentally-assisted cracking behaviour in the transition region of an Alloy182/SA 508 Cl.2 dissimilar metal weld joint in simulated boiling water reactor normal water chemistry environment, Journal of Nuclear Materials 378 (2008) 197–210.

28. Toloczko, M., Olszta, M., Overman, N., and Bruemmer, S., Alloy 152-LAS Dilution Zone PWSCC Testing, Alloy 690/52/125 Research Collaboration Meeting, Tampa, Florida, December 2-5, 2014.

29. Yonezawa, T., personal communication, December 2015.

30. Hanninen, H., personal communication, September 2015.

31. Nelson, T.W., Lippold, J.C., and Mills, M.J., Nature and Evolution of the Fusion Boundary in Ferritic-Austenitic Dissimilar Metal Welds — Part 2: On-Cooling Transformations, Supplement to the Welding Journal, October 2000, 267.

NRC FORM 335
(12-2010)
NRCMD 3.7

U.S. NUCLEAR REGULATORY COMMISSION

# BIBLIOGRAPHIC DATA SHEET

*(See instructions on the reverse)*

1. REPORT NUMBER
(Assigned by NRC, Add Vol., Supp., Rev., and Addendum Numbers, if any.)

**NUREG/CR-7226**

2. TITLE AND SUBTITLE

**Primary Water Stress Corrosion Cracking of High-Chromium, Nickel-Base Welds Near Dissimilar Metal Weld Interfaces**

3. DATE REPORT PUBLISHED

| MONTH | YEAR |
|---|---|
| **January** | **2018** |

4. FIN OR GRANT NUMBER

5. AUTHOR(S)

B. Alexandreanu, Y. Chen, K. Natesan, and W. J. Shack

6. TYPE OF REPORT

Technical

7. PERIOD COVERED (Inclusive Dates)

8. PERFORMING ORGANIZATION - NAME AND ADDRESS (If NRC, provide Division, Office or Region, U. S. Nuclear Regulatory Commission, and mailing address; if contractor, provide name and mailing address.)

Argonne National Laboratory
Argonne, IL 60439

9. SPONSORING ORGANIZATION - NAME AND ADDRESS (If NRC, type "Same as above", if contractor, provide NRC Division, Office or Region, U. S. Nuclear Regulatory Commission, and mailing address.)

Division of Engineering
Office of Nuclear Regulatory Research
U.S. Nuclear Regulatory Commission
Washington, D.C. 20555-0001

10. SUPPLEMENTARY NOTES

M. Audrain

11. ABSTRACT (200 words or less)

The report summarizes the SCC susceptibility at or near interfaces between Alloy 52 and 152 weld metals and other weld or base metals. Alloy 52/152 are high-chromium weld metals used in RPV penetration nozzles and as overlays, inlays, or onlays for DM welds. Alloys 52 and 152 typically show very low SCC growth rates in testing and are not known to have cracked in service. Questions remain if localized dilution of chromium content or microstructural features near the interface with the low-chromium weld metals Alloy 82/182 could affect the SCC response. For this study, SCC growth rates were measured on a WOL mockup with Alloy 52M, Alloy 182 and on a butt weld mockup with Alloy 152 joined to LAS. Both mockups resulted in CGRs that are higher than previously reported for weld metals, even though the dendrites were not favorably oriented for cracking. In the WOL mockup, crack branching along the interface was observed when the cracking direction was perpendicular to the interface. In the butt weld mockup, material compositional analyses indicated that locations with the highest measured CGRs did not necessarily correlate with the lowest chromium content. This suggests microstructural factors could affect SCC susceptibility near the interface.

12. KEY WORDS/DESCRIPTORS (List words or phrases that will assist researchers in locating the report.)

Alloy 690
Nickel alloys
Cold work
Stress corrosion cracking

13. AVAILABILITY STATEMENT

unlimited

14. SECURITY CLASSIFICATION

*(This Page)*
unclassified

*(This Report)*
unclassified

15. NUMBER OF PAGES

16. PRICE

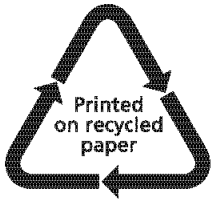


Federal Recycling Program


UNITED STATES
NUCLEAR REGULATORY COMMISSION
WASHINGTON, DC 20555-0001

OFFICIAL BUSINESS

NUREG/CR-7226

# Primary Water Stress Corrosion Cracking of High-Chromium, Nickel-Base Welds Near Dissimilar Metal Weld Interfaces

January 2018